

**UCLA**

**UCLA Electronic Theses and Dissertations**

**Title**

Thermal modeling of electrochemical capacitors

**Permalink**

<https://escholarship.org/uc/item/4r11b122>

**Author**

D'Entremont, Anna Leone

**Publication Date**

2015

Peer reviewed|Thesis/dissertation

UNIVERSITY OF CALIFORNIA  
Los Angeles

# **Thermal modeling of electrochemical capacitors**

A dissertation submitted in partial satisfaction  
of the requirements for the degree  
Doctor of Philosophy in Mechanical Engineering

by

**Anna Leone d'Entremont**

2015

© Copyright by  
Anna Leone d'Entremont  
2015

## ABSTRACT OF THE DISSERTATION

# Thermal modeling of electrochemical capacitors

by

**Anna Leone d’Entremont**

Doctor of Philosophy in Mechanical Engineering

University of California, Los Angeles, 2015

Professor Laurent G. Pilon, Chair

The present study rigorously develops continuum thermal models of electrochemical capacitors (ECs) accounting for the dominant interfacial and transport phenomena. It also aims to identify design rules and modeling tools to define safe modes of operation and to develop appropriate thermal management strategies. ECs are promising electrical energy storage devices, particularly for providing high power or long cycle life. They can be divided into two categories, namely electric double layer capacitors (EDLCs) storing charge electrostatically in the electric double layer (EDL) at the electrode/electrolyte interface and pseudocapacitors using both EDL and chemical charge storage. Unfortunately, ECs generate heat during operation due to a variety of interfacial and transport phenomena. Consequently, they may experience substantial changes in temperature, leading to problems such as accelerated aging and increased self-discharge rates. EC charge storage mechanisms involve complex multiphysics and multiscale transport phenomena and this complexity has impeded the physical understanding of EC heating. This study derives rigorous, physics-based continuum models for both EDLCs and pseudocapacitors from first principles. Then, detailed numerical simulations were performed to investigate characteristic thermal behavior, to physically interpret experimental measurements from the literature, and to develop design rules.

First, thermal models were developed for EDLCs. The heat diffusion equation and associated heat generation rates were derived from first principles and coupled with the transient electrodiffusion of ions in binary and symmetric electrolyte. Irreversible Joule heating and

reversible heat generation rates due to ion diffusion, steric effects, and changes in entropy of mixing in the electrolyte were formulated. The predicted temperature rise for planar EDLCs qualitatively reproduced experimental data from the literature under various charging/discharging conditions. Scaling analysis simplified this model from twelve independent design parameters to seven dimensionless similarity parameters. Scaling laws were developed for the heat generated during a charging step and for the maximum temperature oscillations under galvanostatic cycling. In addition, a first-order thermal analysis for EDLCs was developed based on the lumped-capacitance approximation and accounting for both irreversible and reversible heating. A simple analytical expression for the overall temperature rise during galvanostatic cycling was derived and scaled. This simple thermal model enables rapid estimation of temperature evolution in EDLCs without computationally intensive numerical simulations and was quantitatively validated with experimental measurements from commercial EDLC devices. Moreover, the first-principles thermal model was generalized to account for multiple ion species and/or asymmetric electrolytes. Simulations with binary and asymmetric electrolytes indicated that the irreversible Joule heating decreased with increasing valency and/or diffusion coefficient of either ion while the local reversible heating near a given electrode increased with increasing counterion valency and/or decreasing counterion diameter.

Finally, the first-principles model was extended to hybrid pseudocapacitors by accounting for redox reactions and  $\text{Li}^+$  intercalation and by rigorously deriving the associated irreversible and reversible heat generation rates. The model accounted simultaneously for charge storage by EDL formation and by faradaic reactions. Simulations were performed for a planar hybrid pseudocapacitor to investigate the electrochemical interfacial and transport phenomena as well as the thermal behavior under galvanostatic cycling. Two asymptotic regimes were identified corresponding to (i) dominant faradaic charge storage at low current and low frequency or (ii) dominant EDL charge storage at high current and high frequency. Predicted cell potential, heat generation rates, and temperature showed good qualitative agreement with experimental measurements and can be used to physically interpret experimental observations.

The dissertation of Anna Leone d'Entremont is approved.

Ann Karagozian

Adrienne Lavine

Bruce Dunn

Laurent G. Pilon, Committee Chair

University of California, Los Angeles

2015

# TABLE OF CONTENTS

<b>1</b>	<b>Introduction . . . . .</b>	<b>5</b>
1.1	Need for electrical energy storage . . . . .	5
1.1.1	Hybrid and electric vehicles . . . . .	5
1.1.2	Expanding the usability of energy sources . . . . .	6
1.2	Types of electrical energy storage . . . . .	6
1.2.1	Batteries: Chemical charge storage . . . . .	6
1.2.2	Conventional capacitors: Physical charge storage . . . . .	7
1.2.3	Electrochemical capacitors . . . . .	10
1.2.4	Energy storage performance . . . . .	11
1.3	Motivation of the present study . . . . .	12
1.4	Objectives of the present study . . . . .	13
1.5	Organization of the document . . . . .	13
<b>2</b>	<b>Background . . . . .</b>	<b>15</b>
2.1	Capacitance . . . . .	15
2.2	Electric double layer structure . . . . .	15
2.3	Materials for ECs . . . . .	18
2.4	Modeling ion transport in electrolytes . . . . .	19
2.4.1	Poisson-Nernst-Planck (PNP) model . . . . .	20
2.4.2	Modified Poisson-Nernst-Planck (MPNP) model . . . . .	21
2.4.3	Generalized modified Poisson-Nernst-Planck (GMPNP) model . . . . .	22
2.5	Modeling heat transfer . . . . .	23
2.5.1	Heat diffusion equation . . . . .	23

2.5.2	Joule heating . . . . .	24
2.6	Thermal behavior of ECs . . . . .	25
2.6.1	Effects of temperature on EDLC performance . . . . .	25
2.6.2	Experimentally measured temperature and heat generation rates in ECs	26
2.6.3	Thermal models of ECs . . . . .	31
2.6.4	Equivalent resistances of ECs . . . . .	33
2.6.5	Open questions . . . . .	33
<b>3</b>	<b>Thermal modeling of planar EDLCs under a step change in potential . .</b>	<b>35</b>
3.1	Analysis . . . . .	35
3.1.1	Schematic and assumptions . . . . .	35
3.1.2	Governing equations . . . . .	36
3.1.3	Boundary and initial conditions . . . . .	37
3.1.4	Scaling analysis . . . . .	39
3.1.5	Method of solution . . . . .	41
3.1.6	Data processing . . . . .	42
3.2	Results and discussion . . . . .	43
3.2.1	Illustration of scaling analysis . . . . .	43
3.2.2	Scaling laws for Joule heating in EDLCs under a step change in potential	48
3.3	Conclusion . . . . .	54
<b>4</b>	<b>First-principles thermal modeling of EDLCs under galvanostatic cycling with binary and symmetric electrolyte . . . . .</b>	<b>57</b>
4.1	Analysis . . . . .	57
4.1.1	Schematic and assumptions . . . . .	57
4.1.2	Electrochemical transport model . . . . .	58



4.1.3	Thermal model . . . . .	60
4.1.4	Constitutive relationships . . . . .	65
4.1.5	Method of solution . . . . .	66
4.2	Results and discussion . . . . .	67
4.2.1	Electric potential . . . . .	67
4.2.2	Ion concentrations . . . . .	67
4.2.3	Current density . . . . .	70
4.2.4	Thermal behavior . . . . .	70
4.2.5	Comparison with experimental data . . . . .	77
4.3	Conclusion . . . . .	82
<b>5</b>	<b>First-order thermal model of commercial EDLC devices . . . . .</b>	<b>84</b>
5.1	Analysis . . . . .	84
5.1.1	Dimensional energy balance . . . . .	85
5.1.2	Scaling analysis . . . . .	86
5.1.3	Irreversible and reversible temperatures . . . . .	87
5.1.4	Thermally insulated EDLC . . . . .	87
5.1.5	Method of solution . . . . .	88
5.1.6	Experimental data . . . . .	88
5.2	Results and discussion . . . . .	90
5.2.1	Parametric study . . . . .	90
5.2.2	EDLCs cooled by natural convection . . . . .	92
5.2.3	Thermally insulated EDLC . . . . .	94
5.3	Conclusion . . . . .	99
<b>6</b>	<b>Scaling laws for EDLC heating and temperature oscillations . . . . .</b>	<b>100</b>

6.1	Motivation for scaling . . . . .	100
6.2	Analysis . . . . .	101
6.2.1	Problem statement . . . . .	101
6.2.2	Initial and boundary conditions for planar electrodes . . . . .	102
6.2.3	Scaling analysis . . . . .	102
6.2.4	Dimensionless initial and boundary conditions for planar electrodes . . . . .	104
6.2.5	Physical interpretation . . . . .	106
6.2.6	Numerical simulations . . . . .	107
6.3	Results and discussion . . . . .	109
6.3.1	Illustration of scaling analysis . . . . .	109
6.3.2	Scaling laws for thermal effects . . . . .	115
6.4	Conclusion . . . . .	126
<b>7</b>	<b>Thermal effects of asymmetric electrolytes in EDLCs . . . . .</b>	<b>127</b>
7.1	Analysis . . . . .	127
7.1.1	Schematic and assumptions . . . . .	127
7.1.2	Heat generation in multi-species and asymmetric electrolytes . . . . .	128
7.1.3	Initial and boundary conditions . . . . .	131
7.1.4	Constitutive relationships . . . . .	132
7.1.5	Method of solution . . . . .	133
7.2	Results and discussion . . . . .	133
7.2.1	Electric potential . . . . .	135
7.2.2	Concentrations . . . . .	137
7.2.3	Irreversible Joule heat generation rate $\dot{q}_{J,irr}$ . . . . .	139
7.2.4	Reversible heating . . . . .	139

7.2.5	Temperature . . . . .	150
7.2.6	Asymmetric electrolytes in porous electrodes . . . . .	153
7.3	Conclusion . . . . .	154
<b>8</b>	<b>Electrochemical transport phenomena in hybrid pseudocapacitors under galvanostatic cycling . . . . .</b>	<b>156</b>
8.1	Background . . . . .	157
8.1.1	Experimental studies of pseudocapacitive materials . . . . .	157
8.1.2	Existing models of pseudocapacitors . . . . .	160
8.2	Analysis . . . . .	162
8.2.1	Schematic and assumptions . . . . .	162
8.2.2	Governing equations . . . . .	164
8.2.3	Initial and boundary conditions . . . . .	166
8.2.4	Constitutive relationships . . . . .	169
8.2.5	Method of solution . . . . .	171
8.2.6	Analytical expressions for limiting cases . . . . .	172
8.3	Results and discussion . . . . .	175
8.3.1	Current densities . . . . .	175
8.3.2	Intercalated $\text{Li}^+$ concentration in the pseudocapacitive electrode . . .	177
8.3.3	Electric potentials . . . . .	178
8.3.4	Ion concentrations in the electrolyte . . . . .	182
8.3.5	Effect of variable equilibrium potential drop $\Delta\psi_{eq}$ . . . . .	184
8.3.6	Charging by $\text{Li}^+$ deintercalation . . . . .	187
8.4	Conclusion . . . . .	189
<b>9</b>	<b>First-principles thermal modeling of hybrid pseudocapacitors under gal-</b>	

<b>vanostatic cycling</b>	<b>191</b>
9.1 Analysis	191
9.1.1 Schematic and assumptions	191
9.1.2 Electrochemical transport model	192
9.1.3 Thermal model	192
9.1.4 Initial and boundary conditions	197
9.1.5 Constitutive relationships	199
9.1.6 Method of solution	200
9.1.7 Data processing	201
9.2 Results and discussion	202
9.2.1 Electrochemical transport	202
9.2.2 Heat generation rates	209
9.2.3 Temperature	217
9.3 Conclusion	219
<b>10 Future work</b>	<b>221</b>
10.1 Thermal modeling for porous electrode geometries	221
10.1.1 First-principles simulations of porous electrodes	222
10.1.2 Empirical fitting of scaling laws for planar electrodes	222
10.2 Experimental measurements of heat generation rates and temperature	223
10.3 Expanding available property data for EC materials	224
<b>Appendices</b>	<b>226</b>
<b>A Supplementary material for Chapter 6</b>	<b>227</b>
A.1 Illustration of scaling analysis: Dimensionless heat generation rates	227

A.2	Correlations for thermal effects . . . . .	229
A.2.1	Temperature oscillation amplitude . . . . .	229
A.2.2	Heat generation . . . . .	230
<b>B</b>	<b>Supplementary material for Chapter 7 . . . . .</b>	<b>233</b>
B.1	IR drops in cell potential . . . . .	233
B.2	Irreversible heat generation rate . . . . .	233
<b>C</b>	<b>Three-dimensional formulation of faradaic heat generation rates . . . . .</b>	<b>236</b>
	<b>References . . . . .</b>	<b>239</b>

## LIST OF FIGURES

1.1	Classification of electrical energy storage systems. . . . .	7
1.2	Illustration of the charge storage mechanism of a lithium-ion battery during charging and discharging (from Ref. [11]). . . . .	8
1.3	Illustrations of (a) a dielectric capacitor, (b) an electric double layer capacitor (EDLC), and (c) a hybrid pseudocapacitor. . . . .	9
1.4	Comparison of energy and power densities of different EES systems (from Ref. [6]). . . . .	11
2.1	Illustrations of the (a) Helmholtz, (b) Gouy-Chapman, (c) Stern, and (d) Grahame models of EDL structure. . . . .	16
2.2	Measured EDLC surface temperature as a function of time for galvanostatic cycling at three different currents over the potential window 1.5–2.5 V (Figure 10 from Ref. [29]). . . . .	27
2.3	Measured EDLC surface temperature as a function of time for constant-current cycling beginning with charging versus beginning with discharging. (Figure 8 from Ref. [29]). . . . .	28
2.4	Measured temperature as a function of time for (a) three surface locations [T(Lid-), T <sub>surface</sub> , T(Lid+)] and four internal locations (T1, T2, T3, and T4) as the EDLC rose from its initial temperature to an oscillatory steady state and (b) internal locations T1-T4 at oscillatory steady state. (Figure 10 from Ref. [76]). . . . .	30
3.1	Illustration of simulated 1D cell along with the associated coordinate system and computational domain. . . . .	36

3.2	Predicted (a) electric potential at the Stern/diffuse layer interface $\psi(a/2, t)$ as a function of time $t$ and (b) corresponding dimensionless electric potential $\psi^*(a^*/2, t^*)$ as a function of dimensionless time $t^*$ for Cases 1 to 3 (Table 3.1). Similar results were obtained for other locations. . . . .	45
3.3	Predicted (a) anion concentration at the Stern/diffuse layer interface $c_2(a/2, t)$ as a function of time $t$ and (b) corresponding dimensionless anion concentration $c_2^*(a^*/2, t^*)$ as a function of dimensionless time $t^*$ for Cases 1 to 3 (Table 3.1). . . . .	46
3.4	Predicted (a) temperature rise at the Stern/diffuse layer interface $\Delta T(a/2, t) = T(a/2, t) - T_0$ as a function of time $t$ and (b) corresponding dimensionless temperature rise $T^*(a^*/2, t^*)$ as a function of dimensionless time $t^*$ for Cases 1 to 3 (Table 3.1). . . . .	47
3.5	Predicted (a) heat generation rate $\dot{q}(x, t)$ as a function of location $x$ and at time $t$ such that $t^* = 63$ and (b) corresponding dimensionless heat generation $\dot{q}^*(x^*, 63)$ as a function of dimensionless location $x^*$ for Cases 1 to 3 (Table 3.1). . . . .	49
3.6	Comparison of the dimensionless peak heat generation rate $\dot{q}_{peak}^*$ computed numerically with that predicted by Equation (3.29) for realistic range of dimensionless numbers $0.33 \leq a^* \leq 9.9$ , $2.5 \times 10^4 \leq L^* \leq 1.5 \times 10^6$ , $19.47 \leq \psi_{s,max}^* \leq 58.41$ , and $0.0012 \leq \nu_p < 1.0$ . . . . .	52
3.7	(a) Total dimensionless heat generation $Q_{J,irr}^*$ as a function of $L^*$ for $\psi_{s,max}^* = 19$ . (b) Total dimensionless heat generation $Q_{J,irr}^*$ as a function of $\psi_{s,max}^*$ for $L^* = 6.5 \times 10^4$ and $a^* = 2.2$ . (c) Ratio $\psi_{s,max}^{*2}/Q_{J,irr}^* L^*$ as a function of $1/a^*$ , showing asymptotes $f_1(\nu_p)$ and $f_2(a^*)$ . . . . .	53
3.8	Ratio $\psi_{s,max}^{*2}/Q_{J,irr}^* L^*$ as a function of (a) $\nu_p$ for $a^* \ll 1$ and (b) $a^*$ for $a^* \gg 1$ and $0.0012 \leq \nu_p \leq 0.88$ along with the associated power law fits of the curvilinear asymptotes $f_1(\nu_p)$ and $f_2(a^*)$ . . . . .	55
4.1	Illustration of simulated 1D cell and associated coordinate system. . . . .	58

4.2	(a) Electric potential $\psi(0, t)$ at the surface of Electrode A and (b) anion concentration $c_2(a/2, t)$ at the Stern/diffuse layer interface as functions of time.	68
4.3	Predicted anion concentrations $c_2(x, t)$ (a) near Electrode A and (b) near Electrode B as a function of $x$ at various times during a charging step. . . . .	69
4.4	Predicted current density (a) $j(L, t)$ at the centerline as a function of time $t$ and (b) $j(x, 14 \text{ ms})$ as a function of location $x$ . . . . .	71
4.5	Predicted heat generation rates $\dot{q}_{J,irr}(x, t)$ , $\dot{q}_{E,d}(x, t)$ , $\dot{q}_{E,s}(x, t)$ , $\dot{q}_{S,c}(x, t)$ , and $\dot{q}_{S,T}(x, t)$ as a function of location $x$ (a) at time $t = 14 \text{ ms}$ shortly before the end of a charging step and (b) at time $t = 16 \text{ ms}$ shortly after the beginning of a discharging step. . . . .	72
4.6	Predicted total heat generation rate terms $\dot{Q}''_{J,irr}(t)$ , $\dot{Q}''_{E,d}(t)$ , $\dot{Q}''_{E,s}(t)$ , and $\dot{Q}''_{S,c}(t)$ as well as the overall heat generation rate $\dot{Q}''(t)$ as functions of time $t$ .	74
4.7	Predicted temperature change (a) $T(a/2, t) - T_0$ at the Stern/diffuse layer interface and (b) $T(L, t) - T_0$ at the centerline as a function of time $t$ as each individual heat generation rate term was added. . . . .	76
4.8	(a) Numerically predicted temperature change $T(L, t) - T_0$ at the centerline and (b) measured surface temperature of a commercial EDLC (reproduced from Figure 8 of Ref. [29]) as functions of time $t$ for cases starting with either a charging step or a discharging step. . . . .	78
4.9	(a) Predicted temperature rise $T(L, t) - T_0$ at the centerline for cycling at three different current densities $j_s$ over the same potential window and (b) measured surface temperature of a commercial EDLC during cycling at three different currents $I_s$ over the same potential window (reproduced from Figure 10 of Ref. [29]) as functions of time $t$ . . . . .	80
4.10	(a) Predicted temperature rise $T(L, t) - T_0$ as a function of time $t$ at the centerline for cycling at the same current density $j_s = 14 \text{ mA cm}^{-2}$ over different potential windows. . . . .	81



5.1	Dimensionless temperature $T^*(t^*)$ predicted by solving Equation (5.4) and dimensionless irreversible temperature $T_{irr}^*(t^*)$ given by Equation (5.7) as functions of $t^*$ for (a) different values of $\tau_{th}^*$ with $T_\infty^* = 0$ for $ \dot{Q}_{rev}^*  = 5$ and (b) different values of $ \dot{Q}_{rev}^* $ for $T_\infty^* = 0$ and $\tau_{th}^* = 5$ . . . . .	91
5.2	Measured temperature $T(t)$ as a function of time $t$ at the outer surface of (a) a 1500-F EDLC cycled at $\pm 75$ A (Figure 7 of Ref. [25]) and (b) a 350-F EDLC cycled at $\pm 30$ A (Figure 8 of Ref. [8]), as well as (c) and (d) the corresponding dimensionless temperatures $T^*(t^*)$ as functions of dimensionless time $t^*$ and the predictions by Equation (5.7) using data in Table 5.1. . . . .	93
5.3	(a) Measured temperature $T(t)$ at the surface of a thermally insulated Nesscap 5000-F EDLC as a function of time $t$ for different values of current $I_s$ and cycle period $t_c$ (Figures 8 and 10 of Ref. [29]) and (b) the corresponding dimensionless temperature $T^*(t^*)$ as well as $T_{irr}^*(t^*)$ predicted by Equation (5.10) as functions of dimensionless time $t^*$ . . . . .	95
5.4	Dimensionless temperature $T^*(t^*)$ as a function of dimensionless time $t^*$ based on experimental measurements at the EDLC outer surface [29] and predicted by solving Equation (5.4) for a thermally insulated EDLC cycled at (a) $I_s = 25$ A, (b) $I_s = 50$ A, and (c) $I_s = 100$ A beginning with a charging step as well as (d) cycled at $I_s = 100$ A beginning with a discharging step. . . . .	96
5.5	Procedure to estimate temperature evolution of an EDLC. . . . .	98
6.1	Computed (a) electric potential $\psi(0, t)$ at the surface of Electrode A as a function of time $t$ and (b) dimensionless electric potential $\psi^*(0, t^*)$ as a function of dimensionless time $t^*$ during two consecutive galvanostatic charging/discharging cycles for Cases 1 to 3 (Table 6.2). . . . .	111
6.2	Computed (a) anion concentration $c_2(a/2, t)$ at the Stern/diffuse layer interface as a function of time $t$ and (b) dimensionless anion concentration $c_2^*(a^*/2, t^*)$ as a function of dimensionless time $t^*$ during two consecutive galvanostatic charging/discharging cycles for Cases 1 to 3 (Table 6.2). . . . .	113

6.3	Computed temperature change (a) $T(a/2, t) - T_0$ at the Stern/diffuse layer interface and (b) $T(L, t) - T_0$ at the centerline as functions of time $t$ as well as dimensionless temperature change (c) $T^*(a^*/2, t^*)$ and (d) $T^*(L^*, t^*)$ as functions of dimensionless time $t^*$ during two consecutive galvanostatic charging/discharging cycles for Cases 1 to 3 (Table 6.2). . . . .	114
6.4	Computed values of (a) $\Delta T_{rev}^*(a^*/2)$ as a function of $C^*$ , (b) $\Delta T_{rev}^*(a^*/2)C^*$ as a function of $Le$ , (c) $\Delta T_{rev}^*(a^*/2)C^*Le^{1/2}$ as a function of $Q_{rev}^*$ , and (d) $\Delta T_{rev}^*(a^*/2)C^*Le^{1/2}/Q_{rev}^*$ as a function of $t_c^*$ . . . . .	116
6.5	(a) Computed values of $1/Q_{E,d}^*$ as a function of $\nu_p$ for different values of $j_s^*t_c^*$ along with curve fits of the form $1/Q_{E,d}^* = A_{E,d}\nu_p + B_{E,d}$ [Equation (6.19)] and (b) fitting functions $A_{E,d}$ and $B_{E,d}$ versus $j_s^*t_c^*$ . . . . .	119
6.6	(a) Computed values of $Q_{E,s}^*$ as a function of $\nu_p$ for different values of $j_s^*t_c^*$ along with curve fits of the form $Q_{E,s}^* = [1/A_{E,s}\nu_p + \nu_p/B_{E,s}]^{-1}$ [Equation (6.20)] and (b) fitting functions $A_{E,s}$ and $B_{E,s}$ versus $j_s^*t_c^*$ . . . . .	121
6.7	Computed $Q_{S,c}^*/a^{*3}$ as a function of (a) $\nu_p$ , along with curve fits of the form $Q_{S,c}^*/a^{*3} = [\nu_p/A_{S,c} + \nu_p^2/(1 - \nu_p)^2 B_{S,c}]^{-1}$ [Equation (6.21)] , and (b) $(1 - \nu_p)/\nu_p$ for different values of $j_s^*t_c^*$ . . . . .	122
6.8	Fitting functions (a) $A_{S,c}$ and (b) $B_{S,c}$ versus $j_s^*t_c^*$ in the expression for $Q_{S,c}^*/a^{*3}$ given by Equation (6.21). . . . .	123
7.1	Cell potential $\psi_s(t) = \psi(0, t) - \psi(2L, t)$ as a function of time $t$ over the first cycle and a half for (a) Cases 1–4 featuring different ion valencies $z_i$ and (b) Cases 1, 5, and 6 featuring different effective ion diameters. Results for Cases 7 and 8 featuring different diffusion coefficients $D_i$ were identical to those of Case 1. . . . .	136

7.2	Anion concentration $c_1(x, 3t_c/2)$ near the positive Electrode A as a function of location $x$ for (a) Cases 1–4 with different values of $z_i$ and (c) Cases 1, 5, and 6 with different values of $a_i$ as well as cation concentration $c_2(x, 3t_c/2)$ near the negative Electrode B as a function of location $2L - x$ for (b) Cases 1–4 and (d) Cases 1, 5, and 6. All cases correspond to time $t = 3t_c/2$ at the end of a charging step. . . . .	138
7.3	Diffusion heat generation rate $\dot{q}_{E,d}(x, 11t_c/8)$ as a function of location (a) and (c) $x$ near the positive Electrode A and (b) and (d) $2L - x$ near the negative Electrode B. Plots (a) and (b) show Cases 1–4 with different $z_i$ while plots (c) and (d) show Cases 5 and 6 with different $a_i$ . All cases correspond to time $t = 11t_c/8$ near the end of a charging step. . . . .	140
7.4	Steric heat generation rate $\dot{q}_{E,s}(x, 11t_c/8)$ as a function of location (a) and (c) $x$ near the positive Electrode A and (b) and (d) $2L - x$ near the negative Electrode B. Plots (a) and (b) show Cases 1–4 with different $z_i$ while plots (c) and (d) show Cases 5 and 6 with different $a_i$ . All cases correspond to time $t = 11t_c/8$ near the end of a charging step. . . . .	143
7.5	Heat of mixing heat generation rate $\dot{q}_{S,c}(x, 11t_c/8)$ as a function of location (a) and (c) $x$ near the positive Electrode A and (b) and (d) $2L - x$ near the negative Electrode B. Plots (a) and (b) show Cases 1–4 with different $z_i$ while plots (c) and (d) show Cases 5 and 6 with different $a_i$ . All cases correspond to time $t = 11t_c/8$ near the end of a charging step. . . . .	144
7.6	Overall reversible heat generation rate $\dot{q}_{rev}(x, 11t_c/8)$ as a function of location (a) and (c) $x$ near the positive Electrode A and (b) and (d) $2L - x$ near the negative Electrode B. Plots (a) and (b) show Cases 1–4 with different $z_i$ while plots (c) and (d) show Cases 5 and 6 with different $a_i$ . All cases correspond to time $t = 11t_c/8$ near the end of a charging step. . . . .	146

7.7	Total reversible heat generation rates $\dot{Q}_{rev}''(t)$ as functions of $t$ over one and a half cycles for (a) Cases 1–4 with $a_1 = a_2 = 0.56$ nm, $D_1 = D_2 = 9.3 \times 10^{-9}$ m <sup>2</sup> s <sup>-1</sup> , and different $z_i$ and (b) Cases 1, 5, and 6 featuring $-z_1 = z_2 = 1$ , $D_1 = D_2 = 9.3 \times 10^{-9}$ m <sup>2</sup> s <sup>-1</sup> , and different $a_i$ . . . . .	148
7.8	Temperature rise $T(x, t) - T_0$ as functions of time $t$ for (a)–(c) Cases 1–4 with different $z_i$ and (d)–(f) Cases 1, 5, and 6 with different $a_i$ . Results are shown for three locations, namely, (a) and (d) at $x = a/2$ near the positive Electrode A, (b) and (e) at the centerline $x = L$ , and (c) and (f) at $x = 2L - a/2$ near the negative Electrode B. . . . .	151
8.1	Experimental (a) cell potential $\psi_s(t) = \Delta\psi_C(t) - \Delta\psi_P(t)$ for a hybrid pseudocapacitor using Nb <sub>2</sub> O <sub>5</sub> and potentials of the pseudocapacitive $\Delta\psi_P(t)$ and carbon $\Delta\psi_C(t)$ electrodes relative to a reference electrode, as well as (b) $\psi_s(t) = \Delta\psi_P(t) - \Delta\psi_C(t)$ for a hybrid pseudocapacitor using MnO <sub>2</sub> [117] as functions of time $t$ . . . . .	159
8.2	Illustration of (a) the electric double layer structure of a binary and asymmetric electrolyte with redox reactions near a planar electrode and (b) the simulated hybrid pseudocapacitor with planar electrodes, along with the associated coordinate system. . . . .	163
8.3	Predicted (a) faradaic current density $j_F(t)$ and (b) capacitive current density $j_C(t)$ as well as the faradaic and capacitive fractions (c) $j_F(t)/j_s$ and (d) $j_C(t)/j_s$ of the total current density as functions of dimensionless time $t/t_c$ for different values of $j_s$ and $t_c$ under galvanostatic cycling and oscillatory steady state. Here, $j_s$ and $t_c$ were chosen such that $\Delta q_s = j_s t_c / 2 = 0.3$ C m <sup>-2</sup> . . . .	176
8.4	Predicted concentration $c_{1,P}(-L, t)$ of intercalated Li <sup>+</sup> in the pseudocapacitive electrode as a function of dimensionless time $t/t_c$ over one cycle at oscillatory steady state for different values of $j_s$ and $t_c$ such that $\Delta q_s = j_s t_c / 2 = 0.3$ C m <sup>-2</sup> . The concentration was uniform throughout the pseudocapacitive electrode. . . . .	177

- 8.5 Predicted (a) cell potential  $\psi_s(t) = \Delta\psi_C(t) - \Delta\psi_P(t)$  and (b) pseudocapacitive electrode surface overpotential  $\eta(t)$  as well as the potentials of the (c) pseudocapacitive  $\Delta\psi_P(t) = \psi(-L - L_P, t) - \psi(0, t)$  and (d) carbon  $\Delta\psi_C(t) = \psi(L + L_C, t) - \psi(0, t)$  electrodes relative to the bulk electrolyte as functions of dimensionless time  $t/t_c$  over one cycle during galvanostatic cycling for various values of  $j_s$  and  $t_c$  such that  $\Delta q_s = j_s t_c / 2 = 0.3 \text{ C m}^{-2}$ . . . . . 179
- 8.6 Predicted concentrations of (a)  $\text{Li}^+$  cation  $c_{1,E}(-L + H, t)$  and (b)  $\text{ClO}_4^-$  anion  $c_{2,E}(-L + H, t)$  at the Stern/diffuse layer interface near the pseudocapacitive electrode as well as concentrations of (c)  $\text{Li}^+$   $c_{1,E}(L - H, t)$  and (d)  $\text{ClO}_4^-$   $c_{2,E}(L - H, t)$  at the Stern/diffuse layer interface near the carbon electrode as functions of dimensionless time  $t/t_c$  over one cycle at oscillatory steady state for different values of  $j_s$  and  $t_c$  such that  $\Delta q_s = j_s t_c / 2 = 0.3 \text{ C m}^{-2}$ . . . . . 183
- 8.7 Predicted (a) faradaic  $j_F(t)/j_s$  and (b) capacitive  $j_C(t)/j_s$  fractions of the total current density, (c) potential  $\Delta\psi_P(t)$  of the pseudocapacitive electrode relative to bulk electrolyte, and (d) cell potential  $\psi_s(t)$  as functions of dimensionless time  $t/t_c$  for  $S_{eq} = 0, 1$ , and  $10.5 \text{ V}$  under galvanostatic cycling. The two selected cases  $[j_s, t_c]$  corresponded to the faradaic and capacitive regimes identified for  $S_{eq} = 0 \text{ V}$  and satisfying  $\Delta q_s = j_s t_c / 2 = 0.3 \text{ C m}^{-2}$ . . . . . 185
- 8.8 Predicted (a) the faradaic  $j_F(t)/j_s$  and (b) capacitive  $j_C(t)/j_s$  fractions of the imposed current as well as (c) the surface overpotential  $\eta(t)$  and (d) the cell potential  $\psi_s(t) = \Delta\psi_P(t) - \Delta\psi_C(t)$  for the hybrid pseudocapacitor charged by deintercalation for various  $[j_s, t_c]$  satisfying  $\Delta q_s = j_s t_c / 2 = 0.3 \text{ C m}^{-2}$ . . . . . 188
- 9.1 Predicted cell potential  $\psi_s(t)$  as a function of time  $t - n_c t_c$  for different current densities  $j_s$  at oscillatory steady state between  $\psi_{min} = 0 \text{ V}$  and  $\psi_{max} = 0.45 \text{ V}$ . 203
- 9.2 Predicted (a) faradaic  $j_F(t)/j_s$  and (b) capacitive  $j_C(t)/j_s$  fractions of the imposed current density as functions of dimensionless time  $t/t_c$ . All cases are plotted over one cycle under oscillatory steady state for different values of  $j_s$  and the same potential window  $0 \text{ V} \leq \psi_s \leq 0.45 \text{ V}$ . . . . . 205

- 9.3 Predicted intercalated  $\text{Li}^+$  concentration  $c_{1,P}(-L, t)$  in the pseudocapacitive electrode as a function of dimensionless time  $t/t_c$  for various current densities  $j_s$  at oscillatory steady state as well as the analytical prediction  $c_{1,P,F}$  [Equation (8.26)] for  $j_s = 2 \text{ mA cm}^{-2}$  and  $t_c = 29 \text{ ms}$  in the faradaic regime. 206
- 9.4 Predicted surface overpotential  $\eta(t)$  as a function of dimensionless time  $t/t_c$  for different  $j_s$  as well as the analytical predictions of  $\eta_F$  [Equation (8.27)] for  $j_s = 2 \text{ mA cm}^{-2}$  in the faradaic regime and  $\eta_C$  [Equation (8.28)] for  $j_s = 256 \text{ mA cm}^{-2}$  in the capacitive regime. . . . . 207
- 9.5 Predicted concentrations (a)  $c_{1,E}(-L + H, t)$  of  $\text{Li}^+$  and (b)  $c_{2,E}(-L + H, t)$  of  $\text{ClO}_4^-$  in the electrolyte near the pseudocapacitive electrode as well as (c)  $c_{1,E}(L - H, t)$  of  $\text{Li}^+$  and (d)  $c_{2,E}(L - H, t)$  of  $\text{ClO}_4^-$  near the carbon electrode. 208
- 9.6 Predicted overall (a) irreversible faradaic  $\dot{Q}_{F,irr,P}''(t)$ , (b) reversible faradaic  $\dot{Q}_{F,rev,P}''(t)$ , and reversible EDL  $\dot{Q}_{EDL,rev,P}''(t)$  heat generation rates for (c) small and (d) large current densities  $j_s$  as functions of dimensionless time  $t/t_c$ . All cases are plotted over one cycle under oscillatory steady state for different values of  $j_s$  and the same potential window  $0 \text{ V} \leq \psi_s \leq 0.45 \text{ V}$ . . . 211
- 9.7 Numerically predicted total heat generation rates (a)  $\dot{Q}_P''(t)$  of the pseudocapacitive electrode half-cell and (b)  $\dot{Q}_C''(t)$  of the carbon electrode half-cell for  $0 \text{ V} \leq \psi_s \leq 0.45 \text{ V}$  as well as experimentally measured total heat generation rates minus Joule heating (c)  $\dot{Q}_P''(t) - \overline{\dot{Q}}_{J,irr,P}''$  of the pseudocapacitive electrode half-cell and (d)  $\dot{Q}_C''(t) - \overline{\dot{Q}}_{J,irr,C}''$  of the carbon electrode half-cell for a hybrid pseudocapacitor cycled over the potential window  $0 \text{ V} \leq \psi_s \leq 1.0 \text{ V}$  [78] as functions of dimensionless time  $t/t_c$  for different values of  $j_s$ . . . . . 213
- 9.8 Time-averaged (a) numerically predicted Joule  $\overline{\dot{Q}}_{J,irr}''$ , irreversible faradaic  $\overline{\dot{Q}}_{F,irr,P}''$ , reversible EDL  $\overline{\dot{Q}}_{EDL,rev,P}''$ , and overall  $\overline{\dot{Q}}'' = \overline{\dot{Q}}_{J,irr}'' + \overline{\dot{Q}}_{F,irr,P}'' + \overline{\dot{Q}}_{EDL,rev,P}''$  heat generation rates as well as (b) experimental overall  $\overline{\dot{Q}}''$  [79] and estimated Joule  $\overline{\dot{Q}}_{J,irr}''$  heating as functions of current density  $j_s$ . . . . . 216

9.9	Predicted centerline temperature $T(0, t) - T(0, t_c)$ as a function of time $t$ over the potential window $0 \text{ V} \leq \psi_s \leq 0.45 \text{ V}$ for (a) small and (b) large current densities $j_s$ . . . . .	218
A.1	Computed (a) irreversible volumetric heat generation rate $\dot{q}_{irr}(x, 7t_c/5)$ as a function of location $x$ and (b) corresponding dimensionless irreversible volumetric heat generation rate $\dot{q}_{irr}^*(x^*, 7t_c^*/5)$ as a function of dimensionless location $x^*$ for Cases 1 to 3 (Table 6.2). . . . .	228
A.2	Computed (a) reversible volumetric heat generation rate $\dot{q}_{rev}(x, 7t_c/5)$ as a function of location $x$ and (b) corresponding dimensionless reversible volumetric heat generation rate $\dot{q}_{rev}^*(x^*, 7t_c^*/5)$ as a function of dimensionless location $x^*$ for Cases 1 to 3 (Table 6.2). . . . .	228
A.3	Computed values of $\Delta T_{rev}^* C^* L e^{1/2} t_c^{*1/2} / Q_{rev}^*$ as a function of (a) $a^*$ and (b) $L^*$ . . . . .	229
A.4	Predicted dimensionless heat generation integrals $Q_{E,d}^*$ , $Q_{E,s}^*$ , and $Q_{S,c}^*$ as functions of (a) dimensionless inter-electrode spacing $L^*$ and (b) dimensionless ion diameter $a^*$ . . . . .	230
A.5	Computed dimensionless heat generation (a) $Q_{E,d}^*$ , (b) $Q_{E,s}^*$ , and (c) $Q_{S,c}^*$ as functions of $j_s^* t_c^*$ for $a^* = 2.4$ , $L^* = 7.2 \times 10^4$ , and various $j_s^*$ , $t_c^*$ , and $\nu_p$ . . . . .	231
A.6	Values of (a) $Q_{E,d}^*$ , $Q_{E,s}^*$ , and $Q_{S,c}^*$ and (b) $\Delta T_{rev}^*(a^*/2)$ predicted by correlations as function of those computed numerically. . . . .	232
B.1	Cell potential $\psi_s(t) = \psi(0, t) - \psi(2L, t)$ as a function of time $t$ for a symmetric electrolyte with $-z_1 = z_2 = 1$ , $a_1 = a_2 = 0.56 \text{ nm}$ , and $D_1 = D_2 = 1 \times 10^{-11} \text{ m}^2\text{s}^{-1}$ . Significant IR drops were evident due to the relatively low conductivity $\sigma_\infty$ resulting from the small diffusion coefficients. . . . .	234
B.2	Irreversible heat generation rate $\dot{q}_{irr}(x, 11t_c/8)$ as a function of location $x$ for (a) Cases 1-4 featuring different $z_i$ and (b) Cases 1, 7, and 8 featuring different $D_i$ . All cases correspond to time $t = 11t_c/8$ near the end of a charging step. . . . .	235

## LIST OF TABLES

3.1	Input parameters of three cases used to illustrate the scaling analysis and such that $a^* = 2.0$ , $L^* = 395$ , $\psi_{s,max}^* = 4$ , $\nu_p = 0.2$ , $Le = 50$ , and $C^* = 400$ . . . . .	43
5.1	Properties of commercial EDLC devices and galvanostatic cycling conditions used in experimental studies [8, 25, 29]. The experimental data were used to demonstrate the present analysis and scaling. . . . .	89
6.1	Dimensionless boundary conditions for thermally insulated EDLC with planar electrodes during galvanostatic cycling. . . . .	105
6.2	Input parameters for Cases 1 to 3 used to illustrate the scaling analysis. The dimensionless parameters $a^* = 2.4$ , $L^* = 7.2 \times 10^4$ , $j_s^* = 2.4 \times 10^{-6}$ , $t_c^* = 2.2 \times 10^7$ , $\nu_p = 0.38$ , $Le = 374$ , and $C^* = 310$ are the same for all three cases. . . . .	109
6.3	Baseline values of the seven dimensionless similarity parameters used in Figure 6.4 to develop the correlation for $\Delta T_{rev}^*$ given by Equation (6.17). . . . .	115
7.1	Parameters for the cases simulated, based on the properties of aqueous $H_2SO_4$ [58–60], as well as the resulting areal capacitances $C_{s,int}$ [Equation (2.2)] and irreversible Joule heat generation rate $\dot{q}_{J,irr}$ . Here, the imposed current density and cycle period were equal to $j_s = 14 \text{ mA cm}^{-2}$ and $t_c = 7.6 \text{ ms}$ , respectively. . . . .	134
7.2	Summary of the effects of changing ion properties on the heat generation rates $\dot{q}_{J,irr}$ , $\dot{q}_{rev}$ , $\dot{Q}_{J,irr}''$ , and $\dot{Q}_{rev}''$ as well as the integral capacitance $C_{s,int}$ during galvanostatic cycling. . . . .	153
9.1	Summary of the irreversible and reversible heat generation rates $\dot{q}_{irr}$ and $\dot{q}_{rev}$ simulated in each region for the 1D hybrid pseudocapacitor illustrated in Figure 8.2 such that $\dot{q} = \dot{q}_{irr} + \dot{q}_{rev}$ . . . . .	197
9.2	Electrochemical transport properties used for simulating the hybrid pseudocapacitor with binary and asymmetric electrolyte [161]. . . . .	200



## ACKNOWLEDGMENTS

This material is based upon work supported by the National Science Foundation Graduate Research Fellowship under Grant No. DGE-0707424 and DGE-1144087 and as part of Molecularly Engineered Energy Materials, an Energy Frontier Research Center funded by the U.S. Department of Energy, Office of Science, Office of Basic Energy Sciences under Award Number DE-SC0001342.

The principal chapters of this dissertation are versions of my publications with Prof. Laurent Pilon as principal investigator. Chapter 3 is a version of Ref. [1]. Co-author Dr. Hainan Wang assisted with the initial implementation of the model and in interpreting the results. Chapter 4 is a version of Ref. [2]. Chapter 5 is a version of Ref. [3]. Chapter 6 is a version of Ref. [4]. Chapter 7 is a version of Ref. [5]. Chapter 8 is based on material being prepared for publication with co-authors Henri-Louis Girard and Dr. Hainan Wang and principal investigator Prof. Laurent Pilon. Mr. Girard and Dr. Wang developed the electrochemical transport model, and Mr. Girard assisted in interpreting the results. Chapter 9 is based on material being prepared for publication with principal investigator Prof. Laurent Pilon.

## VITA

- 2005-2009      B.S. Mechanical Engineering, Clemson University, Clemson, SC.
- 2006-2008      Co-op engineer, Electrolux Home Products, Anderson, SC.
- 2009-2010      Congress-Bundestag Youth Exchange (CBYX) Program.
- Feb.-June 2010   Student Researcher, Laboratory for Machine Tools and Production Engineering (Werkzeugmaschinenlabor, WZL), RWTH Aachen University, Aachen, Germany.
- 2011–2015      Graduate Student Researcher, Mechanical and Aerospace Engineering Department, University of California, Los Angeles.
- Oct.-Dec. 2014   Teaching Assistant, Mechanical and Aerospace Engineering Department, University of California, Los Angeles.

## PUBLICATIONS

H.-L. Girard, H. Wang, **A. d’Entremont**, and L. Pilon, 2015, Physical interpretation of cyclic voltammetry for hybrid pseudocapacitors, *The Journal of Physical Chemistry C* 119 (21), pp. 11349-11361.

L. Pilon, H. Wang, and **A. d’Entremont**, 2015, Recent advances in continuum modeling of interfacial and transport phenomena in electric double layer capacitors, *Journal of The Electrochemical Society* 162 (5), pp. A5158-A5178.

**A. L. d’Entremont** and L. Pilon, 2015, Thermal effects of asymmetric electrolytes in electric double layer capacitors, *Journal of Power Sources* 273, pp. 196-209.

**A. L. d'Entremont** and L. Pilon, 2014, Scaling laws for heat generation and temperature oscillations in EDLCs under galvanostatic cycling, *International Journal of Heat and Mass Transfer* 75, pp. 637-649.

**A. L. d'Entremont** and L. Pilon, 2014, First-order thermal model of commercial EDLCs, *Applied Thermal Engineering* 67, pp. 439-446.

**A. L. d'Entremont** and L. Pilon, 2014, First-principles thermal modeling of electric double layer capacitors under constant-current cycling, *Journal of Power Sources* 246, pp. 887-898.

**A. L. d'Entremont**, H. Wang, L. Pilon, 2012, Scaling analysis of thermal behavior of electrical double layers, *Proceedings of the ASME 2012 Heat Transfer Summer Conference*, HT2012-58487.

M. Duscha, F. Klocke, **A. d'Entremont**, B. Linke, and H. Wegner, 2010, Investigation of temperatures and residual stresses in speed stroke grinding via FEA simulation and practical tests, *Proceedings in Manufacturing Systems* 5, pp. 1-10.

# NOMENCLATURE

$A$	External surface area ( $\text{m}^2$ )
$A_j$	Semi-empirical fitting function for heat generation rate contribution $j$
$a$	Effective ion diameter (nm)
$a_i$	Local thermodynamic activity of species $i$
$B_j$	Semi-empirical fitting function for heat generation rate contribution $j$
$C$	Capacitance (F)
$C^*$	Dimensionless heat capacity
$C_{th}$	Heat capacity ( $\text{J K}^{-1}$ )
$c$	Concentration ( $\text{mol m}^{-3}$ )
$c_{max}$	Maximum ion concentration, $c_{max} = 1/N_A a^3$ ( $\text{mol m}^{-3}$ )
$c_p$	Specific heat at constant pressure ( $\text{J kg}^{-1}\text{K}^{-1}$ )
$c_\infty$	Concentration of bulk electrolyte ( $\text{mol m}^{-3}$ )
$D$	Diffusion coefficient ( $\text{m}^2 \text{s}^{-1}$ )
$\mathbf{E}$	Electric field strength ( $\text{V m}^{-1}$ )
$e$	Elementary charge ( $e = 1.602 \times 10^{-19} \text{ C}$ )
$e_{th}$	Thermal effusivity, $e_{th} = (k\rho c_p)^{1/2}$
$F$	Faraday constant ( $F = eN_A = 9.648 \times 10^4 \text{ C mol}^{-1}$ )
$H$	Stern layer thickness (nm)
$\bar{H}_i$	Partial molar enthalpy of species $i$ ( $\text{J mol}^{-1}$ )
$\Delta H_r$	Enthalpy of reaction ( $\text{J mol}^{-1}$ )
$h$	Specific enthalpy ( $\text{J kg}^{-1}$ )
$\bar{h}$	Average convective heat transfer coefficient ( $\text{W m}^{-2} \text{K}^{-1}$ )
$I$	Electric current (A)
$\mathbf{j}$	Current density ( $\text{A m}^{-2}$ )
$j_s$	Magnitude of imposed current density ( $\text{A m}^{-2}$ )
$j_F$	Faradaic current density ( $\text{A m}^{-2}$ )
$j_C$	Capacitive current density ( $\text{A m}^{-2}$ )

$k$	Thermal conductivity ( $\text{W m}^{-1}\text{K}^{-1}$ )
$k_B$	Boltzmann constant ( $\text{J K}^{-1}$ )
$k_0$	Reaction rate constant ( $\text{m}^{5/2} \text{mol}^{-1/2}\text{s}^{-1}$ )
$L$	Half of inter-electrode distance (m)
$L_C$	Thickness of carbon electrode (m)
$L_P$	Thickness of pseudocapacitive electrode (m)
$Le$	Lewis number $Le = \alpha_{th}/D$
$N_A$	Avogadro constant ( $N_A = 6.022 \times 10^{23} \text{mol}^{-1}$ )
$\mathbf{N}_i$	Flux of species $i$ ( $\text{mol m}^{-2}\text{s}^{-1}$ )
$n$	Number of ion species in the electrolyte
$n_c$	Cycle number
$\mathbf{n}_s$	Unit normal vector to electrode/electrolyte interface pointing into electrolyte
$p$	Pressure (Pa)
$Q$	Amount of heat generated per charging step per unit surface area ( $\text{J m}^{-2}$ )
$\dot{Q}''$	Heat generation rate per unit surface area ( $\text{W m}^{-2}$ )
$\dot{Q}$	Heat generation rate (W)
$\mathbf{q}''$	Energy flux ( $\text{W m}^{-2}$ )
$\dot{q}$	Local volumetric heat generation rate ( $\text{W m}^{-3}$ )
$R$	Electrical resistance ( $\Omega$ )
$R_{th}$	Thermal resistance ( $\text{K W}^{-1}$ )
$R_u$	Universal gas constant ( $R_u = 8.314 \text{J mol}^{-1}\text{K}^{-1}$ )
$\mathbf{r}$	Location in three-dimensional space (m)
$\mathbf{r}_s$	Location on electrode/electrolyte interface (m)
$\dot{r}_i$	Rate of production of species $i$ due to chemical reactions ( $\text{mol m}^{-3}\text{s}^{-1}$ )
$\bar{S}$	Partial molar entropy ( $\text{J K}^{-1}$ )
$S_{eq}$	Rate of change of equilibrium potential drop $\Delta\psi_{eq}$ with $c_{1,P}$ (V)
$s$	Stoichiometric coefficient
$T$	Temperature (K)
$T_0$	Initial temperature (K)

$T_\infty$	Ambient temperature (K)
$t$	Time (s)
$t_c$	Cycle period (s)
$u$	Specific internal energy ( $\text{J kg}^{-1}$ )
$V_0$	Volume of electrolyte ( $\text{m}^3$ )
$V_S$	Volume of Stern layer ( $\text{m}^3$ )
$x$	Location in one-dimensional space (m)
$z$	Ion valency

### Greek symbols

$\alpha$	Transfer coefficient for faradaic reaction
$\alpha_{th}$	Thermal diffusivity $\alpha_{th} = k/\rho c_p$ ( $\text{m}^2 \text{s}^{-1}$ )
$\beta$	Semi-empirical parameter characterizing reversible heating (V)
$\gamma_i$	Activity coefficient of species $i$
$\epsilon_0$	Permittivity of vacuum ( $\epsilon_0 = 8.854 \times 10^{-12} \text{ F m}^{-1}$ )
$\epsilon_r$	Relative permittivity of electrolyte
$\eta$	Surface overpotential (V)
$\lambda_D$	Debye length (m)
$\tilde{\mu}_i$	Electrochemical potential of species $i$ ( $\text{J mol}^{-1}$ )
$\mu_i$	Chemical potential of species $i$ ( $\text{J mol}^{-1}$ )
$\mu_i^0$	Chemical potential of species $i$ at standard state ( $\text{J mol}^{-1}$ )
$\nu_p$	Packing parameter, $\nu_p = 2c_\infty N_A a^3$
$\Pi$	Peltier coefficient (V)
$\rho$	Density ( $\text{kg m}^{-3}$ ) ‘
$\sigma$	Electrical conductivity ( $\text{S m}^{-1}$ )
$\sigma_\infty$	Electrical conductivity of electrolyte at bulk concentration $c_\infty$ ( $\text{S m}^{-1}$ )
$\tau_d$	Characteristic time for ion diffusion across EDL (s)
$\tau_{th}$	Characteristic time for heat diffusion across EDL (s)
$\tau_{th}^*$	Dimensionless thermal time constant
$\psi$	Electric potential (V)

$\psi_s$	Cell potential, voltage between electrodes (V)
$\Delta\psi_H$	Potential drop across Stern layer at pseudocapacitive electrode (V)
$\Delta\psi_{eq}$	Equilibrium potential drop across Stern layer (V)

### **Superscripts and subscripts**

$*$	Refers to dimensionless quantities
$\infty$	Refers to bulk electrolyte
$C$	Refers to quantities in the carbon electrode
$E$	Refers to quantities in the electrolyte
$E, d$	Refers to heat generation due to diffusion
$E, s$	Refers to heat generation due to steric effects
$F$	Refers to quantities related to faradaic reaction
$i$	Refers to properties of species $i$
$irr$	Refers to irreversible heat generation
$J$	Refers to Joule heating
$P$	Refers to quantities in the pseudocapacitive electrode
$rev$	Refers to reversible heat generation
$S, c$	Refers to heat of mixing due to concentration gradient
$S, T$	Refers to heat of mixing due to temperature gradient

# CHAPTER 1

## Introduction

### 1.1 Need for electrical energy storage

The importance of electrical energy storage (EES) systems in our society is continually increasing. Compact and efficient EES systems are required for myriad portable electronic devices such as laptop computers and mobile phones. They are increasingly in demand for vehicle applications, due to the increasing popularity of hybrid and fully-electric vehicles to minimize emissions and reduce dependence on fossil fuels. In addition, many sources of “clean” and renewable energy such as solar, wind, or wave energy require EES systems to facilitate electric load following so that they can be effectively integrated into the power grid [6].

#### 1.1.1 Hybrid and electric vehicles

Hybrid and fully-electric vehicles provide a way to reduce dependence on fossil fuels and emission of CO<sub>2</sub>. A major challenge for these vehicles is the development of suitable electrical energy storage systems to enable good vehicle performance and driving range [6]. The use of EES systems to replace or supplement internal combustion engines offers greater flexibility in the choice of energy sources for vehicle applications. It also enables more efficient energy use. For example, hybrid vehicles can shut down the internal combustion engine in situations where its efficiency is low and/or recapture energy that would otherwise be wasted, such as that dissipated during braking [7–9].



### **1.1.2 Expanding the usability of energy sources**

Efficient electrical energy storage is needed to improve the flexibility and applicability of energy sources such as solar energy, wind energy, and nuclear energy. Solar and wind energy are intermittent, while nuclear power provides a set, steady power output over long timescales. Neither of these two extremes is capable of following short-term demand fluctuations in the power grid. EES systems enable the storage of energy during periods when electricity production exceeds demand and the release of that energy during demand peaks that exceed the current production [7].

## **1.2 Types of electrical energy storage**

Electrical energy storage methods can be classified into two major types: chemical storage and physical or capacitive storage [6, 10]. Both types of storage are based on electrochemistry and involve the interaction of complex physical and chemical processes [6, 10]. The fundamental difference is that chemical storage methods store energy in the form of electrically neutral chemical reactants which can produce electric charge [6, 10]. On the other hand, physical storage methods store energy directly as separated electronic and/or ionic charge [6, 10]. Figure 1.1 shows the classifications of various EES devices.

### **1.2.1 Batteries: Chemical charge storage**

Batteries store electrical energy via reversible redox reactions between an electrolyte and an electrode that consume or release electrons and ions. Figure 1.2 illustrates the operating mechanism of a lithium-ion battery during charging and discharging [11]. The electrons flow from one electrode to the other through an external circuit, while the ions travel through the electrolyte. Batteries provide a relatively constant output voltage independent of the state of charge [6, 10]. This voltage is determined by the chemical reaction occurring within the cell [6, 12]. Individual battery cells may be connected in series to provide higher voltage or in parallel to provide higher power [6]. Batteries offer high energy densities because the redox

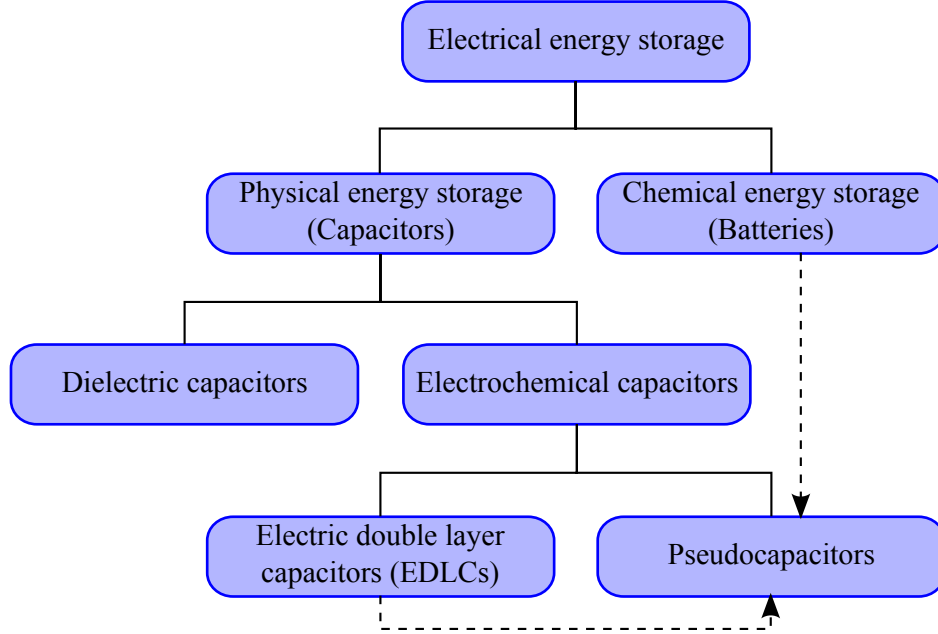


Figure 1.1: Classification of electrical energy storage systems.

reactions can store charge throughout the volume of the electrode material [6]. However, the volume and phase changes associated with ion intercalation into the material severely limit the cycle life due to irreversible changes [6]. As a result, battery cycle life is typically on the order of a few thousand cycles [6, 10, 13]. The power density of batteries is limited by the reaction kinetics and by mass transfer of the reactants [6]. As a result, the charge and discharge rates often differ [6].

### 1.2.2 Conventional capacitors: Physical charge storage

Capacitors store electrical energy electrostatically by physically separating positive and negative electric charges on either side of an electrically insulating layer [6]. Different types of capacitors, e.g., dielectric capacitors or electrolytic capacitors, are differentiated by their structure and the types of charge carrier involved, namely electrons and/or ions. Figure 1.3(a) illustrates a conventional dielectric capacitor. It stores electronic charge within two electrodes separated by a dielectric material [13]. The voltage across a capacitor varies continuously with its state of charge [13]. Conventional capacitors have very high power densities, since they are not limited by reaction kinetics, as well as very long cycle life, since

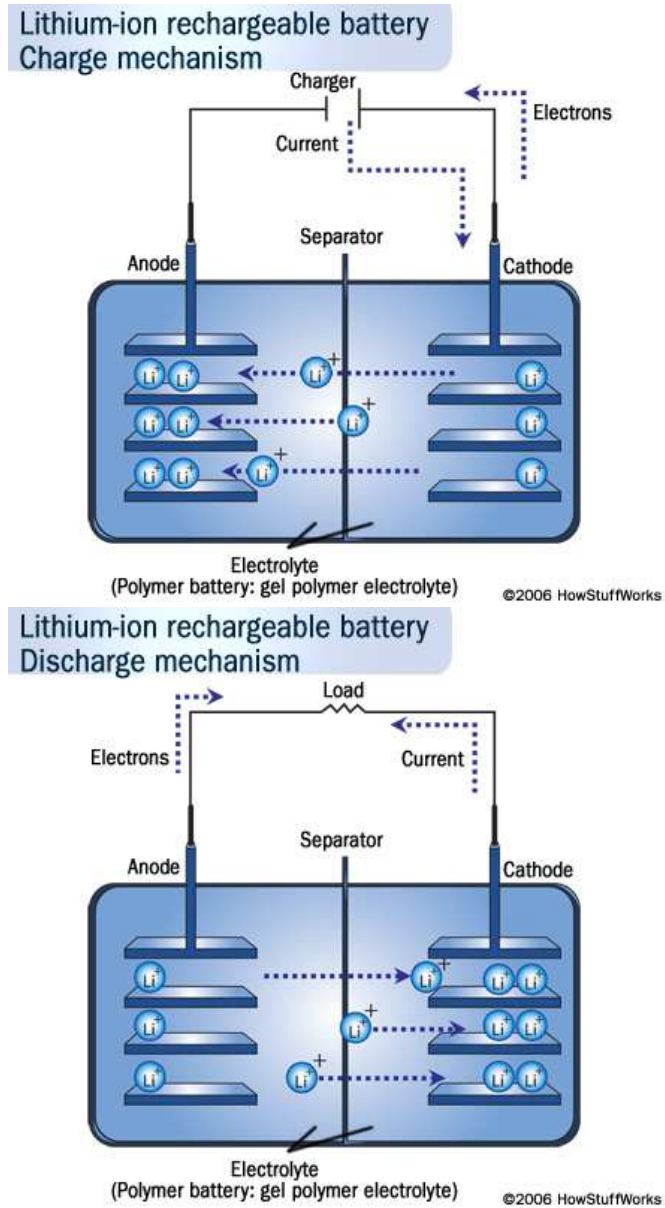


Figure 1.2: Illustration of the charge storage mechanism of a lithium-ion battery during charging and discharging (from Ref. [11]).

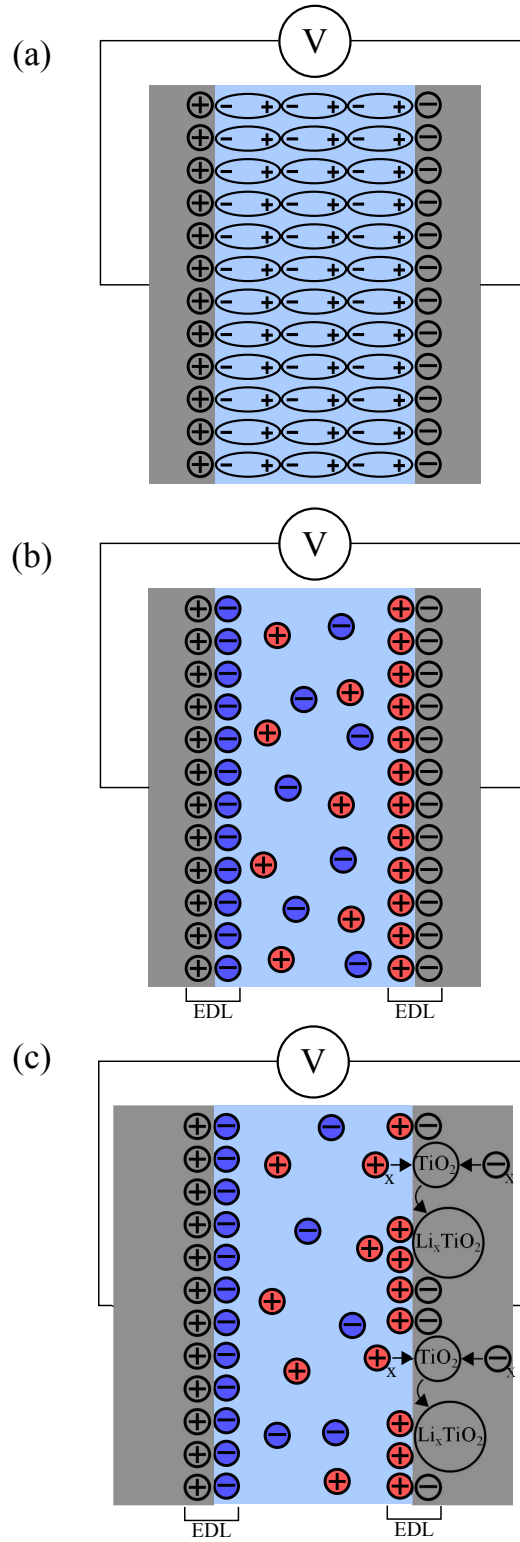


Figure 1.3: Illustrations of (a) a dielectric capacitor, (b) an electric double layer capacitor (EDLC), and (c) a hybrid pseudocapacitor.

electrostatic charge storage is highly reversible [6, 13]. However, they provide very low energy densities, because charge is stored only at the interfaces on either side of the dielectric layer [6, 13].

### 1.2.3 Electrochemical capacitors

Electrochemical capacitors (ECs) involve both electronic and ionic charge. There are two types of ECs, namely electric double layer capacitors (EDLCs) and pseudocapacitors. Both consist of two electrodes immersed in an electrolyte and separated by an ion-permeable separator [6, 13, 14]. Figure 1.3(b) illustrates the charge storage mechanism of EDLCs. They store electrical energy within the electric double layer (EDL) forming at the porous electrode/electrolyte interfaces without chemical reactions or phase changes [10, 15]. The EDL consists of two layers of electric charge on either side of the electrode/electrolyte interface: a layer of electronic charge within the electrode and a layer of ionic charge of opposite sign within the electrolyte [6, 10, 15]. The electrode/electrolyte interface serves as the insulating layer of the capacitor, because neither electrons nor ions cross the surface. By contrast, pseudocapacitors combine both physical and chemical storage mechanisms and consist of a hybrid between EDLCs and batteries. Charge is stored chemically using redox reactions as well as electrostatically within the EDLs [10, 15, 16]. Despite their use of chemical storage, the electrical performance of pseudocapacitors closely resembles that of EDLCs rather than that of batteries [6, 10, 16, 17]. In fact, an ideal battery operates at a constant cell potential independent of its state of charge (SOC), whereas the cell potential of an EDLC or a pseudocapacitor varies continuously with its SOC, analogous to conventional capacitors [6, 10, 18, 19]. Finally, hybrid pseudocapacitors can be designed by pairing a redox-active or pseudocapacitive electrode (e.g.,  $\text{TiO}_2$ ,  $\text{MnO}_2$ ,  $\text{Nb}_2\text{O}_5$ ) with an EDLC-type electrode made of carbon [6, 13, 19]. Figure 1.3(c) illustrates a hybrid pseudocapacitor.

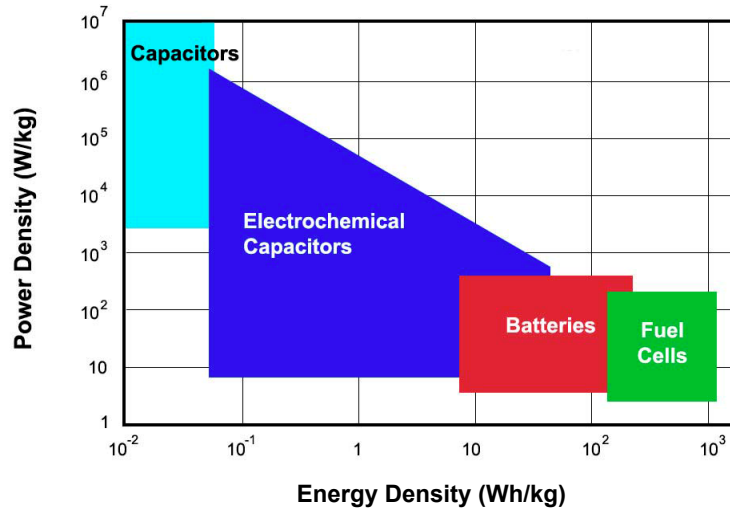


Figure 1.4: Comparison of energy and power densities of different EES systems (from Ref. [6]).

#### 1.2.4 Energy storage performance

The performance of different EES devices can be conveniently compared and assessed based on their specific energy and power densities. The energy density is the energy stored and delivered upon discharge per unit mass of the EES device. Power density is the rated power per unit mass of the EES device [20]. Figure 1.4 shows a Ragone chart plotting the power density as a function of energy density for several types of EES system [6]. The energy and power densities of electrochemical capacitors fall between those of dielectric capacitors and batteries and span several orders of magnitude of both measures [6,10,14,19,21]. The energy storage capacity of EDLCs increases with increasing electrode surface area, since they store energy within the EDL at the electrode/electrolyte interface [6]. For this reason, they use porous electrodes with high surface area, typically made of carbon [6,10,19]. This results in significantly larger energy densities in EDLCs compared with conventional dielectric capacitors. However, their energy densities remain significantly smaller than those of batteries [10,13]. The lack of chemical reactions and phase changes makes EDLC charge storage highly reversible, resulting in cycle life from hundreds of thousands to millions of cycles [6,10,12–14]. EDLC power densities are significantly larger than those of batteries

because no chemical reaction kinetics limit the charge and discharge rates [6, 10]. However, their power densities are significantly smaller than those of dielectric capacitors. ECs have response times on the order of seconds, while dielectric capacitors have response times on the order of nanoseconds [6]. EDLC power is limited primarily by the ionic conductivity through the separator [6, 13]. Pseudocapacitors offer higher capacitances and energy densities than EDLCs because they combine faradaic and EDL charge storage and thus can accommodate more charge per unit electrode surface area and volume than EDL charge storage alone [13, 16, 17, 19, 22, 23]. However, their electrode materials, such as noble metal oxides  $\text{RuO}_2$  and  $\text{IrO}_2$ , are typically more costly than those of EDLCs [6].

The operating voltage across an EC changes continuously during charging and discharging, providing an indication of the state of charge at all times [6, 10]. The operating voltage is limited by the breakdown voltage of the electrolyte, equal to about 1.2 V for aqueous electrolytes and about 2.3 – 2.7 V for organic electrolytes [6, 13]. Individual EC cells are often connected in series for applications where higher voltages are required [6].

### 1.3 Motivation of the present study

Electrochemical capacitors (ECs) are a promising form of electrical energy storage for applications requiring high power, rapid cycling, or long cycle life [6, 10, 19]. Such high power applications include (i) hybrid or electric vehicles, where they can provide high power for acceleration and can capture braking energy more efficiently than batteries, (ii) load-leveling to allow the electrical grid to follow short-term fluctuations or accommodate intermittent energy sources, or (iii) fast restarting and recharging of equipment. Long cycle lives are advantageous for applications where EES replacement is difficult, such as those in remote locations [13]. Depending on the application, ECs may supplement battery systems or replace them entirely.

Like batteries, electrochemical capacitors dissipate energy as heat during charging or discharging. Elevated temperatures increase EDLC capacitance, decrease EC resistance, and increase faradaic reaction rates [9, 24–28]. However, they also accelerate EDLC aging

[7, 8, 21, 25, 29, 30] and increase self-discharge rates [8, 21, 25, 29]. Previous studies have demonstrated that the heat generation in EDLCs can cause temperature rises exceeding the operating range of the device [25].

To avoid these harmful effects, temperature changes in ECs should be mitigated. To this end, thermal modeling should be developed (i) to improve understanding of the physical processes resulting in EC heating, (ii) to provide simulation tools for predicting device operating temperatures in existing and novel EC devices, and (iii) to identify design rules and thermal management strategies for ECs to avoid excessive heating.

## 1.4 Objectives of the present study

The present study aims to develop a physical understanding of coupled electrodiffusion and heat transfer occurring during the operation of electrochemical capacitors. To do so, a physics-based, continuum thermal model will be developed step by step. This model will be solved numerically for simple EC cells and used to physically interpret the thermal behavior of ECs observed in experimental studies. Scaling analyses will be used to identify key dimensionless numbers governing ion transport and EC heating. This can facilitate the formulation of design rules to mitigate undesirable temperature rise in ECs.

## 1.5 Organization of the document

Chapter 2 reviews previous models of the electric double layer and of ion transport within electrolytes, materials used in electrochemical capacitors, Joule heating, and existing experimental and modeling studies of the thermal behavior of ECs. Chapter 3 presents a model and scaling analysis of coupled electrodiffusion and heat transfer in planar EDLCs. The chapter considers the simple case of charging with a step change in potential and includes heat generation due to irreversible Joule heating only. Chapter 4 derives the irreversible and reversible heat generation rates within binary and symmetric electrolyte based on energy conservation. Several contributions to the heat generation rate arising from EDL formation are



introduced and discussed. The model was applied to the practical case of galvanostatic cycling. The results of numerical simulations are qualitatively compared to experimental data from the literature. Chapter 5 presents a simplified first-order thermal model for predicting the transient temperature of an EDLC device based on the lumped-capacitance model. Its predictions showed good quantitative agreement with experimental measurements for the literature for a variety of commercial EDLCs. Chapter 6 presents a scaling analysis of the thermal model from Chapter 4. It reduced the number of independent design parameters, facilitating the identification of scaling laws for the heat generation rate. Chapter 7 generalizes the thermal model from Chapter 4 to account for multi-species and/or asymmetric electrolytes. Numerical simulations were performed for binary and asymmetric electrolytes to investigate the effects of asymmetric ion valencies, ion diameters, and ion diffusion coefficients on the heat generation rates and temperature. Chapter 8 applies a first-principles electrochemical transport model for hybrid pseudocapacitors to galvanostatic cycling. It accounts for redox reactions and ion intercalation in addition to the transport processes previously derived for EDLCs. Simulations were performed to investigate the characteristic electrochemical transport behavior associated with galvanostatic cycling. Chapter 9 uses the electrochemical model from Chapter 8 to derive the heat generation rates associated with a hybrid pseudocapacitor, including all of the heat generation rates derived for EDLCs plus additional irreversible and reversible heat generation rates due to faradaic reactions. Simulations were performed for a planar hybrid pseudocapacitor cycled galvanostatically, and the predicted heat generation rates and temperature evolution were qualitatively compared to experimental measurements from the literature. Finally, Chapter 10 discusses recommendations for future work.

# CHAPTER 2

## Background

### 2.1 Capacitance

The capacitance of an EC characterizes the amount of electric charge (in C) stored from the external circuit as a function of the cell potential  $\psi_s$  (in V). The differential  $C_{s,diff}$  and integral  $C_{s,int}$  areal capacitances (in F m<sup>-2</sup>) per unit electrode/electrolyte interfacial area are defined as [10,31]

$$C_{s,diff} = \frac{dq_s}{d\psi_s} \quad \text{and} \quad C_{s,int} = \frac{q_s}{\psi_s} \quad (2.1)$$

where  $q_s$  is the surface charge density (in C m<sup>-2</sup>). For galvanostatic cycling consisting of alternating charging and discharging steps at a constant imposed current density  $\pm j_s = dq_s/dt$ , the differential and integral capacitances can be expressed as [10,31]

$$C_{s,diff} = \frac{j_s}{|d\psi_s/dt|} \quad \text{and} \quad C_{s,int} = \frac{j_s t_c / 2}{\psi_{max} - \psi_{min}} \quad (2.2)$$

where  $t_c$  is the cycle period and  $\psi_{max}$  and  $\psi_{min}$  are the upper and lower limits of the cell potential.

### 2.2 Electric double layer structure

The distribution of ions in an electrolyte is perturbed near a charged surface. The charged surface attracts ions of opposite charge, called counterions, and repels ions of like charge, called coions [32]. At the same time, the ions are subject to random thermal motion [32]. The distribution of ions at equilibrium is governed by the combination of these competing influences of electrostatic attraction/repulsion and of diffusion due to the presence of concentration gradients. This results in a region of electrolyte near the electrode surface with a net

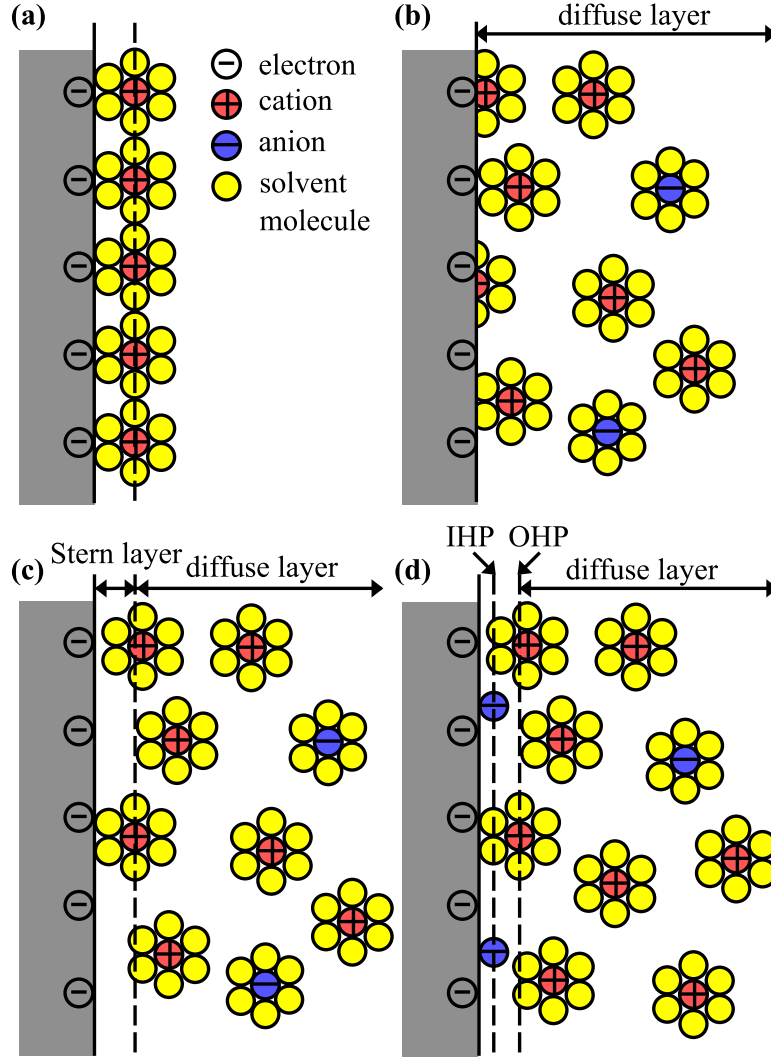


Figure 2.1: Illustrations of the (a) Helmholtz, (b) Gouy-Chapman, (c) Stern, and (d) Grahame models of EDL structure.

ionic space charge density in contrast to the electrically neutral bulk electrolyte. Together, the layer of electronic charge within the electrode and the corresponding layer of ionic charge within the electrolyte are called the electric double layer (EDL) [26,32]. The net ionic charge in the EDL per unit electrode surface area (in  $\text{C m}^{-2}$ ) is equal and opposite to the electronic surface charge density in the electrode so that the region around the interface is electrically neutral overall [26–28].

Several proposed models for the electric double layer structure are illustrated in Figure 2.1. The earliest model and the term “double layer” were both proposed by Helmholtz

[10, 26, 33]. In his model, the counterions form a single layer along the electrode surface, resulting in two layers of electric charge separated by a distance on the order of molecular dimensions, as illustrated in Figure 2.1(a) [10, 26]. This model predicts a constant differential capacitance similar to that of a parallel-plate dielectric capacitor. However, experimental measurements have shown that the differential capacitance of ECs is not constant. It varies with the electrode potential and the electrolyte concentration [26].

The Gouy-Chapman model illustrated in Figure 2.1(b) instead proposed that the ions form a diffuse layer in the electrolyte under the competing influences of electrostatic forces and random thermal motion [10, 34–36]. In this model, the concentration of excess charge is largest next to the electrode surface, where the electrostatic forces are strongest and override the effect of diffusion. The excess charge decreases with increasing distance from the electrode [26]. In this model, the ions are assumed to be point charges [10]. The thickness of the diffuse layer varies with electrolyte concentration, ion valencies, and temperature [26, 27]. The differential capacitance predicted by the Gouy-Chapman model qualitatively resembles that measured experimentally at low concentrations and potentials [10, 26, 27]. However, at higher concentrations and potentials, the model breaks down and overpredicts the differential capacitance [10, 26, 27].

The present study uses the Stern model [37] illustrated in Figure 2.1(c). This model combined the concepts behind the Helmholtz and Gouy-Chapman models. It proposed that the excess charge in the electrolyte can be divided into two layers, the Stern layer and the diffuse layer. The Stern layer is the compact layer adjacent to the electrode surface and containing no free charge [19, 26, 27, 32]. This layer accounts for the fact that ions have finite size [26, 32] and resembles the Helmholtz model of the EDL. The Stern/diffuse layer interface corresponds to the closest distance of approach for an electrostatically adsorbed ion [28]. Ions in the diffuse layer move under the competing influences of electrostatic forces, diffusion, and steric effects [26, 27, 38], as in the Gouy-Chapman diffuse layer. The concentration of excess charge is the largest at the Stern/diffuse layer interface and decreases with increasing distance from the electrode [26, 32]. The Stern model accounts for the major behavior observed in real systems [26].

It should be noted that a further extension of the Stern model exists. Grahame [39] observed that the capacitive behavior of an EDL next to a mercury electrode depended on the type of cations and anions in the electrolyte, especially on the properties of the anion [10]. The Grahame model thus subdivides the compact layer at the electrode surface into the inner Helmholtz layer and the outer Helmholtz layer [10, 26, 27], as illustrated in Figure 2.1(d). These layers correspond to different distances of closest approach for different ions [10, 26, 27]. The inner Helmholtz plane (IHP) is the locus of the centers of ions that are specifically or covalently adsorbed to the surface [26, 27]. The specifically adsorbed ions are unsolvated [26, 27]. The outer Helmholtz plane (OHP) corresponds to the Stern/diffuse layer interface of the Stern model. It is the locus of the centers of electrostatically adsorbed ions [26, 27]. These ions remain solvated [26, 27].

## 2.3 Materials for ECs

There are a variety of desirable material properties for an EC electrode. Among the more obvious ones are high specific area (on the order of  $1000 - 2000 \text{ m}^2/\text{g}$ ) to maximize energy density and low electrical resistance [10]. The electrical resistance depends not only on the conductivity of the electrode material, but also on its structure, since the structure determines the paths an electron must follow to reach the current collectors. The resistance to ion transport in the pores should also be low [10]. This depends on the pore structure and must be balanced with the need for high surface area. In addition, good wettability enables the electrolyte to penetrate into the pores and create the necessary electrode/electrolyte interface for charge storage [10]. Finally, cost must be considered.

EDLC electrodes should not react chemically with the electrolyte or current collector materials [10, 14]. They are typically made of carbon, which has the advantages of low cost and well established fabrication techniques [6, 13, 14]. Different forms of carbon, including activated carbon, carbon aerogels, and carbon nanotubes have been used for EDLCs. Activated carbon is used most commonly due to its low cost and high surface area [13]. By contrast, pseudocapacitive electrodes must react reversibly with an ion in the electrolyte.

They typically consist of metal oxides or conducting polymers and react with cations such as  $\text{Li}^+$ ,  $\text{K}^+$ ,  $\text{H}^+$  [13].

Desirable properties for electrolytes include high relative permittivity or dielectric constant, high decomposition voltage, high ionic conductivity, and a wide usable temperature range [10]. Aqueous electrolytes, such as aqueous  $\text{H}_2\text{SO}_4$  or  $\text{KOH}$ , offer very high dielectric constants as well as relatively low resistivity and minimum pore size requirements [10, 14]. However, water has a low decomposition voltage ( $\approx 1.23$  V) and a relatively high freezing point [10, 13, 14]. Nonaqueous solvents such as acetonitrile and propylene carbonate offer substantially higher decomposition voltages at the cost of lower dielectric constants and higher resistivities [10, 14]. Most commercial EDLCs use nonaqueous electrolytes [12].

## 2.4 Modeling ion transport in electrolytes

An electrolyte is an ionic conductor, so the electric current is carried by the movement of ions [27]. The current density  $\mathbf{j}$  within an electrolyte, expressed in  $\text{A m}^{-2}$ , can be expressed in terms of ion fluxes as [28, 32, 40]

$$\mathbf{j} = F \sum_{i=1}^n z_i \mathbf{N}_i \quad (2.3)$$

where  $F = 9.648 \times 10^4 \text{ C mol}^{-1}$  is the Faraday constant,  $z_i$  and  $\mathbf{N}_i$  are the valency and molar flux (in  $\text{mol m}^{-2}\text{s}^{-1}$ ) of species  $i$ , respectively, and  $n$  is the number of ion species present. The electrical conductivity  $\sigma$  of the electrolyte depends on the concentration  $c_i$  and ionic mobility  $u_i$  of each ion species  $i$  present [27] and can be expressed as  $\sigma = F^2 \sum_{i=1}^n z_i^2 u_i c_i$ . The mobility  $u_i$  of an ion species can be interpreted as the average velocity of an ion under a force of  $1 \text{ N mol}^{-1}$ , with units  $\text{m mol s}^{-1}\text{N}^{-1}$  [32]. The mobility  $u_i$  and the diffusion coefficient  $D_i$  of an ion species are directly linked. For dilute solutions, they are related by the Nernst-Einstein equation  $u_i = D_i/R_u T$ , where  $R_u$  is the universal gas constant and  $T$  is the absolute temperature [28, 32, 41]. Thus, the electrical conductivity  $\sigma$  of an electrolyte can also be expressed as [28, 32]

$$\sigma = \frac{F^2}{R_u T} \sum_{i=1}^n z_i^2 D_i c_i. \quad (2.4)$$

### 2.4.1 Poisson-Nernst-Planck (PNP) model

Within an electrolyte, ions may move due to diffusion, advection, and migration due to an electric field, also called electromigration [32]. The distribution of the electric potential  $\psi$  and the ion distributions are intimately coupled, such that the ion distributions determine the electric potential profile at any instant while the potential profile simultaneously drives ion motion. The classical model for time-dependent local potential and ion transport within the diffuse layer is the Poisson-Nernst-Planck (PNP) model [38]. This model is based on dilute solution theory and treats the ions as non-interacting point charges [38] in motion due to diffusion, electromigration, and advection. The Poisson equation describes the local electric potential  $\psi(\mathbf{r}, t)$  at time  $t$  in terms of the volumetric charge density and is expressed as [38, 41–43]

$$-\nabla \cdot (\epsilon_0 \epsilon_r \nabla \psi) = \begin{cases} 0 & \text{in the Stern layers} \\ F \sum_{i=1}^n z_i c_i & \text{in the diffuse layer} \end{cases} \quad (2.5)$$

where  $\epsilon_0 = 8.854 \times 10^{-12} \text{ F m}^{-1}$  and  $\epsilon_r$  are the vacuum permittivity and the relative permittivity of the electrolyte, respectively. Here, the potential profile within the Stern layers is linear due to the lack of free charge.

In the absence of chemical reactions, the concentration  $c_i(\mathbf{r}, t)$  (in mol L<sup>-1</sup>) of each ion species  $i$  satisfies the mass conservation equation given by [38]

$$\frac{\partial c_i}{\partial t} = -\nabla \cdot \mathbf{N}_i \quad \text{for } i = 1, 2, \dots, n \text{ in the diffuse layer.} \quad (2.6)$$

For dilute solutions, the ion fluxes due to diffusion, electromigration, and advection can be linearly superimposed [32] and the total ion flux is given by [32, 41]

$$\mathbf{N}_i = -D_i \nabla c_i - \frac{D_i z_i F c_i}{R_u T} \nabla \psi + c_i \mathbf{u} \quad (2.7)$$

where  $\mathbf{u}$  is the velocity of the bulk electrolyte. The first, second, and third terms on the right-hand side of Equation (2.7) represent the flux contributions of (i) diffusion due to concentration gradients, (ii) electromigration due to the electric field, and (iii) advection due to bulk electrolyte motion, respectively. The combination of Equations (2.6) and (2.7) forms

the transient transport equation for each ion species  $i$ . These are called the Nernst-Planck equations.

Because the PNP model assumes the ions behave as non-interacting point charges, there is no upper limit to the ion concentrations at the electrode surface [38]. When either the bulk ion concentration or the surface potential is large, the point charges can accumulate without limit and reach unrealistically high concentrations [38]. In reality, ion accumulation is limited by the finite size of the ions and by repulsive forces between them. Assuming simple cubic packing of ions with effective diameter  $a$ , the theoretical maximum concentration  $c_{max}$  is given by  $c_{max} = 1/N_A a^3$  where  $N_A = 6.022 \times 10^{23} \text{ mol}^{-1}$  is the Avogadro constant [38]. The PNP model predicts concentrations exceeding  $c_{max}$  for surface potentials only a few times larger than the thermal voltage  $\psi_T = R_u T / zF$  [38]. Thus, the validity of the PNP model is limited to cases with dilute electrolytes and low surface potentials.

#### 2.4.2 Modified Poisson-Nernst-Planck (MPNP) model

In order to model ion transport for large electrolyte concentrations and/or surface potentials, Kilic *et al.* [38] derived a modified Poisson-Nernst-Planck (MPNP) model of the local potential and ion transport within the diffuse layer accounting for the finite size of ions. This model was developed by accounting for steric effects in the expression of the free energy of the electrolyte used to derive the chemical potentials and the corresponding ion fluxes [38]. The model assumed the electrolyte was binary and symmetric with constant permittivity and negligible advection [38]. In symmetric electrolytes, the valency  $z_i$ , diffusion coefficient  $D_i$ , and effective diameter  $a_i$  are assumed to be identical in magnitude for both ion species. Thus, the subscripts  $i$  may be dropped from the diffusion coefficient  $D$ , the ion diameter  $a$ , and the valency magnitude  $z$ . However, the valencies  $z_i$  of the two ion species still differ in sign, i.e.,  $z_1 = -z_2$ , so the subscript are retained where the sign is relevant. Note that symmetric electrolytes have also been defined based on symmetric valency alone, i.e.,  $z_1 = -z_2$ , without considering the ion diameter or the diffusion coefficient [10,26,27]. However, detailed models accounting for transient ion transport and finite ion size require a more restrictive



definition of electrolyte symmetry. The MPNP model uses the same Poisson Equation (2.5) and mass conservation Equation (2.6) defined above, with  $n = 2$  for binary electrolyte, while the modified ion flux is given by [38]

$$\mathbf{N}_i = -D\nabla c_i - D\frac{z_i F}{R_u T} c_i \nabla \psi - D\frac{N_A a^3 c_i}{1 - N_A a^3 (c_1 + c_2)} \nabla (c_1 + c_2). \quad (2.8)$$

The last term on the right-hand side of Equation (2.8) accounts for the finite ion size. It prevents the total ion concentration  $c_1 + c_2$  from exceeding the theoretical maximum concentration  $c_{max} = 1/N_A a^3$  corresponding to simple cubic packing of ions.

In the limit of negligible ion diameter, i.e.,  $a \rightarrow 0$ , the MPNP model reduces to the classical PNP model. The MPNP model has been validated against established models of EDL behavior for planar electrodes. Ref. [42] confirmed that the equilibrium electric potential profile predicted by the MPNP model for small surface potential and dilute electrolyte (i.e., small  $c_\infty$ ) agreed well with the exact solution predicted using the Gouy-Chapman model [44–46]. Ref. [42] also showed that the MPNP predictions of equilibrium Stern and diffuse layer capacitances agreed well with those based on the modified Poisson-Boltzmann model [40, 47], which accounts for finite ion size and has successfully reproduced the experimentally measured equilibrium capacitance of a three-dimensional ordered EDLC electrode [48].

#### 2.4.3 Generalized modified Poisson-Nernst-Planck (GMPNP) model

Many of the existing ion transport models accounting for finite ion size, like the MPNP model described above, are limited to binary and/or symmetric electrolytes [38, 49–56]. However, many widely used electrolytes are asymmetric, such as aqueous  $\text{H}_2\text{SO}_4$  [57–60]. In addition, electrolyte mixtures including more than two ion species have attracted interest for EDLC applications because certain mixtures perform better than either of the original electrolytes. For example, eutectic mixtures of ionic liquids can provide broader operating temperature ranges than either constituent individually [61–63]. The generalized modified Poisson-Nernst-Planck (GMPNP) model developed by Wang *et al.* [57] predicts the local electric potential and ion concentrations in asymmetric and multi-species electrolytes with finite ion size. The Poisson Equation (2.5) for the electric potential and the mass conserva-

tion Equation (2.6) for the ion concentrations remain the same [57]. In general, the ion flux  $\mathbf{N}_i$  can be written as [57]

$$\mathbf{N}_i = -D_i c_i \left[ \frac{z_i F}{R_u T} \nabla \psi + \nabla \ln(\gamma_{i,L} c_i) \right] \quad (2.9)$$

where  $\gamma_{i,L}$  is the activity coefficient of ion species  $i$ . The GMPNP model assumed the activity coefficient  $\gamma_{i,L}$  obeys a Langmuir-type law accounting for the excluded volume due to finite ion size and expressed as [57, 64]

$$\gamma_{i,L} = \frac{1}{1 - \sum_{i=1}^n \frac{c_i}{c_{i,max}}}. \quad (2.10)$$

Here,  $c_{i,max} = 1/N_A a_i^3$  is the theoretical maximum concentration of ion species  $i$  assuming simple cubic packing of ions with effective ion diameter  $a_i$ . Then, the GMPNP ion flux can be expressed as [57]

$$\mathbf{N}_i = -\frac{D_i F z_i c_i}{R_u T} \nabla \psi - D_i \nabla c_i - \frac{D_i N_A c_i}{1 - N_A \sum_{j=1}^n a_j^3 c_j} \sum_{j=1}^n a_j^3 \nabla c_j. \quad (2.11)$$

Here, the derivation assumed that the effective ion diameters  $a_i$  are independent of location, i.e., they did not vary with the local ion concentrations or temperature. The first, second, and third terms on the right-hand side of Equation (2.11) correspond to the ion fluxes due to electromigration, diffusion, and steric effects, respectively.

For binary and symmetric electrolytes, i.e.,  $n = 2$ ,  $a_1 = a_2 = a$ , and  $|z_1| = |z_2| = z$ , the GMPNP model reduces to the MPNP model. Similarly, in the limit of negligible ion diameter, i.e.,  $a_i \rightarrow 0$  for all ion species  $i$ , it reduces to the PNP model.

## 2.5 Modeling heat transfer

### 2.5.1 Heat diffusion equation

The governing equation for the temperature in a medium can be derived from energy conservation principles applied to a differential control volume [65]. For a medium with no bulk

motion, the temperature is governed by the heat diffusion equation expressed as [65]

$$\rho c_p \frac{\partial T}{\partial t} = \nabla \cdot (k \nabla T) + \dot{q} \quad (2.12)$$

where  $\rho$ ,  $c_p$ , and  $k$  are the density, specific heat, and thermal conductivity of the material, respectively. The local volumetric heat generation rate  $\dot{q}$  (in W/m<sup>3</sup>) represents the conversion of other forms of energy (e.g., electrical, chemical, etc.) into thermal energy [65]. It may be either positive (exothermic), as other types of energy are converted into thermal energy, or negative (endothermic), as thermal energy is converted into another form.

### 2.5.2 Joule heating

Joule heating refers to a form of volumetric heating occurring when electric current flows through a conducting medium [66]. It occurs in electrolytes as well as electronic conductors [66] and corresponds to a conversion of electrical energy into thermal energy [67]. The Joule heat generation rate was empirically formulated by J.P. Joule [68] as  $\dot{Q}_J = I^2 R$  (in W), where  $R$  is the electrical resistance of the conductor. It was irreversible, i.e., always positive regardless of the direction of the current. For conductors obeying Ohm's law, the current can be expressed as  $I = V/R$  or  $\mathbf{j} = \sigma \mathbf{E}$  where  $V$  and  $\mathbf{E}$  are respectively the voltage across the conductor and the electric field vector while  $\sigma$  is the electrical conductivity [69, 70]. For such ohmic conductors, the Joule heat generation rate  $\dot{Q}_J$  can be expressed in the equivalent forms  $\dot{Q}_J = I^2 R = IV = V^2/R$  or in volumetric form as  $\dot{q}_J = |\mathbf{j}|^2/\sigma = \mathbf{j} \cdot \mathbf{E} = \sigma |\mathbf{E}|^2$  (in W/m<sup>3</sup>). The form  $I^2 R$  is used in several existing thermal models of EDLCs [25, 29, 30], and several studies of Joule heating in electrolytes use the forms  $j^2/\sigma$  [71] or  $\sigma |\mathbf{E}|^2$  [66, 72]. However, electrolytes are ohmic conductors only in the absence of concentration gradients. Thus, it is important to carefully choose the correct expression for the model and to clearly define "Joule heating." Unfortunately, there does not appear to be a clear consensus on the definition of Joule heating for non-ohmic conductors. Some studies, for example that by Biesheuvel *et al.* [73], have defined Joule heating in electrolytes as  $\mathbf{j} \cdot \mathbf{E}$ . This heat generation rate can be either positive or negative within the EDLs. Biesheuvel *et al.* [73] described the cooling phenomenon as "negative Joule heating." In the present study, I use the term

“Joule heating” solely for the irreversible contribution  $\dot{q}_{J,irr} = |\mathbf{j}|^2/\sigma$  by analogy to Joule heating in ohmic conductors and to the expression originally defined by Joule [68]. Here, the electrical conductivity  $\sigma$  for an electrolyte is given by Equation (2.4) and depends on the local concentrations of all ion species. Chapter 4 will derive the heat generation rate due to Joule heating in an electrolyte from conservation of energy and discuss the physics in more depth.

## 2.6 Thermal behavior of ECs

### 2.6.1 Effects of temperature on EDLC performance

Several experimental studies have investigated the effect of temperature on EDLC performance and properties. Experimental measurements on commercial EDLCs with carbon electrodes and organic electrolytes have shown that the effective resistance increased and the capacitance decreased with decreasing temperature [9, 24, 25]. This was attributed to the increase in solvent viscosity and electrolyte resistivity at low temperatures [9, 24, 25]. This temperature dependence varied with the frequency of the electrochemical impedance spectroscopy (EIS) measurements and with the solvent type in otherwise identical EDLCs [9, 24, 25]. The temperature dependence of both resistance and capacitance of EDLCs was the strongest for temperatures below 0°C [9, 24, 25].

Increased temperatures can also significantly increase the aging rate of EDLCs by accelerating undesirable electrochemical reactions [29, 74]. The aging process results in permanently decreased capacitance and increased internal resistance of the EDLCs [74]. Indeed, a 20% decrease in capacitance and/or a 100% increase in internal resistance typically define the end of life for an EDLC [75]. A 10 K temperature increase or a 100 mV increase in cell voltage approximately doubles the aging rate [29, 74]. The temperature influence on aging was confirmed experimentally with commercial EDLCs held at elevated temperatures and voltages [74]. Electrical impedance spectroscopy (EIS) measurements performed periodically at the test voltage and temperature indicated a continual increase in the effective resistance

of the EDLCs over time. This increase accelerated towards the end of the tests [74]. There was a simultaneous decrease in the effective capacitance [74]. Bohlen *et al.* [30] developed a equivalent electric circuit model based on experimental data. It accounted for the cell's inductance, the resistance due to conductors and bulk electrolyte, and the impedance associated with the electrode pores [30]. This circuit was used to model an EDLC module under current loads from actual hybrid vehicle tests. The temperature distribution resulting from constant-temperature boundaries and internal heat generation was predicted using a thermal circuit model. Their model indicated that even a moderately non-uniform temperature distribution (initially  $\approx 2$  K differences between the hottest and coolest cells) caused a self-accelerating cycle that led to dramatic differences in cell resistances, capacitances, and operating temperatures after 7 years of simulated operation [30]. Hotter cells aged faster, leading to higher resistances and lower capacitances than their neighbors [30]. This caused increased internal heat generation and larger cell voltages in the higher-temperature cells [30]. Both of these effects further accelerated aging.

### **2.6.2 Experimentally measured temperature and heat generation rates in ECs**

Various experimental studies have investigated the temperature rise and/or heat generation rate occurring during charging and discharging of commercial [7, 8, 25, 29, 76] or lab-built [77, 78] EDLCs. These studies have typically focused on galvanostatic cycling under current  $\pm I_s$  [7, 8, 25, 29, 76–78]. Miller [7] tested a variety of commercial EDLCs with capacitances ranging from 2000 to 3500 F as well as a commercial 10000 F hybrid pseudocapacitor. The ECs were cycled between their rated voltage and one half of their rated voltage [7]. The efficiency of the ECs, defined as the ratio of the energy retrieved during discharging to that added during charging, decreased substantially as the charging current increased [7]. Simultaneously, the EC temperature increased over time as the lost energy was dissipated as heat [7].

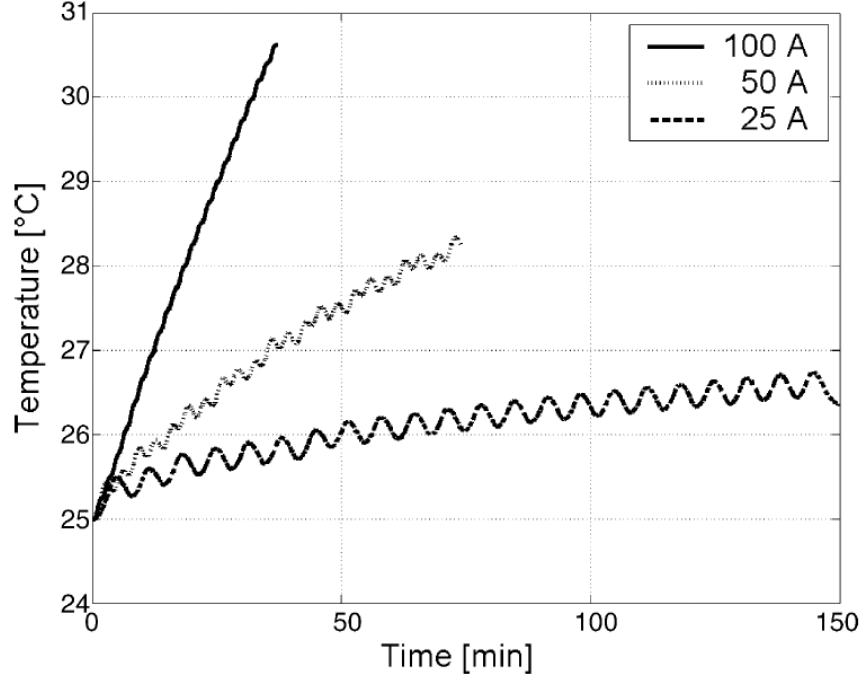


Figure 2.2: Measured EDLC surface temperature as a function of time for galvanostatic cycling at three different currents over the potential window 1.5 – 2.5 V (Figure 10 from Ref. [29]).

### 2.6.2.1 Electric double layer capacitors (EDLCs)

EDLC temperature evolution during galvanostatic cycling featured both an overall temperature rise from cycle to cycle attributed to irreversible heating and superimposed temperature oscillations at the same frequency as the charge-discharge cycles attributed to reversible heating [29, 76–78]. For example, Figure 2.2 shows the temperature measured at the surface of a thermally insulated 5000-F commercial EDLC cycled galvanostatically at several currents  $I_s$  [29]. Both the overall temperature rise and superimposed oscillations or “ripple” were evident for all values of  $I_s$ . For the thermally insulated EDLC, the overall temperature rise was approximately linear and was proportional to  $I_s^2$  [29]. Indeed, it was consistent with that predicted by Joule heating based on the imposed current and cell resistances fitted from impedance data [29]. By contrast, for commercial EDLCs cooled by natural convection in air, the overall temperature rise measured under galvanostatic cycling was not linear. Although it rose initially, it eventually leveled off to a steady-state value as the internal heat generation

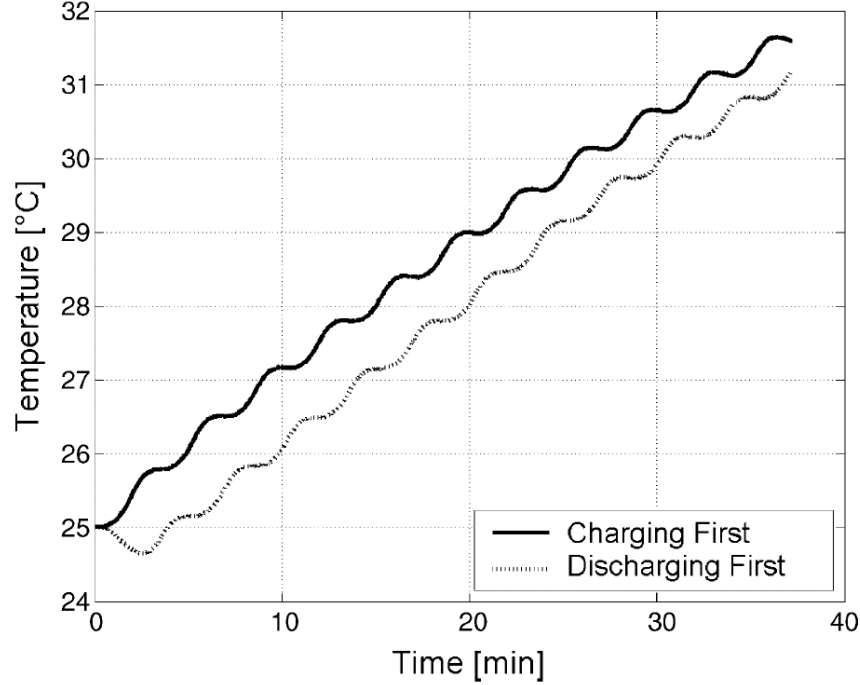


Figure 2.3: Measured EDLC surface temperature as a function of time for constant-current cycling beginning with charging versus beginning with discharging. (Figure 8 from Ref. [29]).

rate was balanced by the convective heat losses to the surroundings [8, 25]. For example, a 1500-F EDLC cycled at 75 A reached a steady-state temperature about 9 K above the ambient temperature after 1 hour [25]. Note that this was enough to approximately double the aging rate per Bohlen *et al.* [30].

The reversible heat generation rate responsible for the temperature oscillations was found to be exothermic during charging, endothermic during discharging, and proportional to the current  $I_s$  based on experimentally measured temperature and heat generation rates [29, 78]. Indeed, Figure 2.3 illustrates this with the measured temperature as a function of time during two tests that were identical, except that one began with a charging step while the other began with a discharging step [29]. Here, the test beginning with charging initial resulted in an initial temperature rise, while the test beginning with discharging had an initial temperature drop. Finally, the amplitude of the temperature oscillations was found to increase with increasing potential window [29].

Gualous *et al.* [76] measured the internal temperature of an EDLC at several locations

using embedded thermocouples. Figure 2.4(a) shows the measured temperatures versus time at three surface locations and four internal locations (T1–T4) as the EDLC temperature rose from its initial temperature to an oscillatory steady state and (b) at the same four internal locations during oscillatory steady-state. The temperature oscillations inside the EDLC were significantly larger in amplitude than those at the surface. They were also approximately triangular, in contrast to the rounded oscillations observed in the surface temperatures in Figure 2.4(a) as well as in Figures 2.2 and 2.3.

### 2.6.2.2 Pseudocapacitors

Dandeville *et al.* [78,79] measured the time-dependent heat generation rates during galvanostatic cycling of a hybrid pseudocapacitor consisting of an  $\text{MnO}_2$  positive electrode and an activated carbon negative electrode in 0.5 M aqueous  $\text{K}_2\text{SO}_4$  electrolyte. Here,  $\text{K}^+$  ions from the electrolyte reacted reversibly with  $\text{MnO}_2$  so that the positive electrode charged by deintercalation of  $\text{K}^+$  ions. The authors also considered an EDLC consisting of two activated carbon electrodes identical to that of the hybrid pseudocapacitor [78]. The heat generation rates in each carbon electrode, either in the EDLC or in the hybrid pseudocapacitor, were assumed to be identical at any given current. This enabled the authors to identify the reversible heat generation rates associated with each half-cell in the hybrid pseudocapacitor. In contrast to EDLCs, the reversible heat generation rate associated with the pseudocapacitive  $\text{MnO}_2$  electrode half-cell was found to be (i) endothermic during charging by deintercalation of  $\text{K}^+$  and (ii) exothermic during discharging by intercalation of  $\text{K}^+$  [78]. However, its magnitude was proportional to  $I_s$ , as observed in EDLCs [78]. Note that it was not possible to differentiate between faradaic and EDL contributions to the heat generation rate in the pseudocapacitive electrode half-cell.



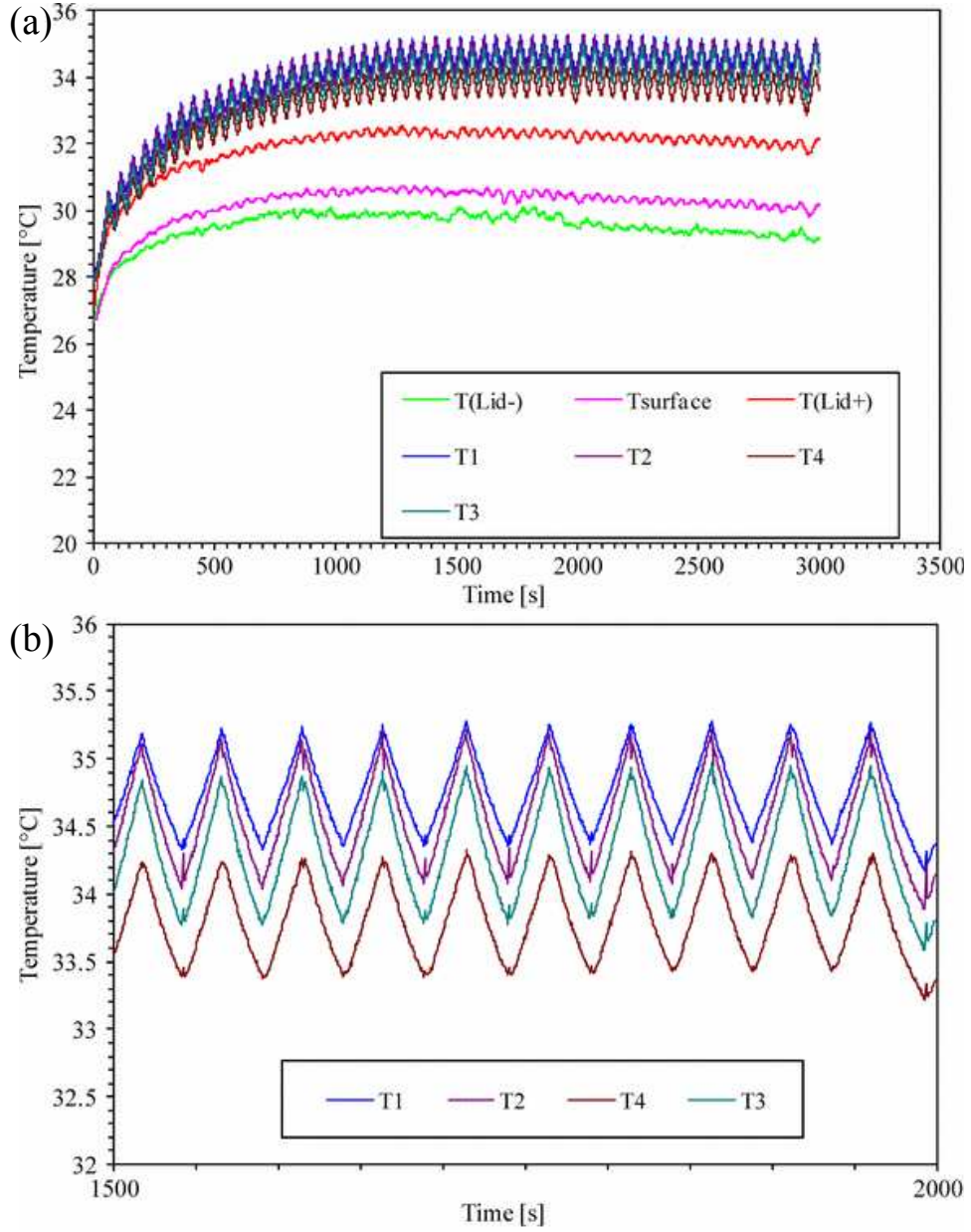


Figure 2.4: Measured temperature as a function of time for (a) three surface locations [T(Lid-), Tsurface, T(Lid+)] and four internal locations (T1, T2, T3, and T4) as the EDLC rose from its initial temperature to an oscillatory steady state and (b) internal locations T1-T4 at oscillatory steady state. (Figure 10 from Ref. [76]).

### 2.6.3 Thermal models of ECs

#### 2.6.3.1 Electric double layer capacitors (EDLCs)

Previous EDLC thermal models typically predicted the temperature of the device by solving the transient heat diffusion equation in two [8, 76] or three dimensions [77, 80, 81]. Guillemet *et al.* [21] solved the two-dimensional steady-state heat diffusion equation to predict the steady-state local temperature and ignored temperature oscillations due to reversible heat generation. In addition, several models have predicted the transient EDLC temperature while assuming uniform temperature throughout the device [82] or by treating the device as multiple regions of uniform temperature connected by thermal resistances [21, 25, 30, 83]. Most of these studies treated EDLCs as “black boxes” characterized experimentally to retrieve parameters necessary for the thermal models [8, 21, 25, 30, 80, 81]. The heat generation rate was prescribed as either (i) uniform throughout the entire device [8, 25, 76, 77, 82], (ii) uniform in the “active components,” i.e., the electrodes and separator [80, 81], or (iii) as having different values in the current collectors, electrodes, and separator [21]. The irreversible heat generation rate was either imposed as an input parameter [8, 21, 77, 80] or predicted as Joule heating (in W) equal to  $I_s^2 R$ , where  $R$  was the experimentally measured resistance of the EDLC cell [25, 29, 30, 81, 82].

Most existing thermal models ignored reversible heat generation and typically did not consider in detail the electrochemical phenomena occurring inside the device [8, 21, 25, 77, 80, 81]. However, Schiffer *et al.* [29] developed an expression for the reversible heat generation rate  $\dot{Q}_{rev}$  based on estimated changes in the entropy of the ions due to electric double layer formation. Their derivation approximated the EDL as a monolayer of ions (i.e., the Helmholtz model) and assumed that the capacitance was independent of the cell potential. The reversible heat generation rate (in W) was expressed as [29]

$$\dot{Q}_{rev} = -2 \frac{T k_B}{e} \ln \left( \frac{V_S}{V_0} \right) C \frac{d\psi_s}{dt} = -2 \frac{T k_B}{e} \ln \left( \frac{V_S}{V_0} \right) I_s(t) \quad (2.13)$$

where  $T$  is the temperature,  $k_B$  is the Boltzmann constant, and  $e$  is the elementary charge. The cell capacitance, cell voltage, and current were denoted by  $C$ ,  $\psi_s$ , and  $I_s$ , respectively.

The total electrolyte volume and the Stern layer volume were given by  $V_S$  and  $V_0$ . However, the value of  $V_S/V_0$  was difficult to evaluate for porous electrodes. Instead, it was used as a fitting parameter. Nonetheless, the expression of  $\dot{Q}_{rev}$  given by Equation (2.13) was later adopted by other thermal models [30, 76, 82].

Models developed for individual EDLC cells were also combined to predict the temperatures of EDLC modules. Bohlen *et al.* [30] and Al Sakka *et al.* [25] developed thermal-circuit models of 12-cell and 20-cell EDLC modules, respectively, and tested them using current loads obtained from actual vehicle tests. The model by Bohlen *et al.* [30] predicted coupled temperature behavior and aging effects such as resistance and capacitance changes over a period of 7 years in simulation time. It demonstrated that even small initial temperature differences would cause the component EDLC cells to age at different rates, leading to even larger temperature differences [30]. The model of Al Sakka *et al.* [25] predicted that natural convection in air was insufficient to keep the 20-cell module within the operating temperature range of the EDLCs and that substantial temperature differences would exist between different parts of the module, with  $\approx 10$  K differences between the maximum and minimum temperatures under forced convection cooling and even larger differences for natural convection [25].

### 2.6.3.2 Pseudocapacitors

Fewer thermal models for pseudocapacitors are available in the literature. Srinivasan and Weidner [84] predicted the transient temperature evolution of a pseudocapacitor cell assuming (i) uniform temperature, (ii) uniform electrolyte concentration at all times, i.e., ignoring the EDL formation, and (iii) heat generation solely due to irreversible Joule heating [84]. Wang *et al.* [81] predicted the local temperature for a commercial hybrid pseudocapacitor under galvanostatic cycling by solving the 3D heat diffusion equation with heat generation. They accounted only for irreversible Joule heating based on the experimentally measured resistance of the device and neglected reversible heating [81]. The numerically predicted maximum temperature in the core of a commercial hybrid pseudocapacitor was considered

to be in good agreement with experimental surface temperature measurements, although the model underpredicted the surface temperature by several degrees [81].

#### 2.6.4 Equivalent resistances of ECs

Joule heating in existing models has been predicted using equivalent resistances. The most commonly used equivalent resistance was the equivalent series resistance (ESR), defined as the resistance in a series RC-circuit model of the EC [10]. The ESR was determined from experimental data in various ways. Several studies determined the ESR using impedance data, either taking the real component of measured EC impedance as the ESR [9, 25] or plotting the impedance data in the complex plane and taking the intersection with the real axis as the ESR [7]. The ESR was also evaluated based on the instantaneous voltage drops or “IR drops” at the beginning or end of a charging cycle with known current [24]. According to Liu *et al.* [24], resistances measured by this method correlate well with those measured using impedance. It should be noted that Miller [7] compared the energy efficiencies predicted by a series RC-circuit model to experimental measurements of four commercial EDLCs and one hybrid pseudocapacitor. He concluded that in general, the series RC-circuit model failed to adequately represent EC electrical behavior and attributed this to the effects of electrode porosity [7]. The studies by Schiffer *et al.* [29] and Bohlen *et al.* [74] used a more complex equivalent electric circuit including multiple resistances with values fitted based on impedance data instead of using the ESR to account for all resistive behavior.

#### 2.6.5 Open questions

Existing models of EC thermal behavior are relatively simple and designed to predict the temperature evolution of experimentally characterized ECs. To do so, they take a macroscopic approach, imposing uniform heat generation rates rather than computing the local heat generation rates inside the device from first principles and accounting for their spatial variation. They generally account only for Joule heating without considering other heat generation rates. Although a few existing models [30, 76, 82] have incorporated the reversible heat

generation rate estimated by Schiffer *et al.* [29], even this formula was estimated using a very simplified model of the EDL. The existing models allow the prediction of the temperature distributions within a device whose properties have been characterized experimentally, but provide little physical insight for interpreting experimental data or designing novel EDLCs. For pseudocapacitors, few thermal models exist at all. To the best of my knowledge, no existing model accounts for reversible heat generation rates present in pseudocapacitors.

The present study aims to analyze the heat generation rates and temperature based on the electrochemical transport processes occurring within EDLCs and pseudocapacitors. It aims to address the following fundamental questions: (1) What physical phenomena cause reversible heat generation rates in EDLCs and in pseudocapacitors? (2) How do these heat generation rates vary in space and/or time? (3) How can they be practically accounted for, e.g., by use of scaling laws and/or analytical approximations? A coupled thermal-electrochemical model facilitates the understanding of experimentally observed thermal behavior such as the temperature oscillations observed in several studies [29, 77, 78]. This physical understanding of EC heating will aid (i) physical interpretation of experimental measurements and (ii) formulation of design rules for new ECs.

## CHAPTER 3

### Thermal modeling of planar EDLCs under a step change in potential

This chapter aims to develop physical understanding of the coupled electrodiffusion and thermal transport taking place in electric double layer capacitors during operation in order to facilitate the modeling and optimization of actual EDLCs. To this end, scaling analysis and detailed numerical simulations were performed for EDLCs with planar electrodes. This chapter focuses on the heat generation rate due to irreversible Joule heating alone and the resulting temperature rise, as considered by most existing thermal models. Here, I consider the simple case of a step change in cell potential. Scaling laws were identified for the peak heat generation rate and for the total amount of heat generated due to the step change in potential.

#### 3.1 Analysis

##### 3.1.1 Schematic and assumptions

Figure 3.1 illustrates the simulated one-dimensional cell of thickness  $2L$  consisting of one planar electrode with surface potential  $\psi_s(t)$  and a counterelectrode with surface potential  $-\psi_s(t)$  separated by an electrolyte. To make the problem mathematically tractable, the following assumptions were made: (1) Chemical reactions and ion insertion into the electrode were absent. (2) The electrolyte was binary and symmetric and obeyed the MPNP model. (3) Dissociation of the electrolyte was complete. (4) Bulk movement of the electrolyte, i.e., advection, was negligible. (5) All electrolyte properties were constant and independent of local

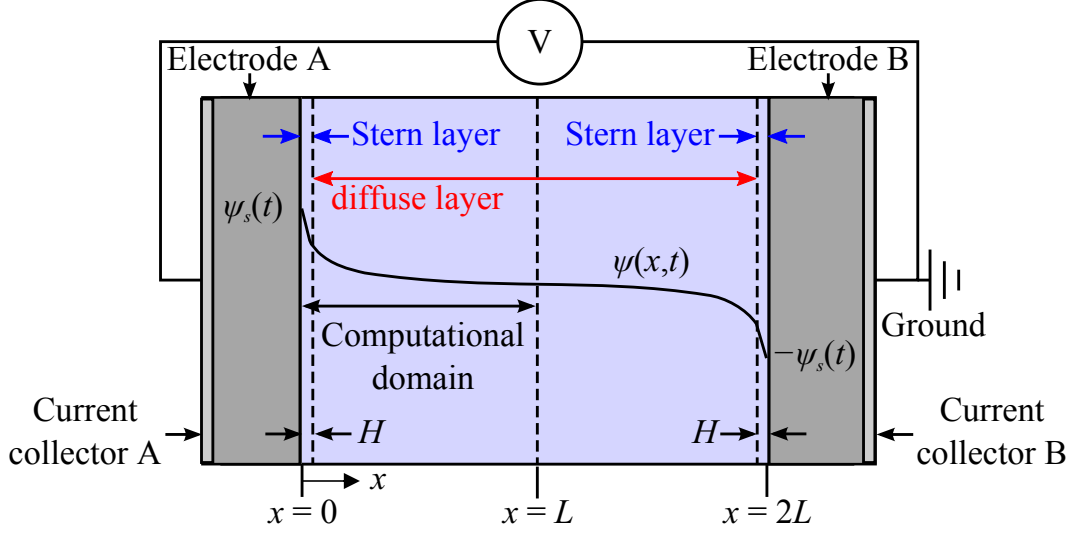


Figure 3.1: Illustration of simulated 1D cell along with the associated coordinate system and computational domain.

ion concentrations or temperature, with the sole exception of the concentration-dependent electrical conductivity  $\sigma$  of the electrolyte. (6) The EDLC was thermally insulated, and (7) the Stern layer thickness  $H$  was assumed to be equal to half of the effective ion diameter, i.e.,  $H = a/2$ .

Assumptions (1) to (3) are realistic for typical EDLC devices using, for example, aqueous KOH or TEABF<sub>4</sub> in acetonitrile as electrolyte [29, 85]. Bazant *et al.* [52] suggested that the assumption of symmetric ion size is reasonable for solvated ions since smaller bare ions tend to be more solvated than larger ions. Assumption (4) is satisfied if the electrolyte is confined in a porous separator inhibiting bulk fluid motion [8, 9, 21]. Assumptions (5) and (6) are appropriate first-order approximations for relatively small temperature variations. The effects of temperature on the electrolyte properties and ion transport are expected to become significant for large temperature rises. These assumptions will be relaxed in future work, but they are appropriate and often used for the purpose of scaling analysis.

### 3.1.2 Governing equations

The coupled one-dimensional governing equations for the electric potential and the cation and anion concentrations solved in this study account for the Stern ( $0 \leq x < a/2$ ) and diffuse

layers ( $a/2 \leq x \leq L$ ) and for steric effects. The electric potential  $\psi(x, t)$  is governed by the Poisson equation (2.5). The anion  $c_1(x, t)$  and cation  $c_2(x, t)$  concentrations in the diffuse layer ( $a/2 \leq x \leq L$ ) satisfy the mass diffusion Equation (2.6) with ion flux  $N_i(x, t)$  given by the MPNP model according to Equation (2.8). The ion flux  $N_i(x, t)$  was evaluated based on the initial temperature  $T_0$ , assuming that ion transport was independent of the temperature rise.

The absolute local temperature  $T(x, t)$  at time  $t$  was computed by solving the heat diffusion Equation (2.12). The heat generation rate  $\dot{q}$  was solely due to irreversible Joule heating expressed as [65]

$$\dot{q} = \dot{q}_{J,irr} = \frac{j^2}{\sigma} \quad (3.1)$$

with the local ionic current density  $j$  and the local electrical conductivity  $\sigma$  given by Equations (2.3) and (2.4), respectively. Because there was no ion insertion into the electrode [Assumption (1)], the ion flux  $N_i$  was equal to zero within the Stern layer. Consequently, the current density  $j$  and Joule heat generation rate  $\dot{q}_{J,irr}$  vanished within this compact layer.

### 3.1.3 Boundary and initial conditions

One initial condition and two boundary conditions were necessary to solve each governing equation for  $\psi(x, t)$ ,  $c_i(x, t)$ , and  $T(x, t)$ . Initially, the potential, ion concentrations, and temperature were assumed to be uniform throughout the computational domain so that

$$\psi(x, 0) = 0 \text{ V}, \quad c_1(x, 0) = c_2(x, 0) = c_\infty, \quad \text{and } T(x, 0) = T_0. \quad (3.2)$$

The potential  $\psi_s(t)$  at the electrode surface was imposed as a step function,

$$\psi(0, t) = \psi_s(t) = \psi_{s,max} \mathcal{H}(t) \quad (3.3)$$

where  $\mathcal{H}(t)$  is the Heaviside step function. In addition, the electrode surface was assumed to be thermally insulated, i.e.,

$$-k \frac{\partial T}{\partial x}(0, t) = 0 \text{ W m}^{-2}. \quad (3.4)$$



The electric potential and electric displacement were continuous across the Stern/diffuse layer interface located at  $x = H$ , so that [42,43,45],

$$\psi(H^-, t) = \psi(H^+, t) \quad \text{and} \quad \epsilon_0 \epsilon_r \frac{\partial \psi}{\partial x}(H^-, t) = \epsilon_0 \epsilon_r \frac{\partial \psi}{\partial x}(H^+, t). \quad (3.5)$$

As previously mentioned, ion insertion into the electrode was ignored, so the ion fluxes at the Stern/diffuse layer interface were zero, i.e.,

$$N_1(H, t) = N_2(H, t) = 0 \text{ mol m}^{-2} \text{s}^{-1}. \quad (3.6)$$

In addition, the temperature and heat flux were also continuous across the Stern/diffuse layer interface such that

$$T(H^-, t) = T(H^+, t) \quad \text{and} \quad -k \frac{\partial T}{\partial x}(H^-, t) = -k \frac{\partial T}{\partial x}(H^+, t). \quad (3.7)$$

At the plane of antisymmetry between the two electrodes ( $x = L$ ), the electric potential, ion concentrations, and heat flux were such that [42,43],

$$\psi(L, t) = 0 \text{ V}, \quad c_1(L, t) = c_2(L, t) = c_\infty, \quad \text{and} \quad -k \frac{\partial T}{\partial x}(L, t) = 0 \text{ W m}^{-2} \quad (3.8)$$

where  $c_\infty$  is the bulk concentration for both ion species.

### 3.1.3.1 Heat generation in the electrode

The magnitudes of the heat generation rates due to Joule heating within the electrolyte relative to that within the carbon electrode can be estimated as

$$\frac{\dot{q}_{electrolyte}}{\dot{q}_{electrode}} = \frac{j^2/\sigma}{j^2/\sigma_C} = \frac{\sigma_C}{\sigma} \quad (3.9)$$

where  $\sigma$  is the electrolyte conductivity and  $\sigma_C$  the carbon electrode conductivity. The current in the electrolyte and in the electrode is the same based on charge conservation. Taking for example 1 mol L<sup>-1</sup> aqueous KCl with valency  $z = 1$  and diffusion coefficient  $D \approx 2 \times 10^{-9} \text{ m}^2/\text{s}$  [60] at room temperature  $T_0 = 298 \text{ K}$  yields  $\sigma = 15 \text{ S/m}$ . The electrical conductivity  $\sigma_C$  of activated carbon falls in the range between 90 and 1000 S m<sup>-1</sup> [14,86,87]. Under these conditions, the volumetric Joule heat generation rate in the electrolyte would be

6 to 67 times larger than that in the electrode. Thus, only heat generation in the electrolyte was considered in this study. Note that the fraction of the total heat generation (in J) contributed by each component would depend on their relative volumes in the device.

### 3.1.4 Scaling analysis

#### 3.1.4.1 Dimensionless equations and parameters

The governing Equations (2.5), (2.6), and (2.12) along with the boundary and initial conditions given by Equations (3.2) to (3.8) were non-dimensionalized using the following dimensionless variables:

$$\begin{aligned} x^* &= \frac{x}{\lambda_D}, \quad t^* = \frac{t}{\lambda_D^2/D}, \quad \psi^*(x^*, t^*) = \frac{\psi(x, t)}{R_u T_0 / zF}, \\ T^*(x^*, t^*) &= \frac{T(x, t) - T_0}{T_0}, \quad \text{and} \quad c_i^*(x^*, t^*) = \frac{c_i(x, t)}{c_\infty}. \end{aligned} \quad (3.10)$$

Here, the location  $x$  was scaled by the Debye length  $\lambda_D$  corresponding to an estimate of the EDL thickness at the initial temperature  $T_0$  and defined for a binary and symmetric electrolyte as  $\lambda_D = \sqrt{\epsilon_0 \epsilon_r R_u T_0 / 2z^2 F^2 c_\infty}$  [40, 41]. The time  $t$  was scaled by the characteristic diffusion time  $\lambda_D^2/D$  [65]. The thermal voltage  $R_u T_0 / zF$  represents the voltage that would induce a potential energy equivalent to the thermal energy of an ion of charge  $z$  [41]. The dimensionless surface potential  $\psi^*$  thus characterizes the extent to which the potential perturbs the ion concentrations from their distribution under zero electric field. Finally, the concentration  $c_i(x, t)$  was scaled by the bulk ion concentration  $c_\infty$ .

Substituting Equation (3.10) into Equations (2.5) yields the following governing equation for the dimensionless potential  $\psi^*(x^*, t^*)$

$$-2 \frac{\partial^2 \psi^*}{\partial x^{*2}} = \begin{cases} 0 & 0 \leq x^* < a/2\lambda_D \\ c_1^* - c_2^* & a/2\lambda_D \leq x^* \leq L/\lambda_D. \end{cases} \quad (3.11)$$

Similarly, in the diffuse layer corresponding to  $a/2\lambda_D \leq x^* \leq L/\lambda_D$ , the dimensionless concentration  $c_i^*(x^*, t^*)$  satisfies

$$\frac{\partial c_i^*}{\partial t^*} = - \frac{\partial N_i^*}{\partial x^*} \quad i = 1 \text{ or } 2 \quad (3.12)$$

where  $N_i^*$  is the dimensionless ion flux defined as  $N_i^* = N_i/(Dc_\infty/\lambda_D)$  and expressed as

$$N_i^* = - \left[ \frac{\partial c_i^*}{\partial x^*} + \text{sgn}(z_i) c_i^* \frac{\partial \psi^*}{\partial x^*} + \frac{(c_\infty/c_{max}) c_i^*}{1 - (c_\infty/c_{max})(c_1^* + c_2^*)} \frac{\partial (c_1^* + c_2^*)}{\partial x^*} \right] \quad (3.13)$$

where  $\text{sgn}(z_i)$  is the function equal to +1 or -1 depending on the sign of the valency  $z_i$ .

Finally, the dimensionless form of the heat diffusion Equation (2.12) can be expressed as

$$\frac{\partial T^*}{\partial t^*} = Le \frac{\partial^2 T^*}{\partial x^{*2}} + \left( \frac{R_u T_0 c_\infty}{\rho c_p T_0} \right) \frac{j^{*2}}{c_1^* + c_2^*}. \quad (3.14)$$

where the Lewis number is denoted by  $Le$  and defined as  $Le = \alpha_{th}/D$  where  $\alpha_{th} = k/\rho c_p$  is the thermal diffusivity of the electrolyte [65]. Here,  $j^*$  is the dimensionless current density defined as

$$j^* = \frac{j}{z F D c_\infty / \lambda_D} = \sum_{i=1}^2 \text{sgn}(z_i) N_i^*. \quad (3.15)$$

Substituting the dimensionless variables into the boundary and initial conditions given by Equations (3.2) to (3.8) yields the following dimensionless initial conditions corresponding to  $t^* = 0$

$$\psi^*(x^*, 0) = 0, \quad c_1^*(x^*, 0) = c_2^*(x^*, 0) = 1, \quad \text{and} \quad T^*(x^*, 0) = 0. \quad (3.16)$$

The dimensionless boundary conditions at the electrode surface ( $x^* = 0$ ) can be expressed as

$$\psi^*(0, t^*) = \frac{\psi_{s,max}}{R_u T_0 / z F} \mathcal{H}(t^*) \quad \text{and} \quad \frac{\partial T^*}{\partial x^*}(0, t^*) = 0. \quad (3.17)$$

At the Stern/diffuse layer interface located at  $x^* = H/\lambda_D = a/2\lambda_D$ , the dimensionless potential satisfies

$$\psi^* \left( \frac{a^-}{2\lambda_D}, t^* \right) = \psi^* \left( \frac{a^+}{2\lambda_D}, t^* \right) \quad \text{and} \quad \frac{\partial \psi^*}{\partial x^*} \left( \frac{a^-}{2\lambda_D}, t^* \right) = \frac{\partial \psi^*}{\partial x^*} \left( \frac{a^+}{2\lambda_D}, t^* \right). \quad (3.18)$$

In addition, the dimensionless ion flux at the Stern/diffuse layer interface is equal to zero, i.e.,

$$N_1^*(a/2\lambda_D, t^*) = N_2^*(a/2\lambda_D, t^*) = 0. \quad (3.19)$$

The boundary conditions for the dimensionless temperature at the Stern/diffuse layer interface are expressed as

$$T^* \left( \frac{a^-}{2\lambda_D}, t^* \right) = T^* \left( \frac{a^+}{2\lambda_D}, t^* \right) \quad \text{and} \quad \frac{\partial T^*}{\partial x^*} \left( \frac{a^-}{2\lambda_D}, t^* \right) = \frac{\partial T^*}{\partial x^*} \left( \frac{a^+}{2\lambda_D}, t^* \right). \quad (3.20)$$

Finally, at the separator centerline, corresponding to  $x^* = L/\lambda_D$ , the boundary conditions simplify to

$$\psi^* \left( \frac{L}{\lambda_D}, t^* \right) = 0, \quad c_1^* \left( \frac{L}{\lambda_D}, t^* \right) = c_2^* \left( \frac{L}{\lambda_D}, t^* \right) = 1, \quad \text{and} \quad \frac{\partial T^*}{\partial x^*} \left( \frac{L}{\lambda_D}, t^* \right) = 0. \quad (3.21)$$

#### 3.1.4.2 Physical interpretation of dimensionless numbers

Overall, the dimensionless governing equations along with the boundary and initial conditions for a step change in potential yield six dimensionless numbers expressed as

$$\begin{aligned} a^* &= \frac{a}{\lambda_D}, \quad L^* = \frac{L}{\lambda_D}, \quad \psi_{s,max}^* = \frac{\psi_{s,max}}{R_u T_0 / z F}, \\ \nu_p &= \frac{2c_\infty}{c_{max}}, \quad Le = \frac{\alpha_{th}}{D}, \quad \text{and} \quad C^* = \frac{\rho c_p T_0}{R_u T_0 c_\infty}. \end{aligned} \quad (3.22)$$

Dimensionless numbers  $a^*$  and  $L^*$  respectively scale the Stern layer thickness and the domain size by the Debye length. Dimensionless number  $\psi_{s,max}^*$  represents the ratio of the maximum imposed surface potential to the thermal voltage. The packing parameter  $\nu_p$  [38] is the ratio of the volume per ion at the theoretical maximum concentration for close-packed ions to that at the bulk concentration, and  $Le$  is the ratio of the characteristic time for heat diffusion to that for ion diffusion. Finally,  $C^*$  represents the ratio of the thermal energy density of the solvent  $\rho c_p T_0$  to the thermal energy density of the ions  $RT_0 c_\infty$ , both expressed in  $\text{J m}^{-3}$ .

#### 3.1.5 Method of solution

The governing Equations (2.5), (2.6), and (2.12) were solved in dimensional form using finite element methods. Due to antisymmetry of the electric potential and symmetry of the electrolyte, both the electric potential and the ion concentrations at the cell centerline remain unchanged from their initial values when  $L$  is much larger than the EDL thickness [43]. Therefore, it suffices to simulate only half of the cell by imposing zero electric potential and bulk ion concentrations at the centerline  $x = L$  [Equation (3.8)] [43]. The computational domain considered in this study therefore comprises only the electrolyte between the electrode/electrolyte interface at  $x = 0$  and the cell centerline at  $x = L$ .

Numerical convergence was assessed based on the computed local electric potential  $\psi$ , ion

concentrations  $c_1$  and  $c_2$ , and temperature  $T$  at time  $t$ . Of these quantities, the temperature was the most sensitive to the mesh refinement. The mesh size was the smallest at the Stern/diffuse layer boundary due to the large potential and concentration gradients and then gradually increased away from this interface. The mesh was refined by reducing the element size at the Stern/diffuse layer interface and the maximum element growth rate. The time step was refined by decreasing the relative and absolute tolerances [88]. During each time step, these tolerances were compared to the estimated local error between solutions at the previous and current time steps for each degree of freedom in the model [88]. The dimensional solutions for  $\psi(x, t)$ ,  $c_i(x, t)$ , and  $T(x, t)$  were scaled by COMSOL before performing this procedure [88]. The time step was then adjusted until a convergence criterion was satisfied, as described in Ref. [88]. This enabled the use of very small time steps during the initial charging phase while using a larger time step for the rest of the computation. The convergence criteria for the mesh and time step were defined so that the maximum relative difference in the local temperature rise  $(T - T_0)$  was less than 0.5% when dividing by two (i) the element size at the Stern/diffuse layer interface, (ii) the maximum element growth rate, and (iii) both the relative and absolute tolerances.

### 3.1.6 Data processing

Several dimensional and dimensionless variables are of particular interest, namely the temperature rise  $\Delta T = T - T_0$  and the local heat generation rate  $\dot{q}_{J,irr}$ . Based on the scaled variables given by Equations (3.10) and the expressions for  $j$  and  $\sigma$ , the dimensionless heat generation rate can be defined as

$$\dot{q}_{J,irr}^*(x^*, t^*) = \frac{j^2/\sigma}{R_u T_0 D c_\infty / \lambda_D^2} = \frac{j^{*2}}{c_1^* + c_2^*}. \quad (3.23)$$

Moreover, the total thermal energy  $Q_{J,irr}(x)$  generated per unit volume at location  $x$  due to the potential step is defined as the integral of the local volumetric heat generation rate  $\dot{q}_{J,irr}(x, t) = j^2/\sigma$  with respect to time

$$Q_{J,irr}(x) = \int_0^\infty \dot{q}_{J,irr}(x, t) dt. \quad (3.24)$$

Table 3.1: Input parameters of three cases used to illustrate the scaling analysis and such that  $a^* = 2.0$ ,  $L^* = 395$ ,  $\psi_{s,max}^* = 4$ ,  $\nu_p = 0.2$ ,  $Le = 50$ , and  $C^* = 400$ .

	Case 1	Case 2	Case 3
$z$	1	2	2
$a$ (nm)	0.5	0.25	1
$D$ (m <sup>2</sup> s <sup>-1</sup> )	$2.626 \times 10^{-9}$	$3.282 \times 10^{-10}$	$2.626 \times 10^{-9}$
$c_\infty$ (mol L <sup>-1</sup> )	1.329	10.630	0.1661
$\epsilon_r$	72.15	288.6	144.3
$k$ (W m <sup>-1</sup> K <sup>-1</sup> )	0.58	0.58	0.0725
$\rho$ (kg m <sup>-2</sup> )	1000	1000	125
$c_p$ (J kg <sup>-1</sup> K <sup>-1</sup> )	4418	35340	4418
$\psi_{s,max}$ (V)	0.10273	0.10273	0.05137
$L$ (nm)	100	50	200
$T_0$ (K)	298	596	298

This value was evaluated by numerically integrating the local heat generation  $\dot{q}_{J,irr}(x, t)$  over the entire simulation time necessary to reach steady state when  $j$  and  $\dot{q}_{J,irr}$  vanished. The corresponding total dimensionless heat generation can be expressed as

$$Q_{J,irr}^*(x^*) = \frac{Q_{J,irr}(x)}{R_u T_0 c_\infty} = \int_0^\infty \dot{q}_{J,irr}^*(x^*, t^*) dt^*. \quad (3.25)$$

The scaling analysis shows that the dimensionless heat generation rate  $\dot{q}_{J,irr}^*(x^*, t^*)$  and consequently the total heat generation  $Q_{J,irr}^*(x^*)$  depend on only four of the six dimensionless numbers defined in Equation (3.22), namely  $a^*$ ,  $L^*$ ,  $\psi_{s,max}^*$ , and  $\nu_p$ .

## 3.2 Results and discussion

### 3.2.1 Illustration of scaling analysis

Table 3.1 summarizes three sets of input parameters used to illustrate the scaling analysis. Case 1 was based on properties of aqueous KOH electrolyte for concentration  $c_\infty = 1$  mol L<sup>-1</sup>

[60] and potential  $\psi_{s,max} = 0.1$  V. The associated dimensionless numbers were  $a^* = 2.0$ ,  $L^* = 395$ ,  $\psi_{s,max}^* = 4$ ,  $\nu_p = 0.2$ ,  $Le = 50$ , and  $C^* = 400$ . The input parameters  $z$ ,  $a$ ,  $D$ ,  $c_\infty$ ,  $\epsilon_r$ ,  $k$ ,  $\rho$ ,  $c_p$ ,  $\psi_{s,max}$ ,  $L$ , and  $T_0$  for Cases 2 and 3 were all varied arbitrarily. However, the six dimensionless numbers  $a^*$ ,  $L^*$ ,  $\psi_{s,max}^*$ ,  $\nu_p$ ,  $Le$ , and  $C^*$  were identical for Cases 1 to 3. If the scaling analysis based on Equations (3.10) is correct, any cases with identical dimensionless groups should yield the same scaled results for  $\psi^*$ ,  $c_1^*$ ,  $c_2^*$ , and  $T^*$  for all values of  $x^*$  and  $t^*$ .

### 3.2.1.1 Scaling of $\psi(x, t)$ , $c_i(x, t)$ , and $T(x, t)$

Figure 3.2(a) shows the predicted electric potential at the Stern/diffuse layer interface  $\psi(H, t)$  as a function of time  $t$  after imposing the step change in surface potential given by Equation (3.3). The electric potential at the Stern/diffuse layer interface decreased from its initial value very close to  $\psi_{s,max}$  at  $t = 0^+$  to a steady-state value as counter-ions migrated towards the electrode to form the EDL. As expected, the temporal evolution of  $\psi(H, t)$  and/or its equilibrium value were different for the three cases considered. The steady-state potentials for Cases 1 and 2 were identical since  $\psi_{s,max}$  was the same in both cases. Figure 3.2(b) plots the same results shown in Figure 3.2(a) in terms of dimensionless potential  $\psi^*(x^* = a^*/2, t^*)$  as a function of dimensionless time  $t^*$ . All three cases collapsed onto a single curve. The same results were obtained at all locations in the domain.

Similarly, Figures 3.3(a) and 3.4(a) show the temporal evolution of the predicted anion concentration  $c_2(H, t)$  and the temperature rise  $\Delta T(H, t) = T(H, t) - T_0$  at the Stern/diffuse layer interface, respectively. Both the anion concentration and the temperature increased with time as the ions migrated to form the EDL before reaching their respective equilibrium values. Due to the low surface potential in this case, the electrode surface was not saturated with ions, i.e.,  $c_2(H, t)$  did not reach  $c_{max}$ . Similarly, the temperature rise was very small. The same data are presented in dimensionless form in Figures 3.3(b) and 3.4(b). Here also, the dimensionless concentration  $c_2^*(a^*/2, t^*)$  and dimensionless temperature rise  $T^*(a^*/2, t^*)$  collapsed onto a single curve for the three different cases considered. Similar results were obtained at other locations in the domain.

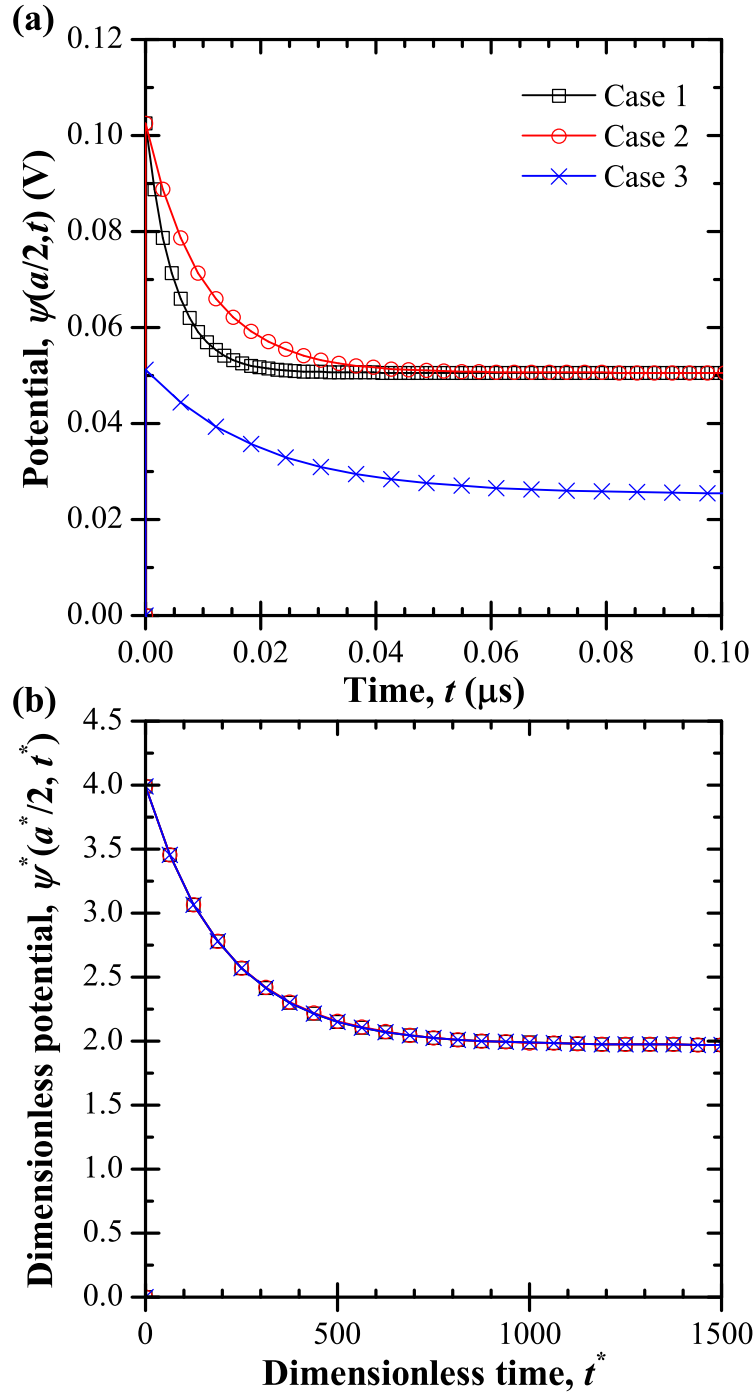


Figure 3.2: Predicted (a) electric potential at the Stern/diffuse layer interface  $\psi(a/2, t)$  as a function of time  $t$  and (b) corresponding dimensionless electric potential  $\psi^*(a^*/2, t^*)$  as a function of dimensionless time  $t^*$  for Cases 1 to 3 (Table 3.1). Similar results were obtained for other locations.



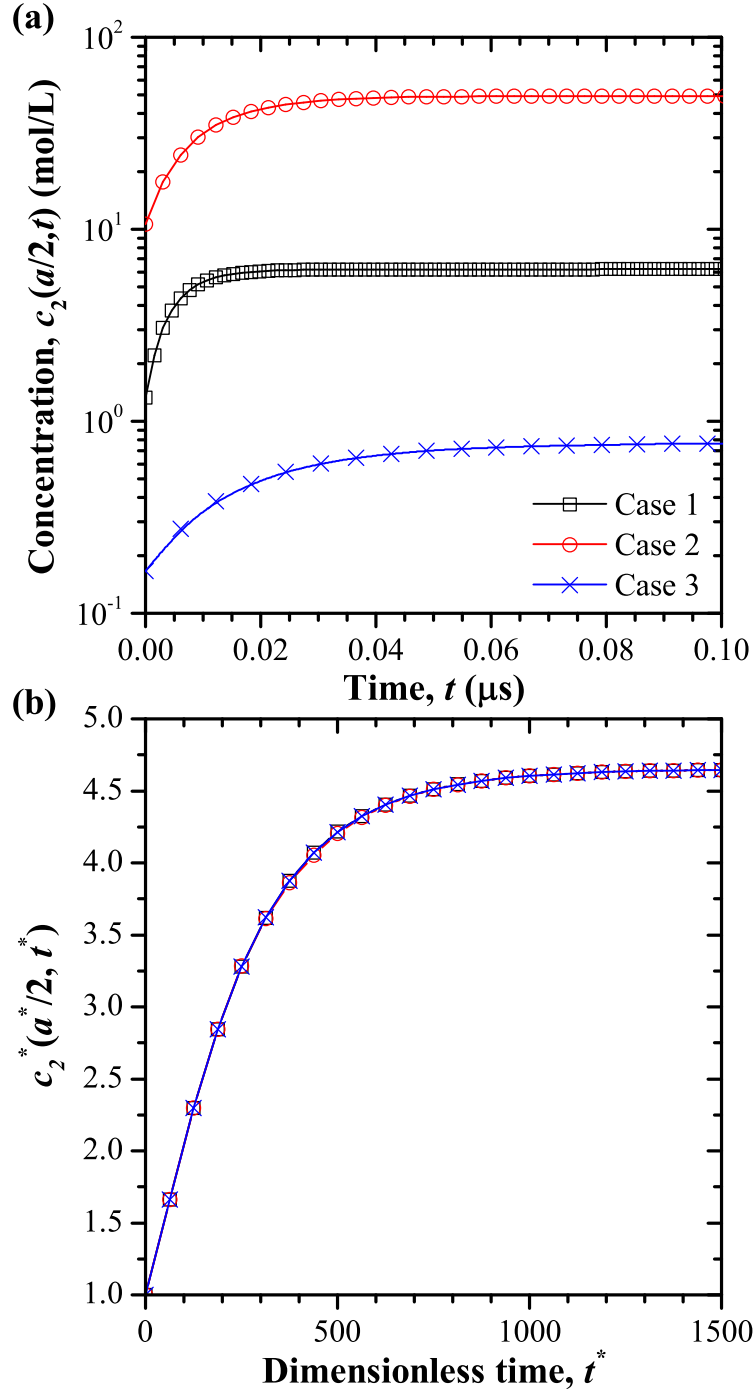


Figure 3.3: Predicted (a) anion concentration at the Stern/diffuse layer interface  $c_2(a/2, t)$  as a function of time  $t$  and (b) corresponding dimensionless anion concentration  $c_2^*(a^*/2, t^*)$  as a function of dimensionless time  $t^*$  for Cases 1 to 3 (Table 3.1).

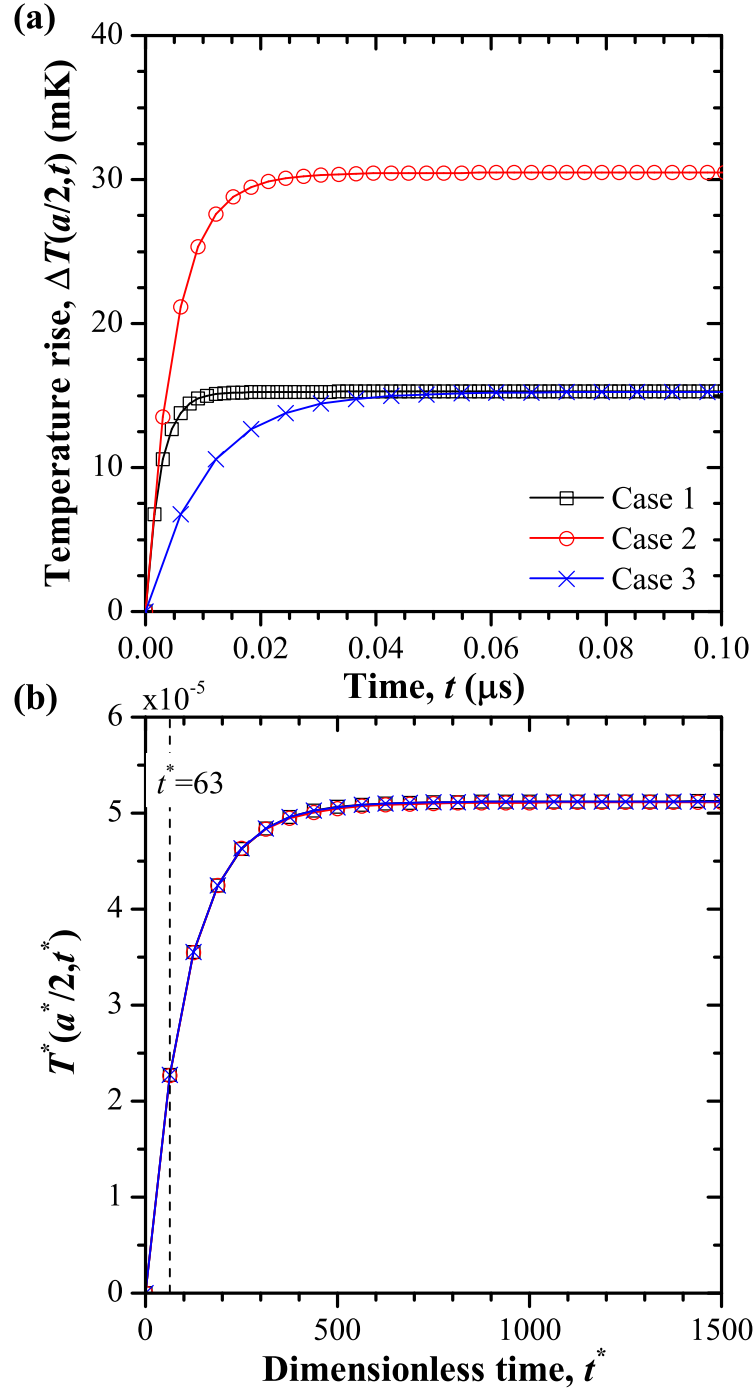


Figure 3.4: Predicted (a) temperature rise at the Stern/diffuse layer interface  $\Delta T(a/2, t) = T(a/2, t) - T_0$  as a function of time  $t$  and (b) corresponding dimensionless temperature rise  $T^*(a^*/2, t^*)$  as a function of dimensionless time  $t^*$  for Cases 1 to 3 (Table 3.1).

### 3.2.1.2 Scaling of Joule heat generation rate $\dot{q}_{J,irr}(x, t)$

Figure 3.5(a) shows the Joule heat generation rate  $\dot{q}_{J,irr}(x, t)$  as a function of location  $x$  for Cases 1 to 3 at different times corresponding to the same dimensionless time  $t^* = 63$  shown in Figure 3.4(b) and within the period of intense heat generation shortly after the step change in potential. It is evident that the heat generation rate varied significantly among the three cases simulated. However, in all cases, the heat generation rate  $\dot{q}_{J,irr}$  was uniform across 99% of the computational domain, only decreasing sharply to zero very close to the Stern/diffuse layer interface where the current density vanished. This resulted in uniform temperature rise across the domain (not shown). Therefore, the heat generation rate and temperature rise at the cell centerline ( $x = L$ ) can be used to estimate their values everywhere in the domain at any given time.

Figure 3.5(b) shows the same data from Figure 3.5(a) plotted in terms of dimensionless heat generation rate  $\dot{q}_{J,irr}^*(x^*, t^*)$  as a function of  $x^*$  for  $t^* = 63$ . It establishes that all three cases collapsed onto a single curve when the results were plotted in dimensionless form.

Overall, these results illustrate the scaling analysis performed on the coupled MPNP and heat diffusion equations and their initial and boundary conditions for EDLCs with binary and symmetric electrolytes under a step change in potential. The dimensionless variables  $\psi^*(x^*, t^*)$ ,  $c_i^*(x^*, t^*)$ , and  $T^*(x^*, t^*)$  depended only on the six similarity parameters  $a^*$ ,  $L^*$ ,  $\psi_{s,max}^*$ ,  $\nu_p$ ,  $Le$ , and  $C^*$ . This substantially reduces the number of independent design parameters to be considered, facilitating the development scaling laws for Joule heating in EDLCs.

## 3.2.2 Scaling laws for Joule heating in EDLCs under a step change in potential

A step change in cell potential was used to investigate the effect of different dimensionless numbers on Joule heating in EDLCs. This charging method is one of the simplest possible, being completely characterized by the single value  $\psi_{s,max}$ . The scaling analysis of Section 3.1.4 indicates that the dimensionless Joule heat generation rate  $\dot{q}_{J,irr}^*(x^*, t^*)$  is a function of dimensionless numbers  $a^*$ ,  $L^*$ ,  $\psi_{s,max}^*$ , and  $\nu_p$  only.

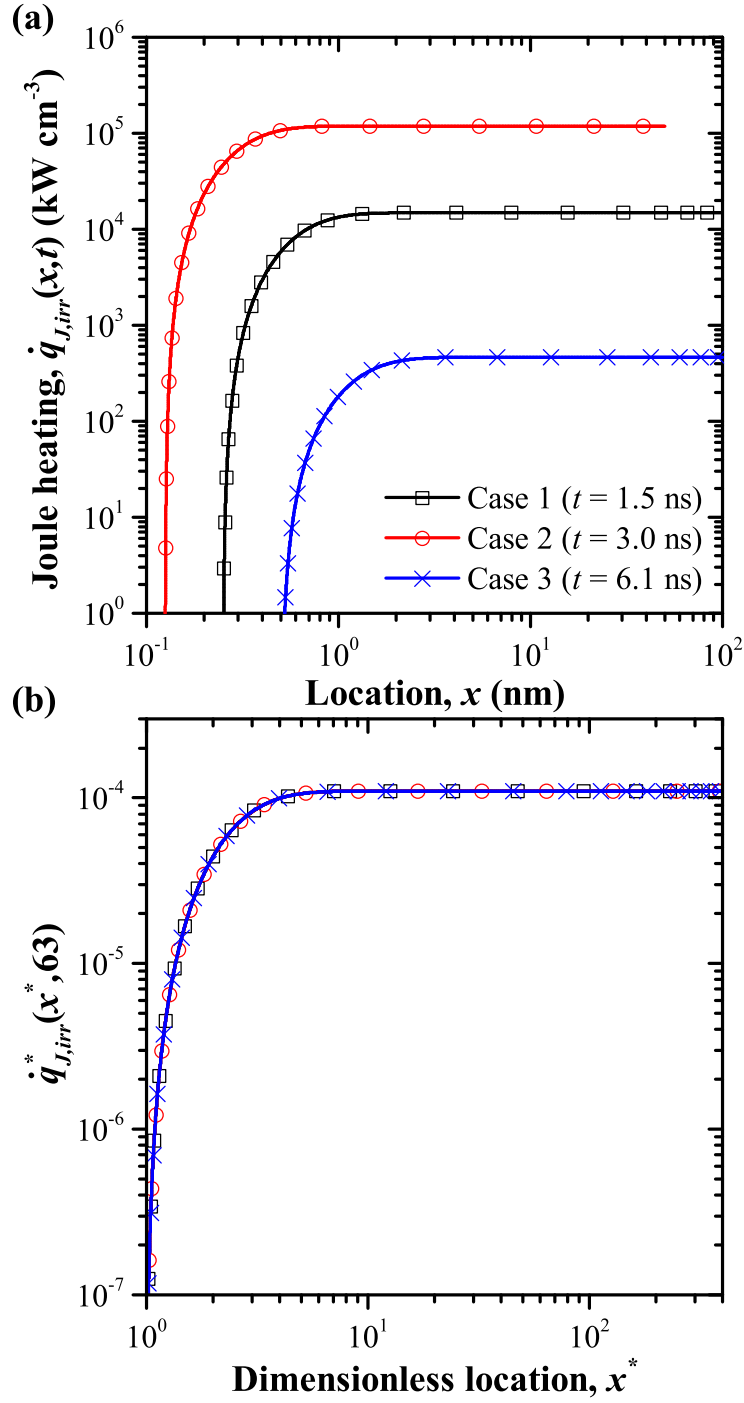


Figure 3.5: Predicted (a) heat generation rate  $\dot{q}(x,t)$  as a function of location  $x$  and at time  $t$  such that  $t^* = 63$  and (b) corresponding dimensionless heat generation  $\dot{q}^*(x^*, 63)$  as a function of dimensionless location  $x^*$  for Cases 1 to 3 (Table 3.1).

A realistic range for each one of these dimensionless numbers can be estimated based on typical values of  $z$ ,  $a$ ,  $L$ ,  $\epsilon_r$ ,  $T_0$ , and  $\psi_{s,max}$ . For aqueous electrolyte EDLCs, the dielectric constant and the surface potential are typically  $\epsilon_r = 78.5$  and  $\psi_{s,max} = 0.5$  V (for a total cell potential of 1.0 V) with bulk concentration and initial temperature equal to  $c_\infty = 1$  mol L<sup>-1</sup> and  $T_0 = 298$  K, respectively. The ion diameter can range from 0.1 to 0.9 nm encompassing small non-hydrated ions to large hydrated ions [60]. The ion valency  $z$  typically ranges between 1 and 3. The domain size is such that  $10 \mu\text{m} \leq L \leq 150 \mu\text{m}$  based on reported commercial separator thickness [89]. Under these conditions, the dimensionless numbers  $a^*$ ,  $L^*$ ,  $\psi_{s,max}^*$ , and  $\nu_p$  fall within the ranges  $0.33 \leq a^* \leq 9.9$ ,  $2.5 \times 10^4 \leq L^* \leq 1.5 \times 10^6$ ,  $19.47 \leq \psi_{s,max}^* \leq 58.41$ , and  $0.0012 \leq \nu_p < 1.0$ . Here,  $\nu_p$  is strictly less than 1 because the bulk ion concentration must be less than  $c_{max}$ .

### 3.2.2.1 Peak Joule heat generation rate $\dot{q}_{peak}$

Simulations showed that the maximum heat generation rate in response to a step change in potential occurred immediately after the step, i.e., at  $t = 0^+$ . Then, this peak heat generation rate, denoted as  $\dot{q}_{peak}(x)$ , is given by

$$\dot{q}_{peak} = \dot{q}_{J,irr}(x, 0^+) = \frac{[j(x, 0^+)]^2}{\sigma(x, 0^+)}. \quad (3.26)$$

At  $t = 0^+$ , the ions have not had time to migrate so their concentrations are uniform, i.e.,  $c_1(x, 0^+) = c_2(x, 0^+) = c_\infty$  and  $\partial c_1 / \partial x(x, 0^+) = \partial c_2 / \partial x(x, 0^+) = 0$ . Under these conditions, the Poisson Equation (2.5) simplifies to  $\partial^2 \psi / \partial x^2 = 0$ , indicating that the potential profile is linear over the entire domain between  $x = 0$  and  $x = L$ . Then, the ion fluxes  $N_1$  and  $N_2$ , defined by Equation (2.8), simplify as

$$N_i(x, 0^+) = D \frac{z_i F}{R_u T_0} c_\infty \frac{\psi_{s,max}}{L} \quad i = 1 \text{ or } 2. \quad (3.27)$$

In addition, the ionic current density and electrical conductivity at  $t = 0^+$  can be written as

$$j(x, 0^+) = F \sum_{i=1}^2 z_i N_i(x, 0^+) = \frac{2z^2 F^2 D c_\infty \psi_{s,max}}{R_u T_0 L} \quad \text{and} \quad \sigma(x, 0^+) = \frac{2D z^2 F^2 c_\infty}{R_u T_0}. \quad (3.28)$$

Finally, the peak heat generation can be expressed, in dimensional and dimensionless forms, as

$$\dot{q}_{peak} = \frac{2z^2 F^2 D c_\infty \psi_{s,max}^2}{R_u T_0 L^2} \quad \text{and} \quad \dot{q}_{peak}^* = 2 \frac{\psi_{s,max}^{*2}}{L^{*2}}. \quad (3.29)$$

Figure 3.6 compares the dimensionless peak heat generation rate  $\dot{q}_{peak}^*$  computed numerically with that predicted by Equation (3.29) for the range of dimensionless numbers previously discussed. It shows that there was excellent agreement between the analytical and the numerical predictions over a very wide range of  $\dot{q}_{peak}^*$ . Thus, the expression given by Equation (3.29) can be used as an upper bound for the Joule heat generation rate in EDLCs for a step change in potential.

Equation (3.29) indicates that the peak heat generation rate  $\dot{q}_{peak}$  increased linearly with increasing electrolyte concentration  $c_\infty$  and diffusion coefficient  $D$  and increased quadratically with increasing ion valency  $z$ . This corresponds to  $\dot{q}_{peak}$  increasing with increasing conductivity  $\sigma$ . Although  $\sigma$  appears in the denominator of  $\dot{q}_{J,irr}$ , large  $\sigma$  also resulted in larger current density  $j$  in response to the same potential drop, increasing the Joule heating. In addition,  $\dot{q}_{peak}$  increased quadratically with increasing surface potential  $\psi_{s,max}$  and with decreasing electrode separation  $L$ , i.e., with increasing initial electric field and thus larger current. Note that, in order to increase energy and power densities of EDLCs, it is desirable to use large potential windows and to maximize electrolyte conductivity [13, 14]. The present results show that these measures would also increase the peak heat generation rate in EDLCs subjected to abrupt changes in cell potential. This further confirms the importance of understanding and predicting heat transfer in high-performance EDLCs.

### 3.2.2.2 Total Joule heat generated $Q_{J,irr}$

In contrast to  $\dot{q}_{peak}$ , the total Joule heat  $Q_{J,irr}$  [Equation (3.24)] generated by the step change in potential was more difficult to predict analytically and did not lend itself to a simple analytical expression. However, some clear trends relating  $Q_{J,irr}^*$  [Equation (3.25)] to the dimensionless groups could be observed. Figure 3.7(a) shows  $Q_{J,irr}^*$  as a function of  $L^*$  for  $\psi_{s,max}^* = 19$  and different combinations of  $a^*$  and  $\nu_p$  values. It indicates that  $Q_{J,irr}^*$  was

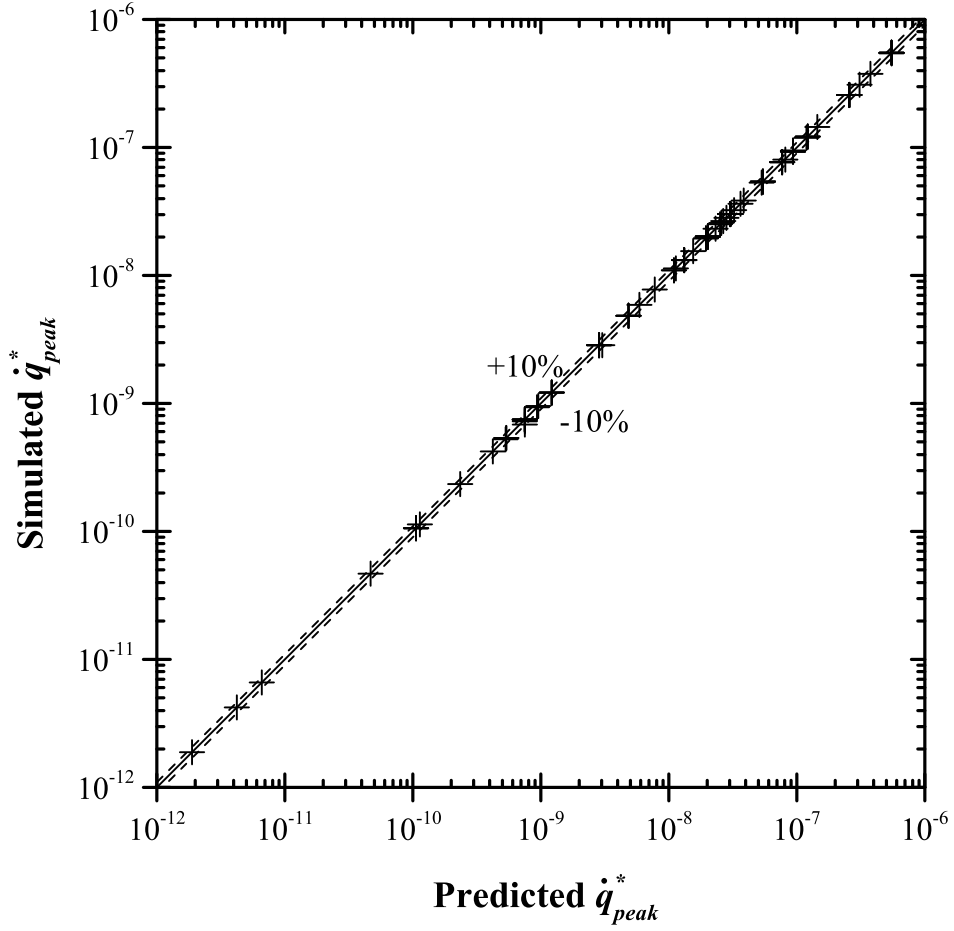


Figure 3.6: Comparison of the dimensionless peak heat generation rate  $\dot{q}_{peak}^*$  computed numerically with that predicted by Equation (3.29) for realistic range of dimensionless numbers  $0.33 \leq a^* \leq 9.9$ ,  $2.5 \times 10^4 \leq L^* \leq 1.5 \times 10^6$ ,  $19.47 \leq \psi_{s,max}^* \leq 58.41$ , and  $0.0012 \leq \nu_p < 1.0$ .

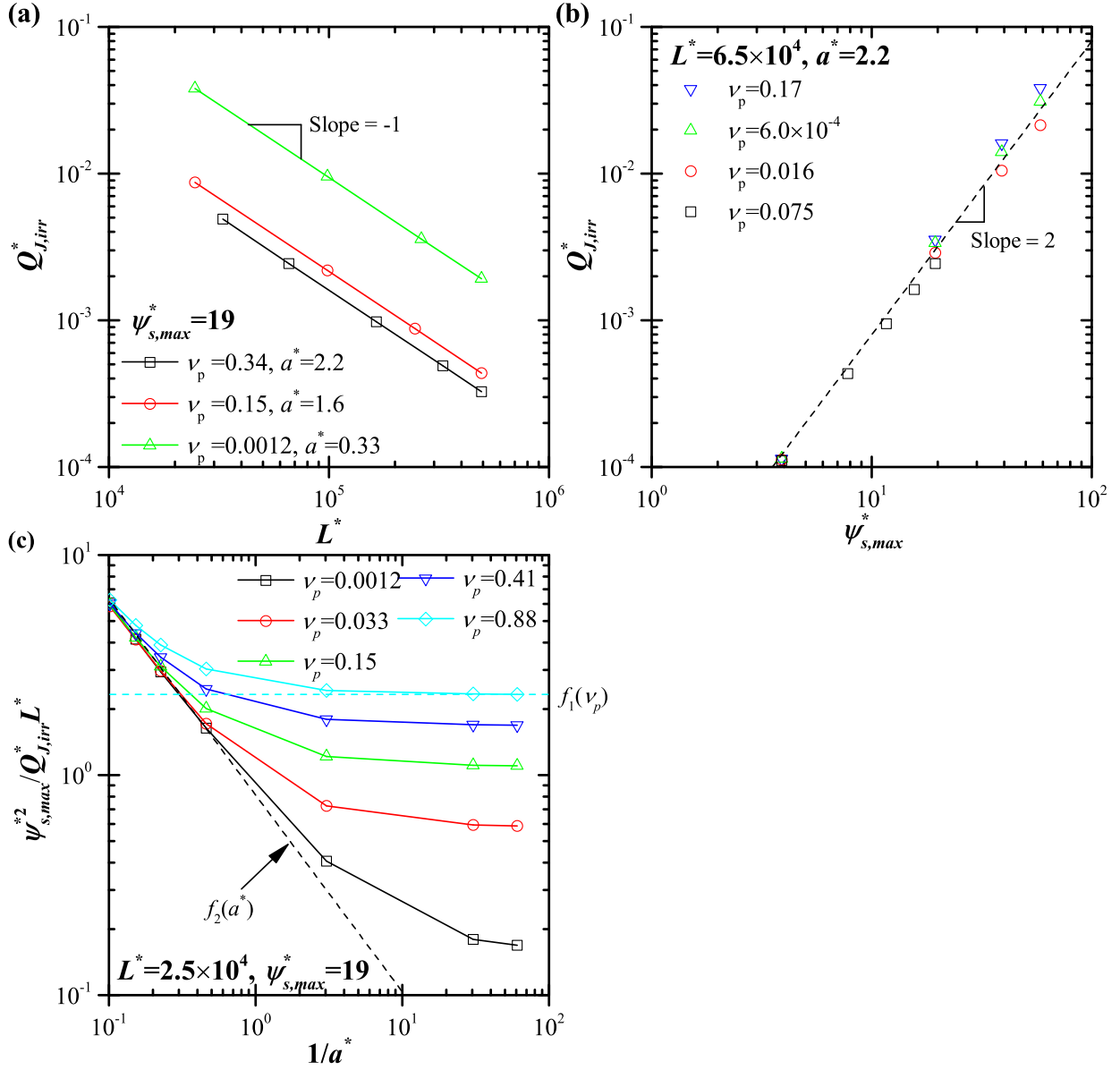


Figure 3.7: (a) Total dimensionless heat generation  $Q_{J,irr}^*$  as a function of  $L^*$  for  $\psi_{s,max}^* = 19$ . (b) Total dimensionless heat generation  $Q_{J,irr}^*$  as a function of  $\psi_{s,max}^*$  for  $L^* = 6.5 \times 10^4$  and  $a^* = 2.2$ . (c) Ratio  $\psi_{s,max}^{*2} / Q_{J,irr}^* L^*$  as a function of  $1/a^*$ , showing asymptotes  $f_1(\nu_p)$  and  $f_2(a^*)$ .



inversely proportional to  $L^*$ . Similar plots were obtained for different values of  $\psi_{s,max}^*$ ,  $\nu_p$ , and  $a^*$ . Similarly, Figure 3.7(b) shows the dimensionless total heat generation  $Q_{J,irr}^*$  as a function of dimensionless surface potential  $\psi_{s,max}^*$  for different values of  $\nu_p$  and for  $a^* = 2.2$  and  $L^* = 6.5 \times 10^4$ . Here,  $Q_{J,irr}^*$  was approximately proportional to  $\psi_{s,max}^{*2}$ . The same trends were observed for different values of  $a^*$  and  $L^*$ . Based on these results, Figure 3.7(c) shows the ratio  $\psi_{s,max}^{*2}/Q_{J,irr}^*L^*$  as a function of  $1/a^*$  for  $L^* = 2.5 \times 10^4$  and  $\psi_{s,max}^* = 19$  and different values of  $\nu_p$ . It indicates that  $\psi_{s,max}^{*2}/Q_{J,irr}^*L^*$  was independent of  $a^*$  for  $a^* \ll 1$  and reached a plateau whose value, denoted as  $f_1(\nu_p)$ , depended on  $\nu_p$  only. Similarly, for  $a^* \gg 1$ , it was independent of  $\nu_p$  and approached a curvilinear asymptote  $f_2(a^*)$ . In fact, Figure 3.8 shows the values of  $\psi_{s,max}^{*2}/Q_{J,irr}^*L^*$  (a) as a function of  $\nu_p$  for  $a^* = 0.016$  and  $0.033$  and (b) as a function of  $a^*$  for  $a^* \gg 1$  with packing parameters  $\nu_p$  ranging from  $0.0012$  to  $0.88$ . Both plots were fitted by power laws to find the curvilinear asymptotes

$$f_1(\nu_p) = 2.43\nu_p^{0.4} \quad \text{and} \quad f_2(a^*) = 0.83a^{*0.86}. \quad (3.30)$$

For all values of  $a^*$  and  $\nu_p$ , the dimensionless total heat generation can be expressed as

$$Q_{J,irr}^* = \frac{\psi_{s,max}^{*2}}{L^*} [(f_1(\nu_p))^2 + (f_2(a^*))^2]^{-1/2} = \frac{\psi_{s,max}^{*2}}{L^*} [(2.43\nu_p^{0.4})^2 + (0.83a^{*0.86})^2]^{-1/2}. \quad (3.31)$$

The average relative error between the total heat generation  $Q_{J,irr}^*$  predicted by Equation (3.31) and that predicted numerically was less than 6% for all values of  $a^*$ ,  $L^*$ ,  $\psi_{s,max}^*$ , and  $\nu_p$  considered.

### 3.3 Conclusion

This chapter presented a model for coupled electrodiffusion and Joule heating during charging of electric double layer capacitors by a step change in cell potential. The model accounted for the presence of the Stern layer and for the finite size of ions by using the modified Poisson-Nernst-Planck model. One-dimensional transient electrodiffusion and heat diffusion with Joule heating for the EDLC was found to be governed by eleven dimensional parameters. Scaling analysis reduced the number of independent governing parameters to only six

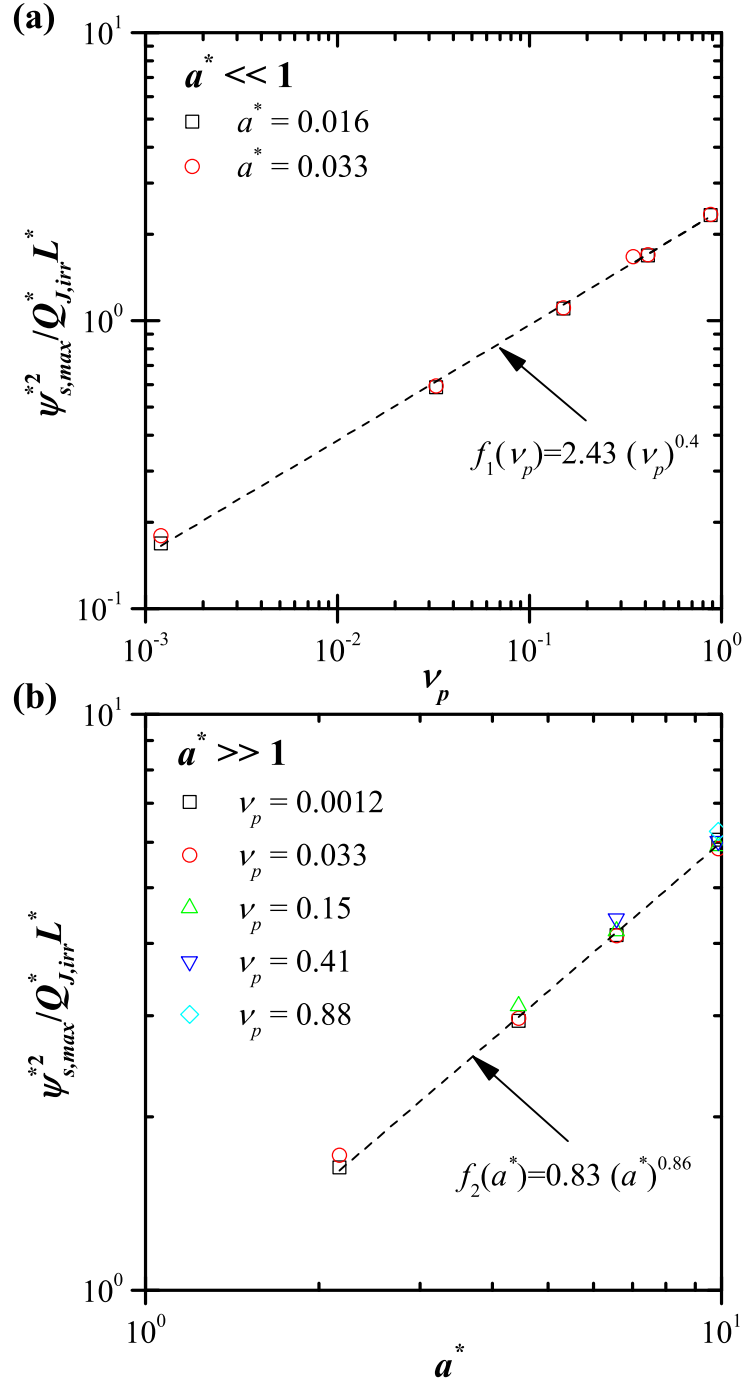


Figure 3.8: Ratio  $\psi_{s,max}^{*2} / Q_{J,irr}^* L^*$  as a function of (a)  $\nu_p$  for  $a^* \ll 1$  and (b)  $a^*$  for  $a^* \gg 1$  and  $0.0012 \leq \nu_p \leq 0.88$  along with the associated power law fits of the curvilinear asymptotes  $f_1(\nu_p)$  and  $f_2(a^*)$ .

meaningful dimensionless numbers. The Joule heat generation rate was found to depend on the dimensionless surface potential  $\psi_{s,max}^*$ , domain length  $L^*$ , packing parameter  $\nu_p$ , and ion diameter  $a^*$  only. An analytical expression for the peak Joule heat generation rate  $\dot{q}_{peak}$  was derived and validated against simulation results. This expression provides an upper bound for the Joule heat generation rate during a step change in potential. It also indicates that strategies for increasing energy and power densities, such as increasing the potential window, ion concentrations, diffusion coefficient, and valency or decreasing the electrode spacing and ion diameter, would also increase Joule heat generated by abrupt changes in cell potential. Simulation results were also used to identify the asymptotic behaviors of the total heat generation  $Q_{J,irr}^*$  and to develop a simple scaling law. This chapter illustrated the importance of heat transfer in EDLCs and provided scaling analysis tools to interpret and to model their thermal behavior.

## CHAPTER 4

# First-principles thermal modeling of EDLCs under galvanostatic cycling with binary and symmetric electrolyte

This chapter aims to develop a physical model and physical understanding of the coupled electrodiffusion, irreversible and reversible heat generation rates, and thermal transport occurring in electric double layer capacitors during galvanostatic cycling. To do so, the heat diffusion equation including irreversible and reversible heat generation rates was derived from first principles for binary and symmetric electrolyte. Detailed numerical simulations of an EDLC with planar electrodes were performed and qualitatively compared with experimental data reported in the literature. The results were used to (i) physically interpret the experimentally observed temperature oscillations and (ii) to investigate how the irreversible and/or reversible heat generation rates varied with space and/or time.

### 4.1 Analysis

#### 4.1.1 Schematic and assumptions

Figure 4.1 schematically shows a one-dimensional cell consisting of two planar electrodes separated by liquid electrolyte of thickness  $2L$ . The electrode located at  $x = 0$  will be denoted by Electrode A and the electrode at  $x = 2L$  by Electrode B. The electrolyte is divided three regions: a Stern layer adjacent to each electrode and one diffuse layer. As in Chapter 3, the present study models the electrolyte only. The EDLC is charged and discharged under current density  $j_{im}(t)$  imposed at Electrode A. To make the problem mathematically

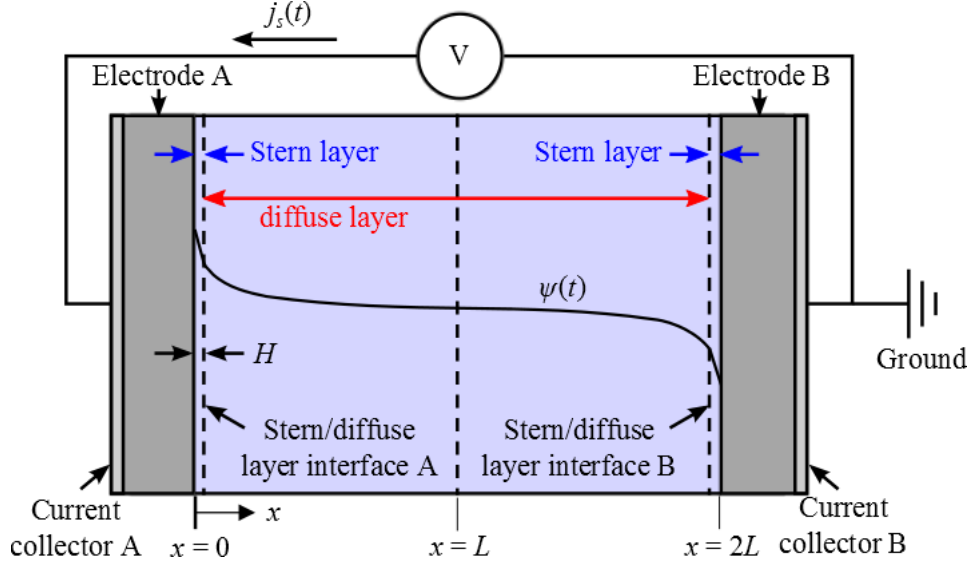


Figure 4.1: Illustration of simulated 1D cell and associated coordinate system.

tractable, the same Assumptions (1)–(7) used in Chapter 3 were made.

## 4.1.2 Electrochemical transport model

### 4.1.2.1 Governing equations

The electric potential and ion concentrations in the binary and symmetric electrolyte obey the MPNP model. The electric potential  $\psi(\mathbf{r}, t)$  at location  $\mathbf{r}$  and time  $t$  is governed by the Poisson Equation (2.5) where  $n = 2$  and  $z_1 = -z_2$  for binary and symmetric electrolytes. The cation  $c_1(\mathbf{r}, t)$  and anion  $c_2(\mathbf{r}, t)$  concentrations satisfy the mass conservation Equation (2.6) with the MPNP ion flux  $\mathbf{N}_i(\mathbf{r}, t)$  given by Equation (2.8). The ion flux  $\mathbf{N}_i(\mathbf{r}, t)$  was evaluated based on the initial temperature  $T_0$  assuming that ion transport was independent of the temperature rise.

### 4.1.2.2 Boundary and initial conditions

The one-dimensional Poisson Equation (2.5) and mass conservation Equation (2.6) in Cartesian coordinates are first-order partial differential equations (PDE) in time and second-order in space. Each equation required one initial condition and two boundary conditions in each

region where it was solved. The Poisson equation was solved within both the Stern and the diffuse layers while the mass conservation equation was solved only in the diffuse layer.

The electric potential was initially assumed to be uniform throughout the entire EDLC and equal to

$$\psi(x, 0) = 0 \text{ V.} \quad (4.1)$$

The current density  $j_{im}(t)$  at the electrode/electrolyte interface of Electrode A at  $x = 0$  was imposed as a square signal alternating between  $j_s$  and  $-j_s$ . The imposed current corresponds to an electronic current in the external circuit which induces an ion flux within the electrolyte. The boundary condition at the surface of Electrode A corresponds to charge conservation across the electrode/electrolyte interface so that the displacement current equals the imposed electronic current  $j_{im}(t)$ , i.e.,

$$-\epsilon_0\epsilon_r \frac{\partial^2 \psi}{\partial t \partial x}(0, t) = j_{im}(t) = \begin{cases} j_s & \text{for } (n_c - 1)t_c \leq t < (n_c - 1/2)t_c \\ -j_s & \text{for } (n_c - 1/2)t_c \leq t < n_c t_c \end{cases} \quad (4.2)$$

where  $j_s$  is the magnitude of the imposed current density and  $n_c$  is the cycle number. In addition, the electric potential and electric displacement were continuous across the Stern/diffuse layer interface located at  $x = H$  so that [42, 43, 45]

$$\psi(H^-, t) = \psi(H^+, t) \quad \text{and} \quad \epsilon_0\epsilon_r \frac{\partial \psi}{\partial x}(H^-, t) = \epsilon_0\epsilon_r \frac{\partial \psi}{\partial x}(H^+, t). \quad (4.3)$$

Similarly, they were continuous across the second Stern/diffuse layer interface located at  $x = 2L - H$ , i.e. [42, 43, 45],

$$\begin{aligned} \psi(2L - H^-, t) &= \psi(2L - H^+, t) \\ \text{and} \quad \epsilon_0\epsilon_r \frac{\partial \psi}{\partial x}(2L - H^-, t) &= \epsilon_0\epsilon_r \frac{\partial \psi}{\partial x}(2L - H^+, t). \end{aligned} \quad (4.4)$$

Furthermore, the electrical ground was defined at the surface of Electrode B, located at  $x = 2L$ , i.e.,

$$\psi(2L, t) = 0 \text{ V.} \quad (4.5)$$

The choice of reference potential is arbitrary and does not affect ion transport or heat transfer.

Both ion species were assumed to start at the same uniform bulk concentration  $c_\infty$  throughout the diffuse layer ( $H \leq x \leq 2L - H$ ) such that

$$c_1(x, 0) = c_2(x, 0) = c_\infty. \quad (4.6)$$

Since ion insertion into the electrode was ignored, the ion flux vanished at the Stern/diffuse layer interface located at  $x = H$  so that

$$N_1(H, t) = N_2(H, t) = 0 \text{ mol m}^{-2}\text{s}^{-1} \quad (4.7)$$

and at the second Stern/diffuse layer interface located at  $x = 2L - H$ , i.e.,

$$N_1(2L - H, t) = N_2(2L - H, t) = 0 \text{ mol m}^{-2}\text{s}^{-1}. \quad (4.8)$$

### 4.1.3 Thermal model

#### 4.1.3.1 Energy conservation equation

Applying energy conservation principles to a fixed control volume of electrolyte in the absence of bulk motion and chemical reactions yields the following energy conservation equation [32]

$$\frac{\partial}{\partial t}(\rho u) = -\nabla \cdot \mathbf{q}'' \quad (4.9)$$

where  $\rho(\mathbf{r}, t)$  is the electrolyte density,  $u(\mathbf{r}, t)$  is the specific internal energy of the electrolyte, and  $\mathbf{q}''(\mathbf{r}, t)$  is the local energy flux at location  $\mathbf{r}$  and time  $t$ . For a multicomponent system with concentration gradients, the energy flux  $\mathbf{q}''$  includes contributions from Fourier heat conduction, interdiffusion of species, and the Dufour effect [28, 32]. The Dufour or diffusion thermo-effect refers to an energy flux driven by a gradient of electrochemical potential or pressure [90]. It is the reverse of the Soret effect or thermal diffusion [90]. The contribution from the Dufour effect is usually negligible [28, 32, 90] and will not be included here. Thus, the energy flux can be expressed as [28, 32]

$$\mathbf{q}'' = -k\nabla T + \sum_{i=0}^n \bar{H}_i \mathbf{N}_i \quad (4.10)$$

where  $k$  is the electrolyte thermal conductivity,  $\bar{H}_i$  is the partial molar enthalpy of species  $i$  in the electrolyte (in  $\text{J mol}^{-1}$ ),  $n$  is the number of ion species, and subscript  $i = 0$  refers to the

solvent. Substituting Equation (4.10) into Equation (4.9) and using the mass conservation Equation (2.6) yields

$$\frac{\partial}{\partial t}(\rho u) = \nabla \cdot (k \nabla T) + \sum_{i=0}^n \bar{H}_i \frac{\partial c_i}{\partial t} - \sum_{i=0}^n \mathbf{N}_i \cdot \nabla \bar{H}_i. \quad (4.11)$$

The first, second, and third terms on the right-hand side of Equation (4.11) represent the net increase of energy within the control volume due to (i) heat conduction, (ii) accumulation of ions and/or solvent molecules, and (iii) flow of ions and/or solvent from regions with different partial molar enthalpy  $\bar{H}_i$ , respectively.

The energy balance given by Equation (4.11) can be transformed into a thermal energy balance in terms of local temperature  $T(\mathbf{r}, t)$ . First, the change in  $\rho u$  can be expressed in terms of the enthalpy per unit volume, defined by  $\rho h$ , as

$$\frac{\partial}{\partial t}(\rho u) = \frac{\partial}{\partial t}(\rho h) - \frac{\partial p}{\partial t} \quad (4.12)$$

where  $h(\mathbf{r}, t)$  and  $p(\mathbf{r}, t)$  are respectively the specific enthalpy of the electrolyte in J kg<sup>-1</sup> and the pressure in Pa at location  $\mathbf{r}$  and time  $t$ . The term  $\partial(\rho h)/\partial t$  can be expanded further. The exact differential of the enthalpy per unit volume  $\rho h$  of an  $n$ -component mixture can be expressed as [91]

$$d(\rho h) = \rho c_p dT + \left[ 1 + \left( \frac{\partial \ln \rho}{\partial \ln T} \right)_{p, c_i} \right] dp + \sum_{i=0}^n \bar{H}_i dc_i \quad (4.13)$$

where  $c_p$  is the specific heat of the electrolyte in J kg<sup>-1</sup>K<sup>-1</sup>. Typically  $(\partial \ln \rho / \partial \ln T)_{p, n_i} \ll 1$  for liquids and solids [91]. Then, combining Equations (4.12) and (4.13) yields

$$\frac{\partial}{\partial t}(\rho u) = \rho c_p \frac{\partial T}{\partial t} + \sum_{i=0}^n \bar{H}_i \frac{\partial c_i}{\partial t}. \quad (4.14)$$

The first and second terms on the right-hand side of Equation (4.14) represent the time rates of change of the thermal energy and of the electrochemical potential energy, respectively. Combining Equation (4.14) with Equation (4.11) yields the governing equation for the temperature  $T$  within the electrolyte

$$\rho c_p \frac{\partial T}{\partial t} = \nabla \cdot (k \nabla T) - \sum_{i=0}^n \mathbf{N}_i \cdot \nabla \bar{H}_i. \quad (4.15)$$



This expression corresponds to the heat diffusion Equation (2.12) with the heat generation rate  $\dot{q}$  expressed as

$$\dot{q} = - \sum_{i=0}^n \mathbf{N}_i \cdot \nabla \bar{H}_i. \quad (4.16)$$

#### 4.1.3.2 Heat generation rate

The partial molar enthalpy of species  $i$  can be expressed as a function of the electrochemical potential  $\tilde{\mu}_i$  and the partial molar entropy  $\bar{S}_i = -\partial\mu_i/\partial T$  according to [91]

$$\bar{H}_i = \tilde{\mu}_i + T\bar{S}_i. \quad (4.17)$$

The electrochemical potential  $\tilde{\mu}_i = z_i F \psi + \mu_i$  of species  $i$  accounts for the electrical potential energy  $z_i F \psi$  of charged species as well as the chemical potential  $\mu_i = \mu_i^0 + R_u T \ln a_i$  [28, 91]. Here,  $\mu_i^0$  is the chemical potential of species  $i$  at a standard state and is a function of  $T$  only, while  $a_i$  is the local thermodynamic activity of species  $i$  [28, 91]. Thus, the gradient  $\nabla \bar{H}_i$  can be written as

$$\nabla \bar{H}_i = z_i F \nabla \psi + \nabla \mu_i + \nabla (T\bar{S}_i). \quad (4.18)$$

Finally, substituting Equation (4.18) and the expressions for  $\mu_i$  and  $\bar{S}_i$  into Equation (4.16), the heat generation rate  $\dot{q}$  can be written as

$$\dot{q} = \dot{q}_E + \dot{q}_S = -\nabla \psi \cdot \left( \sum_{i=1}^n z_i F \mathbf{N}_i \right) + \sum_{i=0}^n \mathbf{N}_i \cdot R_u \nabla \left( T^2 \frac{\partial \ln a_i}{\partial T} \right). \quad (4.19)$$

The first term on the right-hand side of Equation (4.19) represents the thermal energy released due to ion flow into regions of lower electrical potential energy. It will be denoted as the “electrical heating.” It is summed over the  $n$  charged ion species  $i$ , with  $z_0 = 0$  for the neutral solvent. The second term arises from the gradient  $\nabla (T\bar{S}_i)$  and is the net contribution to the heat generation rate due to the gradients of chemical potential, partial molar entropy, and temperature. This term represents the thermal energy released due to flow towards regions of lower  $(T\bar{S}_i)$  and will be denoted as the “entropic heating.”

**Electrical Heating.** The first term on the right-hand side of Equation (4.19) can alternatively be written as  $\dot{q}_E = \mathbf{j} \cdot \mathbf{E}$  where the ionic current density vector  $\mathbf{j}$  is given by Equa-

tion (2.3) and  $\mathbf{E} = -\nabla\psi$  is the electric field vector. This term corresponds to conversion of electrical energy into thermal energy [67].

As mentioned in Section 2.5.2, an electrolyte with non-uniform concentration is a non-ohmic conductor wherein the current density may depend on diffusion and steric effects as well as on the electric field. Indeed, for a binary and symmetric electrolyte with cations referred to by  $i = 1$  and anions by  $i = 2$ , the local ionic current density  $\mathbf{j}$  can be expressed by combining Equations (2.3) and (2.8) as

$$\mathbf{j} = \sigma\mathbf{E} - DzF\nabla(c_1 - c_2) - \frac{Da^3N_AzF(c_1 - c_2)}{1 - a^3N_A(c_1 + c_2)}\nabla(c_1 + c_2) \quad (4.20)$$

with electrical conductivity  $\sigma$  depending on the local ion concentrations and given by Equation (2.4). After some manipulations, Equation (4.20) can be used to express the electric field vector  $\mathbf{E}$  and substitute it into the expression of the electrical heat generation rate  $\dot{q}_E$ . Then,  $\dot{q}_E$  for an electrolyte obeying the MPNP model can be written as the sum of three contributions

$$\dot{q}_E(\mathbf{r}, t) = \dot{q}_{J,irr}(\mathbf{r}, t) + \dot{q}_{E,d}(\mathbf{r}, t) + \dot{q}_{E,s}(\mathbf{r}, t). \quad (4.21)$$

The heat generation rates  $\dot{q}_{J,irr}$ ,  $\dot{q}_{E,d}$ , and  $\dot{q}_{E,s}$  correspond to the contributions of irreversible Joule heating, ion diffusion, and steric effects, respectively. These three contributions are expressed as

$$\begin{aligned} \dot{q}_{J,irr}(\mathbf{r}, t) &= \frac{|\mathbf{j}|^2}{\sigma}, \quad \dot{q}_{E,d}(\mathbf{r}, t) = \frac{DzF}{\sigma}\mathbf{j} \cdot \nabla(c_1 - c_2), \\ \text{and } \dot{q}_{E,s}(\mathbf{r}, t) &= \frac{DzFa^3N_A(c_1 - c_2)}{\sigma[1 - a^3N_A(c_1 + c_2)]}\mathbf{j} \cdot \nabla(c_1 + c_2). \end{aligned} \quad (4.22)$$

If the ion concentrations  $c_i(\mathbf{r}, t)$  are uniform or if the concentration gradients are perpendicular to the current density  $\mathbf{j}$ , then  $\dot{q}_{E,d}$  and  $\dot{q}_{E,s}$  vanish and the electric heat generation reduces to Joule heating  $\dot{q}_{J,irr}$ . The latter condition applies to applications such as electroosmosis, where the electric current is parallel to the electric double layer. The Joule heating term  $\dot{q}_{J,irr}$  is always positive whereas  $\dot{q}_{E,d}$  and  $\dot{q}_{E,s}$  can be either positive or negative.

**Entropic Heating.** The second term on the right-hand side of Equation (4.19) is a function of the thermodynamic activity gradients and of the temperature gradient. Gu *et al.* [67]

also derived this term in modeling transport phenomena in battery systems. The activity can be expressed in terms of the activity coefficient  $\gamma_i$  defined as  $a_i = \gamma_i c_i / c_{ref}$  where  $c_{ref}$  is a reference concentration [91]. Then, the entropic heat generation rate  $\dot{q}_S$  is given by

$$\dot{q}_S(\mathbf{r}, t) = \sum_{i=0}^n \mathbf{N}_i \cdot \nabla \left[ T^2 R_u \frac{\partial \ln \gamma_i}{\partial T} \right]. \quad (4.23)$$

An expression for  $\gamma_i$  in terms of the temperature and ion concentrations is required to evaluate this expression. For dilute solutions of binary and symmetric electrolytes, the activity coefficient  $\gamma_i$  of ion species  $i$  can be evaluated using the Debye-Hückel limiting law expressed as [28, 91]

$$\ln \gamma_i = -\frac{z^3 e F^2 (c_1 + c_2)^{1/2}}{8\pi (\epsilon_0 \epsilon_r R_u T)^{3/2}}. \quad (4.24)$$

Combining Equations (4.23) and (7.6) and assuming the contribution from the flow of solvent is negligible compared to that of the ions yields  $\dot{q}_S = \dot{q}_{S,c} + \dot{q}_{S,T}$  where

$$\begin{aligned} \dot{q}_{S,c}(\mathbf{r}, t) &= \frac{3}{32\pi} \frac{z^3 e F^2}{(\epsilon_0 \epsilon_r)^{3/2} R_u^{1/2} T^{1/2} (c_1 + c_2)^{1/2}} (\mathbf{N}_1 + \mathbf{N}_2) \cdot \nabla (c_1 + c_2) \\ \text{and} \quad \dot{q}_{S,T}(\mathbf{r}, t) &= -\frac{3}{32\pi} \frac{z^3 e F^2 (c_1 + c_2)^{1/2}}{(\epsilon_0 \epsilon_r)^{3/2} R_u^{1/2} T^{3/2}} (\mathbf{N}_1 + \mathbf{N}_2) \cdot \nabla T. \end{aligned} \quad (4.25)$$

In the absence of concentration gradients,  $\dot{q}_{S,c}$  vanishes, while  $\dot{q}_{S,T}$  vanishes if the temperature is uniform. Here also,  $\dot{q}_{S,c}$  and  $\dot{q}_{S,T}$  can be either positive or negative.

Overall, the temperature is governed by the heat diffusion Equation (2.12) with a heat generation rate  $\dot{q}$  consisting of five contributions such that

$$\dot{q} = \dot{q}_{J,irr} + \dot{q}_{E,d} + \dot{q}_{E,s} + \dot{q}_{S,c} + \dot{q}_{S,T} \quad (4.26)$$

where the electrical heat generation rates due to (i) Joule heating  $\dot{q}_{J,irr}$ , (ii) ion diffusion  $\dot{q}_{E,d}$ , and (iii) steric effects  $\dot{q}_{E,s}$  are given by Equation (4.22). The entropic heat generation terms due to (iv) concentration gradients  $\dot{q}_{S,c}$  and (v) temperature gradients  $\dot{q}_{S,T}$  are defined in Equation (4.25).

Finally, because there was no ion insertion into the electrodes [Assumption (1)], the ion fluxes  $\mathbf{N}_i$  were equal to zero within the Stern layers. Consequently, the ionic current density and the heat generation rates  $\dot{q}_E(\mathbf{r}, t)$  and  $\dot{q}_S(\mathbf{r}, t)$  vanished within this compact layer.

#### 4.1.3.3 Boundary and initial conditions

The one-dimensional heat diffusion Equation (2.12) in Cartesian coordinates is a first-order PDE in time and second-order in space. It was solved in both the Stern and the diffuse layers and required one initial condition and two boundary conditions for each layer. The temperature was initially assumed to be uniform throughout the EDLC and equal to

$$T(x, 0) = T_0. \quad (4.27)$$

The surface of Electrode A located at  $x = 0$  was assumed to be thermally insulated, i.e.,

$$-k \frac{\partial T}{\partial x}(0, t) = 0 \text{ W m}^{-2}. \quad (4.28)$$

The temperature and heat flux were continuous across the Stern/diffuse layer interface located at  $x = H$  so that

$$T(H^-, t) = T(H^+, t) \quad \text{and} \quad -k \frac{\partial T}{\partial x}(H^-, t) = -k \frac{\partial T}{\partial x}(H^+, t) \quad (4.29)$$

and across the second Stern/diffuse layer interface located at  $x = 2L - H$ , i.e.,

$$T(2L - H^-, t) = T(2L - H^+, t) \quad \text{and} \quad -k \frac{\partial T}{\partial x}(2L - H^-, t) = -k \frac{\partial T}{\partial x}(2L - H^+, t), \quad (4.30)$$

Finally, the surface of Electrode B located at  $x = 2L$  was thermally insulated, i.e.,

$$-k \frac{\partial T}{\partial x}(2L, t) = 0 \text{ W m}^{-2}. \quad (4.31)$$

#### 4.1.4 Constitutive relationships

The current chapter focuses on tetraethylammonium tetrafluoroborate ( $\text{TEABF}_4$ ) electrolyte in propylene carbonate (PC) solvent. The ions  $\text{TEA}^+$  ( $i = 1$ ) and  $\text{BF}_4^-$  ( $i = 2$ ) had valency  $z_1 = -z_2 = 1$  [48, 92, 93]. Their effective diameter was taken as  $a = 0.68 \text{ nm}$  [48, 92]. The dielectric constant, thermal conductivity, density, and specific heat were taken as the properties of the PC solvent and equal to  $\epsilon_r = 66.1$ ,  $k = 0.164 \text{ W m}^{-1}\text{K}^{-1}$ ,  $\rho = 1205 \text{ kg m}^{-3}$ , and  $c_p = 2141 \text{ J kg}^{-1}\text{K}^{-1}$ , respectively [94]. All properties were evaluated at approximately  $T_0 = 298 \text{ K}$ . The diffusion coefficient was estimated to be  $D = 1.7 \times 10^{-10} \text{ m}^2 \text{ s}^{-1}$  using

Equation (2.4) from electrical conductivity data for a concentration of  $c_1 = c_2 = c_\infty = 1 \text{ mol L}^{-1}$  [93].

The simulations were performed for  $c_\infty = 1 \text{ mol L}^{-1}$  of TEABF<sub>4</sub> in PC with a domain size of  $L = 50 \text{ }\mu\text{m}$  and an initial temperature of  $T_0 = 298 \text{ K}$ . The EDLC was cycled at constant current of  $j_s = 14 \text{ mA cm}^{-2}$  with a cycle period  $t_c = 10 \text{ ms}$ .

#### 4.1.5 Method of solution

The one-dimensional governing Equations (2.5), (2.6), and (2.12) and the associated initial and boundary conditions were solved numerically using finite element methods. The numerical convergence of the solution was assessed based on the predicted local electric potential  $\psi(x, t)$ , ion concentrations  $c_1(x, t)$  and  $c_2(x, t)$ , and temperature  $T(x, t)$ . The temperature was the most sensitive to the choice of mesh element size and time step. The mesh element size was smallest at the Stern/diffuse layer interfaces due to the large gradients of potential and concentrations in this region and gradually increased away from these boundaries. The mesh was refined by reducing the element size at the Stern/diffuse layer interface and by reducing the maximum element growth rate. The time step was controlled by the relative and absolute time tolerances [95]. At each time step, the estimated local error between the solutions at the previous and the current time step was compared with the time tolerances. The time step was then adjusted until the convergence criterion was satisfied, as described in Ref. [95]. This enabled the use of small time steps during periods of rapid changes in  $\psi(x, t)$ ,  $c_i(x, t)$ , and/or  $T(x, t)$ , while using a larger time step for the rest of the simulation. The numerical solution was considered converged when halving (i) the element size at the Stern/diffuse layer interface, (ii) the maximum element growth rate, and (iii) both the relative and absolute tolerances resulted in less than 0.5% maximum relative difference in the local temperature rise  $T(x, t) - T_0$ .

## 4.2 Results and discussion

### 4.2.1 Electric potential

Figure 4.2(a) shows the electric potential  $\psi(0, t)$  at the surface of Electrode A as a function of time  $t$ . The surface potential  $\psi(0, t)$  corresponded to the total voltage across the cell, since Electrode B was electrically grounded. Figure 4.2(a) shows that the surface potential varied nearly linearly between the minimum potential of 0 V and the maximum potential of 2.5 V. The potential window was determined by the combination of the imposed current density  $j_s$  and the cycle period  $t_c$ . The maximum potential of 2.5 V was chosen by analogy with the operating voltage of many commercial EDLCs using organic electrolytes [10, 12].

### 4.2.2 Ion concentrations

Figure 4.2(b) shows the anion concentration  $c_2(a/2, t)$  at the Stern/diffuse layer interface near Electrode A as a function of time  $t$ . It shows that the anion concentration at the Stern/diffuse layer interface increased rapidly at the beginning of the charge step. It then leveled off to the maximum concentration  $c_{max}$  and remained at this value for most of the cycle. It decreased back to the bulk concentration at the end of the discharge step. The plateau of  $c_2(a/2, t)$  corresponded to the surface potential  $\psi(0, t)$  exceeding 0.75 V.

Figure 4.3 shows the anion concentration  $c_2(x, t)$  as a function of location  $x$  for several times  $t$  during a charging step (a) near Electrode A and (b) near Electrode B. Figure 4.3(a) indicates that the anion concentration near Electrode A increased from the initial concentration  $c_\infty = 1 \text{ mol L}^{-1}$  to  $c_{max}$  as the electric double layer formed. After the surface concentration reached  $c_{max}$ , a close-packed layer with uniform concentration  $c_2 = c_{max}$  formed next to the surface. Beyond the close-packed layer, the concentration decreased to the bulk concentration  $c_\infty$  over a narrow region with large concentration gradients. This transition region will be referred to as the EDL region. As charging proceeded, the close-packed layer became thicker and the EDL region propagated within the electrolyte in the positive  $x$ -direction. By contrast, Figure 4.3(b) shows that the anion concentration near

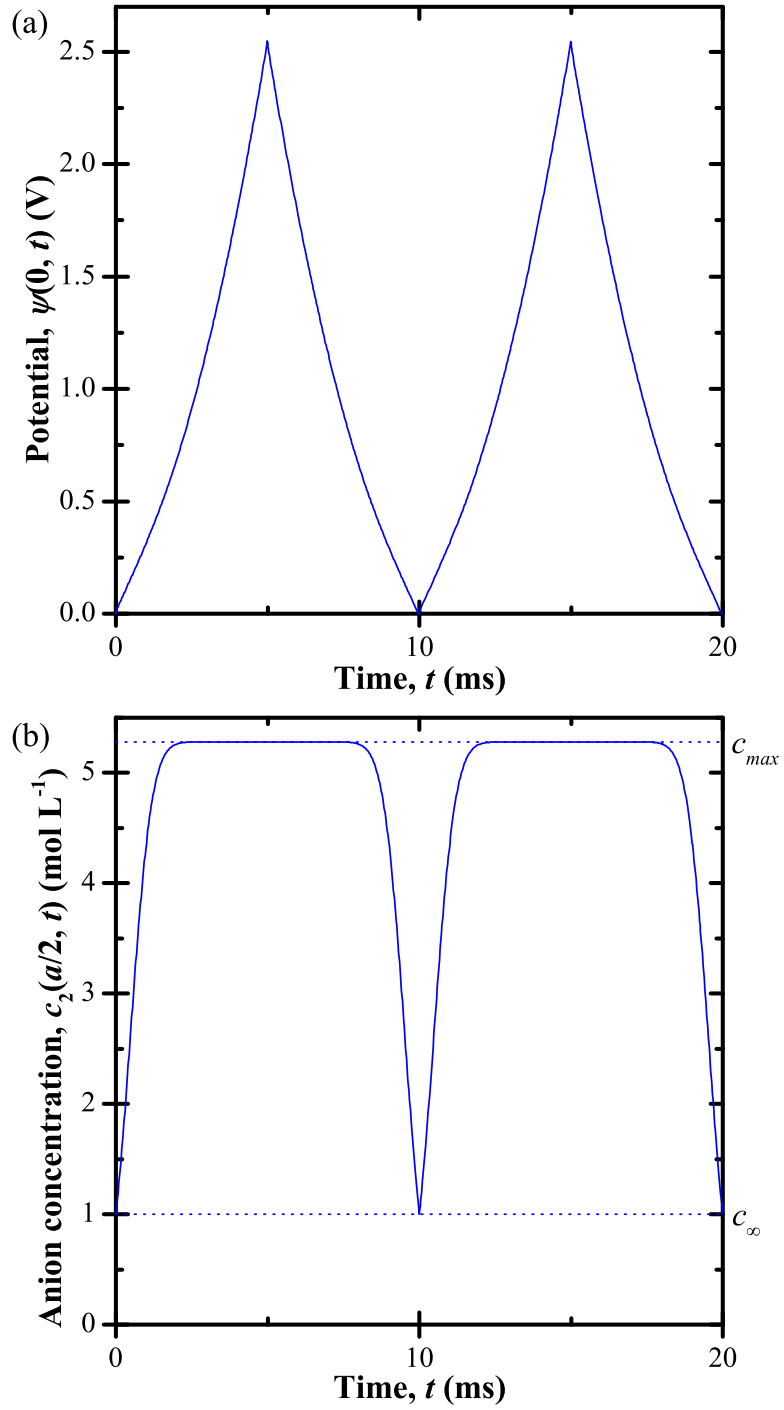


Figure 4.2: (a) Electric potential  $\psi(0, t)$  at the surface of Electrode A and (b) anion concentration  $c_2(a/2, t)$  at the Stern/diffuse layer interface as functions of time.

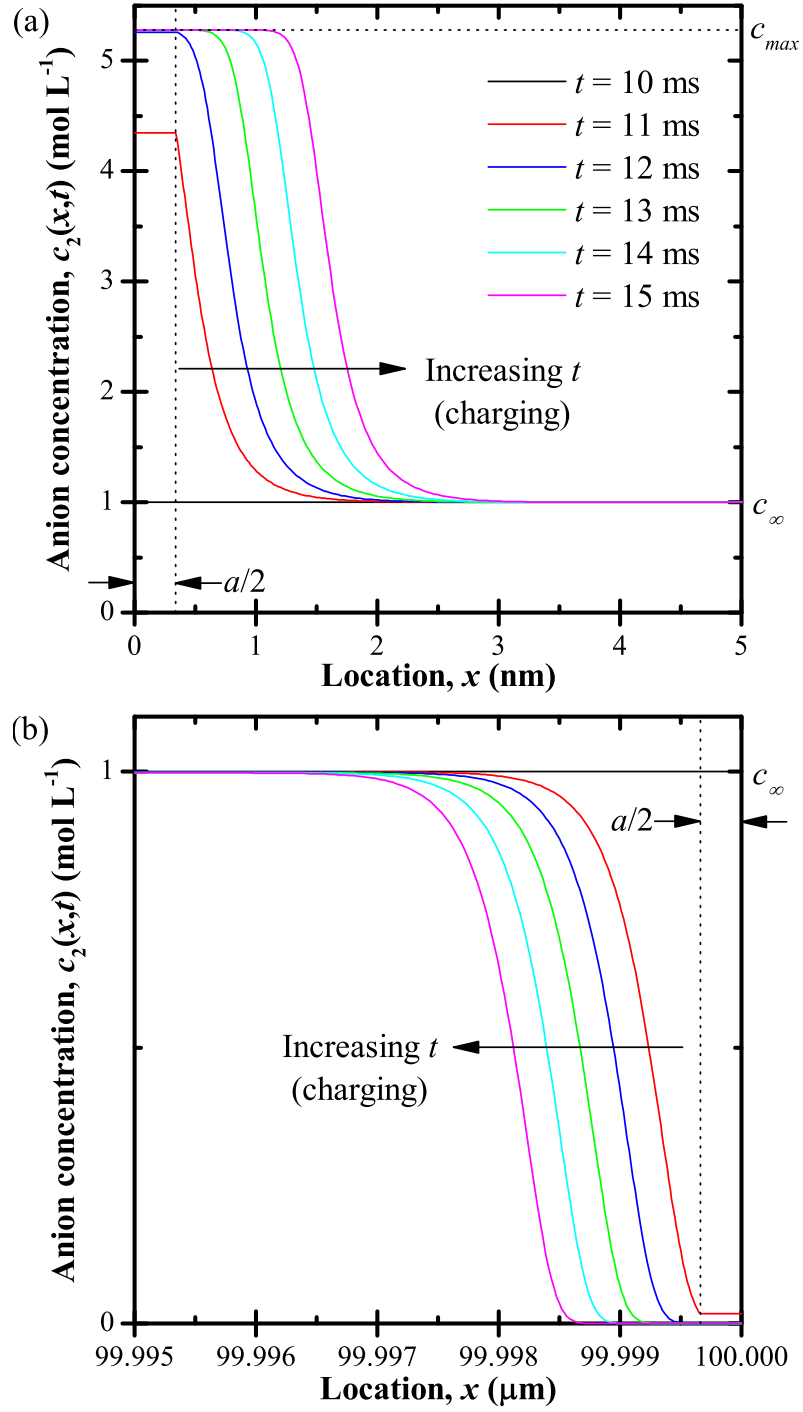


Figure 4.3: Predicted anion concentrations  $c_2(x, t)$  (a) near Electrode A and (b) near Electrode B as a function of  $x$  at various times during a charging step.



Electrode B decreased from the initial concentration  $c_\infty$  to zero as the EDL charged. The concentration decreased from the bulk concentration to zero over a narrow EDL region. As charging proceeded, the EDL region propagated within the electrolyte in the negative  $x$ -direction and the region of anion depletion adjacent to electrode B became wider. The cation concentration  $c_1(x, t)$  (not shown) was the mirror image of the anion concentration  $c_2(x, t)$  such that  $c_1(x, t) = c_2(2L - x, t)$ .

### 4.2.3 Current density

Figure 4.4(a) shows the predicted current density  $j(L, t)$  at the centerline as a function of time  $t$ . It demonstrates that the current  $\pm j_s$  imposed at Electrode A [Equation (4.2)] resulted in cycles of constant ionic current density of the same magnitude, i.e.,  $j(L, t) = \pm 14 \text{ mA/cm}^2$ . In addition, there was no significant delay between the switching of the imposed current density and the response of the current density  $j(L, t)$  at the centerline between Electrodes A and B. Figure 4.4(b) shows the current density  $j(x, 14 \text{ ms})$  as a function of location  $x$  shortly before the end of the charging step. The current density was uniform across the domain, except very close to the electrodes where it sharply decreased to zero due to the absence of ion insertion. The current density was symmetric about the centerline such that  $j(x, t) = j(2L - x, t)$ . Similar results were observed at all times.

### 4.2.4 Thermal behavior

#### 4.2.4.1 Local heat generation rates

Figure 4.5(a) shows the five heat generation rates  $\dot{q}_{J,irr}(x, 14 \text{ ms})$ ,  $\dot{q}_{E,d}(x, 14 \text{ ms})$ ,  $\dot{q}_{E,s}(x, 14 \text{ ms})$ ,  $\dot{q}_{S,c}(x, 14 \text{ ms})$ , and  $\dot{q}_{S,T}(x, 14 \text{ ms})$  as a function of location  $x$  at time  $t = 14 \text{ ms}$  shortly before the end of a charging step. The main figure shows the heat generation rates very close to Electrode A, while the inset plots them over the entire electrolyte domain. Note that all of the heat generation rates were symmetric about the centerline. Figure 4.5(a) indicates that  $\dot{q}_{E,d}$ ,  $\dot{q}_{E,s}$ , and  $\dot{q}_{S,c}$  featured large peaks near the electrode surfaces. They were several orders of magnitude larger than  $\dot{q}_{J,irr}$  within this narrow region but vanished in the rest of

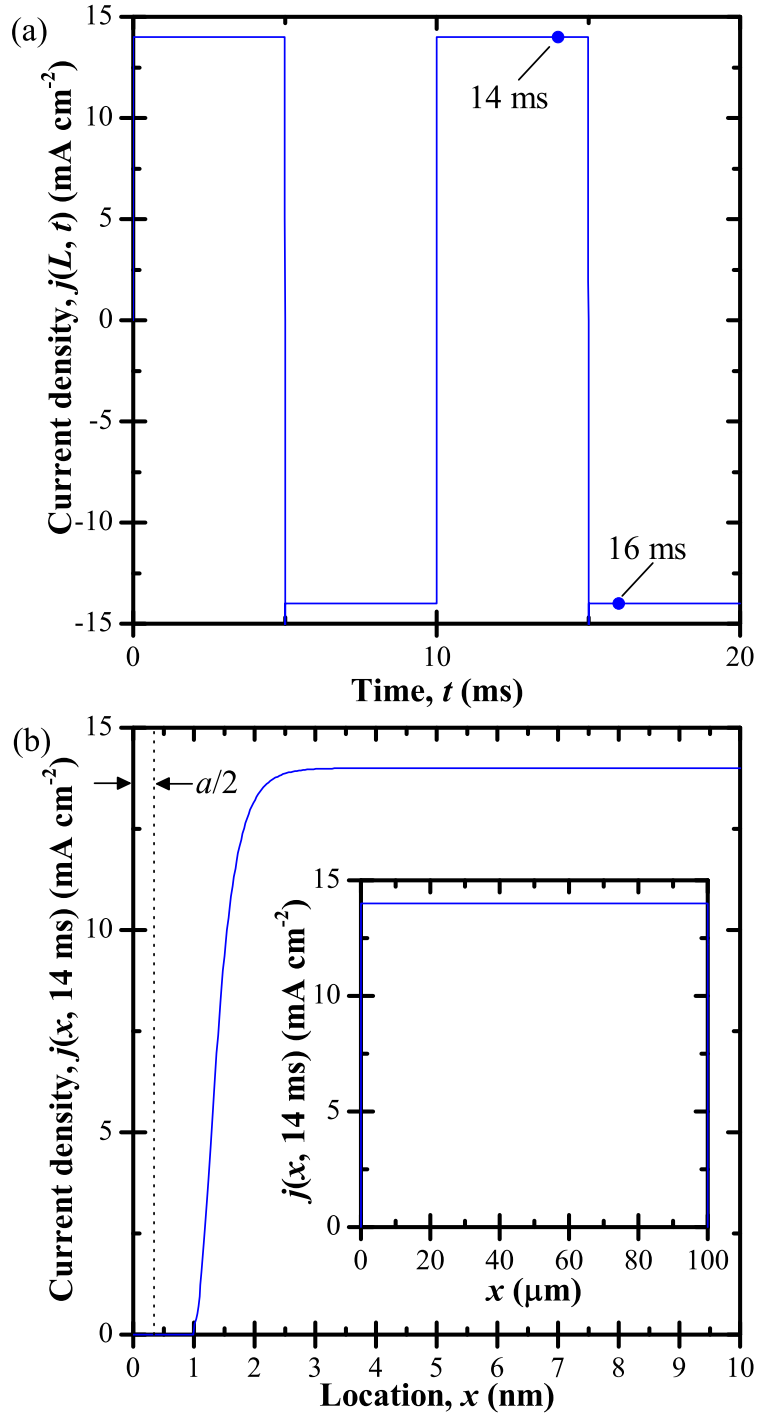


Figure 4.4: Predicted current density (a)  $j(L, t)$  at the centerline as a function of time  $t$  and (b)  $j(x, 14 \text{ ms})$  as a function of location  $x$ .

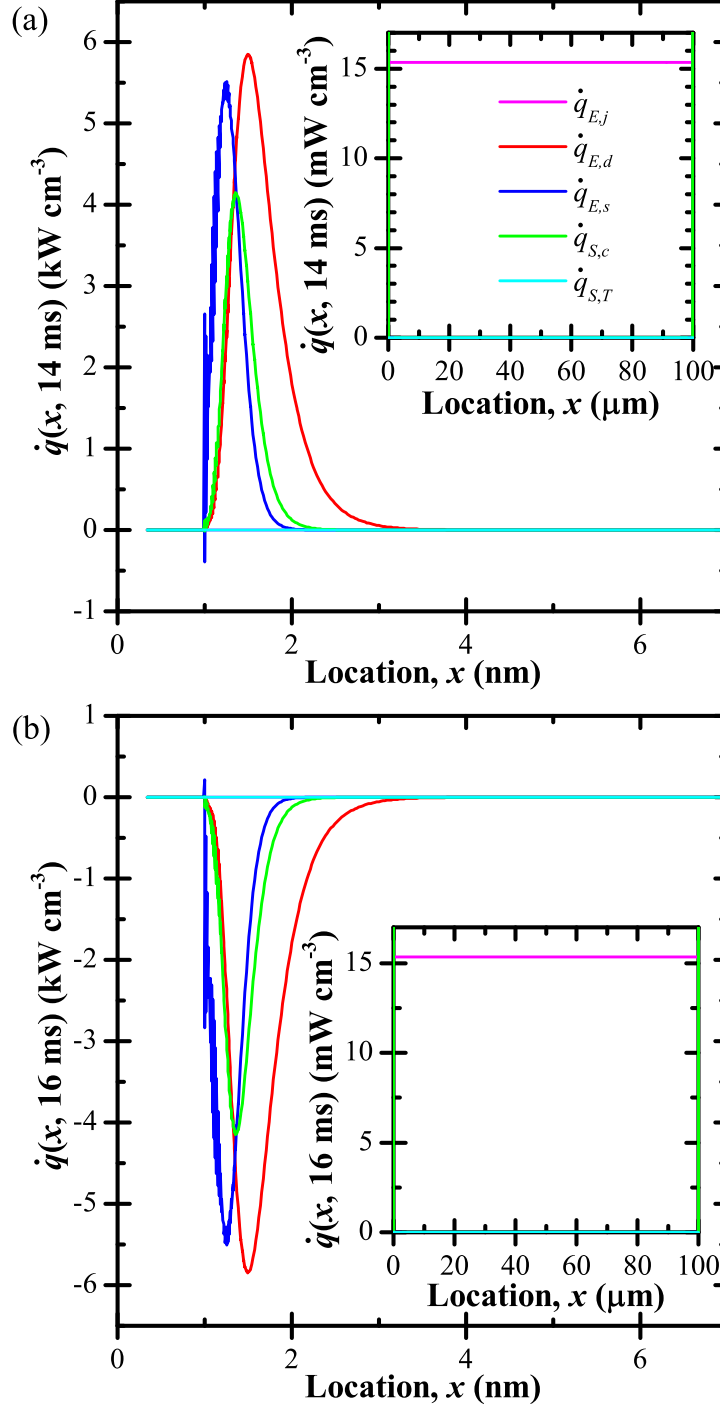


Figure 4.5: Predicted heat generation rates  $\dot{q}_{J,irr}(x,t)$ ,  $\dot{q}_{E,d}(x,t)$ ,  $\dot{q}_{E,s}(x,t)$ ,  $\dot{q}_{S,c}(x,t)$ , and  $\dot{q}_{S,T}(x,t)$  as a function of location  $x$  (a) at time  $t = 14$  ms shortly before the end of a charging step and (b) at time  $t = 16$  ms shortly after the beginning of a discharging step.

the electrolyte domain. The locations of the peaks corresponded to the regions of large concentration gradients shown in Figure 4.3. All three terms were positive during the charging step. By contrast, the inset of Figure 4.5(a) shows that the Joule heating  $\dot{q}_{J,irr}$  was uniform throughout the electrolyte. Indeed, the ionic current density  $j$  was uniform and equal to  $j_s$  nearly everywhere in the electrolyte [Figure 4.4(b)]. Joule heating  $\dot{q}_{J,irr}$  was also the only significant heat generation rate in most of the electrolyte. Finally,  $\dot{q}_{S,T}$  was negligible compared to the other heat generation rates over the entire domain at all times.

Similarly, Figure 4.5(b) shows the five heat generation rates  $\dot{q}_{J,irr}(x, 16 \text{ ms})$ ,  $\dot{q}_{E,d}(x, 16 \text{ ms})$ ,  $\dot{q}_{E,s}(x, 16 \text{ ms})$ ,  $\dot{q}_{S,c}(x, 16 \text{ ms})$ , and  $\dot{q}_{S,T}(x, 16 \text{ ms})$  as a function of location  $x$  at time  $t = 16 \text{ ms}$  shortly after the beginning of the discharging step. This time was chosen because the concentration profiles were almost identical to those at time  $t = 14 \text{ ms}$ . Figure 4.5(b) indicates that  $\dot{q}_{E,d}$ ,  $\dot{q}_{E,s}$ , and  $\dot{q}_{S,c}$  had large negative peaks near the electrode surface. These peaks had identical location and magnitude but opposite sign to those shown in Figure 4.5(a). The inset of Figure 4.5 establishes that  $\dot{q}_{J,irr}$  remained positive, uniform, and the only significant source of heat generation in most of the electrolyte domain. Here also,  $\dot{q}_{S,T}$  remained everywhere negligible compared with the other heat generation rates.

Overall, these results suggest that Joule heating  $\dot{q}_{J,irr}$  accounts for all irreversible heat generation within the electrolyte while  $\dot{q}_{E,d}$ ,  $\dot{q}_{E,s}$ , and  $\dot{q}_{S,c}$  are reversible heat generation processes. Finally,  $\dot{q}_{S,T}$  could be ignored compared to the other heat generation processes for the conditions tested. Furthermore, the expressions for these heat generation rates corroborate experimental observations presented in Section 2.6.2. The irreversible heat generation rate  $\dot{q}_{J,irr}$  derived here was proportional to  $j^2$ . Two of the reversible heat generation rates,  $\dot{q}_{E,d}$  and  $\dot{q}_{E,s}$ , are directly proportional to the current density  $j$ . For a binary, symmetric electrolyte, the third reversible heat generation rate  $\dot{q}_{S,c}$  is directly proportional to the sum of the ion fluxes  $\mathbf{N}_1 + \mathbf{N}_2$ , where the ion fluxes  $\mathbf{N}_i$  and the current density  $j$  are related by Equation (2.3). As in the analysis by Schiffer *et al.* [29], the present study identified a reversible heat generation rate  $\dot{q}_{S,c}$  associated with changes in entropy. It was exothermic during charging and endothermic during discharging, as they predicted [29]. However, other reversible heat generation rates  $\dot{q}_{E,d}$  and  $\dot{q}_{E,s}$  were also identified and found to be associated

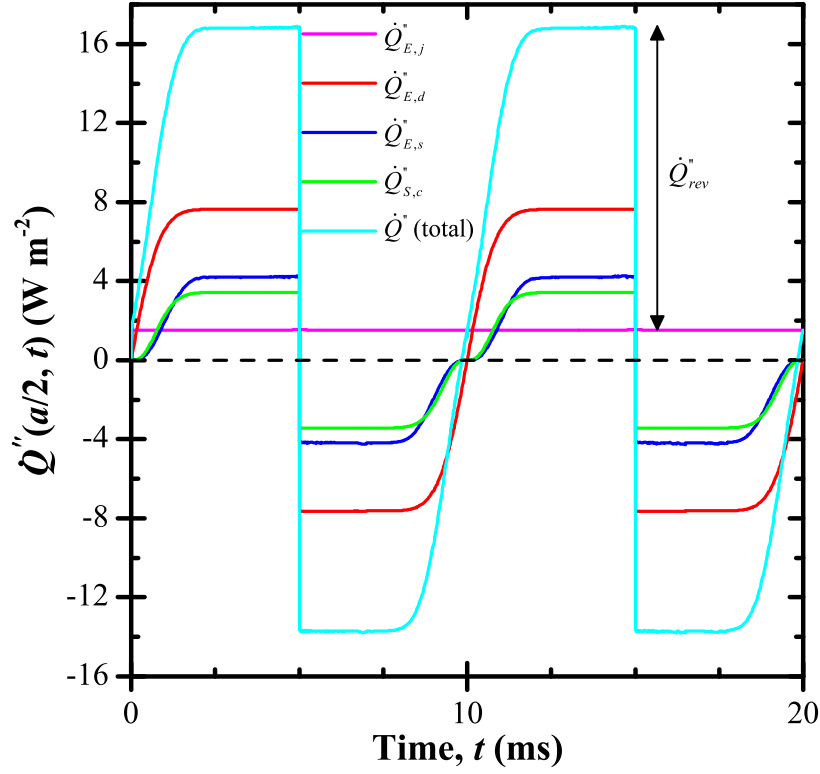


Figure 4.6: Predicted total heat generation rate terms  $\dot{Q}''_{J,irr}(t)$ ,  $\dot{Q}''_{E,d}(t)$ ,  $\dot{Q}''_{E,s}(t)$ , and  $\dot{Q}''_{S,c}(t)$  as well as the overall heat generation rate  $\dot{Q}''(t)$  as functions of time  $t$ .

with changes in the electrical potential energy. During the charging step, the ions migrated in the direction of decreasing electric potential energy to form the EDLs, releasing thermal energy in the process. During discharging, the ion motion was driven by diffusion and steric effects as the EDLs relaxed. The ion fluxes were then in the direction of increasing electric potential energy and thermal energy was absorbed.

#### 4.2.4.2 Total heat generation rates

The heat generation terms  $\dot{q}_{E,d}$ ,  $\dot{q}_{E,s}$ , and  $\dot{q}_{S,c}$  were very large. However, unlike  $\dot{q}_{J,irr}$ , they were confined to very small regions near the electrode surfaces. To fully assess their relative significance, one should consider their total contributions integrated over the electrolyte domain. The total heat generation rate per unit separator area (in  $\text{W m}^{-2}$ ) associated with local heat generation rate  $\dot{q}_i(x, t)$  is defined as  $\dot{Q}''_i(t) = \int_0^{2L} \dot{q}_i(x, t) dx$ . Figure 4.6 shows the

individual total heat generation rates as well as the overall heat generation rate  $\dot{Q}''(t) = \dot{Q}_{J,irr}''(t) + \dot{Q}_{E,d}''(t) + \dot{Q}_{E,s}''(t) + \dot{Q}_{S,c}''(t)$  as a function of time. First, it indicates that the irreversible Joule heating  $\dot{Q}_{J,irr}''$  was positive and constant over the entire simulation time. In addition, the reversible heat generation rates  $\dot{Q}_{E,d}''$ ,  $\dot{Q}_{E,s}''$ , and  $\dot{Q}_{S,c}''$  were positive during charging and negative during discharging, as observed experimentally [78]. Their magnitudes quickly reached a plateau whose duration corresponded to that observed in the concentration at the Stern/diffuse layer interface, i.e., when  $c_2(a/2, t) = c_{max}$  [Figure 4.2(a)]. For the conditions tested, this corresponded to a surface potential  $\psi(0, t) \geq 0.75$  V. It is interesting to note that EDLCs are often operated between their rated voltage and one-half of their rated voltage, typically 1.25–2.5 V or 1.35–2.7 V for commercial EDLCs with organic electrolyte [7, 8, 25, 76]. Under such conditions, the magnitude of the reversible heat generation rates would remain constant for the entire cycle. Finally, the four heat generation rates considered had the same order of magnitude and all contributed to the total heat generation rate  $\dot{Q}''(t)$  in the electrolyte. The net heat generation over an entire cycle was positive and equal to the irreversible Joule heating  $\dot{Q}_{J,irr}'' t_c$ .

#### 4.2.4.3 Temperature profiles

Figures 4.7 shows the predicted temperature change (a)  $T(a/2, t) - T_0$  at the Stern/diffuse layer interface and (b)  $T(L, t) - T_0$  at the centerline as a function of time  $t$  as each contribution  $\dot{q}_{J,irr}$ ,  $\dot{q}_{E,d}$ ,  $\dot{q}_{E,s}$ , and  $\dot{q}_{S,c}$  was accounted for sequentially. Note that the Stern/diffuse layer interface  $x = a/2$  was very close to the EDL region where the reversible heat generation terms  $\dot{q}_{E,d}$ ,  $\dot{q}_{E,s}$ , and  $\dot{q}_{S,c}$  were maximum. By contrast, only the Joule heat generation rate was significant at the centerline  $x = L$ . Both figures indicate that  $\dot{q}_{J,irr}$  alone would cause the temperature to rise linearly. The reversible heat generation terms  $\dot{q}_{E,d}$ ,  $\dot{q}_{E,s}$ , and  $\dot{q}_{S,c}$  all contributed to temperature oscillations. Figure 4.7(a) shows that the oscillations of  $T(a/2, t)$  at the Stern/diffuse layer interface were relatively large. In addition,  $T(a/2, t)$  responded quickly to switches from charging to discharging and vice versa. During the first charging step, the  $T(a/2, t)$  predictions accounting for the reversible heat generation rates diverged immediately from those accounting for Joule heating only. Similarly,  $T(a/2, t)$

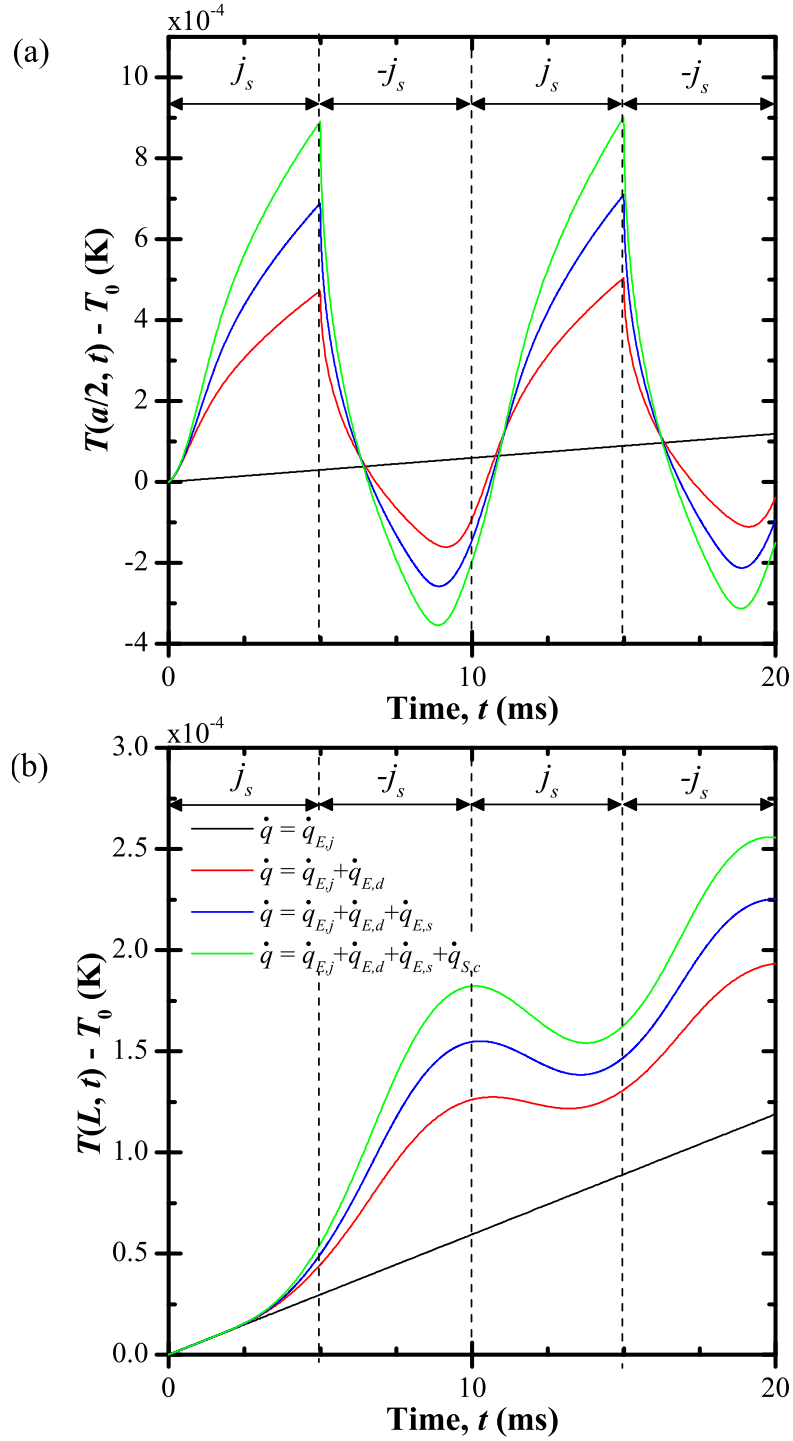


Figure 4.7: Predicted temperature change (a)  $T(a/2, t) - T_0$  at the Stern/diffuse layer interface and (b)  $T(L, t) - T_0$  at the centerline as a function of time  $t$  as each individual heat generation rate term was added.

started to decrease immediately as the discharging step began. By contrast, the response of the centerline temperature  $T(L, t)$  showed a delayed response to changes in the reversible heat generation rates occurring near the electrode surface. In particular,  $T(L, t)$  diverged only slightly from that predicted using  $\dot{q}_{J,irr}$  alone through most of the first charging step. Thereafter, the rise and fall of the temperature appeared to be delayed by almost half a cycle period from that predicted at  $x = a/2$ . In fact, the centerline temperature rose through most of the discharging step and fell through most of the charging step. The oscillations of  $T(L, t)$  were also smaller and more rounded than those of  $T(a/2, t)$ . Temperature profiles at locations between  $x = a/2$  and  $x = L$  (not shown) were intermediate between those shown in Figures 4.7(a) and 4.7(b). In particular, the temperature oscillations became smaller, more rounded, and more delayed with increasing distance from the electrode surface.

#### 4.2.5 Comparison with experimental data

The numerically predicted temperature behavior qualitatively resembled experimental temperature measurements. Temperature measurements inside a commercial EDLC reported by Gualous *et al.* [76] (Figure 2.4) showed angular temperature oscillations similar to those shown in Figure 4.7(a). Similarly, temperature measurements at the outer surface, i.e., far from the electrode/electrolyte interfaces, of commercial EDLCs (e.g., Figures 2.2, 2.3, and 2.4(a) [29, 76]) showed smaller and smoother oscillations similar to those shown in Figure 4.7(b).

Figure 4.8(a) compares the predicted temperature change  $T(L, t) - T_0$  at the centerline as a function of time  $t$  for simulations starting with either a charging step or a discharging step. In both cases, the predicted temperature increased linearly for a short period ( $t < 2.5$  ms) with a slope equal to  $\dot{q}_{J,irr}/\rho c_p = j_s^2/\sigma \rho c_p$ . For the case starting with a charging step under  $+j_s$ , the temperature continued increasing to reach a peak at  $t \approx 10$  s. However, for the case starting with a discharging step under  $-j_s$ , the temperature decreased to reach a minimum also around  $t \approx 10$  ms. After the first cycle, the temperature in both cases oscillated around an overall temperature rise of slope  $\dot{q}_{J,irr}/\rho c_p = j^2/\sigma \rho c_p$  corresponding to irreversible Joule



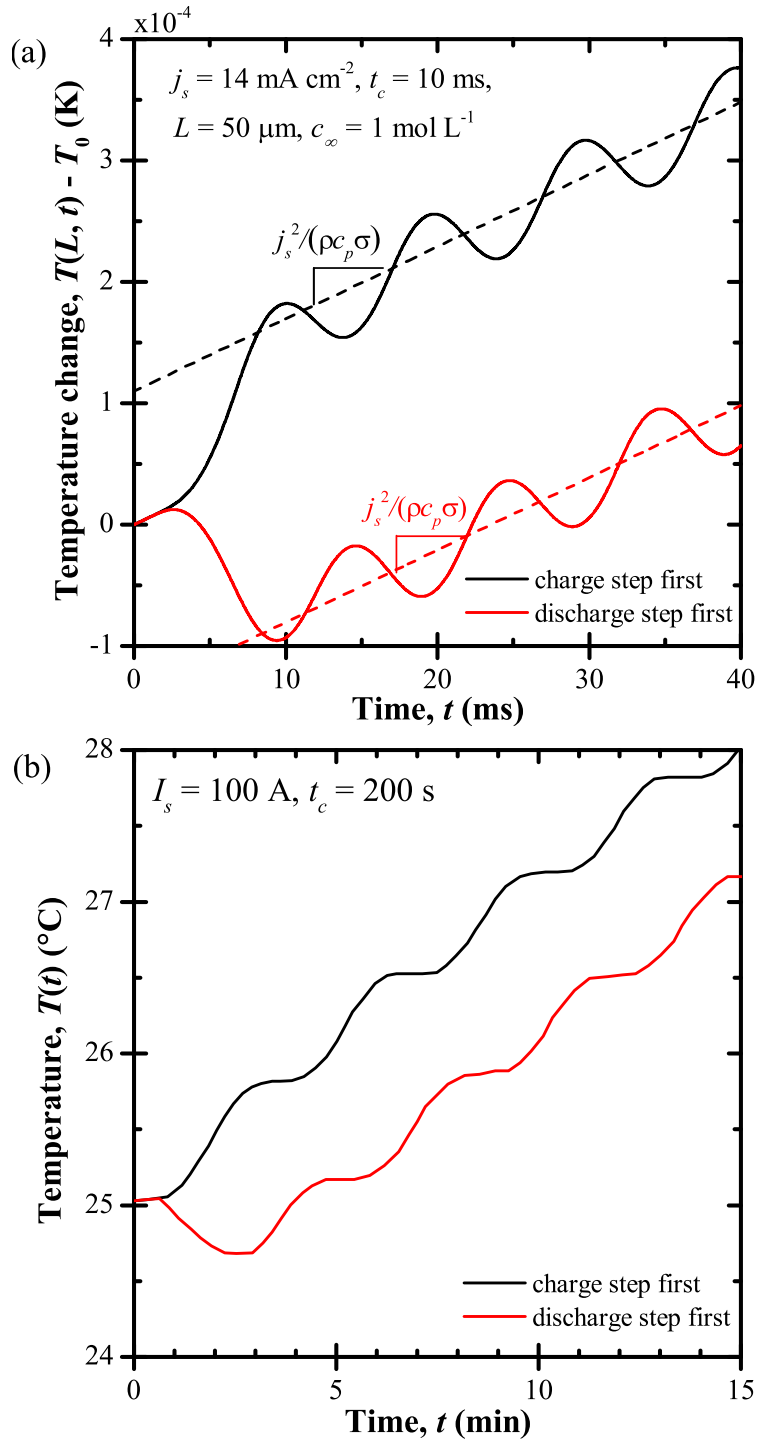


Figure 4.8: (a) Numerically predicted temperature change  $T(L, t) - T_0$  at the centerline and (b) measured surface temperature of a commercial EDLC (reproduced from Figure 8 of Ref. [29]) as functions of time  $t$  for cases starting with either a charging step or a discharging step.

heating. Figure 4.8(b) shows the reported surface temperature of a commercial EDLC as a function of time  $t$  for several charging/discharging cycles starting with either a charging step or a discharging step [29]. The predicted thermal behavior shown in Figure 4.8(a) was remarkably similar to that observed experimentally. Note that quantitative comparison could not be performed due to the complexity of the porous electrode architecture in the actual EDLC compared with the simple planar electrode simulated. However, the results indicate that the physical model captured the physical phenomena governing the EDLC thermal response during galvanostatic cycling.

Figure 4.9(a) shows the predicted temperature change  $T(L, t) - T_0$  at the centerline as a function of time  $t$  for cycling at three different current densities over the same potential window  $0 \text{ V} \leq \psi(0, t) \leq 2.5 \text{ V}$ . For all cases, the slope of the overall temperature rise was equal to  $j_s^2 / \rho c_p \sigma$ , corresponding to irreversible Joule heating. The amplitude of the temperature oscillations decreased with increasing current density  $j_s$ . Figure 4.9(b) shows the reported surface temperatures of a commercial EDLC cycled at three different currents  $I_s$  over the same potential window 1.5–2.5 V. Here also, the predicted temperature behavior shown in Figure 4.9(a) closely resembled that observed experimentally.

Both the predicted and experimental results in Figure 4.9 indicate that the amplitude of the temperature oscillations decreased with increasing current density. Initially, this appears to contradict earlier observations that the reversible heat generation rates derived here increase with increasing current density. However, the temperatures close to the EDL region showed quite different behavior than that shown in Figure 4.9. The temperature oscillations at the Stern/diffuse layer  $x = a/2$  (not shown) resembled those shown in Figure 4.7(a) in shape. They were significantly larger in amplitude than those at the centerline and increased in amplitude with increasing current density. Thus, the apparent contradiction can be attributed to the fact that the reversible heat generated near the electrode/electrolyte interface did not have time to propagate deep into the electrolyte due to the reduction in cycle period with increasing current density. Therefore, temperature oscillations at the outer surface of a device behave differently from those near the electrode/electrolyte interface and underestimate the internal temperature oscillations. In fact, the large temperature

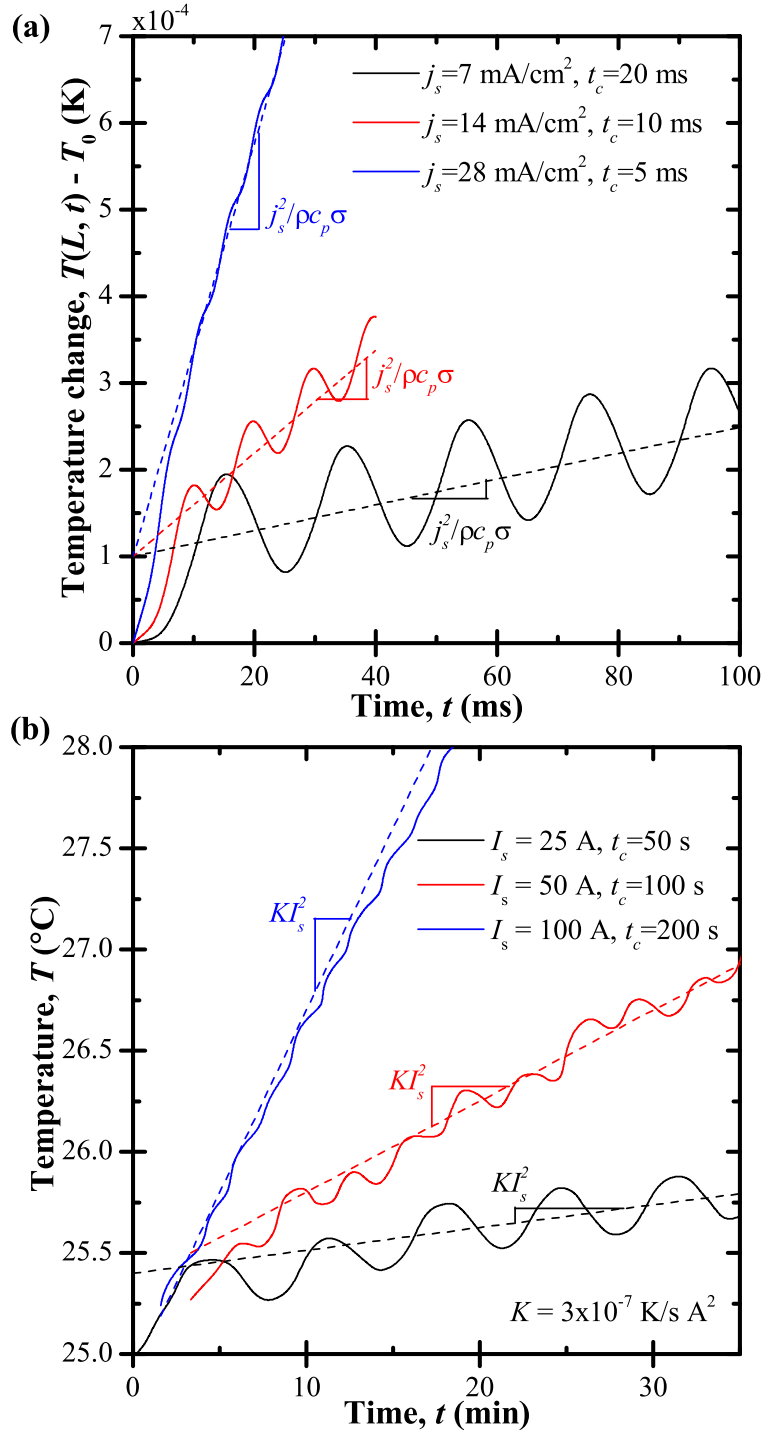


Figure 4.9: (a) Predicted temperature rise  $T(L, t) - T_0$  at the centerline for cycling at three different current densities  $j_s$  over the same potential window and (b) measured surface temperature of a commercial EDLC during cycling at three different currents  $I_s$  over the same potential window (reproduced from Figure 10 of Ref. [29]) as functions of time  $t$ .

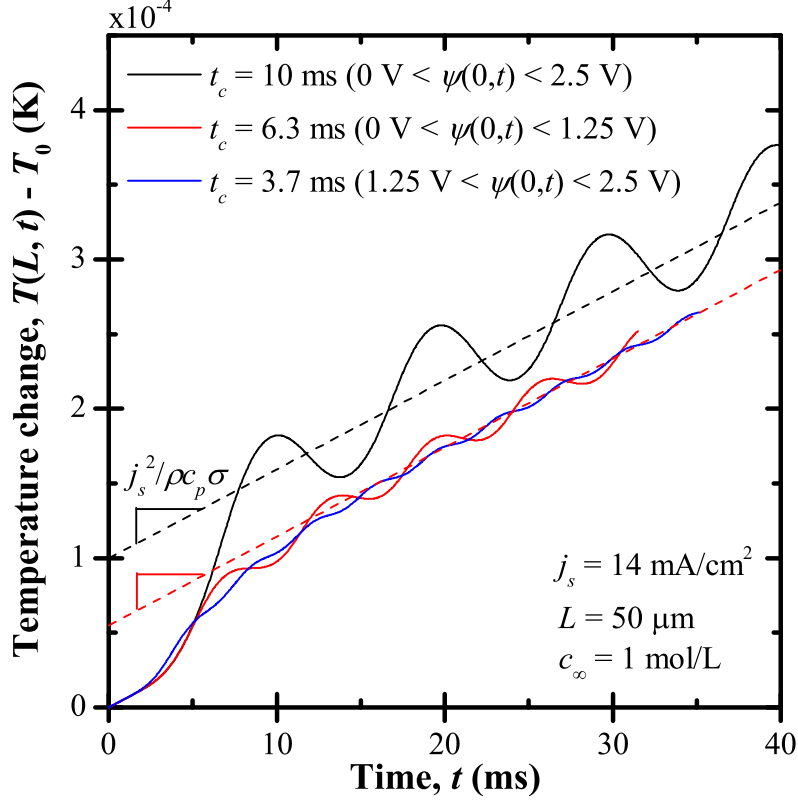


Figure 4.10: (a) Predicted temperature rise  $T(L, t) - T_0$  as a function of time  $t$  at the centerline for cycling at the same current density  $j_s = 14 \text{ mA cm}^{-2}$  over different potential windows.

fluctuations near the electrodes create “hot spots” with maximum temperatures significantly higher than those predicted by Joule heating alone. These local high temperatures may contribute to premature degradation of EDLC materials or electrolyte decomposition [10].

Finally, Figure 4.10 shows the predicted temperature change  $T(L, t) - T_0$  at the centerline as a function of time  $t$  for cycling at current density  $j_s = 14 \text{ mA cm}^{-2}$  over different potential windows, namely 0–2.5 V, 0–1.25 V, and 1.25–2.5 V. It indicates that the temperature rise in all three cases had the same overall slope since the current density  $j_s$ , and thus  $\dot{q}_{J,irr}$ , was the same. The largest temperature oscillations were observed for the 2.5 V potential window. The amplitudes of the temperature oscillations for the two 1.25 V potential windows were significantly smaller than those for the 2.5 V window and of similar magnitude to one another. Similarly, Schiffer *et al.* [29] reported that the measured temperature oscillation amplitudes

for an EDLC cycled over the potential windows 0.5–1.5 V and 1.5–2.5 V were almost identical while that measured for the broader potential window 0.5–2.5 V was significantly larger. However, the authors did not include the temperature evolution over time to compare to Figure 4.10.

The physical model developed in the present chapter captured the thermal behavior of EDLCs observed experimentally [29,76]. Unlike previous thermal models, the present model predicts the local heat generation rate based on first principles. The Joule heat generation rate  $\dot{q}_{J,irr}$  accounted for the irreversible heating within the electrolyte. Three additional reversible heat generation rates arose in the presence of concentration gradients due to diffusion, steric effects, and entropy changes. These reversible heat generation rates caused the temperature to oscillate, particularly near the electrode surfaces. Although the irreversible heat generation rate was uniform, the reversible heat generation rates were localized to large peaks close to the electrode surfaces. The location and magnitude of the maximum internal temperatures may thus differ significantly from that predicted under the common assumptions of uniform heat generation rate and Joule heating alone. The irreversible heat generation rate was constant during galvanostatic cycling, as expected. Moreover, the magnitudes of the reversible heat generation rates were constant above a certain cell potential.

### 4.3 Conclusion

This chapter presented a physics-based model for coupled electrodiffusion and heat transfer during galvanostatic charging and discharging of electric double layer capacitors. The model accounted for the presence of the Stern layer and for the finite size of ions by using the modified Poisson-Nernst-Planck model. Several contributions to the total heat generation rate were derived. One took the familiar form  $\dot{q}_{J,irr} = j^2/\sigma$  of irreversible Joule heating and was always positive. Reversible heat generation rates arose in the presence of concentration gradients. They were exothermic during charging and endothermic during discharging. The inclusion of the reversible heat generation rates resulted in thermal behavior remarkably similar to that observed in experiments. The comparison with experimental data indicates

that my physical model captures the key physical phenomena governing EDLC thermal behavior.

The present model is important in that it enables the prediction of both the spatial and the temporal variation of the heat generation rates inside the EDLC based on first principles. The results indicated that the total heat generation rate is not uniform, as is frequently assumed in existing thermal models. While the irreversible heat generation was indeed uniform, the reversible heat generation rates had large peaks close to the electrodes. This resulted in large temperature oscillations with maximum temperatures significantly higher than those predicted by Joule heating alone. The present physical model also shows how local heat generation rate is affected by individual electrolyte properties. This would be difficult or impossible to determine experimentally. Such information can facilitate the selection of EDLC materials for better thermal performance.

## CHAPTER 5

### First-order thermal model of commercial EDLC devices

This chapter develops a first-order thermal analysis for electric double layer capacitors (EDLCs). It is based on the lumped-capacitance approximation and accounts for both irreversible and reversible heat generation rates. A simple analytical expression for the overall temperature rise during galvanostatic cycling was derived. In addition, a scaling analysis was performed and demonstrated with experimental data collected from commercial EDLCs. Scaling analysis has been widely used in physics and engineering analyses of complex systems. It reduces the number of independent parameters to be considered in the analysis and facilitates the development of widely applicable thermal design rules [65]. This thermal model and scaling analysis enable rapid estimation of the temperature evolution resulting from irreversible and reversible heating in EDLCs without performing computationally intensive numerical simulations. Model predictions were validated using experimental measurements on commercial EDLCs reported in the literature [8, 29].

#### 5.1 Analysis

The following assumptions were made: (1) The device properties were constant. (2) The thermal resistance to heat transfer between the EDLC and its surroundings was constant, and (3) temperature gradients within the device were small compared to that between the EDLC and its surroundings, so that lumped-capacitance analysis was appropriate. In fact, for large cycling currents, the measured temperature difference between the outer surface of commercial devices and their surroundings was significantly larger than the temperature

difference inside the device [8, 25].

### 5.1.1 Dimensional energy balance

The thermal energy balance performed on the entire EDLC device yields the governing equation for its temperature  $T(t)$  expressed as [65]

$$C_{th} \frac{dT}{dt} = \dot{Q}(t) - \frac{(T - T_{\infty})}{R_{th}} \quad (5.1)$$

where  $C_{th}$  is the heat capacity of the device (in J K<sup>-1</sup>) and  $\dot{Q}(t)$  is the internal heat generation rate for the entire EDLC (in W), including both irreversible and reversible heating. The second term on the right-hand side of Equation (5.1) represents the rate of heat transfer (in W) from the device to its surrounding environment at temperature  $T_{\infty}$ , characterized by the thermal resistance  $R_{th}$  (in K W<sup>-1</sup>). The latter may be expressed for convective heat transfer as  $R_{th} = 1/\bar{h}A$ , where  $\bar{h}$  is the average convective heat transfer coefficient (in W m<sup>-2</sup>K<sup>-1</sup>) and  $A$  is the external surface area of the device (in m<sup>2</sup>).

The total heat generation rate consists of irreversible and reversible contributions, i.e.,  $\dot{Q}(t) = \dot{Q}_{irr}(t) + \dot{Q}_{rev}(t)$ . The detailed, first-principles thermal model derived in Chapter 4 indicates that irreversible Joule heating is the only irreversible heat generation rate in EDLCs, while reversible heating arises from several phenomena involved in EDL formation. During galvanostatic cycling, the current  $I(t)$  is a square signal of magnitude  $I_s$  with cycle period  $t_c$ . Then, the irreversible Joule heat generation rate is constant and equal to  $\dot{Q}_{irr} = I_s^2 R$ , where  $R$  is the electrical resistance of the EDLC [2, 29, 78]. Experimental measurements and the model from Chapter 4 have shown that the reversible heat generation rate is exothermic during charging, endothermic during discharging, and proportional to  $I_s$  [2, 29, 78]. Here, it is assumed to be a square wave expressed as

$$\dot{Q}_{rev}(t) = \begin{cases} +\beta I_s & \text{during charging} \\ -\beta I_s & \text{during discharging} \end{cases} \quad (5.2)$$

where  $\beta$  is a positive semi-empirical parameter specific to each device and expressed in V. As previously mentioned, Chapter 4 showed that the reversible heat generation rates



were constant in magnitude in the upper half of the cell potential range considered, and commercial EDLCs are frequently operated within this range [7, 8, 25, 76].

Finally, Equation (5.1) is a first-order, linear ordinary differential equation (ODE) requiring one initial condition. Here, the EDLC's initial temperature was assumed to be equal to  $T_0$ , i.e.,  $T(t = 0) = T_0$ .

### 5.1.2 Scaling analysis

The governing Equation (5.1) was non-dimensionalized using the dimensionless variables

$$t^* = \frac{t}{t_c} \quad \text{and} \quad T^*(t^*) = \frac{T(t) - T_0}{I_s^2 R t_c / C_{th}}. \quad (5.3)$$

The time  $t$  was scaled by the cycle period  $t_c$ , while the temperature change  $T(t) - T_0$  was scaled by the temperature rise per cycle associated with irreversible Joule heating and expressed as  $\dot{Q}_{irr} t_c / C_{th} = I_s^2 R t_c / C_{th}$ .

Substituting Equation (5.3) into the energy conservation Equation (5.1) yields the governing equation for the dimensionless temperature  $T^*(t^*)$

$$\frac{dT^*}{dt^*} = 1 - \frac{T^*(t^*) - T_\infty^*}{\tau_{th}^*} + \dot{Q}_{rev}^*(t^*). \quad (5.4)$$

Here,  $T_\infty^* = (T_\infty - T_0) / (I_s^2 R t_c / C_{th})$  is the dimensionless ambient temperature. The dimensionless thermal time constant is defined as  $\tau_{th}^* = R_{th} C_{th} / t_c$ , where the thermal time constant  $R_{th} C_{th}$  characterizes how rapidly the EDLC temperature responds to changes in its thermal environment [65]. Finally, the dimensionless heat generation rate  $\dot{Q}_{rev}^* = \dot{Q}_{rev} / \dot{Q}_{irr} = \pm \beta / I_s R$  represents the ratio of the reversible to the irreversible heat generation rates. The initial condition is expressed in dimensionless form as  $T^*(0) = 0$ .

The dimensionless ODE given by Equation (5.4) can be solved to yield the following expression for the dimensionless temperature

$$T^*(t^*) = (\tau_{th}^* + T_\infty^*) (1 - e^{-t^* / \tau_{th}^*}) + e^{-t^* / \tau_{th}^*} \int_0^{t^*} e^{t'^* / \tau_{th}^*} \dot{Q}_{rev}^*(t'^*) dt'^*. \quad (5.5)$$

### 5.1.3 Irreversible and reversible temperatures

Based on the superposition principle, the temperature  $T(t)$  may be viewed as the sum of two contributions associated with irreversible and reversible heat generation so that  $T(t) = T_{irr}(t) + T_{rev}(t)$ . The overall temperature  $T_{irr}(t)$ , resulting from  $\dot{Q}_{irr}$ , accounts for the temperature rise from cycle to cycle, while the superimposed reversible temperature oscillations  $T_{rev}(t)$  result from  $\dot{Q}_{rev}$ . These contributions can be expressed in dimensionless form as

$$T_{irr}^*(t^*) = \frac{T_{irr}(t) - T_0}{I_s^2 R t_c / C_{th}} \quad \text{and} \quad T_{rev}^*(t^*) = \frac{T_{rev}(t)}{I_s^2 R t_c / C_{th}}. \quad (5.6)$$

For an EDLC cooled by convection,  $T_{irr}^*$  is expressed as

$$T_{irr}^*(t^*) = (\tau_{th}^* + T_\infty^*) (1 - e^{-t^*/\tau_{th}^*}) \quad (5.7)$$

and is governed by two dimensionless similarity parameters, namely,  $\tau_{th}^*$  and  $T_\infty^*$ . Over time,  $T_{irr}^*$  approaches a steady-state value given by  $T_{irr}^*(t^* \rightarrow \infty) = \tau_{th}^* + T_\infty^*$ . In dimensional form,  $T_{irr}(t)$  can be written as

$$T_{irr}(t) = T_0 + (I_s^2 R R_{th} + T_\infty - T_0)(1 - e^{-t/R_{th} C_{th}}). \quad (5.8)$$

Thus, under steady-state conditions, the irreversible temperature is expressed as  $T_{irr}(t \rightarrow \infty) = R_{th} I_s^2 R + T_\infty$ . Subtracting Equation (5.7) from Equation (5.5) yields

$$T_{rev}^*(t^*) = e^{-t^*/\tau_{th}^*} \int_0^{t^*} e^{t^{*'}/\tau_{th}^*} \dot{Q}_{rev}^*(t^{*'}) dt^{*'} \quad (5.9)$$

### 5.1.4 Thermally insulated EDLC

In the limiting case of a perfectly thermally insulated EDLC,  $R_{th}$  and  $\tau_{th}^*$  approach infinity. Then,  $\tau_{th}^* \gg t^*$  and  $e^{-t^*/\tau_{th}^*} \approx 1 - t^*/\tau_{th}^*$ , so that the overall dimensionless temperature rise is linear with  $t^*$  and given in dimensionless and dimensional form by

$$T_{irr}^*(t^*) = t^* \quad \text{and} \quad T_{irr}(t) = T_0 + \frac{I_s^2 R}{C_{th}} t. \quad (5.10)$$

Similarly, the dimensionless reversible temperature can be expressed as

$$T_{rev}^*(t^*) = \begin{cases} \pm |\dot{Q}_{rev}^*| (t^* - n_c) & 0 \leq (t^* - n_c) < 1/2 \\ \pm |\dot{Q}_{rev}^*| [(n_c + 1) - t^*] & 1/2 \leq (t^* - n_c) < 1 \end{cases} \quad (5.11)$$

where  $n_c = 0, 1, 2, \dots$  is the number of completed charge-discharge cycles. Here, the positive and negative signs correspond to cycling starting with a charging or a discharging step, respectively. In dimensional form,  $T_{rev}(t)$  can be expressed as

$$T_{rev}(t) = \begin{cases} \pm \frac{\beta I_s}{C_{th}} (t - n_c t_c) & n_c t_c \leq t < (n_c + 1/2)t_c \\ \pm \frac{\beta I_s}{C_{th}} [(n_c + 1)t_c - t] & (n_c + 1/2)t_c \leq t < (n_c + 1)t_c. \end{cases} \quad (5.12)$$

### 5.1.5 Method of solution

The dimensionless temperature  $T^*(t^*)$  accounting for reversible heat generation was evaluated by numerically solving Equation (5.4) using an explicit third-order Runge-Kutta method [96]. The solver adjusted the time step to satisfy specified relative and absolute tolerances. It compared the estimated error associated with  $T^*(t^*)$  to these tolerances at each time step. The convergence criterion was defined such that the relative error in the dimensionless temperature  $T^*$  was less than 0.5% when dividing both tolerances by two.

### 5.1.6 Experimental data

Table 5.1 summarizes the values of the capacitance  $C$ , electrical resistance  $R$ , heat capacity  $C_{th}$ , and thermal resistance  $R_{th}$  of commercial EDLCs whose thermal behaviors have been investigated in the literature [8, 25, 29] including Maxwell BCAP1500 [97], Maxwell BCAP0350 [98], and Nesscap ESHCP-5000C0-002R7 [99]. Note that  $C_{th}$  for the Nesscap 5000-F cell was measured experimentally and reported in Ref. [29]. The Maxwell EDLCs were cooled by natural convection in air at  $T_\infty$  [8, 25] while the Nesscap cell was thermally insulated [29]. Table 5.1 also provides the operating conditions including the current  $I_s$ , potential window  $\Delta\psi$ , initial temperature  $T_0$ , and ambient air temperature  $T_\infty$ , used in three experimental studies reported in the literature [8, 25, 29]. The cycle period  $t_c$  was estimated from the device capacitance  $C$ , the potential window  $\Delta\psi$ , and the current  $I_s$  according to  $t_c = 2C\Delta\psi/I_s$  [29]. Experimental data from these different studies were used to validate the present model and the associated scaling analysis.

Table 5.1: Properties of commercial EDLC devices and galvanostatic cycling conditions used in experimental studies [8, 25, 29].  
The experimental data were used to demonstrate the present analysis and scaling.

Manufacturer	Maxwell Tech. [97]	Maxwell Tech. [98]	Nesscap Co. [99]
	Units	BCAP1500	BCAP0350
$C$	(F)	1500	350
$R$	(m $\Omega$ )	0.47	3.2
$C_{th}$	(J K $^{-1}$ )	320	60
$R_{th}$	(K W $^{-1}$ )	3.2	10.9
$\beta$	(V)	0.04 – 0.07	0.1 – 0.2
			0.06
Exp. studies	Al Sakka <i>et al.</i> [25]	Gualous <i>et al.</i> [8]	Schiffer <i>et al.</i> [29]
$I_s$	(A)	75	30
$\Delta\psi$	(V)	1.35	1.25
$t_c = 2C\Delta\psi/I_s$	(s)	54	29
$T_0$	( $^{\circ}$ C)	17.5	20
$T_{\infty}$	( $^{\circ}$ C)	17.5	20
			N/A
Dimensionless similarity parameters			
$\tau_{th}^*$	19.0	22.4	$\infty$
$T_{\infty}^*$	0	0	N/A
$T^*(t^* \rightarrow \infty)$	19.0	22.4	$\infty$

## 5.2 Results and discussion

### 5.2.1 Parametric study

Figure 5.1(a) shows  $T^*(t^*)$  predicted by numerically solving Equation (5.4) and  $T_{irr}^*(t^*)$  predicted analytically by Equation (5.7) as functions of  $t^*$  for  $\tau_{th}^*$  ranging from 10 to  $\infty$  with  $T_\infty^* = 0$ , i.e., the EDLC started at the same temperature as its surroundings. The cycles started with a charging step and  $|\dot{Q}_{rev}^*|$  was equal to 5. In all cases, the temperature  $T^*(t^*)$  featured nearly triangular temperature oscillations around  $T_{irr}^*$ , as predicted by Equation (5.11) in the limiting case of  $\tau_{th}^*$  approaching infinity. For finite values of  $\tau_{th}^*$ ,  $T_{irr}^*$  initially satisfied  $T_{irr}^*(t^* \approx 0) \approx t^*$ , and then  $T_{irr}^*$  approached the steady-state value  $T_{irr}^*(t^* \rightarrow \infty) = T_\infty^* + \tau_{th}^*$  as convective heat losses increased due to the increasing temperature difference between the device and the surroundings. In other words, in the oscillatory steady-state regime, the rate of heat loss to the surroundings balanced the irreversible heat generation rate. This relationship could be used in practice to determine the values of  $\tau_{th}^*$  and  $R_{th} = t_c \tau_{th}^* / C_{th}$  of actual EDLCs.

Similarly, Figure 5.1(b) shows  $T^*(t^*)$  predicted by solving Equation (5.4) and  $T_{irr}^*(t^*)$  given by Equation (5.7) as functions of  $t^*$  for  $\tau_{th}^* = 5$  and  $T_\infty^* = 0$ . Here,  $|\dot{Q}_{rev}^*|$  was equal to either 2 or 5 and the cycle started with either a discharging or a charging step. The local maxima and minima of  $T^*(t^*)$  occurred at the end of the charging steps and of the discharging steps, respectively. In cases beginning with a charging step,  $T^*(t^*)$  initially increased and oscillated within the envelope  $T_{irr}^*(t^*) \leq T^*(t^*) \leq T_{irr}^*(t^*) + |\dot{Q}_{rev}^*|/2$  where  $T_{irr}^*(t^*)$  is given by Equation (5.7). By contrast, in cases beginning with a discharging step,  $T^*(t^*)$  initially decreased, oscillating within the range  $T_{irr}^*(t^*) \geq T^*(t^*) \geq T_{irr}^*(t^*) - |\dot{Q}_{rev}^*|/2$ . However, as  $T^*(t^*)$  approached oscillatory steady-state, all cases fell within the envelope  $T_{irr}^*(t^*) - |\dot{Q}_{rev}^*|/4 \leq T^*(t^*) \leq T_{irr}^*(t^*) + |\dot{Q}_{rev}^*|/4$ . Interestingly, the amplitude of the dimensionless temperature oscillations  $\Delta T_{rev}^*$  was equal to  $|\dot{Q}_{rev}^*|/2 = \beta/2I_s R$  at all times and for all cases considered, as illustrated in Figure 5.1(b). In dimensional form, it is expressed as  $\Delta T_{rev} = \beta I_s t_c / 2C_{th}$ . In fact, this provides a simple and convenient way to estimate the coefficient of proportionality  $\beta$  associated with reversible heat generation

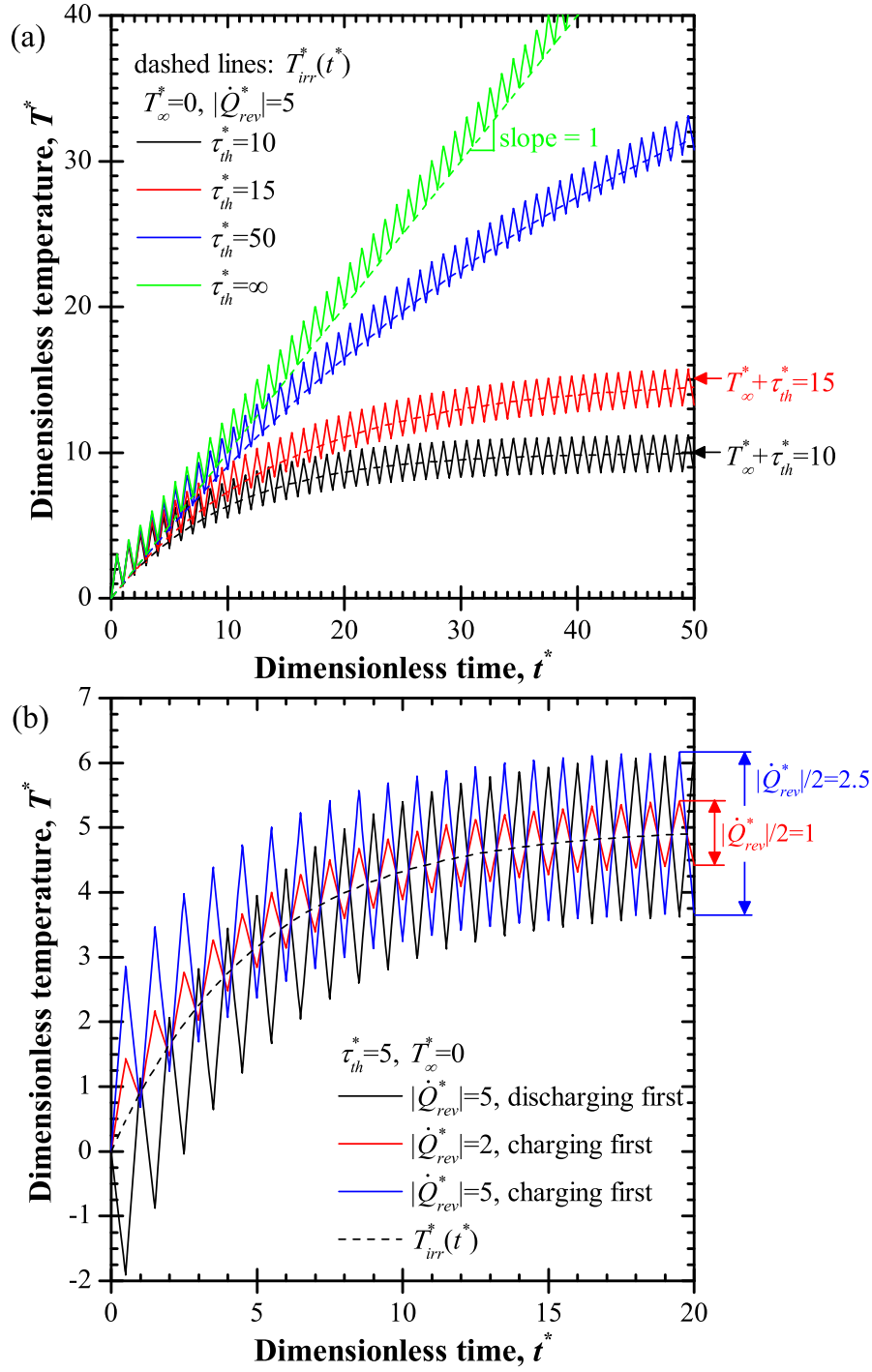


Figure 5.1: Dimensionless temperature  $T^*(t^*)$  predicted by solving Equation (5.4) and dimensionless irreversible temperature  $T_{irr}^*(t^*)$  given by Equation (5.7) as functions of  $t^*$  for (a) different values of  $\tau_{th}^*$  with  $T_\infty^* = 0$  for  $|\dot{Q}_{rev}^*| = 5$  and (b) different values of  $|\dot{Q}_{rev}^*|$  for  $T_\infty^* = 0$  and  $\tau_{th}^* = 5$ .

directly from experimental data as  $\beta = 2C_{th}\Delta T_{rev}/I_s t_c$ .

### 5.2.2 EDLCs cooled by natural convection

Figure 5.2 shows the temperatures  $T(t)$  as a function of time  $t$  measured by Gualous and coworkers at the outer surface of (a) a 1500-F EDLC [25] and (b) a 350-F EDLC [8] galvanostatically cycled at  $\pm 75$  A and  $\pm 30$  A, respectively. These Maxwell Technologies EDLCs were cooled by natural convection in air at  $T_\infty$  of 20°C and 17.5°C, respectively [8,25]. Both figures display a clear overall temperature rise with small temperature oscillations. Here also, the temperature rose quickly at the beginning of the test and then approached an oscillatory steady-state as the rate of convective heat loss balanced the irreversible heat generation rate. Figures 5.2(a) and 5.2(b) also plot  $T_{irr}(t)$  predicted by Equation (6.12) using the properties summarized in Table 5.1 as well as predictions for thermal resistance  $R_{th} \pm 10\%$  to account for the possible uncertainty in the reported values of  $R_{th}$ . In both Figures 5.2(a) and 5.2(b), the experimental data fell approximately between the temperature predictions of Equation (6.12) using  $R_{th} \pm 10\%$ .

Figures 5.2(c) and 5.2(d) plot the data shown in Figures 5.2(a) and 5.2(b) in terms of dimensionless temperature  $T^*(t^*)$  and time  $t^*$ . They also show the overall dimensionless temperature rise  $T_{irr}^*(t^*)$  predicted by Equation (5.7). Here also, predictions for  $T_{irr}^*(t^*)$  were in good agreement with scaled temperature measurements for both EDLCs. In addition, the dimensionless temperature oscillations were small compared to the overall dimensionless temperature rise, i.e.,  $\dot{Q}_{rev}^*/2$  was small compared to  $\tau_{th}^* + T_\infty^*$ . It was difficult to accurately quantify the temperature oscillation amplitude  $\Delta T_{rev}$  in order to retrieve  $\beta$ . However, from visual inspection,  $\Delta T_{rev}^*$  ranged approximately between 1/2 and 1 for both EDLCs, yielding  $\beta$  between 0.04 V and 0.07 V for BCAP1500 and 0.1 V and 0.2 V for BCAP0350. This corresponded to a dimensional temperature oscillation amplitude  $\Delta T_{rev}$  between 0.2 K and 0.4 K for BCAP1500 and between 0.7 K and 1.4 K for BCAP0350.

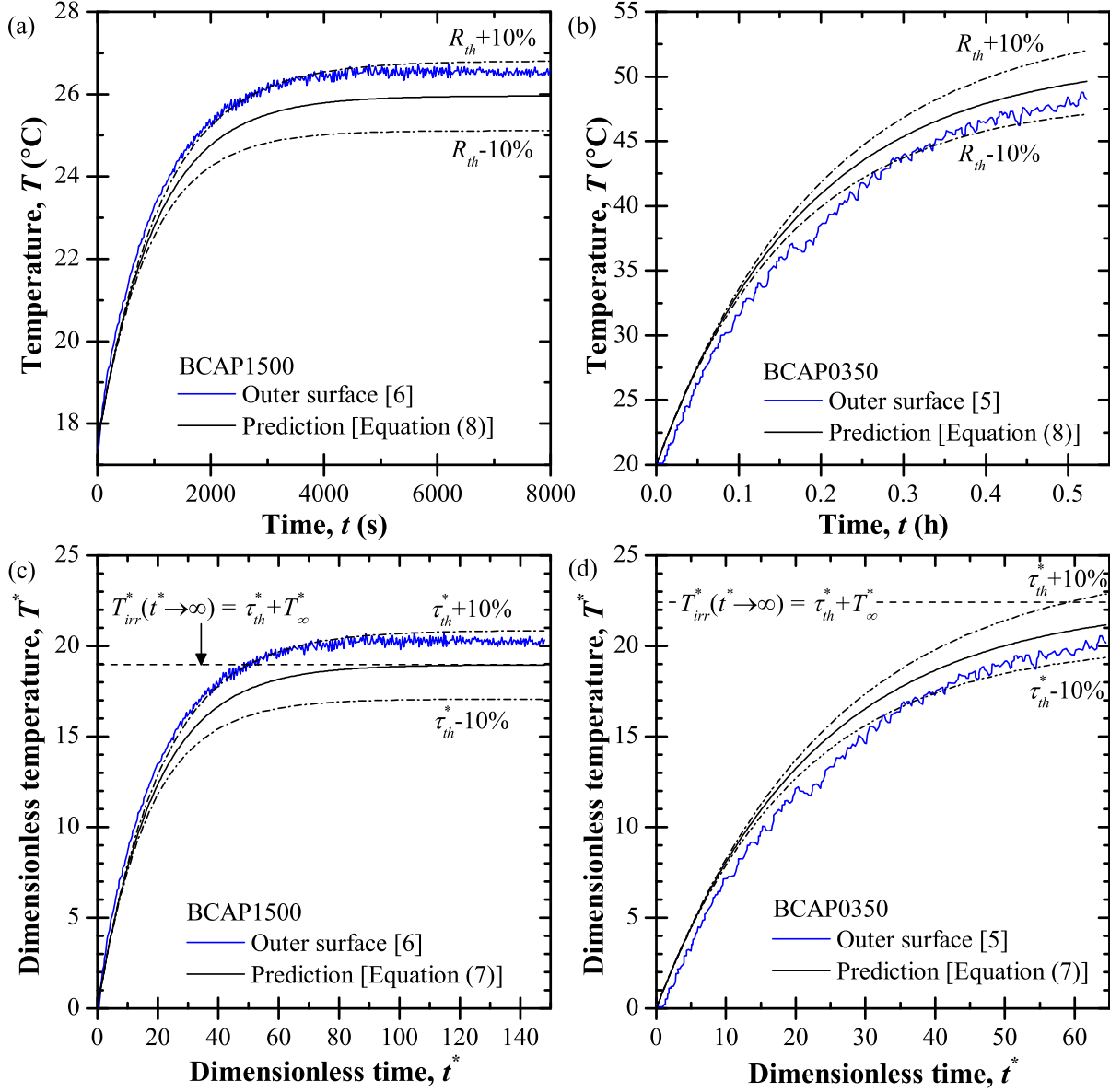


Figure 5.2: Measured temperature  $T(t)$  as a function of time  $t$  at the outer surface of (a) a 1500-F EDLC cycled at  $\pm 75$  A (Figure 7 of Ref. [25]) and (b) a 350-F EDLC cycled at  $\pm 30$  A (Figure 8 of Ref. [8]), as well as (c) and (d) the corresponding dimensionless temperatures  $T^*(t^*)$  as functions of dimensionless time  $t^*$  and the predictions by Equation (5.7) using data in Table 5.1.



### 5.2.3 Thermally insulated EDLC

Figure 5.3(a) shows the temperature  $T(t)$  measured at the surface of a thermally insulated 5000-F EDLC (ESHCP-5000C0-002R7 by Nesscap Co.) as a function of time  $t$ . This EDLC was cycled galvanostatically at currents  $I_s$  between 25 A and 100 A and cycle periods  $t_c$  ranging from 100 s to 400 s [29]. The electrical resistance  $R$ , the heat capacity  $C_{th}$ , the thermal resistance  $R_{th}$ , and the ambient temperature  $T_\infty$  remained the same for all five cases and are summarized in Table 5.1. The temperature featured oscillations superimposed over an approximately linear temperature rise of slope  $I_s^2 R$  [29].

Figure 5.3(b) shows the same data as in Figure 5.3(a) but in dimensionless form. The scaled data for all five cases approximately collapsed around an overall temperature rise predicted by  $T_{irr}^* = t^*$  and corresponding to the limiting case when  $\tau_{th}^*$  or  $R_{th}$  approached infinity. As observed in Figure 5.1, the initial slope  $dT_{irr}^*/dt^*$  in the experimental data was equal to about 1. However, as  $T^*$  increased, the overall slope of the measured  $T^*$  slowly decreased. This can be attributed to heat losses to the surroundings due to imperfect thermal insulation. In fact,  $R_{th}$  and  $\tau_{th}^*$  were large but finite, and  $T^*(t^*)$  would eventually approach an oscillatory steady-state around the dimensionless temperature  $T_{irr}^*(t^* \rightarrow \infty) = \tau_{th}^* + T_\infty^*$  similar to the behavior shown in Figure 5.1. This behavior was more apparent at smaller currents when irreversible heat generation was smaller. For larger current  $I_s$ , heat generation was large compared with convective heat losses to the surroundings in the time frame for which data are available. Unfortunately, the steady-state EDLC temperature could not be evaluated because the actual values of  $R_{th}$  and  $\tau_{th}^*$  were not measured. It is also interesting to note that, by scaling  $t$  by the cycle period  $t_c$ , the temperature maxima and minima occurred at the same dimensionless times  $t^*$ .

Figure 5.4 plots the same data as in Figure 5.3(a) separately in terms of dimensionless temperature  $T^*(t^*)$  as a function of  $t^*$  for cycles beginning with a charging step with (a)  $I_s = 25$  A, (b)  $I_s = 50$  A, and (c)  $I_s = 100$  A as well as (d) a case beginning with a discharging step with  $I_s = 100$  A. It also plots the predictions for  $T^*(t^*)$  obtained by numerically solving Equation (5.4). As previously discussed, the dimensionless temperature oscillation amplitude

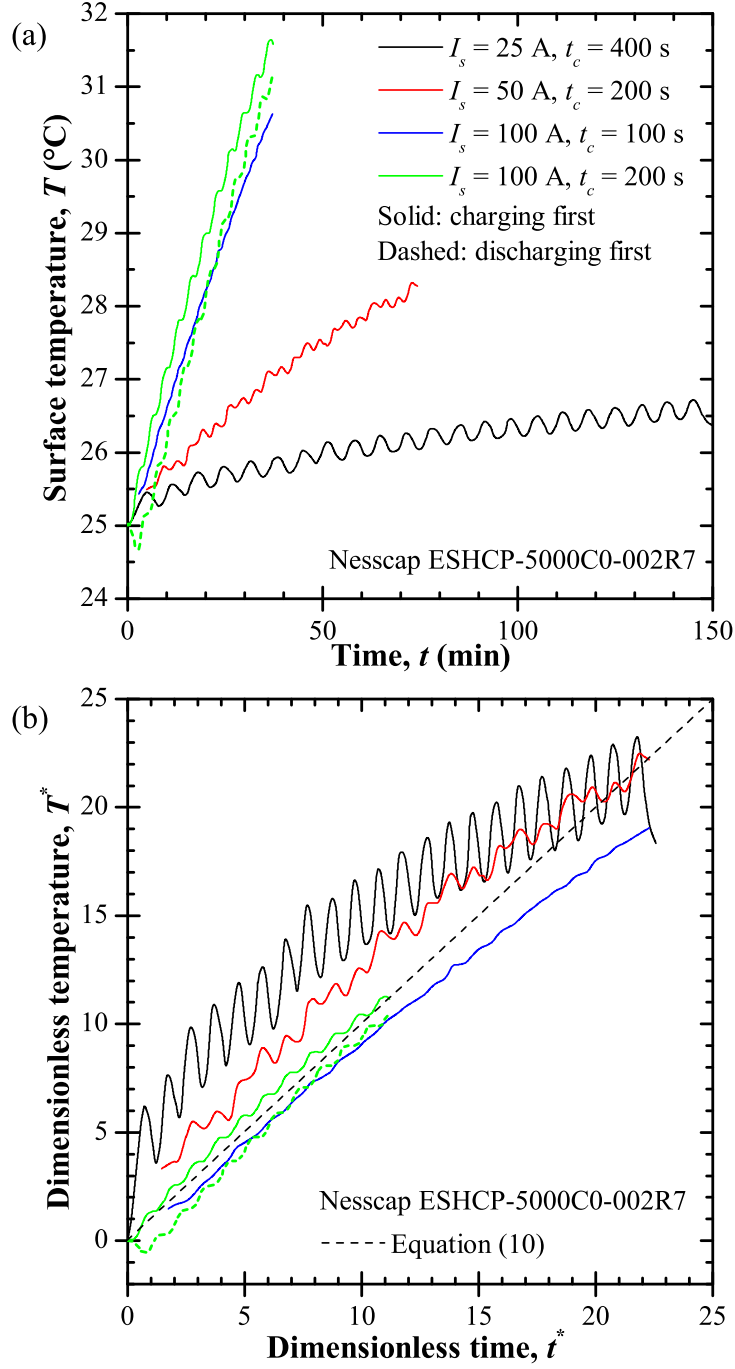


Figure 5.3: (a) Measured temperature  $T(t)$  at the surface of a thermally insulated Nesscap 5000-F EDLC as a function of time  $t$  for different values of current  $I_s$  and cycle period  $t_c$  (Figures 8 and 10 of Ref. [29]) and (b) the corresponding dimensionless temperature  $T^*(t^*)$  as well as  $T_{irr}^*(t^*)$  predicted by Equation (5.10) as functions of dimensionless time  $t^*$ .

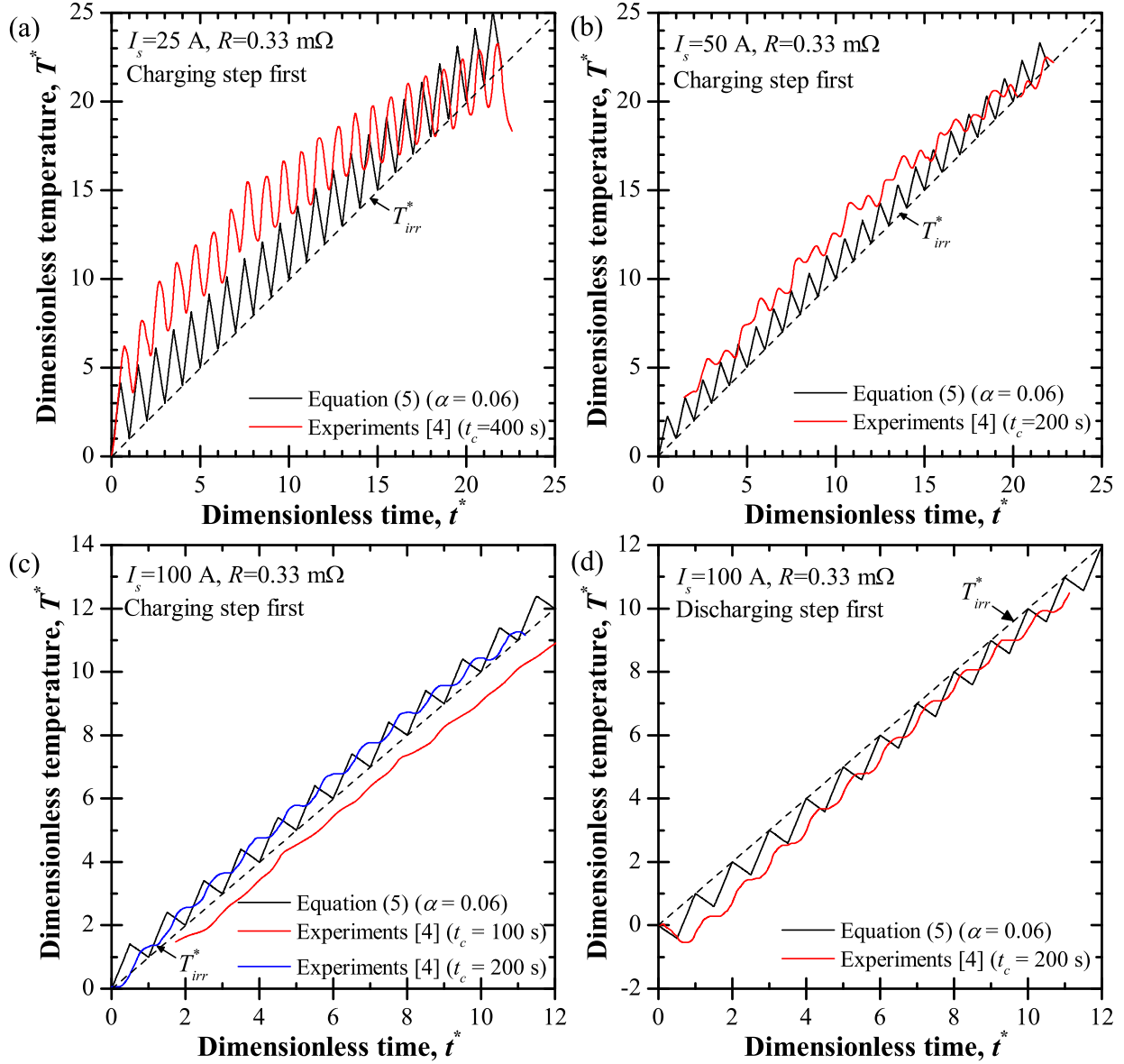


Figure 5.4: Dimensionless temperature  $T^*(t^*)$  as a function of dimensionless time  $t^*$  based on experimental measurements at the EDLC outer surface [29] and predicted by solving Equation (5.4) for a thermally insulated EDLC cycled at (a)  $I_s = 25$  A, (b)  $I_s = 50$  A, and (c)  $I_s = 100$  A beginning with a charging step as well as (d) cycled at  $I_s = 100$  A beginning with a discharging step.

was equal to  $\Delta T_{rev}^* = |\dot{Q}_{rev}^*|/2 = \beta/2I_sR$ . These oscillations were the largest for experimental data with  $I_s = 25$  A [Figure 5.4(a)]. Thus, the average value of  $\Delta T_{rev}^*$  was estimated for this dataset to yield the semi-empirical constant  $\beta = 2\Delta T_{rev}^* I_s R = 0.06 \pm 0.012$  V with 95% confidence interval. This value of  $\beta$  was of the same order of magnitude as those estimated for the other EDLCs. In addition, it was the same for all datasets considered in Figure 5.4, since they were collected with the same EDLC. The corresponding values of  $|\dot{Q}_{rev}^*|$  ranged from 1.8 to 7.3 as the current  $I_s$  decreased from 100 A to 25 A. Here,  $|\dot{Q}_{rev}^*|$  increased with decreasing  $I_s$  because  $|\dot{Q}_{rev}^*|$  characterizes the ratio of the reversible to the irreversible heat generation rates, and  $\dot{Q}_{irr} \propto I_s^2$  decreased faster with decreasing  $I_s$  than  $|\dot{Q}_{rev}^*| \propto I_s$ . This range of  $|\dot{Q}_{rev}^*|$  explained why the temperature oscillations shown in Figure 5.4 were significantly larger than those observed in Figure 5.2, when  $|\dot{Q}_{rev}^*|$  was estimated to range between 1 and 2. The larger values of  $|\dot{Q}_{rev}^*|$  in the Nesscap EDLC were likely due to (i) smaller cycling currents and/or (ii) smaller resistance  $R$  (Table 5.1).

Overall, predictions of  $T^*(t^*)$  closely resembled the measured behavior. However, there was a temporal offset between the predicted and measured temperature oscillations. In fact, Figure 5.4 indicates that the local maxima and minima of the measured  $T^*$  were shifted towards later dimensionless times  $t^*$  compared with predictions obtained by solving Equation (6.12). This effect was also observed in the previous simulations in Chapter 4. The delay was attributed to heat diffusion from the electrode/electrolyte interface to the bulk electrolyte [2]. Indeed, reversible heat generation occurs mainly near the electrode/electrolyte interface where the electric double layer forms and is transported by conduction through the electrolyte and through the electrode to the outer surface of the EDLCs.

Moreover, the measured  $T^*(t^*)$  was larger than the model predictions for cases beginning with a charging step [Figures 5.4(a) and 5.4(b)] and smaller for cases beginning with a discharging step [Figure 5.4(d)]. This can also be attributed to heat diffusion inside the EDLC. In fact, Chapter 4 showed that the temperature oscillation amplitude decreased with increasing distance from the electric double layer. Thus, retrieving the reversible heat generation rate and the parameter  $\beta$  from surface temperature measurements underpredicted its actual value since temperature oscillations were larger inside the device.

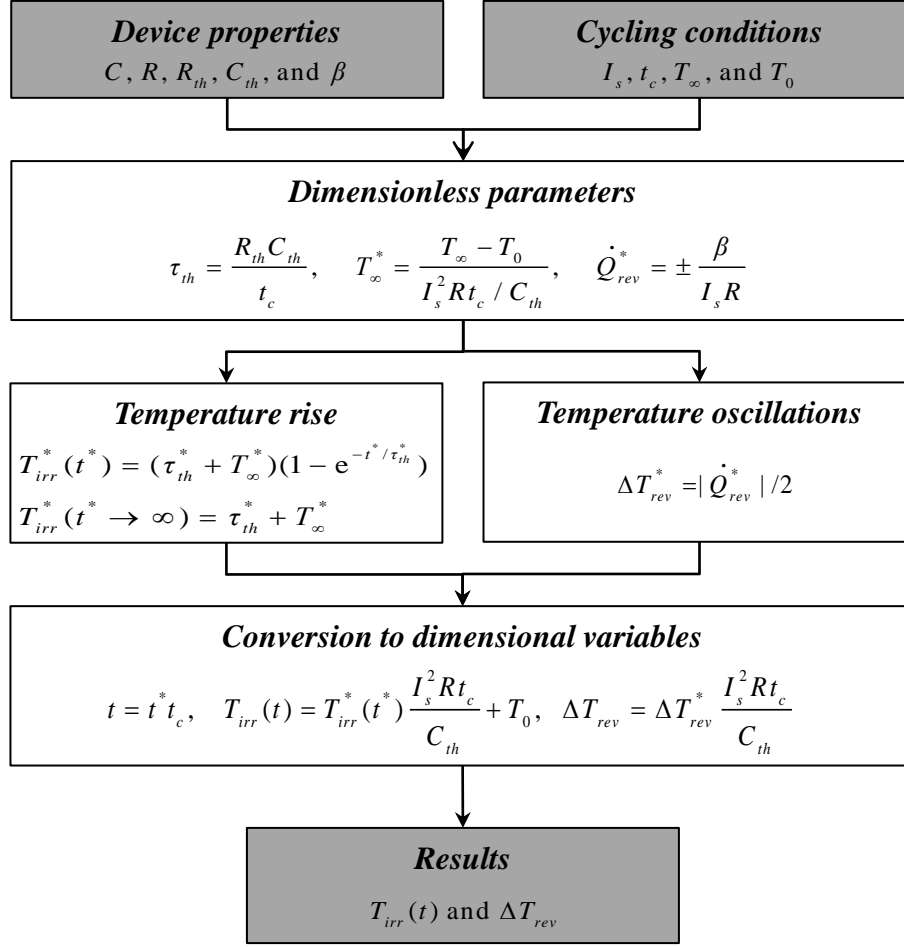


Figure 5.5: Procedure to estimate temperature evolution of an EDLC.

Finally, the present model predicted the main features of the experimental data quite well. Figure 5.5 summarizes the procedure to predict the overall temperature rise  $T_{irr}(t)$  and the temperature oscillation amplitude  $\Delta T_{rev}$ . It provides an excellent first-order estimate of the EDLC temperature behavior without relying on detailed and computationally intensive numerical simulations. In addition, it offers a simple and convenient method for retrieving the thermal resistance  $R_{th}$  and the semi-empirical parameter  $\beta$  for reversible heat generation from experimental temperature measurements. Note that  $\beta$  is the only empirical parameter retrieved from temperature measurements. All the other input parameters can be obtained from product data sheets. In addition, the model's irreversible temperature predictions agreed well with experimental measurements reported in the literature for EDLCs of different sizes and manufacturers. This suggests that the present model is robust and

broadly applicable.

### 5.3 Conclusion

This study developed an engineering thermal model accounting for both irreversible and reversible heat generation to predict the temporal evolution of temperature in EDLC devices during galvanostatic cycling. The dimensionless temperature  $T^*(t^*)$  was governed by three dimensionless similarity parameters, namely,  $\tau_{th}^*$ ,  $T_\infty^*$ , and  $\dot{Q}_{rev}^*$ , characterizing the rate of heat transfer to the surroundings, the ambient temperature, and the reversible heat generation rate, respectively. Temperature predictions showed good agreement with experimental data obtained from different commercial devices and reported in the literature [8, 25, 29]. This first-order model has the advantage of predicting the temperature evolution of actual EDLC devices without relying on computationally intensive numerical simulations. It can be used in designing thermal management strategies for EDLCs.

## CHAPTER 6

### Scaling laws for EDLC heating and temperature oscillations

This chapter provides a framework for developing design rules and thermal management strategies for electric double layer capacitors (EDLCs). First, it presents a scaling analysis of the physical model derived from first principles in Chapter 4 for coupled electrodiffusion and thermal transport in electric double layer capacitors. The model rigorously accounts for irreversible Joule heating and for reversible heat generation rates arising from electric double layer formation in binary and symmetric electrolytes obeying the modified Poisson-Nernst-Planck (MPNP) model. Scaling analysis simplified the problem from twelve independent design parameters to seven meaningful dimensionless similarity parameters governing the spatiotemporal evolution of the electric potential, ion concentrations, heat generation rates, and temperature in the electrolyte. Then, similarity behavior was observed and scaling laws were developed for the total irreversible and reversible heat generated during a charging step and for the maximum temperature oscillations in EDLCs with planar electrodes under galvanostatic cycling using detailed numerical simulations.

#### 6.1 Motivation for scaling

Scaling analysis has proved to be a useful and powerful tool in numerous areas of physics and engineering, particularly in heat transfer [65]. Scaling of the governing Equations (2.5), (2.6), and (2.12) and of the associated initial and boundary conditions could significantly reduce the number of independent parameters that must be considered in performing thermal analysis of EDLC electrolytes. This can facilitate the development of thermal design rules to

mitigate EDLC heating applicable to a wide range of electrolytes and operating conditions.

## 6.2 Analysis

### 6.2.1 Problem statement

Figure 4.1 illustrates the simulated one-dimensional EDLC consisting of two planar electrodes separated by a binary and symmetric electrolyte with inter-electrode distance  $2L$ . The planar electrodes located at  $x = 0$  and  $x = 2L$  were denoted as Electrodes A and B, respectively. The electrolyte was divided into three regions: a Stern layer adjacent to each electrode and a diffuse layer. The same Assumptions (1)–(7) used in Chapters 3 and 4 were used in the present chapter. The assumption of constant properties [Assumption (5)] is reasonable for small changes in temperature and commonly used for scaling analysis. Thus, the temperature  $T$  appearing in the expressions for  $\mathbf{N}_i$ ,  $\dot{q}_{S,e}$ , and  $\dot{q}_{S,T}$  was taken as the initial temperature  $T_0$ . As in Chapters 3 and 4, the present chapter models only the electrolyte region  $0 \leq x \leq 2L$ . In EDLC devices, the electrodes and the current collectors also contribute to irreversible Joule heating and to the thermal inertia. However, electrodes and current collectors obey Ohm's law [28] and thus do not contribute to the reversible heating. In addition, the electrical conductivity of the electrode and current collector materials are expected to be much larger than that of the electrolyte. For example, the bulk electrical conductivity  $\sigma_\infty$  of the electrolyte considered in Chapter 4 and in the current chapter was on the order of  $1 \text{ S m}^{-1}$  while the conductivity of activated carbon is on the order of 100–1000  $\text{S m}^{-1}$  [14, 86, 87]. Thus, the electrolyte is expected to dominate the heat generation in the device.

For an EDLC with binary and symmetric electrolyte, the electric potential  $\psi(\mathbf{r}, t)$ , ion concentrations  $c_i(\mathbf{r}, t)$ , and temperature  $T(x, t)$  were governed by Equation (2.5), Equation (2.6) with MPNP ion flux given by Equation (2.8), and Equation (2.12) with heat generation rate given by Equation (4.26), respectively.



## 6.2.2 Initial and boundary conditions for planar electrodes

In one-dimensional (1D) Cartesian coordinates, the governing Equations (2.5), (2.6), and Equation (2.12) are first-order partial differential equations (PDEs) in time and second-order PDEs in space. They require one initial condition and two boundary conditions in each region. The initial and boundary conditions were identical to those used in Chapter 4 and described in Sections 4.1.2.2 and 4.1.3.3.

## 6.2.3 Scaling analysis

### 6.2.3.1 Dimensionless variables

Equations (2.5), (2.6), (2.8), (2.12), and (4.26) along with the associated initial and boundary conditions were non-dimensionalized using the dimensionless variables

$$\begin{aligned} \mathbf{r}^* &= \frac{\mathbf{r}}{\lambda_D}, \quad t^* = \frac{t}{\lambda_D^2/D}, \quad \psi^*(\mathbf{r}^*, t^*) = \frac{\psi(\mathbf{r}, t)}{R_u T_0 / zF}, \\ c_i^*(\mathbf{r}^*, t^*) &= \frac{c_i(\mathbf{r}, t)}{c_\infty}, \quad \text{and} \quad T^*(\mathbf{r}^*, t^*) = \frac{T(\mathbf{r}, t) - T_0}{T_0}. \end{aligned} \quad (6.1)$$

Here, the position vector  $\mathbf{r}$  was scaled by the Debye length defined for binary and symmetric electrolyte as  $\lambda_D = \sqrt{\epsilon_0 \epsilon_r R_u T_0 / 2z^2 F^2 c_\infty}$  and corresponding to an estimate of the EDL thickness at temperature  $T_0$  [40, 41, 44]. Specifically, it characterizes the distance required for the potential to decay by about 66% from its value at the electrode surface [44]. The time  $t$  was scaled by the characteristic time for ion diffusion across the EDL thickness estimated as  $\tau_d = \lambda_D^2 / D$  [65]. The thermal voltage  $R_u T_0 / zF$  represents the voltage inducing an electrical potential energy equivalent to the thermal energy for an ion of valency  $z$  at temperature  $T_0$  [41]. Thus, the dimensionless surface potential  $\psi^*$  characterizes the extent to which the potential  $\psi$  perturbs the ion concentrations from their equilibrium distribution under zero electric field. Finally, the concentration  $c_i(x, t)$  and the temperature change  $T(x, t) - T_0$  were scaled by the bulk ion concentration  $c_\infty$  and the initial temperature  $T_0$ , respectively.

Note that this scaling analysis is very similar to that used in Chapter 3. However, this chapter extends that scaling analysis to the general three-dimensional (3D) govern-

ing equations as well as the galvanostatic cycling boundary conditions. Using the scaled position vector  $\mathbf{r}^*$ , the gradient, divergence, and Laplacian operators can be respectively non-dimensionalized as

$$\nabla^* f^*(\mathbf{r}^*) = \frac{\lambda_D}{f_0} \nabla f, \quad \nabla^* \cdot \mathbf{v}^*(\mathbf{r}^*) = \frac{\lambda_D}{v_0} \nabla \cdot \mathbf{v}, \quad \text{and} \quad \nabla^{*2} f^* = \frac{\lambda_D^2}{f_0} \nabla^2 f. \quad (6.2)$$

where the function  $f(\mathbf{r})$  and the vector  $\mathbf{v}(\mathbf{r})$  are scaled by the scalars  $f_0$  and  $v_0$ , respectively so that  $f^* = f/f_0$  and  $\mathbf{v}^* = \mathbf{v}/v_0$ .

### 6.2.3.2 Dimensionless Poisson equation

Substituting Equation (6.1) into the 1D Poisson Equation (2.5) yields the following governing equation for the dimensionless electric potential  $\psi^*(x^*, t^*)$  [57]

$$-2\nabla^{*2}\psi^* = \begin{cases} 0 & \text{in the Stern layers} \\ c_1^* - c_2^* & \text{in the diffuse layer.} \end{cases} \quad (6.3)$$

### 6.2.3.3 Dimensionless mass conservation equation

The dimensionless concentrations  $c_i^*(x^*, t^*)$  of the cations and anions in the diffuse layer satisfy the dimensionless 1D mass conservation equations expressed as

$$\frac{\partial c_i^*}{\partial t^*} = -\nabla^* \cdot \mathbf{N}_i^* \quad i = 1 \text{ and } 2. \quad (6.4)$$

The dimensionless local ion flux vector  $\mathbf{N}_i^*(x^*, t^*)$  is defined as  $\mathbf{N}_i^* = \mathbf{N}_i/(Dc_\infty/\lambda_D)$  and expressed for binary and symmetric electrolytes as

$$\mathbf{N}_i^* = - \left[ \nabla^* c_i^* + \text{sgn}(z_i) c_i^* \nabla^* \psi^* + \frac{c_i^* \nu_p / 2}{1 - (c_1^* + c_2^*) \nu_p / 2} \nabla^* (c_1^* + c_2^*) \right]. \quad (6.5)$$

Here, the dimensionless number  $\nu_p = 2c_\infty/c_{max} = 2c_\infty N_A a^3$  is the so-called packing parameter corresponding to the ratio of the total bulk concentration  $2c_\infty$  to the theoretical maximum concentration  $c_{max}$  [38]. It is less than unity as the bulk concentration cannot exceed  $c_{max}$ . It approaches zero in the limiting case of negligibly small ion diameter  $a$ . The function  $\text{sgn}(z_i)$  is equal to  $+1$  or  $-1$  depending on the sign of the valency  $z_i$ .

### 6.2.3.4 Dimensionless heat diffusion equation

The dimensionless energy equation derived from Equation (2.12) can be expressed as

$$\frac{\partial T^*}{\partial t^*} = Le \nabla^{*2} T^* + \frac{\dot{q}^*}{C^*}. \quad (6.6)$$

The Lewis number  $Le$  is defined as  $Le = \alpha_{th}/D$  where  $\alpha_{th} = k/\rho c_p$  is the thermal diffusivity [65]. The dimensionless heat capacity  $C^*$  is defined as  $C^* = \rho c_p/R_u c_\infty$ . Here, the dimensionless local volumetric heat generation rate is given by  $\dot{q}^* = \dot{q}/(R_u T_0 D c_\infty/\lambda_D^2) = \dot{q}_{J,irr}^* + \dot{q}_{rev}^*$  where  $\dot{q}_{rev}^* = \dot{q}_{E,d}^* + \dot{q}_{E,s}^* + \dot{q}_{S,c}^* + \dot{q}_{S,T}^*$ . The irreversible Joule heating  $\dot{q}_{J,irr}$  [Equation (4.22)] is expressed in dimensionless form as

$$\dot{q}_{J,irr}^* = \frac{|\mathbf{j}^*|^2}{c_1^* + c_2^*} \quad (6.7)$$

where  $\mathbf{j}^* = \mathbf{j}/(zFDc_\infty/\lambda_D) = \mathbf{N}_1^* - \mathbf{N}_2^*$  is the dimensionless local current density vector. The diffusion and steric contributions  $\dot{q}_{E,d}$  and  $\dot{q}_{E,s}$  [Equation (4.22)] are expressed in dimensionless form as

$$\dot{q}_{E,d}^* = \frac{\mathbf{j}^* \cdot \nabla^*(c_1^* - c_2^*)}{c_1^* + c_2^*} \quad \text{and} \quad \dot{q}_{E,s}^* = \frac{\mathbf{j}^* \cdot \nabla^*(c_1^* + c_2^*)}{c_1^* + c_2^*} \frac{(c_1^* - c_2^*)\nu_p/2}{[1 - (c_1^* + c_2^*)\nu_p/2]} \quad (6.8)$$

while the heat of mixing contributions  $\dot{q}_{S,c}$  and  $\dot{q}_{S,T}$  [Equation (4.25)] can be non-dimensionalized as

$$\begin{aligned} \dot{q}_{S,c}^* &= \frac{3}{32\sqrt{2}\pi} \frac{a^{*3}}{\nu_p} \frac{(\mathbf{N}_1^* + \mathbf{N}_2^*) \cdot \nabla^*(c_1^* + c_2^*)}{(c_1^* + c_2^*)^{1/2}}, \\ \text{and} \quad \dot{q}_{S,T}^* &= -\frac{3}{32\sqrt{2}\pi} \frac{a^{*3}}{\nu_p} (\mathbf{N}_1^* + \mathbf{N}_2^*)(c_1^* + c_2^*)^{1/2} \cdot \nabla^* T^*. \end{aligned} \quad (6.9)$$

Here,  $a^* = a/\lambda_D$  is the dimensionless effective ion diameter.

### 6.2.4 Dimensionless initial and boundary conditions for planar electrodes

In 1D Cartesian coordinates, the initial conditions for the dimensionless variables  $\psi^*$ ,  $c_i^*$ , and  $T^*$  can be expressed as  $\psi^*(x^*, 0) = 0$ ,  $c_1^*(x^*, 0) = c_2^*(x^*, 0) = 1$ , and  $T^*(x^*, 0) = 0$ . Table 6.1 summarizes the dimensionless boundary conditions for  $\psi^*$ ,  $c_i^*$ , and  $T^*$  at the electrode/electrolyte and Stern/diffuse layer interfaces. The Stern layers for Electrodes A

Table 6.1: Dimensionless boundary conditions for thermally insulated EDLC with planar electrodes during galvanostatic cycling.

Interface	$\psi^*$	$c_i^*$	$T^*$
Electrode A/electrolyte ( $x^* = 0$ )	$-\frac{\partial^2 \psi^*}{\partial t^* \partial x^*} = \begin{cases} \frac{j_s^*}{2} & (n_c - 1)t_c^* \leq t^* < (n_c - 1/2)t_c^* \\ -\frac{j_s^*}{2} & (n_c - 1/2)t_c^* \leq t^* < n_c t_c^* \end{cases}$		$\frac{\partial T^*}{\partial x^*} = 0$
Stern/diffuse layer A ( $x^* = a^*/2$ )	$\psi^* \left( \frac{a^{*-}}{2}, t^* \right) = \psi^* \left( \frac{a^{*+}}{2}, t^* \right)$ $\frac{\partial \psi^*}{\partial x^*} \left( \frac{a^{*-}}{2}, t^* \right) = \frac{\partial \psi^*}{\partial x^*} \left( \frac{a^{*+}}{2}, t^* \right)$	$N_i^* = 0$	$T^* \left( \frac{a^{*-}}{2}, t^* \right) = T^* \left( \frac{a^{*+}}{2}, t^* \right)$ $\frac{\partial T^*}{\partial x^*} \left( \frac{a^{*-}}{2}, t^* \right) = \frac{\partial T^*}{\partial x^*} \left( \frac{a^{*+}}{2}, t^* \right)$
Stern/diffuse layer B ( $x^* = 2L^* - a^*/2$ )	$\psi^* \left( 2L^* - \frac{a^{*-}}{2}, t^* \right) = \psi^* \left( 2L^* - \frac{a^{*+}}{2}, t^* \right)$ $\frac{\partial \psi^*}{\partial x^*} \left( 2L^* - \frac{a^{*-}}{2}, t^* \right) = \frac{\partial \psi^*}{\partial x^*} \left( 2L^* - \frac{a^{*+}}{2}, t^* \right)$	$N_i^* = 0$	$T^* \left( 2L^* - \frac{a^{*-}}{2}, t^* \right) = T^* \left( 2L^* - \frac{a^{*+}}{2}, t^* \right)$ $\frac{\partial T^*}{\partial x^*} \left( 2L^* - \frac{a^{*-}}{2}, t^* \right) = \frac{\partial T^*}{\partial x^*} \left( 2L^* - \frac{a^{*+}}{2}, t^* \right)$
Electrode B/electrolyte ( $x^* = 2L^*$ )	$\psi^* = 0$		$\frac{\partial T^*}{\partial x^*} = 0$

and B are located at  $0 \leq x^* < a^*/2$  and  $(2L^* - a^*/2) < x^* \leq 2L^*$ , respectively, where  $L^* = L/\lambda_D$  is the dimensionless inter-electrode half-width. The diffuse layer is the region  $a^*/2 \leq x^* \leq 2L^* - a^*/2$ . Here,  $j_s^* = j_s/(zFDc_\infty/\lambda_D)$  is the dimensionless current density imposed at the electrode surface and  $t_c^* = t_c/(\lambda_D^2/D)$  is the dimensionless cycle period.

### 6.2.5 Physical interpretation

The solution of the governing Equations (2.5), (2.6), and (2.12) and their initial and boundary conditions for galvanostatic cycling of planar EDLCs with binary and symmetric electrolyte depended on twelve parameters, namely  $z$ ,  $a$ ,  $D$ ,  $\epsilon_r$ ,  $\rho$ ,  $c_p$ ,  $k$ ,  $c_\infty$ ,  $L$ ,  $T_0$ ,  $j_s$ , and  $t_c$ . The scaling analysis of these equations and their initial and boundary conditions revealed that the dimensionless variables  $\psi^*$ ,  $c_i^*$ , and  $T^*$  depended on only seven dimensionless similarity parameters expressed as

$$\begin{aligned} a^* &= \frac{a}{\lambda_D}, \quad L^* = \frac{L}{\lambda_D}, \quad j_s^* = \frac{j_s}{zFDc_\infty/\lambda_D}, \quad t_c^* = \frac{t_c}{\lambda_D^2/D} \\ \nu_p &= \frac{2c_\infty}{c_{max}}, \quad Le = \frac{\alpha_{th}}{D}, \quad \text{and} \quad C^* = \frac{\rho c_p}{R_u c_\infty}. \end{aligned} \quad (6.10)$$

The dimensionless numbers  $a^*$  and  $L^*$  scale the Stern layer thickness and the inter-electrode distance by the Debye length, respectively. The dimensionless current density  $j_s^*$  scales the imposed current density at the electrode by a characteristic diffusion current density driven by a concentration gradient from  $c_\infty$  to 0 mol L<sup>-1</sup> across the Debye length  $\lambda_D$  (equal to the concentration drop of the coion across the EDL). In addition,  $t_c^*$  is the ratio of the cycle period to the characteristic time  $\tau_d = \lambda_D^2/D$  for ion diffusion across the Debye length. The Lewis number  $Le$  can be interpreted as the ratio of the characteristic time for ion diffusion  $\tau_d = \lambda_D^2/D$  to that for heat diffusion  $\tau_{th} = \lambda_D^2/\alpha_{th}$ . The dimensionless heat capacity  $C^*$  represents the ratio of the volumetric heat capacity  $\rho c_p$  of the solvent to that of the ions at bulk concentration  $R_u c_\infty$ , both expressed in J m<sup>-3</sup>K<sup>-1</sup>. Note that  $a^*$ ,  $L^*$ ,  $\nu_p$ ,  $Le$ , and  $C^*$  are defined in the same way as in Chapter 3 [Equation (3.22)].

Finally,  $\psi^*(x^*, t^*)$  and  $c_i^*(x^*, t^*)$  are functions of the dimensionless similarity parameters  $a^*$ ,  $L^*$ ,  $j_s^*$ ,  $t_c^*$ , and  $\nu_p$  only. On the other hand, the Lewis number  $Le$  and the dimensionless heat capacity  $C^*$  govern the transient dimensionless temperature response  $T^*(x^*, t^*)$  for a

given dimensionless volumetric heat generation rate. Since the dimensionless volumetric heat generation rates  $\dot{q}_{J,irr}^*$ ,  $\dot{q}_{E,d}^*$ ,  $\dot{q}_{E,s}^*$ , and  $\dot{q}_{S,c}^*$  do not depend on  $T^*$ ,  $Le$ , or  $C^*$ , they should also be functions of the five parameters  $a^*$ ,  $L^*$ ,  $j_s^*$ ,  $t_c^*$ , and  $\nu_p$ .

## 6.2.6 Numerical simulations

### 6.2.6.1 Method of solution

The governing Equations (2.5), (2.6), and (2.12) were solved numerically in dimensional form using the same method and convergence criteria described in Section 4.1.5.

### 6.2.6.2 Data processing

As in Chapter 5, the temperature evolution can be characterized by the irreversible temperature rise  $T_{irr}$ , the temperature oscillation amplitude  $\Delta T_{rev}$ , and the cycle period  $t_c$  [2]. The irreversible temperature rise  $T_{irr}$  corresponds to the temperature that would result from irreversible Joule heating alone. Chapter 4 showed that  $\dot{q}_{J,irr}$  was uniform through the electrolyte and equal to

$$\dot{q}_{J,irr} = \frac{j_s^2}{\sigma_\infty} \quad (6.11)$$

where  $\sigma_\infty = 2Dz^2F^2c_\infty/R_uT_0$  is the electrolyte conductivity at the bulk concentration  $c_1 = c_2 = c_\infty$ . Thus, for thermally insulated electrode/electrolyte interfaces,  $T_{irr}$  was also uniform and expressed as

$$T_{irr}(t) = T_0 + \frac{\dot{q}_{J,irr}}{\rho c_p} t = T_0 + \frac{j_s^2}{\rho c_p \sigma_\infty} t. \quad (6.12)$$

The irreversible volumetric heat generation rate and the irreversible temperature rise given by Equations (6.11) and (6.12), respectively, are expressed in dimensionless form as

$$\dot{q}_{J,irr}^* = \frac{\dot{q}_{J,irr}}{R_u T_0 D c_\infty / \lambda_D^2} = \frac{j_s^{*2}}{2} \quad (6.13)$$

$$\text{and} \quad T_{irr}^*(t^*) = \frac{T_{irr}(t) - T_0}{T_0} = \frac{\dot{q}_{J,irr}}{C^*} t^* = \frac{j_s^{*2}}{2C^*} t^*. \quad (6.14)$$

The temperature oscillations  $T_{rev}(x, t)$  associated with the reversible heating can be evaluated by subtracting the irreversible temperature rise  $T_{irr}(t)$  from the temperature  $T(x, t)$ ,

i.e.,  $T_{rev}(x, t) = T(x, t) - T_{irr}(t)$ . The temperature oscillations varied with location  $x$  due to the non-uniformity of  $\dot{q}_{rev}$  [2]. For temperature-independent electrolyte properties and ion transport,  $T_{rev}(x, t)$  was a periodic function of  $t$ . In the present study, the oscillation amplitude  $\Delta T_{rev}(x)$  was evaluated at the Stern/diffuse layer interface where it was found to be the largest [2]. It was defined as  $\Delta T_{rev}(a/2) = \max_{t_c \leq t \leq 2t_c} [T_{rev}(a/2, t)] - \min_{t_c \leq t \leq 2t_c} [T_{rev}(a/2, t)]$  and was an unknown function of the twelve parameters characterizing the electrolyte, inter-electrode spacing, and cycling conditions. In dimensionless form, the reversible temperature evolution and the oscillation amplitude are expressed as  $T_{rev}^*(x^*, t^*) = T_{rev}(x, t)/T_0 = T^*(x^*, t^*) - T_{irr}^*(t^*)$  and  $\Delta T_{rev}^*(a^*/2) = \Delta T_{rev}(a/2)/T_0$ . Based on the above dimensional analysis, one can show that  $\Delta T_{rev}^*$  is a function of the seven similarity parameters identified in Equation (6.10). The parameters  $j_s^*$  and  $\nu_p$  do not affect  $\Delta T_{rev}^*$  directly, but they affect the value of  $\dot{q}_{rev}^*$ . A correlation relating  $\Delta T_{rev}^*$  to these seven parameters would enable estimation of the EDLC temperature evolution for various design and operating parameters without performing complex and time-consuming numerical simulations [2].

Finally, the reversible heat generation rate was characterized by the total amount of reversible heat  $Q_{rev}''$  generated per unit electrode surface area during a complete charging step (in  $\text{J m}^{-2}$ ). Here,  $Q_{rev}''$  comprises the sum of all reversible contributions such that  $Q_{rev}'' = Q_{E,d}'' + Q_{E,s}'' + Q_{S,c}''$ . Individual  $Q_i''$  were computed by integrating the corresponding local volumetric heat generation rate  $\dot{q}_i(x, t)$  spatially over the electrolyte domain  $0 \leq x \leq 2L$  and temporally over one charging step  $t_c \leq t \leq 3t_c/2$  so that

$$Q_i'' = \int_{t_c}^{3t_c/2} \int_0^{2L} \dot{q}_i(x, t) dx dt. \quad (6.15)$$

Here, the time integral was taken over the second charging step in the simulation, i.e.,  $t_c \leq t \leq 3t_c/2$ , to avoid start-up effects occurring near  $t = 0$ . Longer simulations showed that two cycles were sufficient to reach oscillatory steady state. In dimensionless form, each individual contribution to the reversible heat generation is expressed as

$$Q_i^* = \frac{Q_i''}{R_u T_0 c_\infty \lambda_D} = \int_{t_c^*}^{3t_c^*/2} \int_0^{2L^*} \dot{q}_i^*(x^*, t^*) dx^* dt^*. \quad (6.16)$$

Note that  $Q_{S,T}''$  was ignored because its contribution to the total  $Q_{rev}''$  was negligible for all cases considered. During the corresponding discharging step ( $3t_c/2 \leq t \leq 2t_c$ ), the

Table 6.2: Input parameters for Cases 1 to 3 used to illustrate the scaling analysis. The dimensionless parameters  $a^* = 2.4$ ,  $L^* = 7.2 \times 10^4$ ,  $j_s^* = 2.4 \times 10^{-6}$ ,  $t_c^* = 2.2 \times 10^7$ ,  $\nu_p = 0.38$ ,  $Le = 374$ , and  $C^* = 310$  are the same for all three cases.

	Case 1	Case 2	Case 3
$z$	1	1	2
$a$ (nm)	0.68	0.34	1.36
$D$ ( $\text{m}^2 \text{s}^{-1}$ )	$1.7 \times 10^{-10}$	$1.7 \times 10^{-10}$	$3.4 \times 10^{-10}$
$\epsilon_r$	66.1	88.2	66.1
$\rho$ ( $\text{kg m}^{-3}$ )	1205	2409	602
$c_p$ ( $\text{J kg}^{-1}\text{K}^{-1}$ )	2141	8564	535
$k$ ( $\text{W m}^{-1}\text{K}^{-1}$ )	0.16	1.3	0.041
$c_\infty$ ( $\text{mol L}^{-1}$ )	1.0	8.0	0.125
$L$ ( $\mu\text{m}$ )	20	10	40
$T_0$ (K)	298	447	596
$j_s$ ( $\text{mA cm}^{-2}$ )	14	224	3.5
$t_c$ (ms)	10	2.5	20

energy  $-Q_i''$  was consumed so that the net reversible heat generation over a complete charging/discharging cycle was zero.

## 6.3 Results and discussion

### 6.3.1 Illustration of scaling analysis

Table 6.2 summarizes three sets of input parameters used to illustrate the scaling analysis. Case 1 was based on the properties of tetraethylammonium tetrafluoroborate ( $\text{TEABF}_4$ ) electrolyte at  $1 \text{ mol L}^{-1}$  in propylene carbonate (PC) solvent. This electrolyte was treated as binary and symmetric. The ions  $\text{TEA}^+$  ( $i = 1$ ) and  $\text{BF}_4^-$  ( $i = 2$ ) have valency  $z_1 = -z_2 = 1$ . Their effective diameter was taken as that of non-solvated  $\text{TEA}^+$  ions, i.e.,  $a = 0.68 \text{ nm}$  [48, 92]. In fact, Wang and Pilon [48] found that using this ion diameter resulted in integral



capacitance predictions for ordered bimodal mesoporous carbon electrodes that agreed well with experimental data. The dielectric constant  $\epsilon_r$ , thermal conductivity  $k$ , density  $\rho$ , and specific heat  $c_p$  were taken as the properties of the PC solvent [94, 100]. The ion diffusion coefficient  $D$  was estimated from the experimentally measured electrical conductivity  $\sigma$  for a concentration of  $c_1 = c_2 = c_\infty = 1$  mol/L using the expression given in Equation (2.4) [93]. The electrolyte properties  $\epsilon_r$ ,  $k$ ,  $\rho$ ,  $c_p$ , and  $\sigma$  were measured at temperatures within 5 K of the simulated initial temperature  $T_0 = 298$  K [93, 94, 100]. The inter-electrode half-width  $L = 20$   $\mu\text{m}$  fell within the range reported in experimental studies of EDLCs [77, 78]. Similarly, the current density  $j_s = 14$  mA cm<sup>-2</sup> was within the typical range of current densities per unit separator surface area [29, 78]. The cycle period  $t_c = 10$  ms was selected to yield a maximum voltage of  $\psi(0, t) - \psi(2L, t) = 2.5$  V chosen by analogy with the operating voltages of many commercial EDLCs using organic electrolytes [10, 12]. Note that planar electrodes charge very rapidly compared to porous electrodes, resulting in a significantly shorter cycle period.

The dimensionless numbers associated with Case 1 were  $a^* = 2.4$ ,  $L^* = 7.2 \times 10^4$ ,  $j_s^* = 2.4 \times 10^{-6}$ ,  $t_c^* = 2.2 \times 10^7$ ,  $\nu_p = 0.38$ ,  $Le = 374$ , and  $C^* = 310$ . The dimensionless governing Equations (6.3), (6.4), and (6.6) and their associated initial and boundary conditions indicate that the dimensionless solution for  $\psi^*$ ,  $c_1^*$ ,  $c_2^*$ , and  $T^*$  depends only on the seven dimensionless numbers defined in Equation (6.10). To illustrate this, the twelve input parameters  $z$ ,  $a$ ,  $D$ ,  $\epsilon_r$ ,  $\rho$ ,  $c_p$ ,  $k$ ,  $c_\infty$ ,  $L$ ,  $T_0$ ,  $j_s$ , and  $t_c$  for Cases 2 and 3 were all varied arbitrarily, while the seven dimensionless numbers  $a^*$ ,  $L^*$ ,  $j_s^*$ ,  $t_c^*$ ,  $\nu_p$ ,  $Le$ , and  $C^*$  remained identical for Cases 1 to 3.

### 6.3.1.1 Dimensionless potential

Figure 6.1(a) shows the computed electric potential  $\psi(0, t)$  at the surface of Electrode A as a function of time  $t$  during two consecutive galvanostatic cycles for Cases 1 to 3. As expected, the surface potential increased during charging and decreased during discharging. The temporal evolution of  $\psi(0, t)$  and/or its peak value differed among the three cases considered. As previously mentioned, Case 1 featured realistic electrolyte properties and

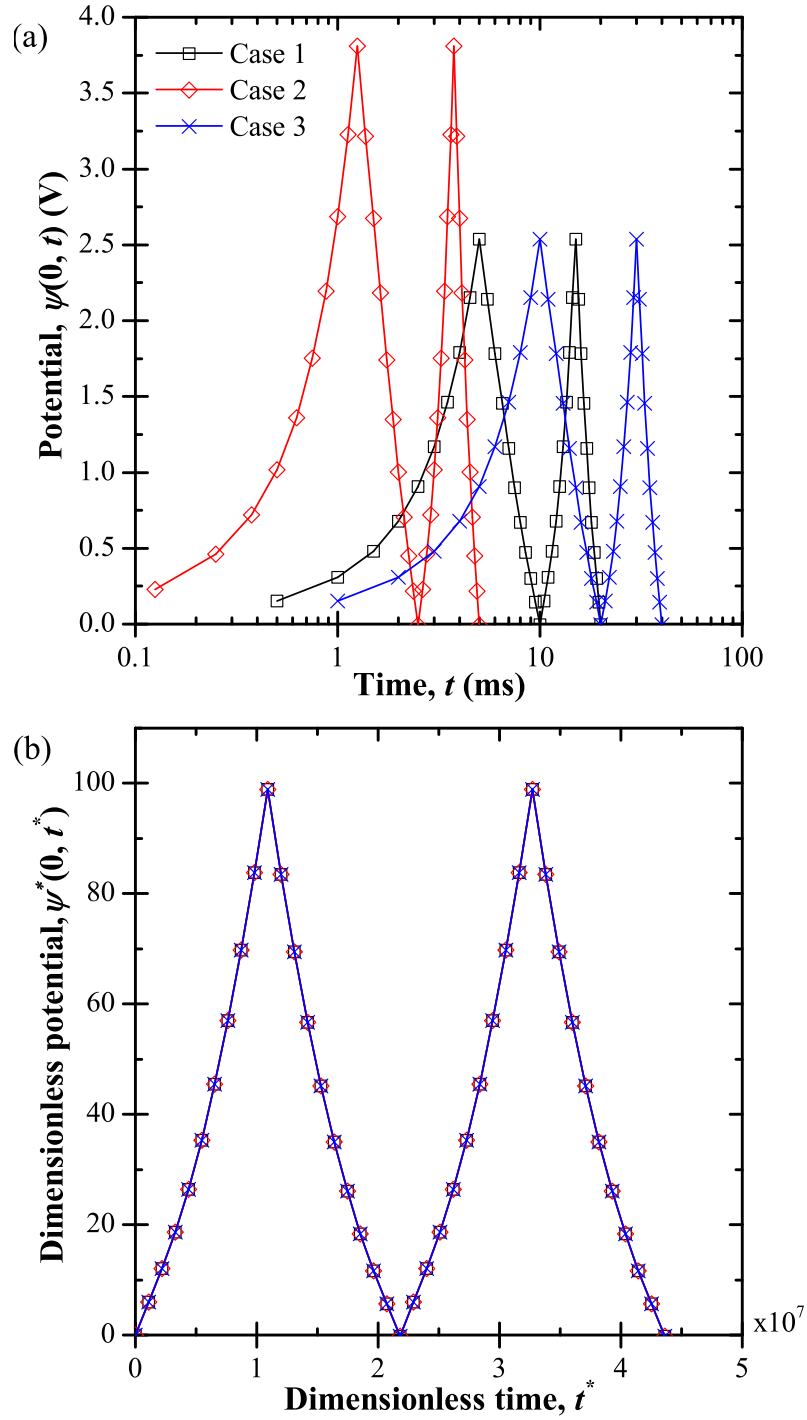


Figure 6.1: Computed (a) electric potential  $\psi(0, t)$  at the surface of Electrode A as a function of time  $t$  and (b) dimensionless electric potential  $\psi^*(0, t^*)$  as a function of dimensionless time  $t^*$  during two consecutive galvanostatic charging/discharging cycles for Cases 1 to 3 (Table 6.2).

cycling conditions resulting in a maximum surface potential of 2.5 V. On the other hand, the surface potential in Case 2 reached values in excess of 3.7 V due to the different properties of a hypothetical electrolyte chosen to maintain the same dimensionless similarity parameters as in Case 1. Figure 6.1(b) plots the same data shown in Figure 6.1(a) in terms of dimensionless potential  $\psi^*(0, t^*)$  as a function of dimensionless time  $t^*$ . It is evident that the dimensionless data for all three cases collapsed onto a single curve. Similar results were obtained at any arbitrary location in the domain (not shown).

### 6.3.1.2 Dimensionless concentration

Similarly, Figure 6.2(a) shows the computed anion concentration  $c_2(a/2, t)$  at the Stern/diffuse layer interface near Electrode A as a function of time  $t$  for Cases 1 to 3. The computed maximum values of  $c_2(a/2, t)$  for the different cases varied by nearly two orders of magnitude. This can be attributed to the differences in ion diameter  $a$  between the different cases causing large differences in  $c_{max}$ . Figure 6.2(b) presents the same data in dimensionless form as  $c_2^*(a^*/2, t^*)$  versus  $t^*$ . Here also, the computed dimensionless concentration  $c_2^*(a^*/2, t^*)$  at the Stern/diffuse layer interface as a function of  $t^*$  collapsed onto a single curve for the three different cases considered. The maximum dimensionless concentration  $c_{max}^*$  was determined by the packing parameter  $\nu_p$  as  $c_{max}^* = 2/\nu_p$ . Similar results were obtained at other locations in the domain as well as for the cation concentration  $c_1(x, t)$  and  $c_1^*(x^*, t^*)$  (not shown).

### 6.3.1.3 Dimensionless temperature

Finally, Figures 6.3(a) and 6.3(b) show the temporal evolution of the computed temperature change  $T(a/2, t) - T_0$  at the Stern/diffuse layer interface and  $T(L, t) - T_0$  at the centerline, respectively. Temperature oscillations about an overall temperature rise were evident at each location. Figures 6.3(c) and 6.3(d) show the same data but in dimensionless form. Here also, the dimensionless temperatures  $T^*(a^*/2, t^*)$  and  $T^*(L^*, t^*)$  for all three cases considered collapsed onto a single curve. Similar results were obtained at other locations in the domain (not shown). Figure 6.3(c) also shows the irreversible temperature rise  $T_{irr}^*(t^*)$  associated

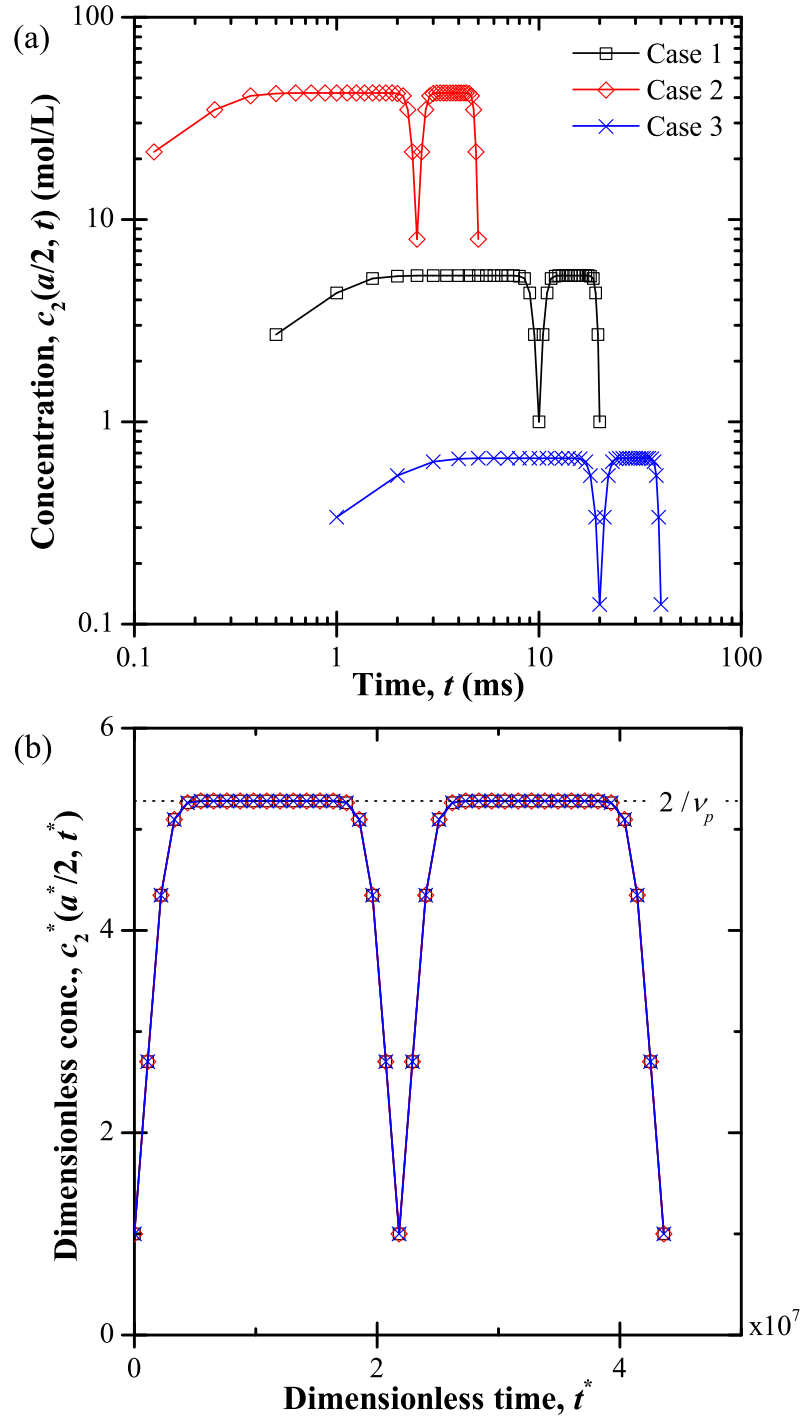


Figure 6.2: Computed (a) anion concentration  $c_2(a/2, t)$  at the Stern/diffuse layer interface as a function of time  $t$  and (b) dimensionless anion concentration  $c_2^*(a^*/2, t^*)$  as a function of dimensionless time  $t^*$  during two consecutive galvanostatic charging/discharging cycles for Cases 1 to 3 (Table 6.2).

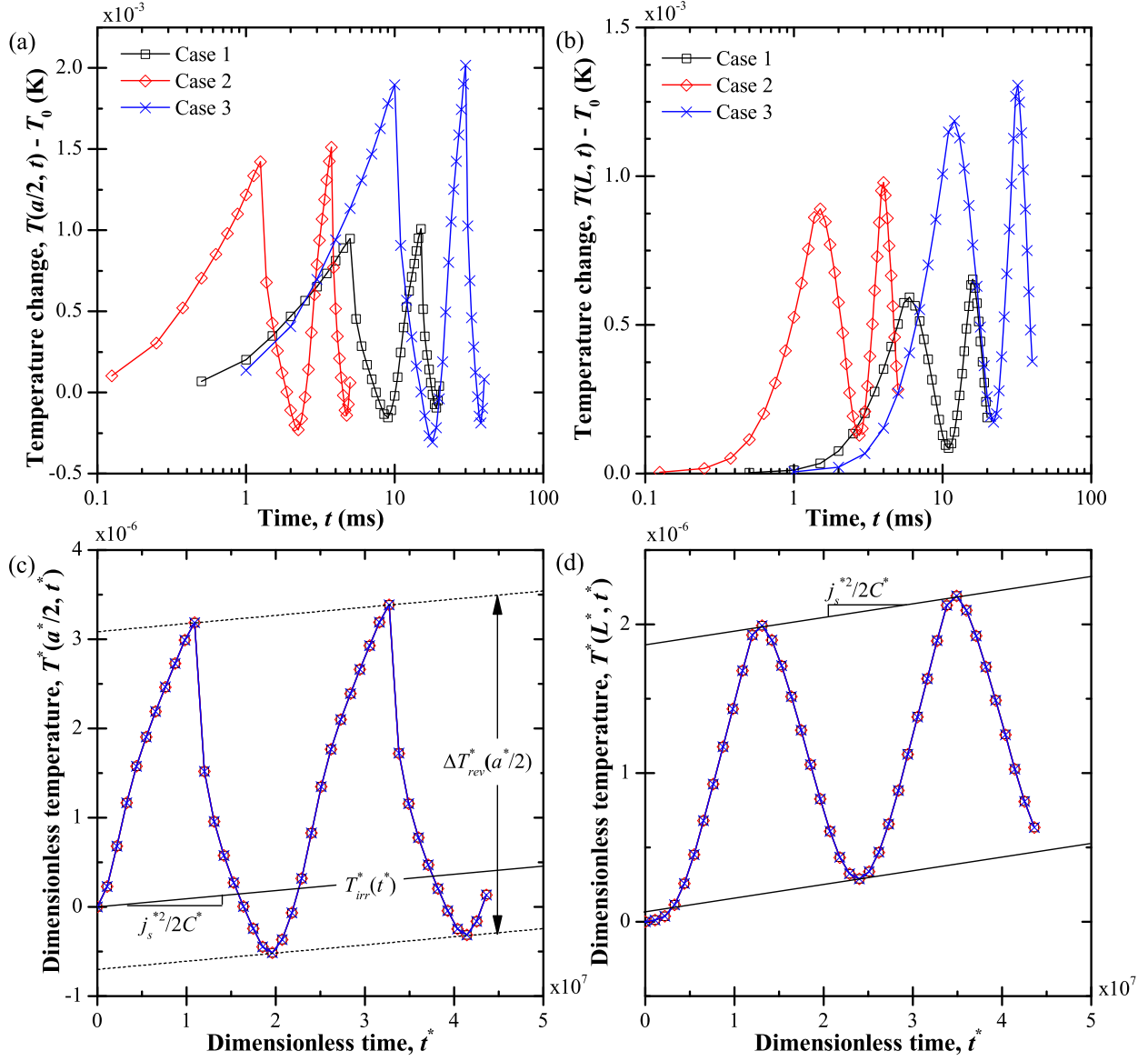


Figure 6.3: Computed temperature change (a)  $T(a/2, t) - T_0$  at the Stern/diffuse layer interface and (b)  $T(L, t) - T_0$  at the centerline as functions of time  $t$  as well as dimensionless temperature change (c)  $T^*(a^*/2, t^*)$  and (d)  $T^*(L^*, t^*)$  as functions of dimensionless time  $t^*$  during two consecutive galvanostatic charging/discharging cycles for Cases 1 to 3 (Table 6.2).

Table 6.3: Baseline values of the seven dimensionless similarity parameters used in Figure 6.4 to develop the correlation for  $\Delta T_{rev}^*$  given by Equation (6.17).

	Case 1	Case 4	Case 5
$a^*$	2.4	1.6	6.1
$L^*$	$7.2 \times 10^4$	$4.7 \times 10^4$	$1.4 \times 10^5$
$j_s^*$	$2.4 \times 10^{-6}$	$8.7 \times 10^{-6}$	$6.0 \times 10^{-7}$
$t_c^*$	$2.2 \times 10^7$	$9.2 \times 10^6$	$4.4 \times 10^7$
$\nu_p$	0.38	0.16	0.74
$Le$	374	748	281
$C^*$	310	735	233

with irreversible Joule heating and given by Equation (6.13) as well as the temperature oscillation amplitude  $\Delta T_{rev}^*(a^*/2)$  associated with reversible heating. As expected, the slope of the overall dimensionless temperature rise was given by  $j_s^{*2}/2C^*$ .

Overall, these results illustrate the scaling analysis performed on the coupled MPNP and energy conservation equations and their initial and boundary conditions for EDLCs with binary and symmetric electrolytes under galvanostatic cycling. The dimensionless variables  $\psi^*(x^*, t^*)$ ,  $c_i^*(x^*, t^*)$ , and  $T^*(x^*, t^*)$  depended only on the seven similarity parameters  $a^*$ ,  $L^*$ ,  $j_s^*$ ,  $t_c^*$ ,  $\nu_p$ ,  $Le$ , and  $C^*$ . The same observations were made for the dimensionless local volumetric heat generation rates  $\dot{q}_{irr}^*$  and  $\dot{q}_{rev}^*$  (see Appendix A).

### 6.3.2 Scaling laws for thermal effects

#### 6.3.2.1 Temperature oscillation amplitude

Table 6.3 summarizes three baseline sets of dimensionless similarity parameters used to develop scaling laws for  $\Delta T_{rev}^*$ . Case 1 corresponds to the similarity parameters for 1 mol L<sup>-1</sup> TEABF<sub>4</sub> in PC solvent, previously used to illustrate the scaling analysis. Cases 4 and 5 feature different values of  $a^*$ ,  $L^*$ ,  $j_s^*$ ,  $t_c^*$ ,  $\nu_p$ ,  $Le$ , and  $C^*$ .

Figure 6.4(a) shows  $\Delta T_{rev}^*(a^*/2)$  as a function of the dimensionless heat capacity  $C^*$

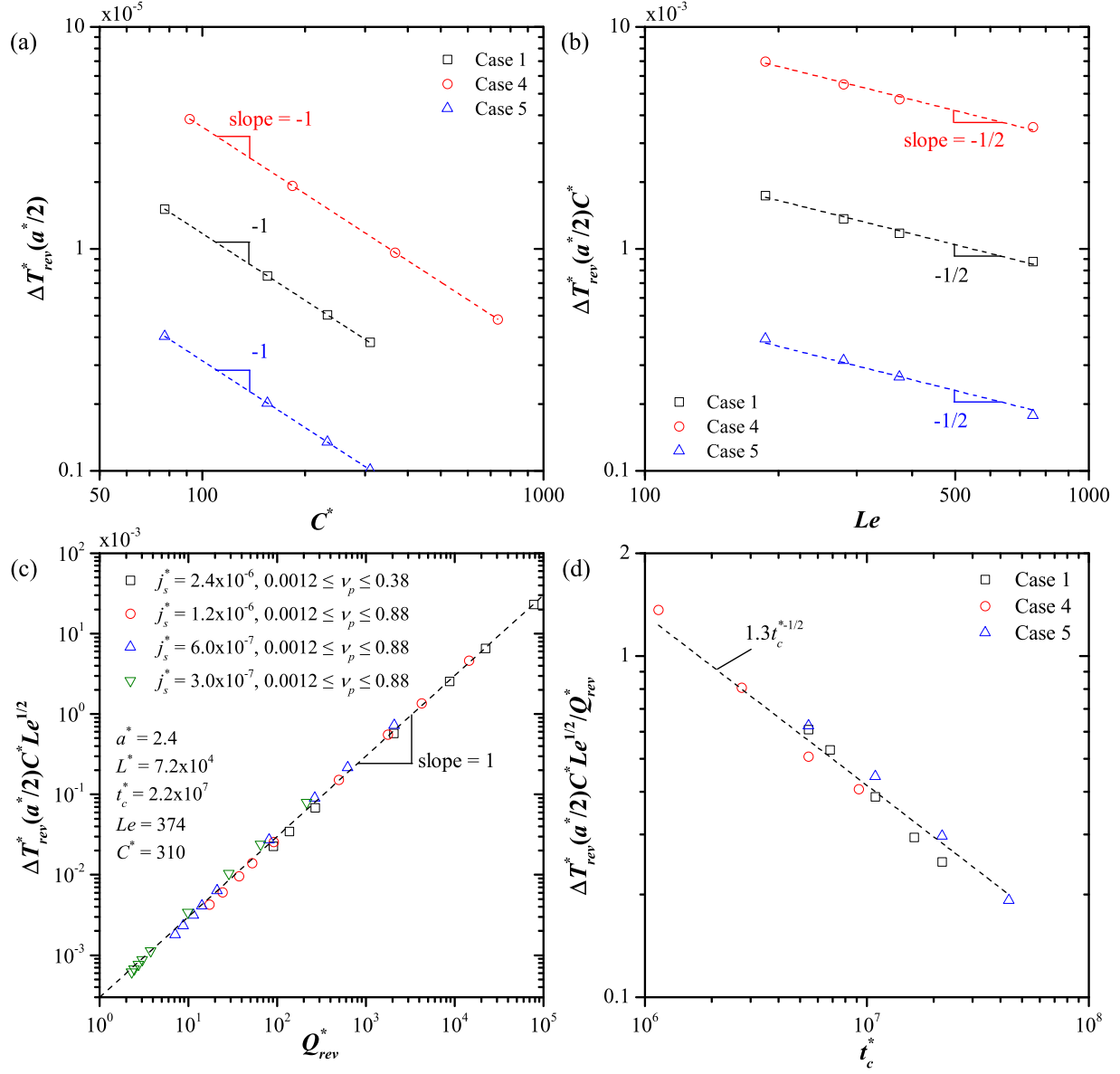


Figure 6.4: Computed values of (a)  $\Delta T_{rev}^*(a^*/2)$  as a function of  $C^*$ , (b)  $\Delta T_{rev}^*(a^*/2)C^*$  as a function of  $Le$ , (c)  $\Delta T_{rev}^*(a^*/2)C^*Le^{1/2}$  as a function of  $Q_{rev}^*$ , and (d)  $\Delta T_{rev}^*(a^*/2)C^*Le^{1/2}/Q_{rev}^*$  as a function of  $t_c^*$ .

varying from 78 to 735 while the other six relevant dimensionless similarity parameters are provided in Table 6.3. Since the reversible heat generation  $Q_{rev}^*$  does not depend on  $C^*$ , it remained identical for all points in each case. Figure 6.4(a) indicates that  $\Delta T_{rev}^*(a^*/2)$  was proportional to  $1/C^*$ . Note that this was consistent with the expression of  $T_{irr}^*$  given by Equation (6.13).

Figure 6.4(b) plots  $\Delta T_{rev}^*(a^*/2)C^*$  as a function of the Lewis number  $Le$  ranging from 187 to 748. Here also, the similarity parameters other than  $Le$  are given in Table 6.3. Figure 6.4(b) reveals that  $\Delta T_{rev}^*(a^*/2)C^*$  was proportional to  $1/Le^{1/2}$ . As previously mentioned, large Lewis numbers correspond to rapid heat diffusion compared to mass diffusion. Thus,  $\Delta T_{rev}^*(a^*/2)$  at the Stern/diffuse layer interface decreased as  $Le$  increased due to the increased rate of heat diffusion within the electrolyte.

Figure 6.4(c) plots  $\Delta T_{rev}^*(a^*/2)C^*Le^{1/2}$  as a function of  $Q_{rev}^*$  computed numerically for various values of  $j_s^*$  and  $\nu_p$  in the ranges  $3 \times 10^{-7} \leq j_s^* \leq 2.4 \times 10^{-6}$  and  $0.0012 \leq \nu_p \leq 0.88$ . It confirms that  $\Delta T_{rev}^*(a^*/2)C^*Le^{1/2}$  was linearly proportional to  $Q_{rev}^*$ .

Figure 6.4(d) shows  $\Delta T_{rev}^*(a^*/2)C^*Le^{1/2}/Q_{rev}^*$  as a function of the cycle period  $t_c^*$  ranging from  $1.2 \times 10^6$  to  $4.4 \times 10^7$  with all other parameters given by Table 6.3. It indicates that  $\Delta T_{rev}^*(a^*/2)C^*Le^{1/2}/Q_{rev}^*$  was proportional to  $1/t_c^{*1/2}$  and that all cases fell on a single curve. In fact, charging over a longer cycle period  $t_c^*$  allows more time for the heat generated to dissipate from the EDL region to the bulk electrolyte, thus reducing the maximum oscillation amplitude.

Finally, the ratio  $\Delta T_{rev}^*(a^*/2)C^*Le^{1/2}t_c^{*1/2}/Q_{rev}^*$  was found to be independent of  $a^*$  and varied negligibly with  $L^*$  (see Appendix A). It was approximately constant and equal to 1.3 so that the dimensionless temperature oscillation amplitude was given by

$$\Delta T_{rev}^*(a^*/2) = 1.3 \frac{Q_{rev}^*}{t_c^{*1/2} Le^{1/2} C^*} = 1.3 \frac{Q_{E,d}^* + Q_{E,s}^* + Q_{S,c}^*}{t_c^{*1/2} Le^{1/2} C^*}. \quad (6.17)$$

It can be expressed in dimensional form as

$$\Delta T_{rev}(a/2) = 1.3 \frac{Q_{rev}''}{(t_c k \rho c_p)^{1/2}}. \quad (6.18)$$

The temperature oscillation amplitude  $\Delta T_{rev}(a/2)$  increased with increasing amount of re-



versible heat generated during the charging step  $Q''_{rev}$  and with decreasing cycle period  $t_c$ , as well as decreasing electrolyte thermal effusivity defined as  $e_{th} = (k\rho c_p)^{1/2}$ . The latter represents the rate at which the electrolyte can absorb heat from its surroundings [101].

### 6.3.2.2 Heat generation

The scaling analysis of Section 6.2.3 indicated that the dimensionless volumetric heat generation rates  $\dot{q}_{E,d}^*$ ,  $\dot{q}_{E,s}^*$ , and  $\dot{q}_{S,c}^*$  were functions of  $a^*$ ,  $L^*$ ,  $j_s^*$ ,  $t_c^*$ , and  $\nu_p$  only. This section aims to derive scaling laws for  $Q_{E,d}^*$ ,  $Q_{E,s}^*$ , and  $Q_{S,c}^*$  as functions of these five similarity parameters to be used in Equation (6.17).

First, plotting  $Q_{E,d}^*$ ,  $Q_{E,s}^*$ , and  $Q_{S,c}^*$  as functions of  $L^*$  and  $a^*$  indicated that the dimensionless inter-electrode spacing  $L^*$  had no effect on  $Q_{E,d}^*$ ,  $Q_{E,s}^*$ , and  $Q_{S,c}^*$  (see Appendix A). Indeed, for sufficiently large  $L^*$ , i.e.,  $L^* \gg 1$ , the EDLs did not overlap, and the EDL concentration profiles, responsible for reversible heating, were independent of  $L^*$  as previously observed by Wang and Pilon [42, 43, 47]. In addition, the heat of mixing contribution  $Q_{S,c}^*$  was found to be proportional to  $a^{*3}$  while  $Q_{E,d}^*$  and  $Q_{E,s}^*$  were independent of  $a^*$ . This is consistent with the expressions for  $\dot{q}_{E,d}^*$ ,  $\dot{q}_{E,s}^*$ , and  $\dot{q}_{S,c}^*$  given by Equations (6.8) and (6.9). Plotting  $Q_{E,d}^*$  as a function of the dimensionless product  $j_s^* t_c^*$  for several combinations of  $\nu_p$ ,  $j_s^*$ , and  $t_c^*$  showed that predictions for the same values of  $\nu_p$  and  $j_s^* t_c^*$  overlapped despite featuring different values of  $j_s^*$  and  $t_c^*$ . This indicates that  $Q_{E,d}^*$  depended only on the product  $j_s^* t_c^*$  rather than on the individual parameters  $j_s^*$  and  $t_c^*$ . This was also true for  $Q_{E,s}^*$  and  $Q_{S,c}^*/a^{*3}$  (see Appendix A).

Figure 6.5(a) shows the reciprocal  $1/Q_{E,d}^*$  as a function of the packing parameter  $\nu_p$  for various values of  $j_s^* t_c^*$ . It indicates that  $1/Q_{E,d}^*$  was a linear function of  $\nu_p$  given by  $1/Q_{E,d}^* = A_{E,d}(j_s^* t_c^*)\nu_p + B_{E,d}(j_s^* t_c^*)$  where  $A_{E,d}$  and  $B_{E,d}$  are semi-empirical functions of  $j_s^* t_c^*$ . As  $\nu_p$  increased and steric effects became more significant,  $Q_{E,d}^*$  decreased, i.e.,  $1/Q_{E,d}^*$  increased. Figure 6.5(b) shows the fitting functions  $A_{E,d}$  and  $B_{E,d}$  as functions of the product  $j_s^* t_c^*$ . Both could be fitted as power law functions of  $j_s^* t_c^*$  so that  $A_{E,d} = 0.4(j_s^* t_c^*)^{-0.6}$  and

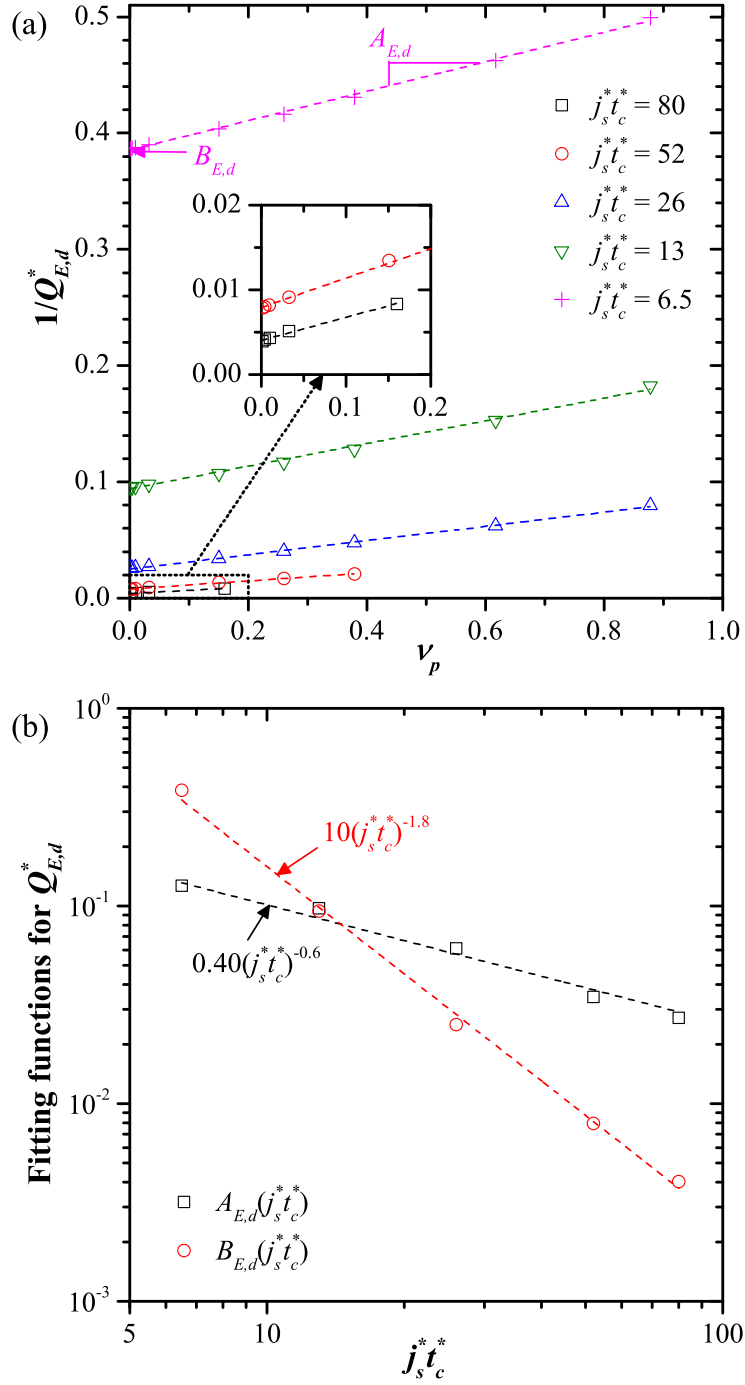


Figure 6.5: (a) Computed values of  $1/Q_{E,d}^*$  as a function of  $\nu_p$  for different values of  $j_s^* t_c^*$  along with curve fits of the form  $1/Q_{E,d}^* = A_{E,d}\nu_p + B_{E,d}$  [Equation (6.19)] and (b) fitting functions  $A_{E,d}$  and  $B_{E,d}$  versus  $j_s^* t_c^*$ .

$B_{E,d} = 10(j_s^* t_c^*)^{-1.8}$ . This yielded the correlation for  $Q_{E,d}^*$

$$Q_{E,d}^* = \frac{1}{10(j_s^* t_c^*)^{-1.8} + 0.4(j_s^* t_c^*)^{-0.6} \nu_p}. \quad (6.19)$$

Note that in the limiting case when  $\nu_p$  approaches zero,  $Q_{E,d}^* = 0.1(j_s^* t_c^*)^{1.8}$ . This corresponds to cases when ions can be treated as point charges whose transport is governed by the Poisson-Nernst-Planck model [38].

Similarly, Figure 6.6(a) plots  $Q_{E,s}^*$  as a function of the packing parameter  $\nu_p$  for different values of  $j_s^* t_c^*$ . It indicates that  $Q_{E,s}^*$  was (i) linearly proportional to  $\nu_p$  for small values of  $\nu_p$  and (ii) inversely proportional to  $\nu_p$  as  $\nu_p$  approached 1. The dashed lines are curve fits of the form  $Q_{E,s}^* = [1/(A_{E,s}(j_s^* t_c^*) \nu_p) + \nu_p/B_{E,s}(j_s^* t_c^*)]^{-1}$  where  $A_{E,s}$  and  $B_{E,s}$  are functions of the product  $j_s^* t_c^*$ . Figure 6.6(b) shows the fitting functions  $A_{E,s}$  and  $B_{E,s}$  versus  $j_s^* t_c^*$ . Both could be fitted as power laws such that  $A_{E,s} = (j_s^* t_c^*)^{3.3}/680$  and  $B_{E,s} = (j_s^* t_c^*)/6.7$ . Then, the correlation for  $Q_{E,s}^*$  can be written as

$$Q_{E,s}^* = \frac{1}{680(j_s^* t_c^*)^{-3.3} \nu_p^{-1} + 6.7(j_s^* t_c^*)^{-1} \nu_p}. \quad (6.20)$$

Finally, Figure 6.7(a) plots  $Q_{S,c}^*/a^{*3}$  as a function of  $\nu_p$  for various values of  $j_s^* t_c^*$ . It is evident that  $Q_{S,c}^*/a^{*3}$  (i) was inversely proportional to  $\nu_p$  when  $\nu_p$  was small and (ii) decreased steeply towards zero as  $\nu_p$  approached 1. In the latter case, the behavior of  $Q_{S,c}^*/a^{*3}$  can be estimated based on the expression for  $\dot{q}_{S,c}^*$  given by Equation (6.9) and indicating that  $\dot{q}_{S,c}^*$  was proportional to the concentration gradient  $\partial(c_1^* + c_2^*)/\partial x^*$ . This concentration gradient could be approximated in the limiting case when the dimensionless surface concentration is  $c_{max}^* = 2/\nu_p$ . Then, the dimensionless concentration sum  $c_1^* + c_2^*$  decreased from  $c_1^* + c_2^* = 2/\nu_p$  at the electrode surface to the bulk concentration  $c_1^* + c_2^* = 2$  over the EDL thickness ( $\Delta x^* \sim 1$ ) so that  $\partial(c_1^* + c_2^*)/\partial x^* \sim (1 - \nu_p)/\nu_p$ . Thus, Figure 6.7(b) plots  $Q_{S,c}^*/a^{*3}$  as a function of  $(1 - \nu_p)/\nu_p$ , along with dashed lines of slope 2 to guide the eye. It indicates that for small values of  $(1 - \nu_p)/\nu_p$ , i.e., for  $\nu_p$  approaching unity,  $Q_{S,c}^*/a^{*3}$  was proportional to  $[(1 - \nu_p)/\nu_p]^2$ . The data can be fitted with curve fits of the form  $Q_{S,c}^*/a^{*3} = [\nu_p/A_{S,c}(j_s^* t_c^*) + \nu_p^2/(1 - \nu_p)^2 B_{S,c}(j_s^* t_c^*)]^{-1}$  represented by the dashed lines in Figure 6.7(a). Figures 6.8(a) and 6.8(b) show the fitting functions  $A_{S,c}$  and  $B_{S,c}$ , respectively,

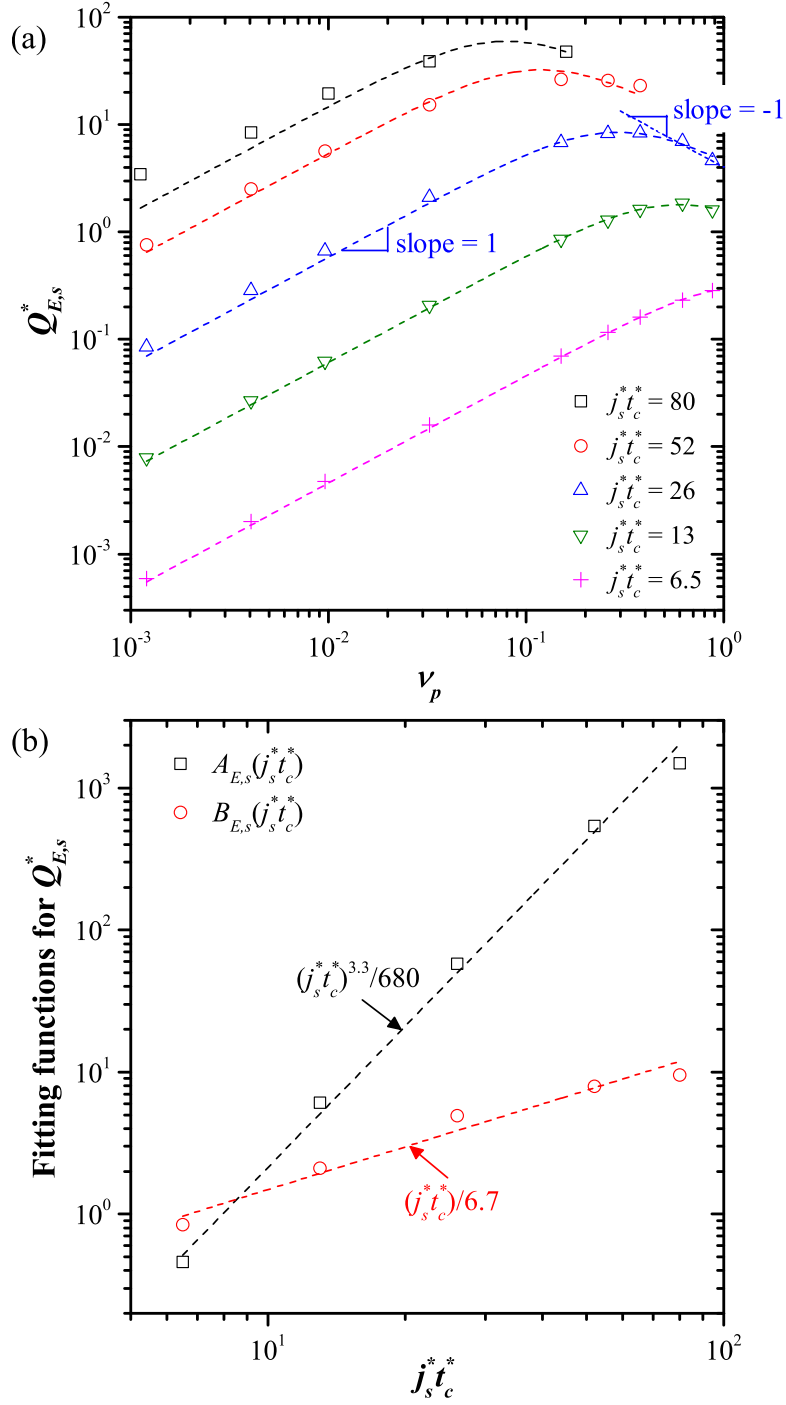


Figure 6.6: (a) Computed values of  $Q_{E,s}^*$  as a function of  $\nu_p$  for different values of  $j_s^* t_c^*$  along with curve fits of the form  $Q_{E,s}^* = [1/A_{E,s}\nu_p + \nu_p/B_{E,s}]^{-1}$  [Equation (6.20)] and (b) fitting functions  $A_{E,s}$  and  $B_{E,s}$  versus  $j_s^* t_c^*$ .

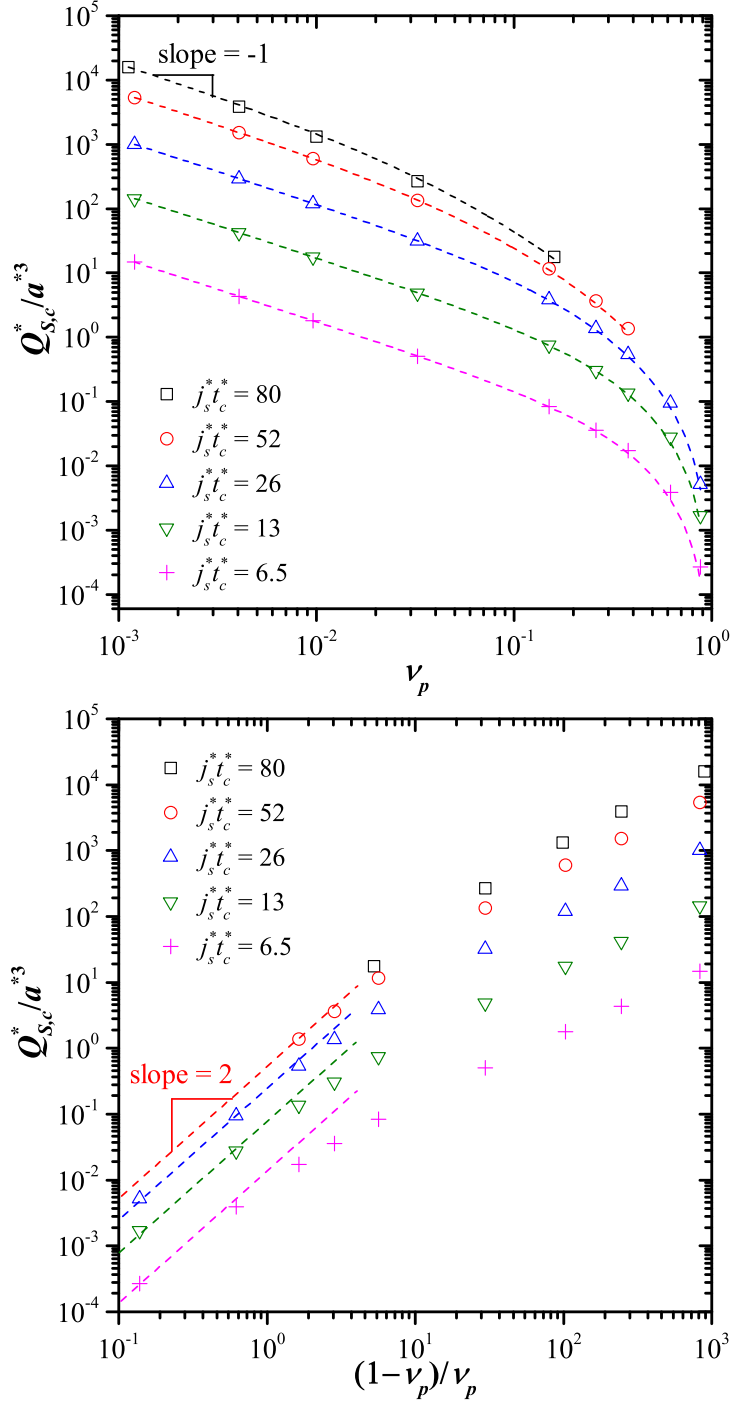


Figure 6.7: Computed  $Q_{S,c}^*/a^{*3}$  as a function of (a)  $\nu_p$ , along with curve fits of the form  $Q_{S,c}^*/a^{*3} = [\nu_p/A_{S,c} + \nu_p^2/(1-\nu_p)^2 B_{S,c}]^{-1}$  [Equation (6.21)], and (b)  $(1-\nu_p)/\nu_p$  for different values of  $j_s^* t_c^*$ .

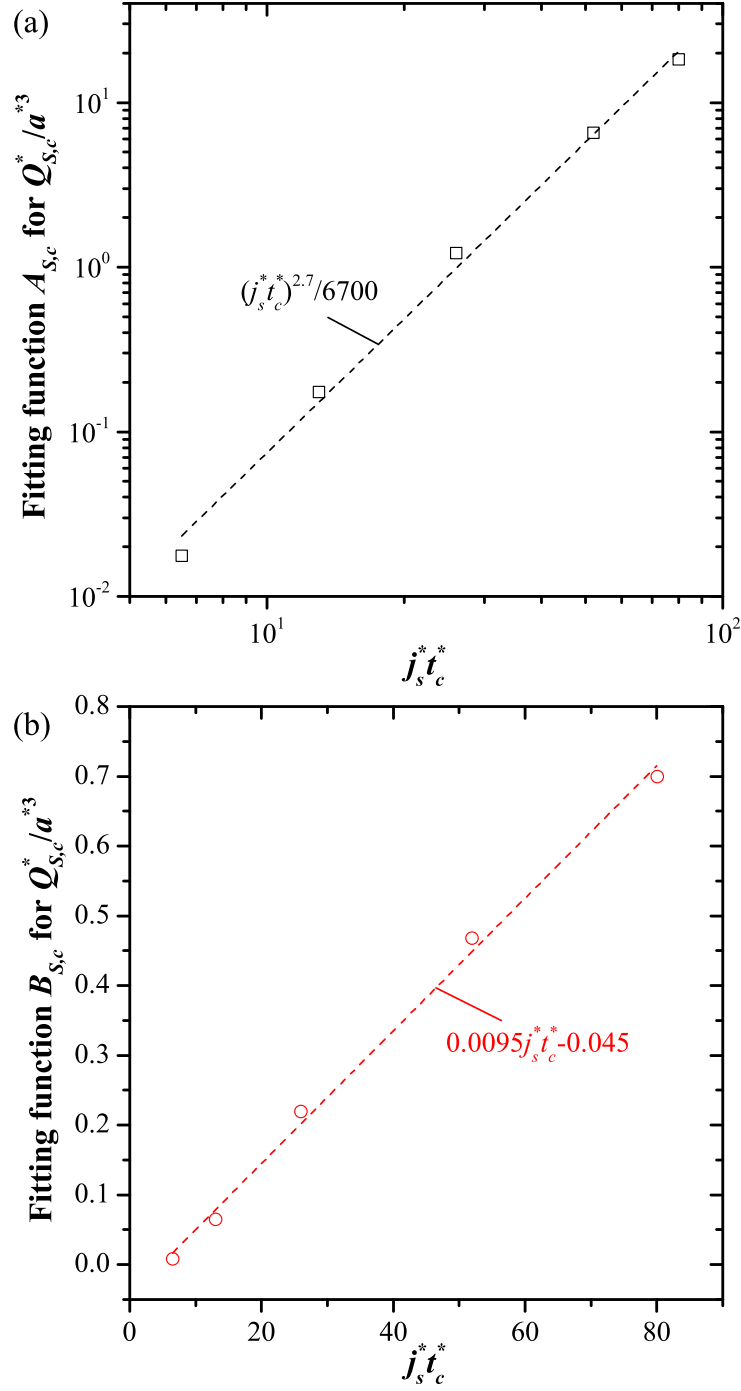


Figure 6.8: Fitting functions (a)  $A_{S,c}$  and (b)  $B_{S,c}$  versus  $j_s^{**}t_c^{**}$  in the expression for  $Q_{S,c}^*/a^{*3}$  given by Equation (6.21).

as functions of  $j_s^* t_c^*$ . They were fitted as  $A_{S,c} = (j_s^* t_c^*)^{2.7}/6700$  and  $B_{S,c} = 0.0095 j_s^* t_c^* - 0.045$ . Thus, the correlation for  $Q_{S,c}^*$  can be expressed as

$$Q_{S,c}^* = \frac{a^{*3}}{6700 \nu_p (j_s^* t_c^*)^{-2.7} + 100 (0.95 j_s^* t_c^* - 4.5)^{-1} [(1 - \nu_p)/\nu_p]^{-2}}. \quad (6.21)$$

The above scaling laws for  $\Delta T_{rev}^*(a^*/2)$  and for  $Q_{E,d}^*$ ,  $Q_{E,s}^*$ , and  $Q_{S,c}^*$  were derived for a wide range of dimensionless parameters, namely,  $1.2 \leq a^* \leq 29$ ,  $3.6 \times 10^4 \leq L^* \leq 2.2 \times 10^5$ ,  $3.0 \times 10^{-7} \leq j_s^* \leq 8.7 \times 10^{-6}$ ,  $1.2 \times 10^6 \leq t_c^* \leq 8.7 \times 10^7$ ,  $0.0012 \leq \nu_p \leq 0.88$ ,  $187 \leq Le \leq 748$ , and  $78 \leq C^* \leq 735$ . Note that  $Q_{E,d}^*$ ,  $Q_{E,s}^*$ , and  $Q_{S,c}^*$  given by Equations (6.19) to (6.21) could predict those computed numerically with average relative error of 5%, 20%, and 46%, respectively, as well as  $\Delta T_{rev}^*$  given by Equation (6.17) with average relative error of 12% (see Appendix A).

The correlations for the reversible heating terms  $Q_{E,d}^*$ ,  $Q_{E,s}^*$ , and  $Q_{S,c}^*$  given by Equations (6.19) to (6.21) offer several interesting insights into the reversible heating in an EDLC. In particular,  $Q_{E,d}^*$ ,  $Q_{E,s}^*$ , and  $Q_{S,c}^*/a^{*3}$  were all found to be functions of  $j_s^* t_c^* = j_s t_c / z F c_\infty \lambda_D = j_s t_c / (\epsilon_0 \epsilon_r R_u T_0 c_\infty / 2)^{1/2}$  and  $\nu_p = 2 N_a a^3 c_\infty$  only. This indicates that the amount of reversible heat generated during a charging step  $Q_{rev}''$  depended only on the electrolyte properties and on the amount of charge added to the EDLC corresponding to  $\Delta q_s = j_s t_c / 2$  (in C/m<sup>2</sup>). In addition, the amount of reversible heat consumed during the discharging step was equal to  $-Q_{rev}''$ . This implies that the net reversible heating in an EDLC is zero over any complete charge/discharge cycle, even if the charging and discharging current densities differ, since the total charge  $\Delta q_s$  would remain the same. Moreover,  $Q_{E,d}''$  and  $Q_{E,s}''$  (in dimensional form) were proportional to  $z^{-1}$  while  $Q_{S,c}''$  was proportional to  $z^2$ . This is consistent with the expressions for  $\dot{q}_{E,d}$  and  $\dot{q}_{E,s}$  [Equation (4.22)], depending on  $z^{-1}$  through the electrical conductivity  $\sigma$ . By contrast, the dependence of  $Q_{S,c}''$  on the valency  $z$  was weaker than that of the local volumetric heat generation rate  $\dot{q}_{S,c}$  [Equation (4.25)] which is proportional to  $z^3$ . This difference can be attributed to the fact that the ion fluxes  $\mathbf{N}_1$  and  $\mathbf{N}_2$  were approximately proportional to  $z^{-1}$ . As a result, the heat of mixing contributed the most to the reversible heat generation rate for electrolytes featuring large valency  $z$ . Interestingly, the diffusion coefficient  $D$  did not affect the amount of reversible heat generated per charging

step represented by  $Q''_{rev}$ . This was due to the fact that, although  $D$  appears in the numerator of the expressions for  $\dot{q}_{E,d}$  and  $\dot{q}_{E,s}$  [Equation (4.22)], the electrical conductivity  $\sigma$ , appearing in the denominator, is also proportional to  $D$ .

### 6.3.2.3 Thermal behavior of porous electrodes

The above scaling laws were derived from simulations of planar electrodes while, in practice, EDLC electrodes are porous. Previous studies using equilibrium models found that electrodes with radii of curvature larger than 40 nm yielded the same areal capacitance as planar electrodes [47, 48]. This suggests that applying scaling laws for planar electrodes to electrodes with large enough pores is a reasonable approximation. However, the choice of surface area used to define the surface current density  $j_s$  must be carefully considered. Indeed, in contrast to planar electrodes, the surface areas of the separator and of the porous electrode differ significantly [29]. Based on charge conservation, the average current density at the electrode/electrolyte interface should equal  $j_s = I_s/A_C$ , where  $I_s$  is the current (in A) imposed at the current collector and  $A_C$  is the accessible surface area of the porous electrode (in  $\text{m}^2$ ).

EDLC electrodes often feature mesopores and micropores smaller than 40 nm [19]. For such systems, the above scaling laws for planar electrodes could be corrected by a factor accounting for the morphology of the electrode. In fact, Wang *et al.* [102] successfully modeled the integral capacitance of nanoporous carbon electrodes as the product of the theoretical planar-electrode capacitance and a function depending only on the average pore radius in the electrode and on the effective ion diameter scaled by the Debye length. In addition, the dielectric constant  $\epsilon_r$  decreases under large electric fields typical of those found near electrode/electrolyte interfaces in EDLCs [103]. However, here,  $\epsilon_r$  was assumed to be constant to facilitate the scaling analysis. Wang *et al.* [102] also made this assumption and showed that the effect of field-dependent relative permittivity was indirectly accounted for by the semi-empirical constants appearing in the correlation. A similar approach could be used to extend the present model to predict the heat generation rates and temperature oscillations



in actual porous electrodes. To do so, a broad range of experimental data for various porous electrode structures and electrolytes would be required to validate this approach. However, this falls beyond the scope of the present study. Moreover, experimental temperature data currently available in the literature for EDLCs would be insufficient to rigorously identify a correction factor for porous electrodes and demonstrate the validity of any scaling analysis [7, 8, 25, 29, 76–78]. Indeed, most of the data were collected on commercial EDLC devices [7, 8, 25, 29, 76] whose electrolyte composition and electrode morphologies are not readily available.

## 6.4 Conclusion

In this chapter, scaling analysis was performed for the thermal model derived from first principles in Chapter 4 for EDLCs with binary and symmetric electrolyte under galvanostatic cycling [2]. The scaling analysis reduced the design problem from twelve independent dimensional parameters to seven physically meaningful dimensionless similarity parameters governing coupled electrodiffusion and thermal transport in EDLC electrolyte. Scaling laws characterizing the maximum temperature fluctuations and the total irreversible and reversible heat generated during a charging step were developed for planar electrodes. These expressions can estimate the heat generation and temperature behavior for various realistic electrolytes and cycling conditions without having to perform sophisticated and time-consuming numerical simulations. These dimensionless numbers and the scaling laws provide a framework that can be used for developing design rules and thermal management strategies for actual EDLCs.

# CHAPTER 7

## Thermal effects of asymmetric electrolytes in EDLCs

This chapter generalizes the first-principles thermal model derived in Chapter 4 for electric double layer capacitors (EDLCs) with binary and symmetric electrolytes to account for multiple ion species and/or asymmetric electrolytes. It accounts for both irreversible and reversible heat generation rates resulting from the transient electrodiffusion of ions within the electrolyte. This generalization is important because many widely used electrolytes, such as aqueous  $\text{H}_2\text{SO}_4$ , are asymmetric [57–60]. In addition, electrolyte mixtures including more than two ion species have attracted interest for EDLC applications because certain mixtures perform better than either of the original electrolytes. For example, eutectic mixtures of ionic liquids can provide broader operating temperature ranges than either constituent [61–63]. These asymmetric and/or multi-species electrolytes cannot be rigorously accounted for by existing thermal models accounting for reversible heating [2, 29, 30, 76, 82], as they were limited to binary and/or symmetric electrolytes. In addition, detailed numerical simulations were performed for EDLCs with planar electrodes and binary and asymmetric electrolytes in order to investigate the effects of electrolyte asymmetry on the irreversible and reversible heat generation rates within the EDLCs and on the resulting local temperature.

### 7.1 Analysis

#### 7.1.1 Schematic and assumptions

Figure 4.1 illustrates the one-dimensional EDLC simulated in the present study. It consists of two planar electrodes separated by an electrolyte with inter-electrode spacing  $2L$ . The electrodes located at  $x = 0$  and  $x = 2L$  are denoted as Electrodes A and B, respectively. The

ion species with the largest effective ion diameter corresponds to  $i = 1$ . In contrast to EDLC cells using symmetric electrolytes, those using asymmetric electrolytes lack antisymmetry in the electric potential and ion concentrations [57]. Thus, for asymmetric electrolytes, the entire electrolyte region must be simulated [57].

To make the problem mathematically tractable, the following assumptions were made: (1) Chemical reactions and ion insertion into the electrode were absent. (2) The electrolyte obeyed the GMPNP model (Section 2.4.3). (3) Dissociation of the electrolyte was complete. (4) Bulk movement of the electrolyte, i.e., advection, was negligible. (5) All electrolyte properties were constant and independent of local ion concentrations and temperature, with the sole exception of the concentration-dependent electrical conductivity of the electrolyte. (6) The simulated EDLC was thermally insulated, and (7) the Stern layer thickness  $H$  was assumed to be equal to the effective radius of the largest ion species, i.e.,  $H = a_1/2$ . Here, Assumption (1) and Assumptions (3)–(6) were identical to those used in Chapters 3, 4, and 6, while Assumptions (2) and (7) were modified to account for multi-species and/or asymmetric electrolytes.

### 7.1.2 Heat generation in multi-species and asymmetric electrolytes

Chapter 4 defined the electrical heat generation rate  $\dot{q}_E$  as

$$\dot{q}_E = \mathbf{j} \cdot \mathbf{E} \quad (7.1)$$

where  $\mathbf{j} = \sum_{i=1}^n z_i F \mathbf{N}_i$  is the ionic current density [28] and  $\mathbf{E} = -\nabla\psi$  is the electric field vector. Based on the expression for the ion flux  $\mathbf{N}_i$  in the GMPNP model [Equation (2.11)], the current density  $\mathbf{j}$  in a general electrolyte solution containing  $n$  ion species can be written as

$$\mathbf{j} = \sigma \mathbf{E} - F \sum_{i=1}^n D_i z_i \nabla c_i - \left( \frac{F N_A \sum_{i=1}^n D_i z_i c_i}{1 - N_A \sum_{j=1}^n a_j^3 c_j} \right) \sum_{j=1}^n a_j^3 \nabla c_j. \quad (7.2)$$

Here,  $\sigma$  is the electrical conductivity of the electrolyte given by Equation (2.4). Equation (7.2) can be rearranged to find an expression for the electric field vector  $\mathbf{E}$  to be substituted into Equation (7.1). As in Chapter 4, this results in three contributions to  $\dot{q}_E$  such that

$\dot{q}_E = \dot{q}_{J,irr} + \dot{q}_{E,d} + \dot{q}_{E,s}$ . The first term  $\dot{q}_{J,irr}$  corresponds to the irreversible Joule heating. Its form is identical to that derived in Chapter 4, i.e.,

$$\dot{q}_{J,irr} = \frac{|\mathbf{j}|^2}{\sigma}. \quad (7.3)$$

The heat generation rates  $\dot{q}_{E,d}$  and  $\dot{q}_{E,s}$  are reversible and arise from ion diffusion and steric repulsion, respectively. They are expressed as

$$\dot{q}_{E,d} = \frac{\mathbf{j}}{\sigma} \cdot \left( F \sum_{i=1}^n D_i z_i \nabla c_i \right) \quad \text{and} \quad \dot{q}_{E,s} = \frac{\mathbf{j}}{\sigma} \cdot \frac{\left( F \sum_{i=1}^n D_i z_i c_i \right) \left( N_A \sum_{i=1}^n a_i^3 \nabla c_i \right)}{\left( 1 - N_A \sum_{i=1}^n a_i^3 c_i \right)} \quad (7.4)$$

and are the more general forms of those in Equation (4.22). Note that  $\dot{q}_{E,d}$  and  $\dot{q}_{E,s}$  differ from zero only in the presence of an ion concentration gradient  $\nabla c_i$ .

Chapter 4 defined the heat of mixing  $\dot{q}_S$  as [2]

$$\dot{q}_S = \sum_{i=0}^n \mathbf{N}_i \cdot R_u \nabla \left( T^2 \frac{\partial \ln \gamma_{i,DH}}{\partial T} \right) \quad (7.5)$$

where  $\gamma_{i,DH}$  is the activity coefficient of ion species  $i$  or of the solvent  $i = 0$ . This chapter again uses the expression of  $\gamma_{i,DH}$  given by the Debye-Hückel limiting law as it accounts for the effects of both temperature and ion concentrations. It was derived for dilute electrolytes and accounts for long-range electrical interactions between ions and for thermal agitation while neglecting short-range ion-solvent or ion-ion interactions [28, 104]. Then, the activity coefficient of ion species  $i$  in a general multi-species and/or asymmetric electrolyte can be expressed as [28, 104]

$$\ln \gamma_{i,DH} = - \frac{z_i^2 e F^2 \left( \sum_{i=1}^n z_i^2 c_i \right)^{1/2}}{8\pi (\epsilon_0 \epsilon_r R_u T)^{3/2}}. \quad (7.6)$$

Substituting Equation (7.6) into the expression for the heat of mixing  $\dot{q}_S$  given by Equation (7.5) and assuming negligible contribution from the solvent ( $i = 0$ ) yields two terms such

that  $\dot{q}_S = \dot{q}_{S,c} + \dot{q}_{S,T}$ , where  $\dot{q}_{S,c}$  and  $\dot{q}_{S,T}$  are expressed as

$$\begin{aligned}\dot{q}_{S,c} &= \frac{3}{32\pi} \frac{eF^2}{(\epsilon_0\epsilon_r)^{3/2} \left( R_u T \sum_{i=1}^n z_i^2 c_i \right)^{1/2}} \left( \sum_{i=1}^n z_i^2 \mathbf{N}_i \right) \cdot \left( \sum_{i=1}^n z_i^2 \nabla c_i \right) \\ \text{and } \dot{q}_{S,T} &= -\frac{3}{32\pi} \frac{eF^2 \left( \sum_{i=1}^n z_i^2 c_i \right)^{1/2}}{(\epsilon_0\epsilon_r)^{3/2} R_u^{1/2} T^{3/2}} \sum_{i=1}^n z_i^2 \mathbf{N}_i \cdot \nabla T\end{aligned}\quad (7.7)$$

and are more general forms of those in Equation (4.25). These terms correspond to the heat of mixing arising from concentration gradients and from temperature gradients, respectively. Here,  $\dot{q}_{S,c}$  represents heat released by ions migrating in the direction of increasing concentration, e.g., into the EDL region, as this leads to a more ordered distribution of ions and consequently smaller entropy. Meanwhile,  $\dot{q}_{S,T}$  represents heat released by ions migrating in the direction of decreasing temperature, as smaller thermal agitation results in smaller entropy. For binary and symmetric electrolytes, Equations (7.3), (7.4), and (7.7) simplify to those derived in Chapter 4.

Note that the expression for the activity coefficient  $\gamma_{i,DH}$  differs from the Langmuir-type activity coefficient  $\gamma_{i,L}$  used to derive the GMPNP model and given by Equation (2.10). The different formulations were used because the heat of mixing  $\dot{q}_S$  must account for the temperature dependence of  $\gamma_{i,DH}$  while the GMPNP derivation must account for the steric effects through  $\gamma_{i,L}$ . Unfortunately, neither  $\gamma_{i,L}$  nor  $\gamma_{i,DH}$  captures all these effects simultaneously. However, the steric repulsion represented by the Langmuir-type activity coefficient  $\gamma_{i,L}$  does affect the heat generation rates through its influence on the ion concentrations  $c_i$ , the ion fluxes  $\mathbf{N}_i$ , and the current density  $\mathbf{j}$  appearing in the expressions of  $\dot{q}_{J,irr}$ ,  $\dot{q}_{E,d}$ ,  $\dot{q}_{E,s}$ ,  $\dot{q}_{S,c}$ , and  $\dot{q}_{S,T}$ .

Overall, the total heat generation rate  $\dot{q}$  can be expressed as the sum of an irreversible  $\dot{q}_{J,irr}$  and a reversible  $\dot{q}_{rev}$  heat generation rate such that  $\dot{q} = \dot{q}_{J,irr} + \dot{q}_{rev}$  where  $\dot{q}_{rev} = \dot{q}_{E,d} + \dot{q}_{E,s} + \dot{q}_{S,c} + \dot{q}_{S,T}$ .

### 7.1.3 Initial and boundary conditions

The one-dimensional governing Equation (2.5) for  $\psi(x, t)$  was solved within the two Stern layers and the diffuse layer. It required one initial condition and two boundary conditions for each region. Initially, the potential was uniform and equal to zero throughout the EDLC ( $0 \leq x \leq 2L$ ) such that

$$\psi(x, 0) = 0 \text{ V.} \quad (7.8)$$

During galvanostatic cycling, the electric current density at Electrode A alternated between charging at current density  $+j_s$  and discharging at current density  $-j_s$  as a square wave of cycle period  $t_c$ . Charge conservation requires the displacement current density in the electrolyte at the surface of Electrode A to equal the electronic current density  $j_{im}(t)$  within the electrode. This condition was expressed as

$$-\epsilon_0 \epsilon_r \frac{\partial^2 \psi}{\partial t \partial x}(0, t) = j_{im}(t) = \begin{cases} j_s & \text{for charging } (n_c - 1)t_c \leq t < (n_c - 1/2)t_c \\ -j_s & \text{for discharging } (n_c - 1/2)t_c \leq t < n_c t_c \end{cases} \quad (7.9)$$

where  $n_c = 1, 2, \dots$  is the cycle number. Moreover, the electric potential and the electric field were continuous across the Stern/diffuse layer interface located at  $x = H$  such that

$$\psi(H^-, t) = \psi(H^+, t) \quad \text{and} \quad \frac{\partial \psi}{\partial x}(H^-, t) = \frac{\partial \psi}{\partial x}(H^+, t). \quad (7.10)$$

Similarly, they were continuous across the Stern/diffuse layer interface at  $x = 2L - H$  so that

$$\psi(2L - H^-, t) = \psi(2L - H^+, t) \quad \text{and} \quad \frac{\partial \psi}{\partial x}(2L - H^-, t) = \frac{\partial \psi}{\partial x}(2L - H^+, t). \quad (7.11)$$

Finally, the surface of Electrode B was electrically grounded, i.e.,  $\psi(2L, t) = 0 \text{ V}$ .

The one-dimensional mass conservation Equation (2.6) with GMPNP ion flux Equation (2.11) for ion concentration  $c_i(x, t)$  was solved only within the diffuse layer since the Stern layer does not contain free charge [26, 27]. Thus, one initial condition and two boundary conditions were required. The ion concentrations were initially uniform, and the solution was electrically neutral, i.e.,

$$c_i(x, 0) = c_{i,\infty} \quad \text{with} \quad \sum_{i=1}^n z_i c_{i,\infty} = 0. \quad (7.12)$$

At the Stern/diffuse layer interfaces located at  $x = H$  and  $x = 2L - H$ , all ion fluxes vanished because there was no ion insertion into the electrodes, i.e.,

$$N_i(H, t) = N_i(2L - H, t) = 0 \text{ mol m}^{-2}\text{s}^{-1}. \quad (7.13)$$

The one-dimensional energy conservation Equation (2.12) expressed in terms of the temperature  $T(x, t)$  was solved within the two Stern layers and the diffuse layer. It required one initial condition and two boundary conditions for each region. The initial temperature was uniform and equal to  $T(x, 0) = T_0$ . The surfaces of Electrode A at  $x = 0$  and of Electrode B at  $x = 2L$  were assumed to be thermally insulated such that

$$-k \frac{\partial T}{\partial x}(0, t) = 0 \text{ W m}^{-2} \quad \text{and} \quad -k \frac{\partial T}{\partial x}(2L, t) = 0 \text{ W m}^{-2}. \quad (7.14)$$

The temperature and heat flux were continuous across the Stern/diffuse layer interface at  $x = H$ , i.e.,

$$T(H^-, t) = T(H^+, t) \quad \text{and} \quad -k \frac{\partial T}{\partial x}(H^-, t) = -k \frac{\partial T}{\partial x}(H^+, t). \quad (7.15)$$

Similarly, they were continuous across the second Stern/diffuse layer interface at  $x = 2L - H$  so that

$$T(2L - H^-, t) = T(2L - H^+, t) \quad \text{and} \quad -k \frac{\partial T}{\partial x}(2L - H^-, t) = -k \frac{\partial T}{\partial x}(2L - H^+, t). \quad (7.16)$$

#### 7.1.4 Constitutive relationships

The electrolytes simulated were based on the properties of aqueous  $\text{H}_2\text{SO}_4$ , a common binary and asymmetric electrolyte used in EDLCs [10]. The ion valencies for aqueous  $\text{H}_2\text{SO}_4$  were equal to  $z_1 = -2$  and  $z_2 = 1$ , where  $i = 1$  and  $i = 2$  corresponded to  $\text{SO}_4^{2-}$  and  $\text{H}^+$ , respectively. The associated solvated ion diameters were taken as  $a_1 = 0.76 \text{ nm}$  and  $a_2 = 0.56 \text{ nm}$  and the diffusion coefficients as  $D_1 = 1.1 \times 10^{-9} \text{ m}^2\text{s}^{-1}$  and  $D_2 = 9.3 \times 10^{-9} \text{ m}^2\text{s}^{-1}$  [58–60]. It is evident that aqueous  $\text{H}_2\text{SO}_4$  was significantly asymmetric with respect to valency, ion diameter, and diffusion coefficient. Finally, the relative permittivity  $\epsilon_r = 78.4$ , density  $\rho = 997 \text{ kg m}^{-3}$ , specific heat  $c_p = 4180 \text{ J kg}^{-1}\text{K}^{-1}$ , and thermal conductivity  $k = 0.61 \text{ W m}^{-1}\text{K}^{-1}$  were taken as those of water [58].

### 7.1.5 Method of solution

The one-dimensional governing Equations (2.5), (2.6), and (2.12) were solved using the same method and same convergence criteria described in Section 4.1.5.

## 7.2 Results and discussion

Table 7.1 summarizes the cases simulated to investigate the effect of asymmetric valencies  $z_i$ , ion diameters  $a_i$ , and diffusion coefficients  $D_i$  on the thermal behavior of EDLCs with binary electrolytes. Case 1 represents a symmetric electrolyte with ion properties corresponding to those of  $H^+$  ions and was used as a baseline case. Cases 2–4 were chosen to illustrate the effect of valency  $z_i$  with all other properties equal to those of Case 1. Case 2 corresponded to symmetric electrolyte with  $-z_1 = z_2 = 2$  based on the valency of  $SO_4^{2-}$  while Case 3 and 4 represented asymmetric electrolytes with  $z_1 = -2$  and  $z_2 = 1$ . Asymmetry in valency required asymmetric bulk ion concentrations  $c_{2,\infty} = -z_1 c_{1,\infty} / z_2$  in order to satisfy electroneutrality. Thus, Cases 3 and 4 were chosen with different bulk concentrations  $c_{i,\infty}$  so that  $z_1$  and  $c_{1,\infty}$  in Case 3 equaled those of Case 2, while  $z_2$  and  $c_{2,\infty}$  in Case 4 equaled those of Case 1.

Similarly, the effect of ion diameter  $a_i$  was demonstrated by Case 5 ( $a_1 = a_2 = 0.76$  nm) and Case 6 ( $a_1 = 0.76$  nm and  $a_2 = 0.56$  nm), while the effect of diffusion coefficient  $D_i$  was shown in Case 7 ( $D_1 = D_2 = 1.1 \times 10^{-9}$  m<sup>2</sup>s<sup>-1</sup>) and Case 8 ( $D_1 = 1.1 \times 10^{-9}$  m<sup>2</sup>s<sup>-1</sup> and  $D_2 = 9.3 \times 10^{-9}$  m<sup>2</sup>s<sup>-1</sup>). The electrolyte relative permittivity  $\epsilon_r$ , density  $\rho$ , specific heat  $c_p$ , and thermal conductivity  $k$  remained the same for all cases. The inter-electrode spacing and initial temperature were equal to  $L = 20$   $\mu$ m and  $T_0 = 298$  K, respectively. The cell was cycled galvanostatically at  $j_s = 14$  mA cm<sup>-2</sup> with cycle period  $t_c = 7.6$  ms. This current density  $j_s$  was within the range of current densities per unit surface area of the current collector reported in experimental studies [29, 78]. The combination of  $j_s$  and  $t_c$  was chosen to yield a maximum cell voltage of 1 V for the baseline Case 1. The current density and cycle period were held constant for all cases to facilitate comparison. The temperature in the



Table 7.1: Parameters for the cases simulated, based on the properties of aqueous  $\text{H}_2\text{SO}_4$  [58–60], as well as the resulting areal capacitances  $C_{s,int}$  [Equation (2.2)] and irreversible Joule heat generation rate  $\dot{q}_{J,irr}$ . Here, the imposed current density and cycle period were equal to  $j_s = 14 \text{ mA cm}^{-2}$  and  $t_c = 7.6 \text{ ms}$ , respectively.

	$a_1$	$a_2$	$z_1$	$z_2$	$D_1$	$D_2$	$c_{1,\infty}$	$c_{2,\infty}$	Symmetric?	$C_{s,int}$	$\dot{q}_{J,irr} = j_s^2/\sigma_\infty$
	(nm)	(nm)			( $\text{m}^2/\text{s}$ )	( $\text{m}^2/\text{s}$ )	(mol/L)	(mol/L)		( $\mu\text{F}/\text{cm}$ )	( $\text{W}/\text{m}^3$ )
<b>Case 1</b>	0.56	0.56	-1	1	$9.3 \times 10^{-9}$	$9.3 \times 10^{-9}$	1	1	yes	53.7	280
<b>Case 2</b>	0.56	0.56	-2	2	$9.3 \times 10^{-9}$	$9.3 \times 10^{-9}$	1	1	yes	75.0	70.1
<b>Case 3</b>	0.56	0.56	-2	1	$9.3 \times 10^{-9}$	$9.3 \times 10^{-9}$	1	2	no	64.0	93.5
<b>Case 4</b>	0.56	0.56	-2	1	$9.3 \times 10^{-9}$	$9.3 \times 10^{-9}$	1/2	1	no	62.0	187
<b>Case 5</b>	0.76	0.76	-1	1	$9.3 \times 10^{-9}$	$9.3 \times 10^{-9}$	1	1	yes	30.2	280
<b>Case 6</b>	0.76	0.56	-1	1	$9.3 \times 10^{-9}$	$9.3 \times 10^{-9}$	1	1	no	36.6	280
<b>Case 7</b>	0.56	0.56	-1	1	$1.1 \times 10^{-9}$	$1.1 \times 10^{-9}$	1	1	yes	53.7	2370
<b>Case 8</b>	0.56	0.56	-1	1	$1.1 \times 10^{-9}$	$9.3 \times 10^{-9}$	1	1	no	53.7	502

expressions of  $\mathbf{N}_i$ ,  $\dot{q}_{S,c}$ , and  $\dot{q}_{S,T}$  was taken as the initial temperature  $T_0$ , since the electrolyte properties were assumed to be constant and independent of temperature [Assumption (5)].

### 7.2.1 Electric potential

Figure 7.1 shows the cell potential  $\psi_s(t) = \psi(0, t) - \psi(2L, t)$  computed as a function of time  $t$  over one and a half cycles for (a) Cases 1–4 featuring different ion valencies  $z_i$  and (b) Cases 1, 5, and 6 featuring different effective ion diameters. Results for Cases 7 and 8 featuring different diffusion coefficients  $D_i$  were not shown because the predicted cell potentials overlapped that of Case 1 ( $D_1 = D_2 = 9.3 \times 10^{-9} \text{ m}^2\text{s}^{-1}$ ) at all times. In all cases, the cell potential increased during the charging step and decreased during the discharging step. As previously mentioned, the current density  $j_s$  and cycle period  $t_c$  were chosen so that the maximum cell potential for the baseline Case 1 would equal 1 V. The numerically predicted cell potential qualitatively resembled those measured during galvanostatic cycling of EDLCs [77, 78]. Note that the measured cell potential often featured a significant “IR drop” due to ohmic resistance. However, the predicted cell potential, shown in Figure 7.1, was almost entirely due to the electric double layer formation. The portion of the cell potential due to ohmic resistance in the electrolyte can be approximated as  $j_s(2L)/\sigma_\infty$  where  $\sigma_\infty$  is the electrical conductivity of the electrolyte given by Equation (2.4) with the bulk ion concentrations  $c_{1,\infty}$  and  $c_{2,\infty}$ . This ohmic potential drop was on the order of  $10^{-3}$  to  $10^{-5}$  V and was less than 0.1% of the maximum cell potential for all Cases 1–8. The IR drop can be reproduced numerically by increasing the electrical resistance of the simulated EDLC, e.g., by reducing the electrolyte conductivity  $\sigma_\infty$ , increasing the inter-electrode spacing, and/or accounting for the electrical resistance of the electrodes and current collectors (see Appendix B).

Figure 7.1(a) indicates that increasing either or both ion valencies  $|z_i|$  resulted in a smaller cell potential at all times. Here, the surface charge density  $\Delta q_s = j_s t_c / 2$  added during the charging step was the same for all cases. Thus, the integral capacitance  $C_{s,int}$ , given by Equation (2.2), increased with increasing  $|z_i|$  (Table 7.1). In addition, Cases 3 and 4 featuring the same ion properties  $z_i$ ,  $a_i$ , and  $D_i$ , but different bulk ion concentrations

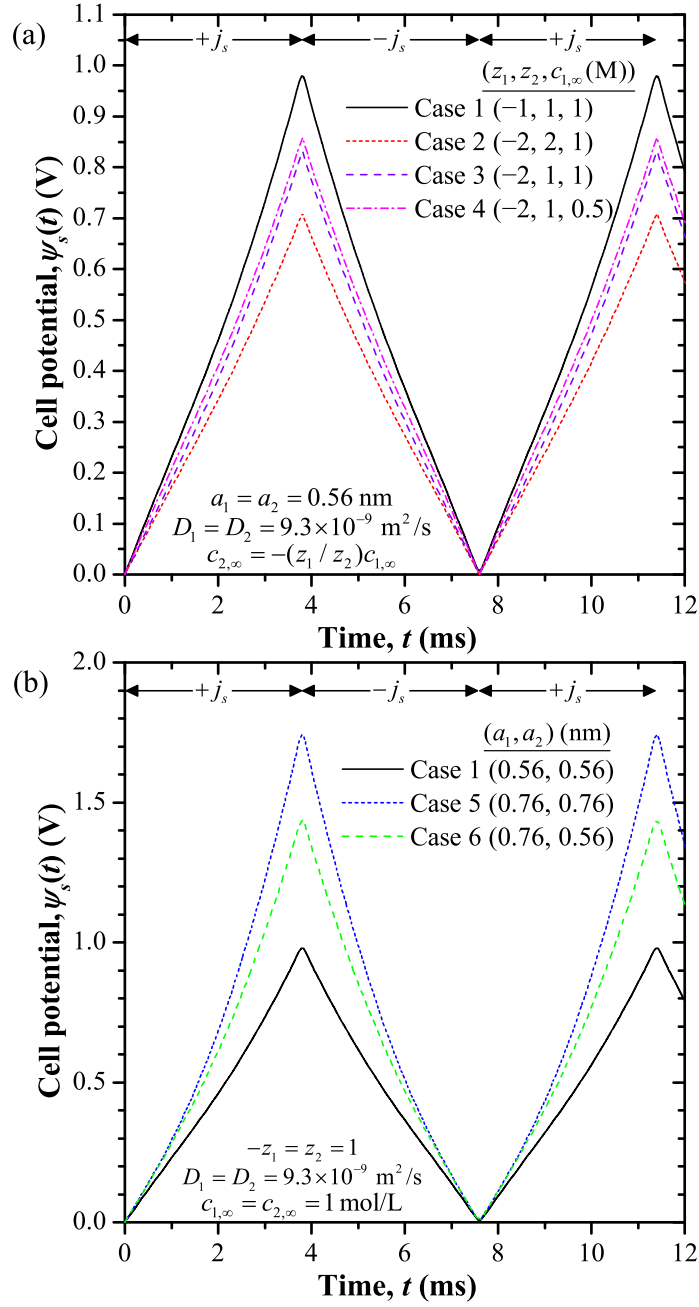


Figure 7.1: Cell potential  $\psi_s(t) = \psi(0, t) - \psi(2L, t)$  as a function of time  $t$  over the first cycle and a half for (a) Cases 1–4 featuring different ion valencies  $z_i$  and (b) Cases 1, 5, and 6 featuring different effective ion diameters. Results for Cases 7 and 8 featuring different diffusion coefficients  $D_i$  were identical to those of Case 1.

$c_{i,\infty}$  demonstrate that doubling  $c_{i,\infty}$  slightly increased  $C_{s,int}$ . By contrast, Figure 7.1(b) indicates that increasing either or both effective ion diameters  $a_i$  substantially increased the cell potential, corresponding to a decrease in capacitance  $C_{s,int}$  (Table 7.1). These changes in integral capacitance with  $|z_i|$  and  $a_i$  were consistent with those observed from cyclic voltammetry simulations of EDLCs with binary and asymmetric electrolytes [57]. Table 7.1 also shows that decreasing either or both ion diffusion coefficients  $D_i$  had no effect on  $C_{s,int}$ . This was also consistent with the results of cyclic voltammetry simulations outside the “diffusion-limited” regime [57].

### 7.2.2 Concentrations

Figure 7.2 shows (a) and (c) the anion concentration  $c_1(x, 3t_c/2)$  near the positive Electrode A as a function of location  $x$  as well as (b) and (d) the cation concentration  $c_2(x, 3t_c/2)$  near the negative Electrode B as a function of  $2L - x$  at time  $t = 3t_c/2$  at the end of a charging step. Figures 7.2(a) and 7.2(b) show Cases 1–4 featuring different ion valencies  $z_i$ , while Figures 7.2(c) and 7.2(d) show Cases 1, 5, and 6 with different effective ion diameters  $a_i$ .

Figure 7.2 indicates that electrolytes with asymmetric  $z_i$  or  $a_i$ , e.g., those in Cases 3, 4, and 6, exhibited spatially asymmetric concentration profiles. Overall, the concentration profiles near each electrode were determined by the properties of the counterion, i.e., by the anion (species 1) near the positive electrode [Figures 7.2(a) and 7.2(c)] and by the cation (species 2) near the negative electrode [Figures 7.2(b) and 7.2(d)]. The ion diameter  $a_i$  controlled the counterion concentration at the Stern/diffuse layer interfaces located at  $x = H$  and  $x = 2L - H$  where the counterion concentration reached its theoretical maximum  $c_{i,max} = 1/N_A a_i^3$ . The maximum concentration gradient also decreased with increasing  $a_i$  due to the smaller concentration drop between the Stern/diffuse layer interface and the bulk electrolyte. By contrast, increasing the counterion valency  $|z_i|$  had no effect on the surface counterion concentration. However, it resulted in a thinner EDL and steeper concentration gradients near the electrodes. These effects can be attributed to the fact that (i) fewer ions were necessary to balance the same electrode charge and (ii) the electrostatic forces were

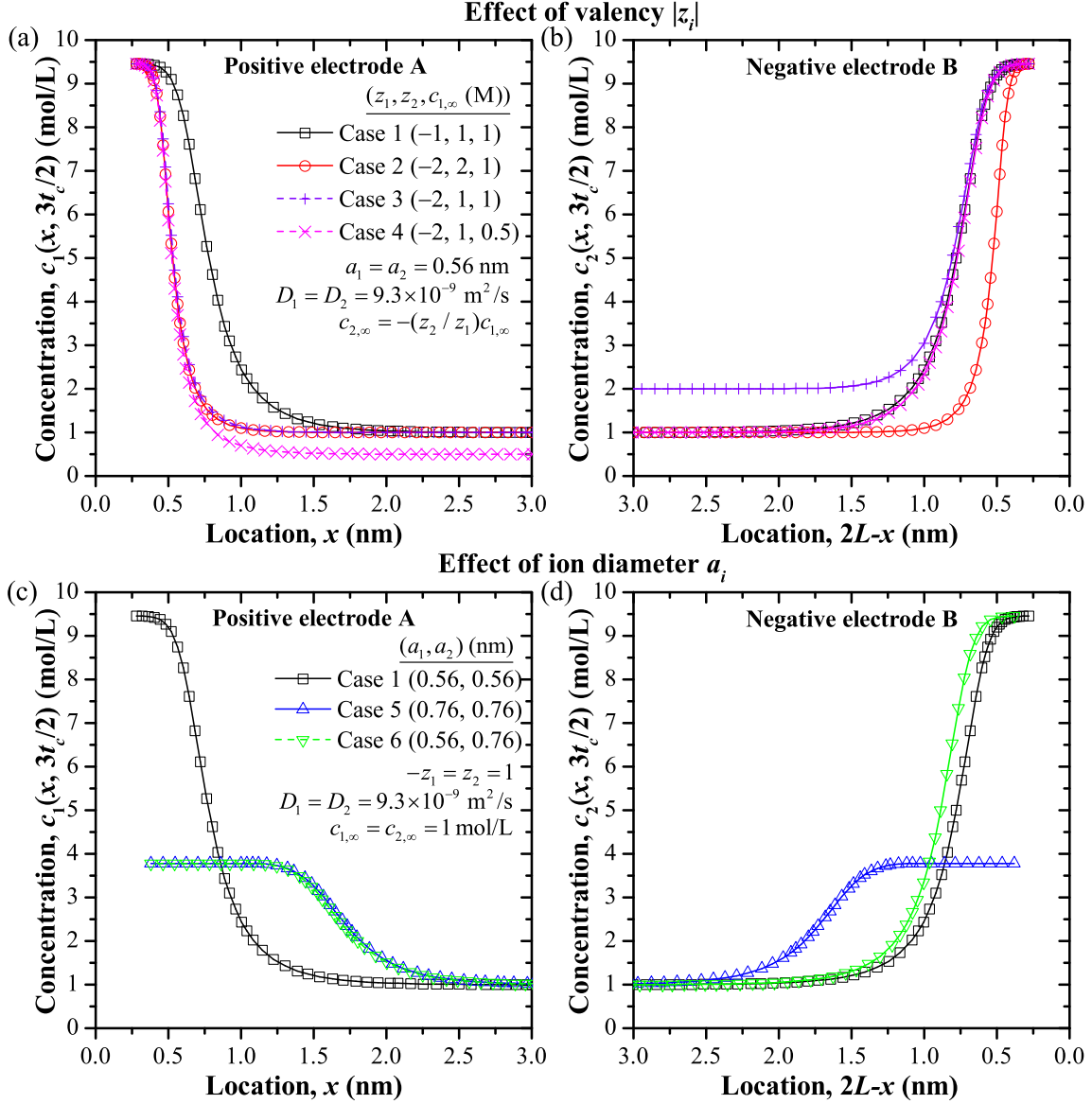


Figure 7.2: Anion concentration  $c_1(x, 3t_c/2)$  near the positive Electrode A as a function of location  $x$  for (a) Cases 1–4 with different values of  $z_i$  and (c) Cases 1, 5, and 6 with different values of  $a_i$  as well as cation concentration  $c_2(x, 3t_c/2)$  near the negative Electrode B as a function of location  $2L - x$  for (b) Cases 1–4 and (d) Cases 1, 5, and 6. All cases correspond to time  $t = 3t_c/2$  at the end of a charging step.

larger on ions of larger valency.

Note that Cases 7 and 8 considered asymmetry in diffusion coefficient  $D_i$  but were not shown since the results were identical to those for Case 1 ( $D_1 = D_2 = 9.3 \times 10^{-9} \text{ m}^2\text{s}^{-1}$ ) everywhere in the electrolyte. Thus, the diffusion coefficient  $D_i$  had no effect on the concentration profiles for the cycling conditions considered. This was attributed to the fact that galvanostatic cycling was simulated so that the current density  $j_s$  was imposed and the fluxes of ions into the EDLs remained the same in all cases. Indeed, the increase in cell potential  $\psi_s(t)$  required to maintain the desired current density  $j_s$  for electrolytes with smaller diffusion coefficients was negligibly small compared to the potential drop due to the EDLs for Cases 1, 7, and 8.

### 7.2.3 Irreversible Joule heat generation rate $\dot{q}_{J,irr}$

For all Cases 1–8,  $\dot{q}_{J,irr}$  (in  $\text{W m}^{-3}$ ) was found to be uniform and equal to  $\dot{q}_{J,irr} = j_s^2/\sigma_\infty$  throughout the entire diffuse layer of the electrolyte, except in the EDL regions within a few nanometers of the electrode where it decreased steeply to zero (see Appendix B). The differences in  $\dot{q}_{J,irr}$  summarized in Table 7.1 reflect the fact that  $\sigma_\infty$  increased with increasing  $|z_i|$ ,  $D_i$ , and/or  $c_{i,\infty}$  of either ion species, as suggested by Equation (2.4). Note also that, like  $\sigma_\infty$ ,  $\dot{q}_{J,irr}$  was independent of the ion diameter  $a_i$ , as illustrated by Cases 1, 5, and 6 in Table 7.1.

### 7.2.4 Reversible heating

#### 7.2.4.1 Diffusion heat generation rate $\dot{q}_{E,d}$

Figures 7.3(a) and 7.3(c) show the diffusion heat generation rate  $\dot{q}_{E,d}(x, 11t_c/8)$  [Equation (7.4)] at time  $t = 11t_c/8$  near the end of a charging step as a function of location  $x$  near the positive Electrode A for Cases 1–4 and for Cases 1, 5, and 6, respectively. Similarly, Figures 7.3(b) and 7.3(d) show  $\dot{q}_{E,d}(x, 11t_c/8)$  as a function of  $2L - x$  near the negative Electrode B for Cases 1–4 and for Cases 1, 5, and 6, respectively. Note that the heat generation rate was

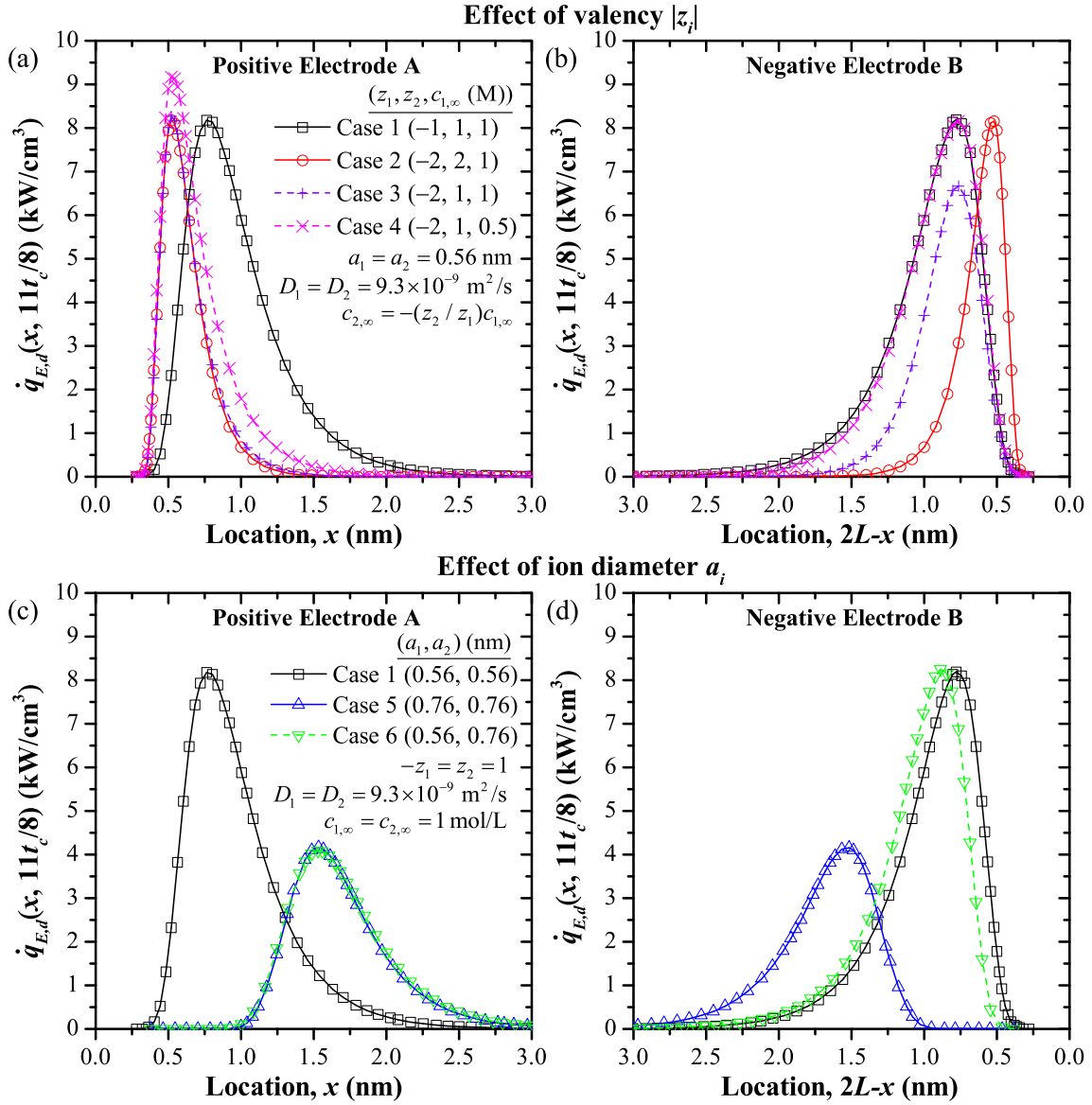


Figure 7.3: Diffusion heat generation rate  $\dot{q}_{E,d}(x, 11t_c/8)$  as a function of location (a) and (c)  $x$  near the positive Electrode A and (b) and (d)  $2L - x$  near the negative Electrode B. Plots (a) and (b) show Cases 1–4 with different  $z_i$  while plots (c) and (d) show Cases 5 and 6 with different  $a_i$ . All cases correspond to time  $t = 11t_c/8$  near the end of a charging step.

plotted at a slightly earlier time than the concentrations shown in Figure 7.2 in order to show the profiles characteristic of the charging step rather than those during the switch in current direction occurring at  $t = 3t_c/2$ . Figure 7.3 indicates that electrolytes with asymmetric valency  $z_i$  or ion diameter  $a_i$ , e.g., those in Cases 3, 4, and 6, yielded spatially asymmetric heat generation rate  $\dot{q}_{E,d}$  profiles. Moreover, for a given electrode, electrolytes sharing the same counterion properties  $z_i$  and  $a_i$  as well as bulk concentration  $c_{i,\infty}$  yielded the same heat generation rate  $\dot{q}_{E,d}$  profiles. In other words,  $\dot{q}_{E,d}$  profiles near the positive electrode were identical for Cases 2 and 3 [Figure 7.3(a)] and for Cases 5 and 6 [Figure 7.3(c)] while those for Cases 1 and 4 were identical near the negative electrode [Figure 7.3(b)]. In addition, the heat generation rate profiles for cases sharing the same counterion properties  $z_i$  and  $a_i$ , but featuring different bulk concentrations  $c_{i,\infty}$ , had the same location and were very similar in shape but had different magnitudes. For example, the peaks of the heat generation rate  $\dot{q}_{E,d}$  for Case 4 spanned the same spatial regions those for Case 3 but were larger in magnitude due to the smaller local electrical conductivity  $\sigma(x, t)$ .

Furthermore, the heat generation rate  $\dot{q}_{E,d}$  was confined to a narrower region as the valency  $|z_i|$  increased due to the narrowing of the EDL region, as discussed previously [Figures 7.2(a) and 7.2(b)]. However, the maximum value of  $\dot{q}_{E,d}$  remained unaffected by changes in  $|z_i|$ . This can be attributed to the fact that increasing  $|z_i|$  increased the local electrical conductivity  $\sigma$  and the concentration gradient by the same proportion in the expression of  $\dot{q}_{E,d}$  given by Equation (7.4).

Finally, increasing the counterion diameter  $a_i$  reduced the magnitude of the heat generation rate  $\dot{q}_{E,d}$ . Although the ion diameter  $a_i$  does not appear directly in the expression of  $\dot{q}_{E,d}$ , it affects  $\dot{q}_{E,d}$  via its strong influence on the concentration profiles [Figures 7.2(c) and 7.2(d)]. Both the concentration gradient and the electrical conductivity  $\sigma$  decreased with increasing  $a_i$ . However, the concentration gradient decreased more than the conductivity, resulting in a net decrease in  $\dot{q}_{E,d}$ . By contrast, changing the diffusion coefficient  $D_i$  had no effect. In fact, values of  $\dot{q}_{E,d}(x, t)$  for Case 7 ( $D_2 = D_2 = 1.1 \times 10^{-9} \text{m}^2 \text{s}^{-1}$ ) and Case 8 ( $D_1 = 1.1 \times 10^{-9} \text{m}^2 \text{s}^{-1}$ ,  $D_2 = 9.3 \times 10^{-9} \text{m}^2 \text{s}^{-1}$ ) were identical to those obtained for Case 1 ( $D_2 = D_2 = 9.3 \times 10^{-9} \text{m}^2 \text{s}^{-1}$ ) at all times and locations. The increase in the diffu-



sion ion fluxes associated with increasing  $D_i$  was balanced by the corresponding increase in the electrical conductivity  $\sigma$ . In fact, for electrolytes with symmetric diffusion coefficients  $D_1 = D_2 = D$ , such as Cases 1 and 7,  $\dot{q}_{E,d}$  was independent of diffusion coefficient  $D$  because  $D$  appearing in the numerator canceled with that in the expression of  $\sigma$  in the denominator [Equation (7.4)].

#### 7.2.4.2 Steric heat generation rate $\dot{q}_{E,s}$

Figures 7.4(a) and 7.4(c) show the steric heat generation rate  $\dot{q}_{E,s}(x, 11t_c/8)$  [Equation (7.4)] as a function of location  $x$  near the positive Electrode A for Cases 1–4 and for Cases 1, 5, and 6, respectively. Similarly, Figures 7.4(b) and 7.4(d) show  $\dot{q}_{E,s}(x, 11t_c/8)$  as a function of  $2L - x$  near the negative Electrode B for Cases 1–4 and for Cases 1, 5, and 6, respectively. Figure 7.4 indicates that the profiles of the heat generation rates  $\dot{q}_{E,s}$  were spatially asymmetric for electrolytes with asymmetric  $z_i$  and/or  $a_i$ , e.g., those in Cases 3, 4, and 6. It is also interesting to note that the heat generation rate  $\dot{q}_{E,s}$  had the same order of magnitude as  $\dot{q}_{E,d}$  (Figure 7.3) for all cases considered. For a given electrode, electrolytes sharing the same counterion properties  $z_i$  and  $a_i$  and bulk concentration  $c_{i,\infty}$  featured the same heat generation rate  $\dot{q}_{E,s}$  profiles. Increasing  $|z_i|$  narrowed the region where the steric heat generation rate  $\dot{q}_{E,s}$  was significant without affecting its maximum value. However, increasing  $a_i$  reduced the magnitude of  $\dot{q}_{E,s}$ . Here also, the steric heat generation rate  $\dot{q}_{E,s}$  was unaffected by the diffusion coefficient  $D_i$ . In fact, in the limiting case of  $D_1 = D_2 = D$ , its expression was independent of diffusion coefficient.

#### 7.2.4.3 Heat of mixing heat generation rate $\dot{q}_{S,c}$

Figures 7.5(a) and 7.5(c) show the heat of mixing heat generation rate  $\dot{q}_{S,c}(x, 11t_c/8)$ , [Equation (7.7)] as a function of location  $x$  near the positive Electrode A for Cases 1–4 and for Cases 1, 5, and 6, respectively. Similarly, Figures 7.5(b) and 7.5(d) show  $\dot{q}_{S,c}(x, 11t_c/8)$  as a function of  $2L - x$  near the negative Electrode B for Cases 1–4 and for Cases 1, 5, and 6, respectively. The heat generation rate profiles  $\dot{q}_{S,c}$  near each electrode were very similar for

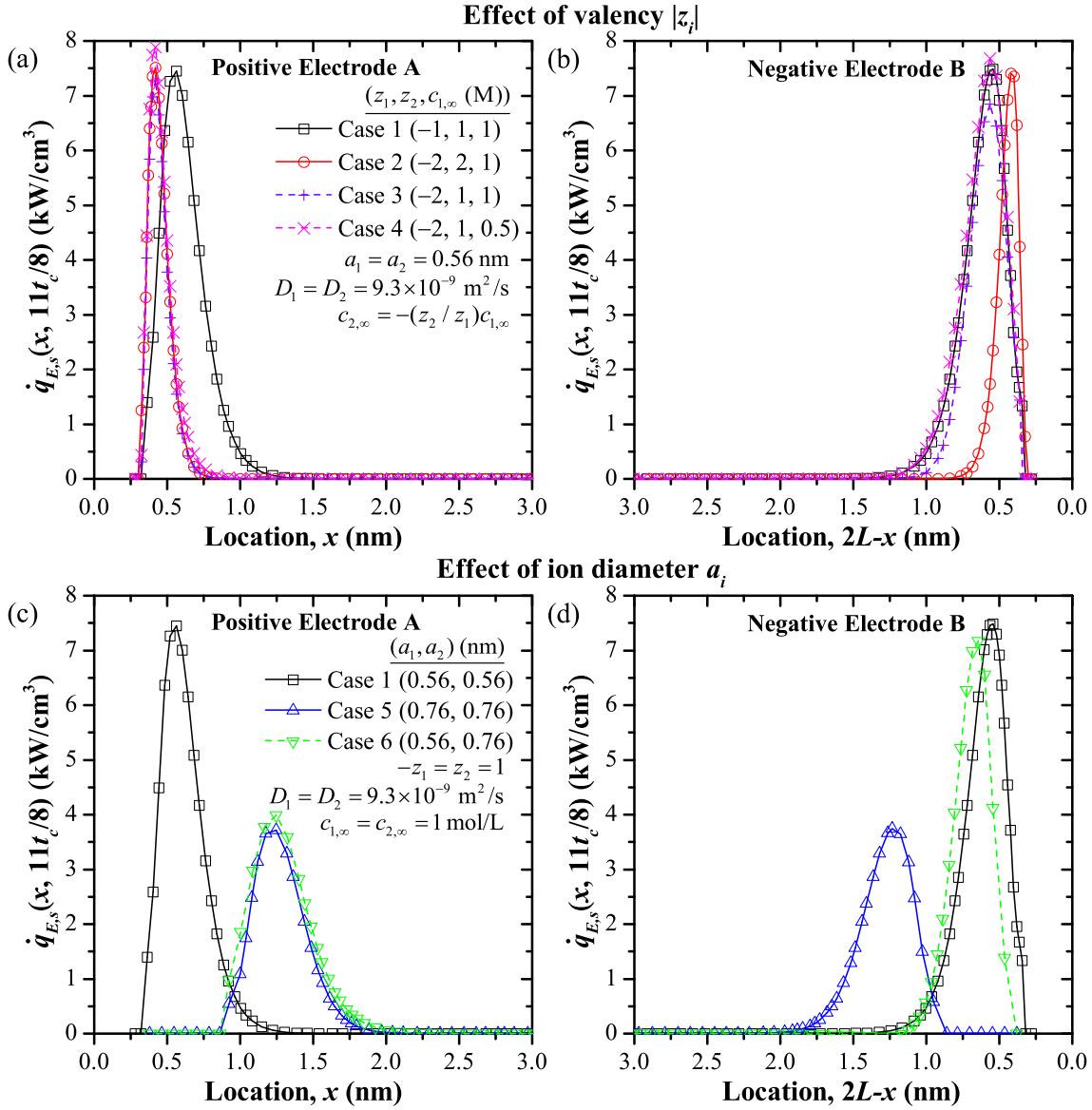


Figure 7.4: Steric heat generation rate  $\dot{q}_{E,s}(x, 11t_c/8)$  as a function of location (a) and (c)  $x$  near the positive Electrode A and (b) and (d)  $2L - x$  near the negative Electrode B. Plots (a) and (b) show Cases 1–4 with different  $z_i$  while plots (c) and (d) show Cases 5 and 6 with different  $a_i$ . All cases correspond to time  $t = 11t_c/8$  near the end of a charging step.

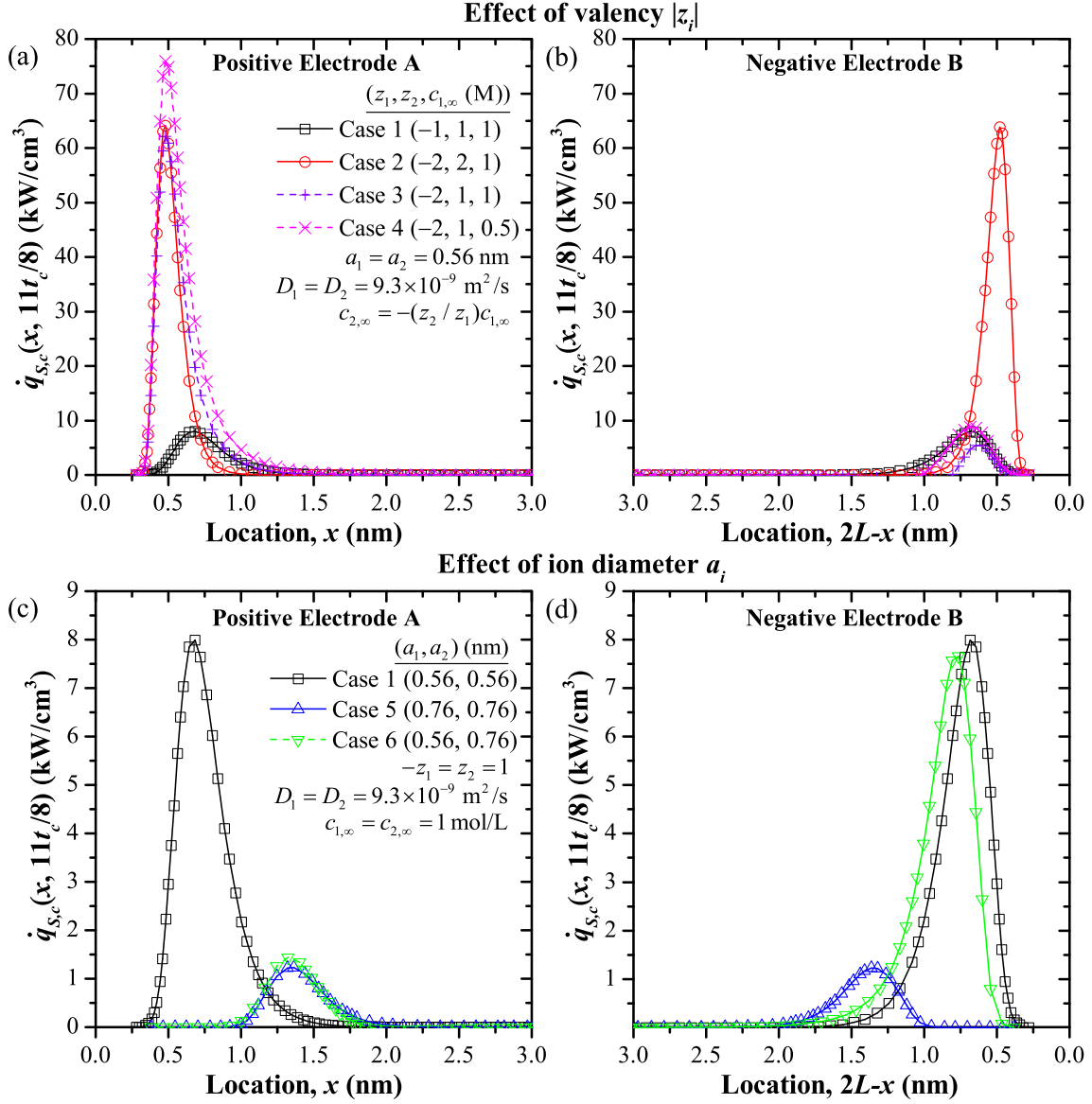


Figure 7.5: Heat of mixing heat generation rate  $\dot{q}_{S,c}(x, 11t_c/8)$  as a function of location (a) and (c)  $x$  near the positive Electrode A and (b) and (d)  $2L - x$  near the negative Electrode B. Plots (a) and (b) show Cases 1–4 with different  $z_i$  while plots (c) and (d) show Cases 5 and 6 with different  $a_i$ . All cases correspond to time  $t = 11t_c/8$  near the end of a charging step.

cases sharing the same counterion properties  $z_i$  and  $a_i$ . The heat of mixing heat generation rate  $\dot{q}_{S,c}$  increased strongly with increasing valency  $|z_i|$ . Indeed, increasing the counterion valency from  $|z_i| = 1$  to  $|z_i| = 2$  increased the maximum value of  $\dot{q}_{S,c}$  by nearly an order of magnitude. By contrast, recall that  $\dot{q}_{E,d}$  and  $\dot{q}_{E,s}$  both decreased with increasing  $|z_i|$ . Equation (7.7) indicates that, for electrolytes with symmetric valency  $-z_1 = z_2 = z$  such as in Cases 1 and 2, the local heat generation rate  $\dot{q}_{S,c}$  was proportional to  $z^3$ . In fact, for  $|z_i| > 1$ ,  $\dot{q}_{S,c}$  provided the largest contribution to the total reversible heat generation rate  $\dot{q}_{rev}$ . The strong effect of  $|z_i|$  on  $\dot{q}_{S,c}$  resulted from strong electrostatic interactions between ions accounted for by the Debye-Hückel activity coefficient [Equation (7.6)]. Moreover, the heat of mixing heat generation rate  $\dot{q}_{S,c}$  decreased with increasing counterion diameter  $a_i$ . Here also, the dependence of  $\dot{q}_{S,c}$  on  $a_i$  was stronger than that of  $\dot{q}_{E,d}$  and  $\dot{q}_{E,s}$ . Finally, results for Cases 7 and 8 with varying  $D_i$  were identical to those of Case 1 everywhere (not shown). This indicates that  $\dot{q}_{S,c}$  was independent of the diffusion coefficient  $D_i$  as suggested by its definition in Equation (7.7).

#### 7.2.4.4 Overall reversible heat generation rate $\dot{q}_{rev}$

Figures 7.6(a) and 7.6(c) show the overall reversible heat generation rate  $\dot{q}_{rev}(x, t) = \dot{q}_{E,d}(x, t) + \dot{q}_{E,s}(x, t) + \dot{q}_{S,c}(x, t) + \dot{q}_{S,T}(x, t)$  as a function of location  $x$  near the positive Electrode A for Cases 1–4 and for Cases 1, 5, and 6, respectively, at time  $t = 11t_c/8$  near the end of a charging step. Similarly, Figures 7.6(b) and 7.6(d) show  $\dot{q}_{rev}(x, 11t_c/8)$  as a function of  $2L - x$  near the negative Electrode B for Cases 1–4 and for Cases 1, 5, and 6, respectively. The overall reversible heat generation rate  $\dot{q}_{rev}$  was spatially asymmetric for electrolytes with asymmetric  $z_i$  and  $a_i$ , e.g., those in Cases 3, 4, and 6. It was larger near the electrode whose counterion had a larger valency  $|z_i|$  and/or a smaller ion diameter  $a_i$ . The strong effect of  $z_i$  on  $\dot{q}_{rev}$  was caused by its effects on  $\dot{q}_{S,c}$  which dominated over the other heat generation terms for  $|z_i| > 1$ . Finally,  $\dot{q}_{rev}$ , like all its components, was independent of the diffusion coefficient  $D_i$  for all cases considered. Note that the heat generation rate  $\dot{q}_{S,T}$  [Equation (7.7)] was negligible compared with the other heat generation rates for Cases 1–8. This was also observed in the simulations of binary and symmetric electrolytes in Chapters 4 and 6.

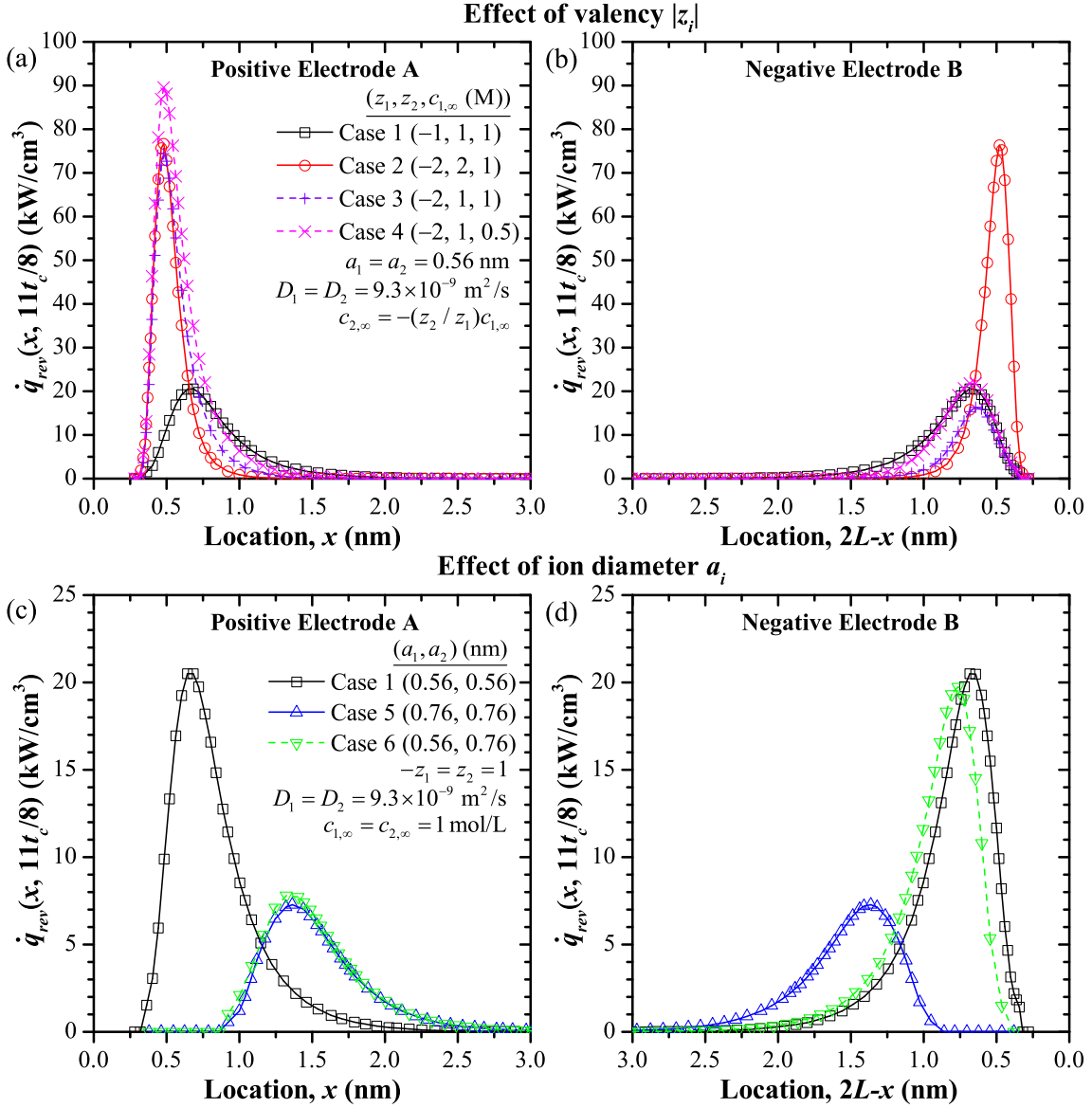


Figure 7.6: Overall reversible heat generation rate  $\dot{q}_{rev}(x, 11t_c/8)$  as a function of location (a) and (c)  $x$  near the positive Electrode A and (b) and (d)  $2L - x$  near the negative Electrode B. Plots (a) and (b) show Cases 1–4 with different  $z_i$  while plots (c) and (d) show Cases 5 and 6 with different  $a_i$ . All cases correspond to time  $t = 11t_c/8$  near the end of a charging step.

#### 7.2.4.5 Total Heat Generation Rates $\dot{Q}_{J,irr}''$ and $\dot{Q}_{rev}''$

It is difficult to directly compare the total irreversible and reversible heating based on the local volumetric heat generation rates  $\dot{q}_{J,irr}$  and  $\dot{q}_{rev}$ . Indeed, in all cases,  $\dot{q}_{J,irr}$  was very small compared to the peak values of  $\dot{q}_{rev}$ . However,  $\dot{q}_{J,irr}$  was uniform throughout the 40  $\mu\text{m}$ -thick electrolyte region while  $\dot{q}_{rev}$  was significant only inside the EDL region located within a few nanometers of the electrode surfaces. To compare their relative significance, they should be integrated over the entire electrolyte volume to assess their overall contribution to the total heat generation. To do so, the total irreversible and reversible heat generation rates per unit separator surface area (in  $\text{W m}^{-2}$ ) were defined as

$$\dot{Q}_{J,irr}''(t) = \int_0^{2L} \dot{q}_{J,irr}(x, t) dx \quad \text{and} \quad \dot{Q}_{rev}''(t) = \int_0^{2L} \dot{q}_{rev}(x, t) dx. \quad (7.17)$$

Figure 7.7 shows the total reversible heat generation rate  $\dot{Q}_{rev}''(t)$  as a function of time  $t$  for (a) Cases 1–4 with different values of  $z_i$  and (b) Cases 1, 5, and 6 with different values of  $a_i$  over one and a half cycles. The corresponding values of  $\dot{Q}_{J,irr}''(t)$  were constant and equal to  $\dot{Q}_{J,irr}'' = 2\dot{q}_{J,irr}L$  where  $L = 20 \mu\text{m}$  and  $\dot{q}_{J,irr}$  is reported in Table 7.1. The total reversible heat generation rate  $\dot{Q}_{rev}''(t)$  was periodic in time  $t$ , positive during charging, and negative during discharging. For the conditions simulated, the reversible heat generation rate  $\dot{Q}_{rev}''(t)$  was systematically larger than  $\dot{Q}_{J,irr}''$ . Indeed, the maximum value of  $|\dot{Q}_{rev}''(t)|$  was on the order of 20 to 40  $\text{W m}^{-2}$  while  $\dot{Q}_{J,irr}''$  was on the order of 0.001 to 0.1  $\text{W m}^{-2}$ . Note that the simulations in Chapter 4 for binary and symmetric organic electrolyte, namely TEABF<sub>4</sub> in propylene carbonate, also predicted that  $|\dot{Q}_{rev}''(t)|$  was larger than  $\dot{Q}_{J,irr}''(t)$  by about one order of magnitude. The relatively small values of  $\dot{Q}_{J,irr}''(t)$  obtained in the present study compared to that in Chapter 4 can be attributed to the larger conductivity  $\sigma_\infty$  of the aqueous electrolyte resulting in smaller Joule heating.

Figure 7.7(a) establishes that increasing either or both ion valencies  $|z_1|$  and  $|z_2|$  led to larger reversible heat generation while Joule heating decreased (Table 7.1). Cases 1–3 corresponded to the same bulk electrolyte concentration  $c_{1,\infty}$ . Comparing these cases reveals that  $\dot{Q}_{rev}''(t)$  and  $\dot{Q}_{J,irr}''(t)$  for Case 3 ( $z_1 = -2$ ,  $z_2 = 1$ ) with asymmetric  $z_i$  fell

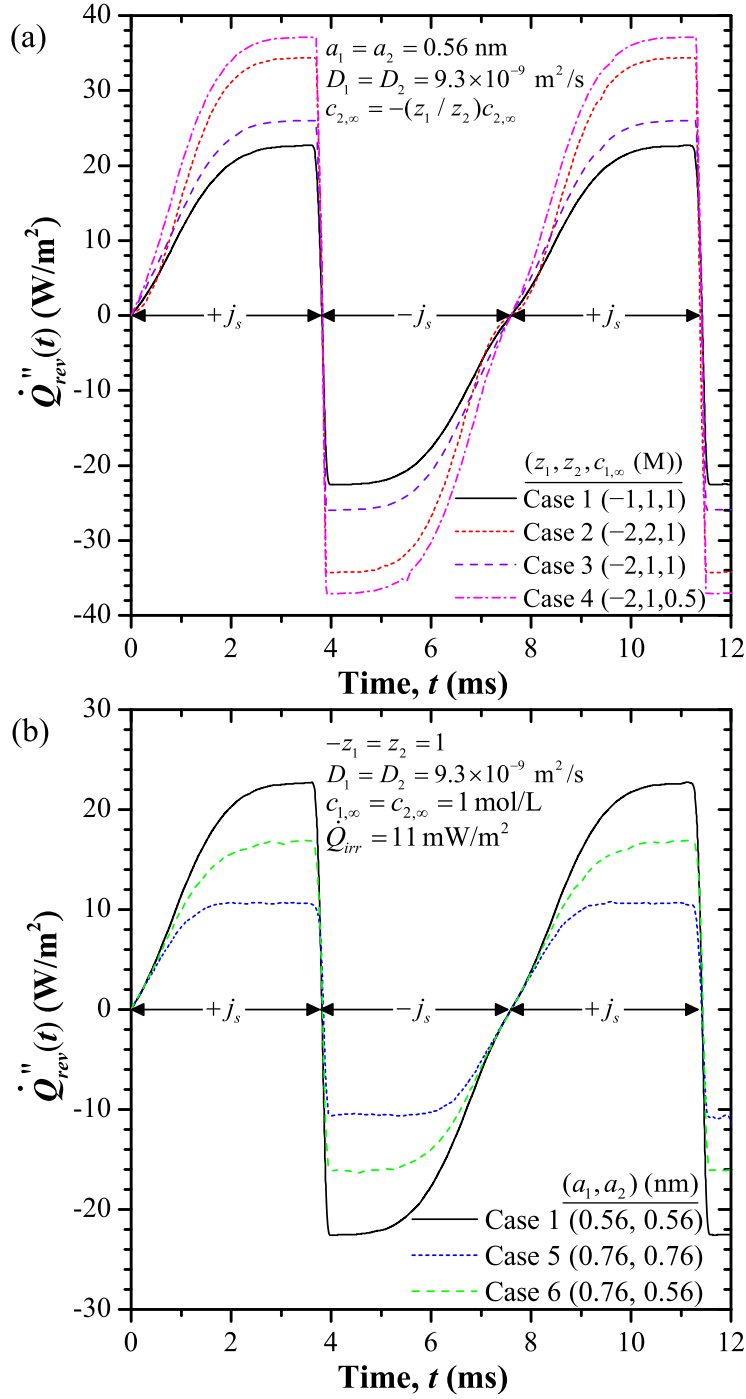


Figure 7.7: Total reversible heat generation rates  $\dot{Q}_{rev}''(t)$  as functions of  $t$  over one and a half cycles for (a) Cases 1–4 with  $a_1 = a_2 = 0.56$  nm,  $D_1 = D_2 = 9.3 \times 10^{-9}$  m<sup>2</sup>s<sup>-1</sup>, and different  $z_i$  and (b) Cases 1, 5, and 6 featuring  $-z_1 = z_2 = 1$ ,  $D_1 = D_2 = 9.3 \times 10^{-9}$  m<sup>2</sup>s<sup>-1</sup>, and different  $a_i$ .

between those corresponding to symmetric electrolytes, namely Case 1 ( $-z_1 = z_2 = 1$ ) and Case 2 ( $-z_1 = z_2 = 2$ ). Cases 3 and 4 demonstrate that the total heat generation rates were also sensitive to the bulk ion concentrations  $c_{i,\infty}$ . These two cases featured the same ion properties  $z_i$ ,  $a_i$ , and  $D_i$  for both ion species, but the bulk ion concentrations  $c_{i,\infty}$  of Case 4 were half those of Case 3. The results established that both  $|\dot{Q}_{rev}''(t)|$  and  $\dot{Q}_{J,irr}''(t)$  increased with decreasing bulk concentrations  $c_{1,\infty}$  and  $c_{2,\infty}$  due to the associated smaller electrical conductivity  $\sigma_\infty$ .

Figure 7.7(b) shows the total reversible heat generation rate  $\dot{Q}_{rev}''(t)$  as a function of time  $t$  over one and a half cycles for Cases 1, 5, and 6 corresponding to different values of  $a_1$  and  $a_2$ . The total irreversible heat generation rate  $\dot{Q}_{J,irr}''(t)$  was unaffected by  $a_i$  and remained constant and equal to  $\dot{Q}_{J,irr}'' = 11 \text{ mW m}^{-2}$ . It was smaller than  $|\dot{Q}_{rev}''(t)|$  by several orders of magnitude. On the other hand, the total reversible heat generation rate  $|\dot{Q}_{rev}''(t)|$  increased with decreasing  $a_i$  for either ion species. For Case 6 with asymmetric  $a_i$  ( $a_1 = 0.76 \text{ nm}$ ,  $a_2 = 0.56 \text{ nm}$ ),  $\dot{Q}_{rev}''(t)$  was approximately equal to the arithmetic mean of those for the corresponding symmetric electrolytes represented by Case 1 ( $a_1 = a_2 = 0.56 \text{ nm}$ ) and Case 5 ( $a_1 = a_2 = 0.76 \text{ nm}$ ).

Finally, the total irreversible heat generation rate  $\dot{Q}_{J,irr}''(t)$  for Case 1 ( $D_1 = D_2 = 9.3 \times 10^{-9} \text{ m}^2\text{s}^{-1}$ ), Case 7 ( $D_1 = D_2 = 1.1 \times 10^{-9} \text{ m}^2\text{s}^{-1}$ ), and Case 8 ( $D_1 = 1.1 \times 10^{-9} \text{ m}^2\text{s}^{-1}$ ,  $D_2 = 9.3 \times 10^{-9} \text{ m}^2\text{s}^{-1}$ ) featuring different values of  $D_i$  was constant and equal to  $11 \text{ mW m}^{-2}$ ,  $95 \text{ mW m}^{-2}$ , and  $20 \text{ mW m}^{-2}$ , respectively. Its magnitude increased with decreasing diffusion coefficient  $D_i$  of either ion. It was more strongly influenced by the larger of the two diffusion coefficients. This can be attributed to the fact that the ion with the larger diffusion coefficient carried the majority of the current density within the bulk electrolyte. On the other hand,  $\dot{Q}_{rev}''(t)$ , like the local reversible heat generation rates  $\dot{q}_{E,d}$ ,  $\dot{q}_{E,s}$ , and  $\dot{q}_{S,c}$ , was unaffected by the values of  $D_i$  and equal to that of the baseline Case 1 (Figure 7.7).



### 7.2.5 Temperature

Figure 7.8 shows the temperature differences (a)  $T(a/2, t) - T_0$  near the positive Electrode A, (b)  $T(L, t) - T_0$  at the centerline, and (c)  $T(2L - a/2, t) - T_0$  near the negative Electrode B for Cases 1–4 featuring different values of  $z_i$ . Note that the temperature rise for the present simulations was on the order of millikelvins. This can be attributed to the very rapid charging of planar electrodes resulting in very small cycle periods on the order of milliseconds. Cases 3 and 4 had asymmetric valency  $z_1 = -2$  and  $z_2 = 1$  and yielded spatially asymmetric temperature oscillations caused by the asymmetric reversible heat generation rate  $\dot{q}_{rev}$ . In both cases, the temperature oscillations near the positive electrode [Figure 7.8(a)] were approximately three times larger than as those near the negative electrode [Figure 7.8(c)]. This can be attributed to the fact that the large valency  $z_1 = -2$  of the anion produced large  $\dot{q}_{S,c}$  near the positive electrode. In addition, the asymmetric electrolyte considered in Cases 3 and 4 produced larger temperature oscillations at  $x = a/2$  than either of the symmetric electrolytes of Case 1 ( $-z_1 = z_2 = 1$ ) and Case 2 ( $-z_1 = z_2 = 2$ ). For symmetric electrolytes as in Cases 1 and 2, the temperature profiles always remained spatially symmetric so that no significant heat fluxes crossed the cell centerline. By contrast, for asymmetric electrolytes as in Cases 3 and 4, there was significant heat exchange between the two halves of the cell. As a result, the temperatures evolved differently between the symmetric and asymmetric electrolytes.

Figures 7.8(d), 7.8(e), and 7.8(f) respectively show the temperature difference  $T(a/2, t) - T_0$  near the positive Electrode A,  $T(L, t) - T_0$  at the centerline, and  $T(2L - a/2, t) - T_0$  near the negative Electrode B for Cases 1, 5, and 6 featuring different values of  $a_i$ . The asymmetric electrolyte of Case 6 ( $a_1 = 0.76$  nm,  $a_2 = 0.56$  nm) exhibited larger temperature oscillations near the negative electrode [Figure 7.8(f)] than near the positive electrode [Figure 7.8(d)]. This can be attributed to the larger reversible heat generation rate  $\dot{q}_{rev}$  associated with the smaller cation diameter  $a_2 = 0.56$  nm.

Moreover, Figures 7.8(b) and 7.8(e) indicate that, for a given case, the temperature oscillations at the centerline were smaller in amplitude, less angular, and slightly delayed

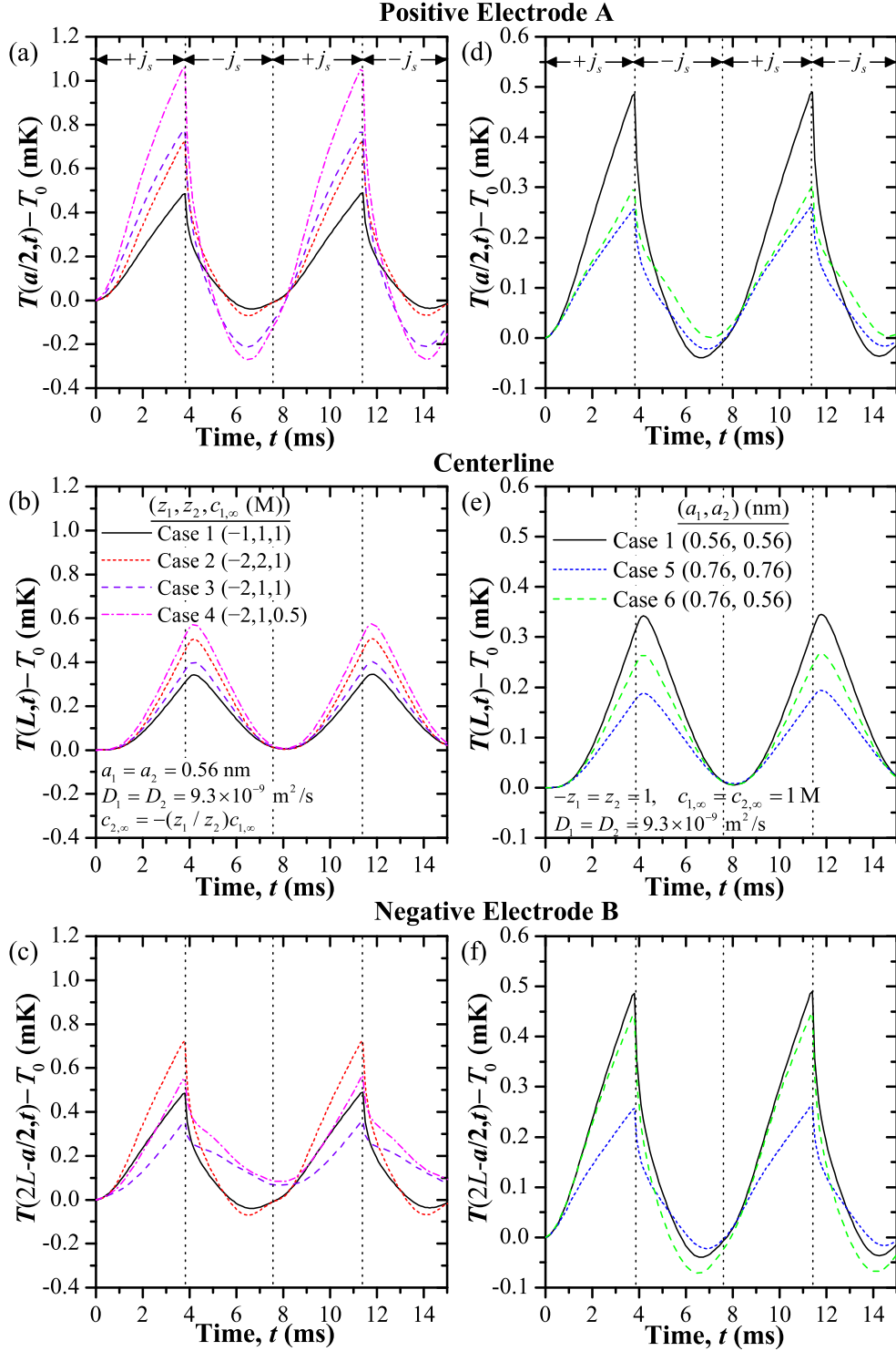


Figure 7.8: Temperature rise  $T(x, t) - T_0$  as functions of time  $t$  for (a)-(c) Cases 1–4 with different  $z_i$  and (d)-(f) Cases 1, 5, and 6 with different  $a_i$ . Results are shown for three locations, namely, (a) and (d) at  $x = a/2$  near the positive Electrode A, (b) and (e) at the centerline  $x = L$ , and (c) and (f) at  $x = 2L - a/2$  near the negative Electrode B.

compared to those close to the electrodes. This was also observed for binary and symmetric electrolytes in Chapters 4 and 6. It was attributed to the fact that the reversible heat generated at the electrode surfaces had to conduct through the electrolyte to reach the centerline [2]. In addition, the centerline temperature  $T(L, t)$  for the asymmetric electrolyte of Case 3 ( $z_1 = -2, z_2 = 1$ ) fell between those of the symmetric electrolytes considered in Case 1 ( $-z_1 = z_2 = 1$ ) and Case 2 ( $-z_1 = z_2 = 2$ ) corresponding to the same bulk concentration  $c_{1,\infty}$ . Likewise, the centerline temperature  $T(L, t)$  [Figure 7.8(e)] for the asymmetric electrolyte of Case 6 ( $a_1 = 0.76$  nm,  $a_2 = 0.56$  nm) fell between those of the corresponding symmetric electrolytes represented by Case 1 ( $a_1 = a_2 = 0.56$  nm) and Case 5 ( $a_1 = a_2 = 0.76$  nm). Note also that the centerline temperature  $T(L, t)$  for Cases 1, 5, and 6 converged to the same value after each complete cycle (e.g.,  $t = 7.6$  ms). Indeed, reversible heating during the charging step was compensated by reversible cooling during the discharging step. Thus, the net reversible heat generated over a complete charge-discharge cycle was  $\int_0^{t_c} \dot{Q}_{rev}''(t) dt = 0$  and the net temperature rise over one cycle was solely due to the irreversible heat generation rate  $\dot{Q}_{J,irr}''$ . For these three cases,  $\dot{Q}_{J,irr}''$  was identical (Table 1).

Table 7.2 summarizes qualitative changes in the heat generation rates  $\dot{q}_{J,irr}$ ,  $\dot{q}_{rev}$ ,  $\dot{Q}_{J,irr}''$ , and  $\dot{Q}_{rev}''$  as well as in the integral areal capacitance  $C_{s,int}$  caused by increasing the ions' effective diameter  $a_i$ , valency  $|z_i|$ , diffusion coefficient  $D_i$ , or bulk concentration  $c_{i,\infty}$ . Note that the bulk concentrations  $c_{1,\infty}$  and  $c_{2,\infty}$  cannot be varied independently, as they are coupled by the requirement for electroneutrality. Table 7.2 suggests a few design rules for choosing electrolytes in order to minimize heat generation in EDLCs. First, large bulk concentrations  $c_{i,\infty}$  are desirable to increase ionic conductivity  $\sigma$  and thus reduce both the total irreversible and reversible heat generation rates  $\dot{Q}_{J,irr}''$  and  $\dot{Q}_{rev}''$  as well as increasing the capacitance. Similarly, at least one ion with large diffusion coefficient  $D_i$  should be used to minimize  $\dot{Q}_{J,irr}''$ . This ion species will carry the majority of the current in the bulk electrolyte. Note that large diffusion coefficient is also beneficial to the EDLC capacitance at large scan rates [43]. Finally, increasing  $|z_i|$  and/or decreasing  $a_i$  increases the EDLC capacitance  $C_{s,int}$  but also increases the reversible heat generation rate  $\dot{Q}_{rev}''$ . In particular, thermal management strategies for EDLCs using large-valency ions should be designed to

Table 7.2: Summary of the effects of changing ion properties on the heat generation rates  $\dot{q}_{J,irr}$ ,  $\dot{q}_{rev}$ ,  $\dot{Q}''_{J,irr}$ , and  $\dot{Q}''_{rev}$  as well as the integral capacitance  $C_{s,int}$  during galvanostatic cycling.

Increasing $\Rightarrow$	Diameter $a_i$	Valency $ z_i $	Diffusion coefficient $D_i$	Bulk concentration $c_{i,\infty}$
$\dot{q}_{J,irr}$	—	↓	↓	↓
$\dot{q}_{rev}$	<b>counter-electrode</b>	↓	↑↑	↓
	<b>co-electrode</b>	—	—	↓
$\dot{Q}''_{J,irr} = 2L\dot{q}_{J,irr}$	—	↓	↓	↓
$\dot{Q}''_{rev}$	↓	↑	—	↓
$C_{s,int}$	↓	↑	—	↑

accommodate large reversible heat generation rates  $\dot{q}_{rev}$  near the counter-electrode.

### 7.2.6 Asymmetric electrolytes in porous electrodes

The present simulations were limited to planar electrodes while practical EDLC devices use porous electrodes. The present model could be extended to porous electrodes in at least three possible ways. First, the continuum model presented in Section 7.1 could be used to predict local heat generation rates and temperature in transient two-dimensional or three-dimensional simulations of porous electrodes. However, such simulations would be computationally very costly and time consuming and fall beyond the scope of the present study. Second, volume averaging theory could be applied to the governing equations derived in the present study, as performed for numerous transport phenomena in porous media [105]. Third, correlations predicting the heat generation rates in porous electrodes could be developed based on scaling analysis of the governing equations for planar electrodes modified by a semi-empirical geometric parameter identified from experimental data for porous electrodes. This method was successfully used to develop a correlation for the equilibrium areal capacitance of porous electrodes in Ref. [102]. I anticipate that the qualitative observations regarding the effects of ion valency and size reported for planar electrodes will also apply to

porous electrodes regardless of their morphology.

Finally, it is important to note that the electrode's porous morphology adds complications that cannot be accounted for in the planar analysis. First, when the effective ion diameter is too large for ions to enter the pores, the active electrode surface area is reduced and consequently the overall reversible heating would be reduced. In addition, ions may shed their solvation shells to enter pores smaller than their solvated radii, resulting in a sharp increase in capacitance [22, 92]. However, the present model assumes that the effective diameter of the ions is constant. As a result, it cannot predict the thermal effects associated with ion desolvation.

### 7.3 Conclusion

The present study developed the first thermal model based on first principles for the local irreversible and reversible heat generation rates and temperature of EDLCs with multiple ion species and/or asymmetric electrolytes. Detailed numerical simulations were performed for different binary and asymmetric electrolytes based on the properties of aqueous  $\text{H}_2\text{SO}_4$ . First, the irreversible heat generation rate  $\dot{q}_{J,irr}$  was uniform across the electrolyte and equal to  $\dot{q}_{J,irr} = j_s^2/\sigma_\infty$ . It decreased with increasing valency  $|z_i|$  or diffusion coefficient  $D_i$  of one or both ion species due to the resulting increase in electrical conductivity  $\sigma_\infty$  of the electrolyte. However,  $\dot{q}_{J,irr}$  was independent of the ion diameter  $a_i$ . The reversible heat generation rate  $\dot{q}_{rev}$  near each electrode was governed by the properties of the counterion. It increased with increasing valency  $|z_i|$  and decreasing ion diameter  $a_i$  but was independent of diffusion coefficient  $D_i$ . As a result, electrolytes with asymmetric valency  $z_i$  or ion diameter  $a_i$  featured spatially asymmetric heat generation rates and larger temperature oscillations near the electrode with the larger  $|z_i|$  or smaller  $a_i$  of the counterion. The results demonstrate that thermal models must account for electrolyte asymmetry in order to accurately predict the local heat generation rates and temperature. This study suggests that to reduce the overall heat generation in EDLCs, electrolytes should feature large bulk concentrations  $c_{i,\infty}$  and at least one ion species with large diffusion coefficient. In addition, electrolytes chosen

to yield large capacitance via ions with large valency  $|z_i|$  and/or small diameter  $a_i$  are likely to feature large reversible heat generation rates generated near the electrode surfaces.

## CHAPTER 8

### **Electrochemical transport phenomena in hybrid pseudocapacitors under galvanostatic cycling**

This chapter aims to provide physical insights into the electrochemical transport and interfacial phenomena in hybrid pseudocapacitors under galvanostatic cycling. Particular attention was paid to determining the respective contributions of EDL formation and faradaic reactions to energy storage (in other words, how effectively the pseudocapacitive charge storage was utilized) under various cycling conditions and to identifying the physical phenomena limiting the faradaic charge storage. These insights were used to physically interpret features of experimentally measured cell potentials, and could help to guide optimization of hybrid pseudocapacitor designs, materials, and operating conditions. To accomplish these objectives, detailed numerical simulations were performed for a hybrid pseudocapacitor with planar electrodes using a first-principles continuum model accounting simultaneously for charge storage by electric double layer (EDL) formation and by faradaic reactions with intercalation [106]. Two asymptotic regimes were identified corresponding to (i) dominant faradaic charge storage at low current and low frequency or (ii) dominant EDL charge storage at high current and high frequency. Analytical expressions for the intercalated ion concentration and surface overpotential were derived for both asymptotic regimes. Features of the experimentally measured cell potential were physically interpreted. These insights could guide the optimization of hybrid pseudocapacitors.

## 8.1 Background

### 8.1.1 Experimental studies of pseudocapacitive materials

Various transition metal oxides have shown promising pseudocapacitive performance [17, 107]. For example, recent studies have demonstrated large capacitance associated with  $\text{Li}^+$  intercalation into crystalline  $\text{Nb}_2\text{O}_5$  [23, 107–110]. In hybrid  $\text{Nb}_2\text{O}_5$ /activated carbon pseudocapacitors, the  $\text{Nb}_2\text{O}_5$  electrode typically serves as the negative electrode relative to the positive activated carbon electrode [107, 109, 110]. This corresponds to  $\text{Li}^+$  intercalation in the  $\text{Nb}_2\text{O}_5$  electrode during charging and deintercalation during discharging. It is interesting to note that the synthesis of  $\text{Nb}_2\text{O}_5$  described in Ref. [108] resulted in  $\text{Nb}_2\text{O}_5$  electrodes with no initial Li and minimal contaminants, based on X-ray photoelectron spectroscopy data [108].

Pseudocapacitance has also been demonstrated with  $\text{MnO}_2$  involved in reversible redox reactions with  $\text{H}^+$ ,  $\text{K}^+$ , and  $\text{Li}^+$  [111–115]. In contrast to  $\text{Nb}_2\text{O}_5$ ,  $\text{MnO}_2$  has typically been used as the positive electrode in hybrid pseudocapacitors [111]. This corresponds to charging the device by deintercalation of the cation. Then, the pseudocapacitive electrode must contain a significant concentration of the reduced cation at the beginning of the cycle. Indeed, several pseudocapacitor studies, featuring  $\text{MnO}_2$  electrodes reacting with  $\text{K}^+$ , synthesized pseudocapacitive  $\text{MnO}_2$  electrodes by reduction of  $\text{KMnO}_4$  [112–114], resulting in the initial electrode composition  $\text{K}_{0.02}\text{MnO}_2\text{H}_{0.33}$  [112]. This corresponded to an initial concentration of K in the pseudocapacitive electrode of around  $1 \text{ mol L}^{-1}$ . Similarly, a study considering pseudocapacitors with  $\text{Li}^+$  intercalation into  $\text{MnO}_2$  synthesized the pseudocapacitive electrodes by reacting  $\text{MnO}_2$  with  $\text{Li}_2\text{CO}_3$  to obtain the initial composition  $\text{Li}_{0.5}\text{MnO}_2$  [115], i.e., an initial  $\text{Li}^+$  concentration around  $30 \text{ mol L}^{-1}$ .

Experimentally, it is difficult to discriminate between the fraction of charge storage achieved from faradaic reactions and that from EDL formation. For cyclic voltammetry (CV) cycling, experimentalists have attempted to differentiate between surface-controlled processes, such as EDL capacitance, and diffusion-controlled processes, such as battery-like faradaic charge storage with intercalation. To do so, they analyzed the relationship between



the amount of charge stored (called the “capacity” in C or in mAh) or the current and the scan rate [23, 110, 116]. However, this analysis was derived from the behavior associated with EDL and faradaic charge storage occurring independently of each other [17]. In practice, EDL formation and redox reactions can take place simultaneously, making it difficult to interpret experimental results for pseudocapacitors. Note also that, to the best of my knowledge, this analysis method is specific to CV and cannot be used for galvanostatic cycling.

For experiments under galvanostatic cycling, the cell potential  $\psi_s(t)$  is typically reported as a function of time. EC cell potentials are typically computed as the potential of the electrode giving up electrons to the external circuit during charging relative to that receiving electrons. Thus, the cell potential  $\psi_s(t)$  increases during charging and decreases during discharging. Figure 8.1 shows some typical examples of cell potential  $\psi_s(t)$  as a function of time for hybrid pseudocapacitors featuring (a) a  $\text{Nb}_2\text{O}_5$  negative electrode reacting with  $\text{Li}^+$  [107] or (b) a  $\text{MnO}_2$  positive electrode reacting with  $\text{K}^+$  [117]. Figure 8.1(a) indicates that, for hybrid pseudocapacitors with  $\text{Nb}_2\text{O}_5$ , the cell potential  $\psi_s(t)$  increased rapidly at the beginning of the charging step [107, 116, 118]. Then, the rate of change  $|\text{d}\psi_s/\text{d}t|$  abruptly decreased, resulting in a distinct “kink” in the potential evolution. The slope  $|\text{d}\psi_s/\text{d}t|$  also increased towards the end of the cycle, although it was not as large as at the beginning of the cycle. The cell potential  $\psi_s$  varied approximately linearly for the rest of the cycle, except for a very brief period of large slope  $|\text{d}\psi_s/\text{d}t|$  immediately after the charging/discharging transition [107, 116, 118]. Figure 8.1(a) also shows experimentally measured potential drops between each electrode and a reference electrode, denoted as  $\Delta\psi_P(t)$  and  $\Delta\psi_C(t)$  for the pseudocapacitive and carbon electrodes, respectively, and such that  $\psi_s(t) = \Delta\psi_C(t) - \Delta\psi_P(t)$ . It indicates that  $\Delta\psi_C(t)$  for the carbon electrode varied linearly and that the variation of  $|\text{d}\psi_s/\text{d}t|$  was associated with the pseudocapacitive electrode. Note that the range of  $\Delta\psi_P(t)$  and of  $\Delta\psi_C(t)$ , and thus the integral capacitances of the individual electrodes, were of the same order of magnitude. This can be attributed to the fact that the carbon electrode’s mass loading was 4.7 times that of the  $\text{Nb}_2\text{O}_5$  electrode, ensuring that both electrodes had the same capacitance at a particular current density [107]. Indeed, it is

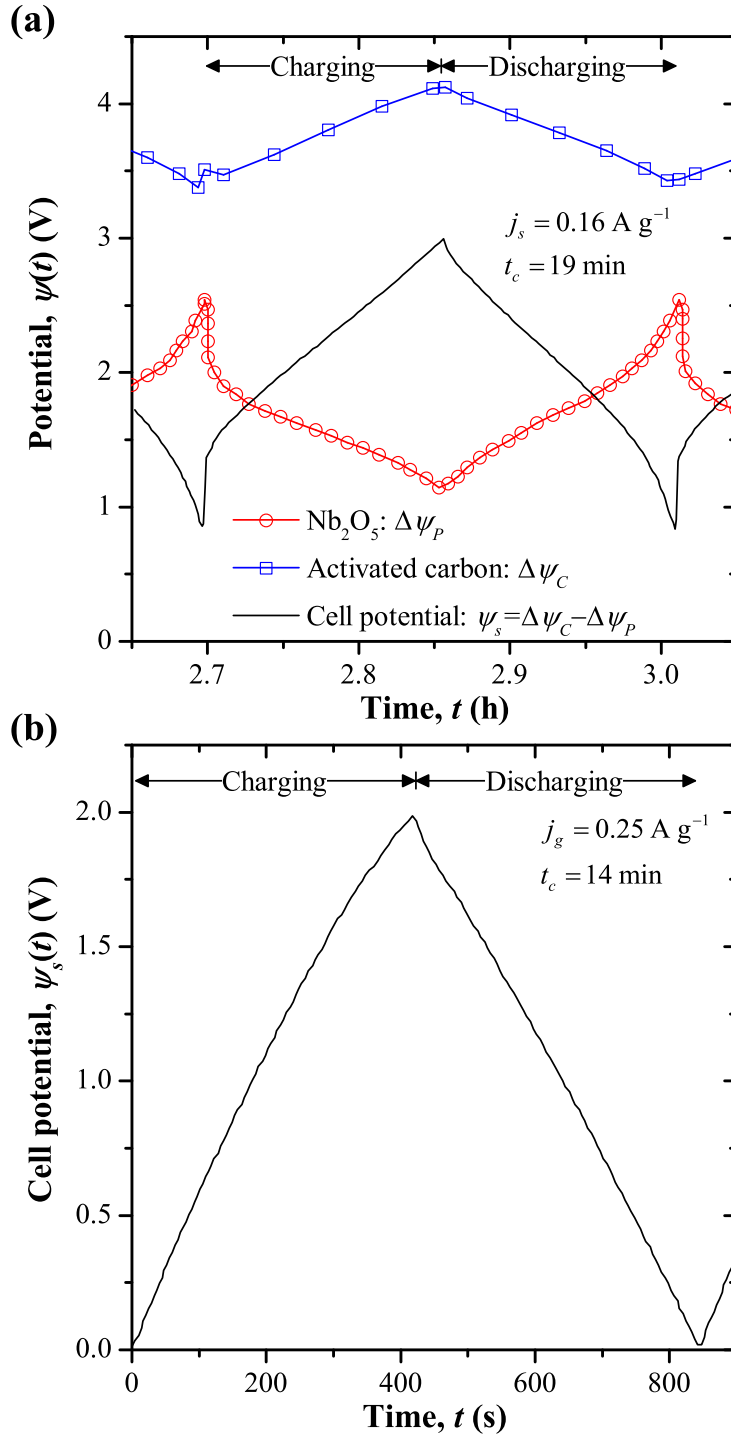


Figure 8.1: Experimental (a) cell potential  $\psi_s(t) = \Delta\psi_C(t) - \Delta\psi_P(t)$  for a hybrid pseudocapacitor using  $\text{Nb}_2\text{O}_5$  and potentials of the pseudocapacitive  $\Delta\psi_P(t)$  and carbon  $\Delta\psi_C(t)$  electrodes relative to a reference electrode, as well as (b)  $\psi_s(t) = \Delta\psi_P(t) - \Delta\psi_C(t)$  for a hybrid pseudocapacitor using  $\text{MnO}_2$  [117] as functions of time  $t$ .

common for hybrid pseudocapacitors to have electrodes with different loadings in order to match their capacitances [114–119]. Figure 8.1(b) indicates that, for hybrid pseudocapacitors featuring  $\text{MnO}_2$  positive electrodes,  $\psi_s(t) = \Delta\psi_P(t) - \Delta\psi_C(t)$  varied approximately linearly through most of the cycle. There was a slightly larger slope  $|\text{d}\psi_s/\text{d}t|$  immediately after the charging/discharging transition. Finally, pseudocapacitors and EDLCs with large electrical resistance and/or cycled at large currents also featured IR drops corresponding to instantaneous jumps in  $\psi_s$  at the transitions between charging and discharging steps and given by Ohm’s law. The present chapter aims to numerically reproduce these typical experimental curves in order to interpret their features.

### 8.1.2 Existing models of pseudocapacitors

Various models have been proposed for the electrochemical behavior of pseudocapacitors. Several studies have employed equivalent RC circuit models composed of ideal resistors and capacitors [18, 120–123]. The values of resistances and capacitances used in such models were fitted from experimental data. RC circuit models can be used for control purposes but, unfortunately, provide little insight into the physical phenomena governing pseudocapacitor operation [124]. In addition, many were developed under the assumption of uniform electrolyte concentration and cannot adequately account for EDL formation [54, 125, 126].

Other proposed models for pseudocapacitors solved the Poisson equation governing local electric potential [106, 127–132], sometimes coupled with the mass transport equation governing the ion concentrations in the electrolyte [106, 128, 129]. Most of these models considered porous electrodes as homogeneous composites with some effective electrical conductivity [127–132] and effective ion diffusion coefficients [128, 129]. They were used to investigate the effects of pseudocapacitive electrode morphology [127, 128, 133], exchange current density [130, 131], and EDL areal capacitance [131] on the temporal evolution of the cell potential during discharging as well as the energy and power densities under galvanostatic operation. Some studies also focused on tool development for simulating stacks of many pseudocapacitor cells with relatively low computational cost [129] or for retrieving

cell properties such as the electrical conductivity of the electrode or electrolyte, the EDL capacitance, and/or the exchange current density from experimental measurements [131]. Such models are valuable for simulating entire devices with porous electrodes of realistic dimensions. However, they often accounted for the EDL formation only via a constant EDL capacitance [127–132] taken from experimental measurements for carbon [127, 128, 132] or used as a fitting parameter [129]. They also typically assumed that the ion concentrations in the electrolyte were uniform [127, 130–133], treated ions as point charges [128, 129], and/or accounted only for ion diffusion while ignoring electromigration [128]. In other words, the two charge storage mechanisms, i.e., EDL formation and redox reactions, were entirely decoupled. Recently, Girard *et al.* [106] presented a continuum model accounting simultaneously for coupled EDL formation and faradaic reactions and for finite ion size [106]. This model was used to physically interpret cyclic voltammetry (CV) measurements for hybrid pseudocapacitors with planar electrodes and binary and asymmetric electrolyte [106]. The study established that CV curves featured a faradaic regime dominated by redox reactions and a capacitive regime dominated by EDL formation. It also clarified the physical interpretation of the so-called “*b*-value” observed experimentally in the power law relating current and scan rate [106].

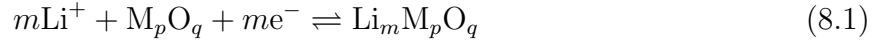
Finally, molecular dynamics (MD) models, accounting for individual atoms and their interactions, have also been developed for pseudocapacitors [134–138]. They have been used to predict the energy barriers associated with surface adsorption and bulk intercalation [134–137] as well as the charge distribution [135] and the crystal structure of the pseudocapacitive electrode material [134, 135, 137, 138]. Unfortunately, the large computational cost limits MD simulations to time and length scales on the order of 10 nm and 10  $\mu$ s [139, 140], respectively. These are much smaller than realistic device dimensions or time scales for pseudocapacitor charging and discharging under galvanostatic cycling, making MD models impractical for simulating realistic device operation.

## 8.2 Analysis

The present chapter adapts the first-principles continuum model presented in Ref. [106] for galvanostatic cycling. In contrast to most existing continuum models [127–133], it simultaneously accounted for the coupling between the EDL formation and the faradaic reaction.

### 8.2.1 Schematic and assumptions

Figure 8.2 illustrates (a) the EDL structure near the pseudocapacitive electrode according to the Stern model and (b) the one-dimensional (1D) hybrid pseudocapacitor considered in the present study along with the associated coordinate system. The simulated device consisted of two current collectors supporting planar electrodes separated by a binary and asymmetric electrolyte with inter-electrode distance  $2L$ . The pseudocapacitive electrode of thickness  $L_P$  consisted of a transition metal oxide  $M_pO_q$  reacting chemically with  $Li^+$  according to the following reversible redox reaction



where  $m$  is the number of  $Li^+$  ions intercalated per molecule of the metal oxide  $M_pO_q$ . Its maximum value depends on the metal oxide. For example,  $Nb_2O_5$  reacting with  $Li^+$  forms  $Li_2Nb_2O_5$  with  $m = 2$  in its fully-lithiated state [107]. The heterogeneous reaction occurring at the pseudocapacitive electrode/electrolyte interface transferred  $Li^+$  ions from the electrolyte into the  $M_pO_q$  matrix [26–28]. Subsequently, the intercalated  $Li^+$  migrated farther into the pseudocapacitive electrode, accompanied by reduction of the transition metal cations [28, 107]. On the other hand, the planar carbon electrode of thickness  $L_C$  did not react chemically with the electrolyte. Instead, it stored charge only in the EDL forming near its surface. Here, the subscripts  $P$ ,  $E$ , and  $C$  will be used to differentiate between concentrations and material properties within the pseudocapacitive electrode, the electrolyte, and the carbon electrode, respectively.

To make the problem mathematically tractable, the following assumptions were made:

- (1) The heterogeneous redox reaction expressed by Equation (8.1) occurred within the Stern

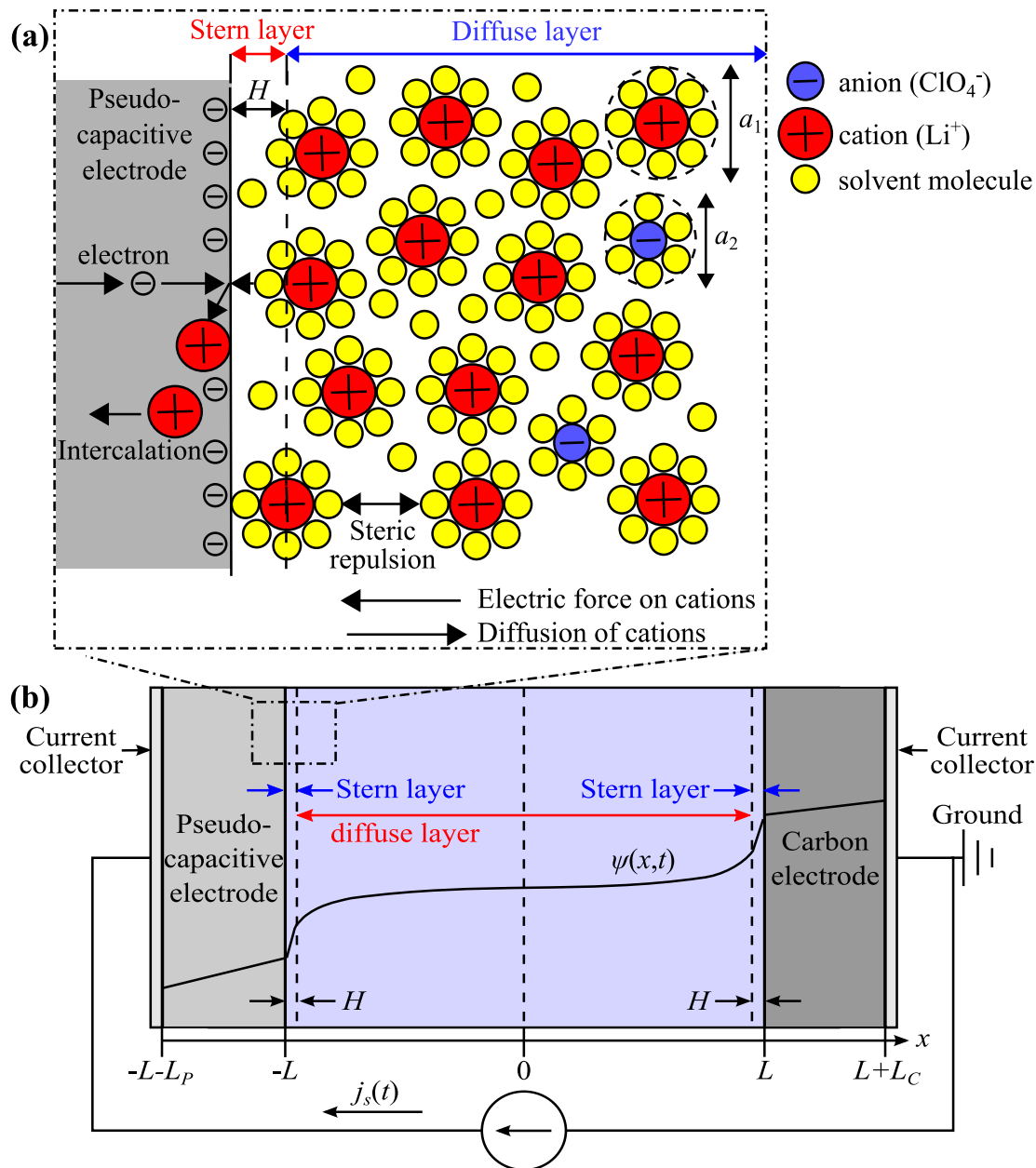


Figure 8.2: Illustration of (a) the electric double layer structure of a binary and asymmetric electrolyte with redox reactions near a planar electrode and (b) the simulated hybrid pseudocapacitor with planar electrodes, along with the associated coordinate system.

layer near the pseudocapacitive electrode. This assumption is commonly used in models of batteries and electrochemical capacitors, since free electrons and free  $\text{Li}^+$  ions are assumed to be confined to the electrodes and to the diffuse layer, respectively [26]. (2) No phase transition occurred in the pseudocapacitive material. This was consistent with experimental observations for  $\text{Nb}_2\text{O}_5$  [107]. (3) Transport of the intercalated species in the pseudocapacitive electrode was treated as a diffusion process. (4) Bulk motion of the electrolyte was negligible. (5) The physicochemical properties of the electrodes and the electrolyte were assumed to be constant. In practice, the electrical conductivity  $\sigma_P$  and the  $\text{Li}^+$  diffusion coefficient  $D_{1,P}$  in the pseudocapacitive electrode may change with the concentration of intercalated  $\text{Li}^+$ . Similarly, the electrolyte transport properties may change with the local electric field and/or ion concentrations. However, to the best of my knowledge, no quantitative models or experimental measurements for  $\sigma_P$  or  $D_{1,P}$  of metal oxides as a function of intercalated  $\text{Li}^+$  concentration exist. (6) The Stern layer thickness  $H$  was identical at both electrodes and equal to half the effective diameter  $a_{i,E}$  of the largest ion species  $i$ , i.e.,  $H = \max(a_{i,E}/2)$ . (7) Non-electrostatic ion adsorption was negligible. In fact, previous simulations of EDLCs using this assumption [48, 141] agreed well with experimental data. (8) The potential drop across the current collectors was negligible, so that only the electrodes and the electrolyte were simulated. (9) The cell temperature was uniform and constant, and heat generation was ignored.

## 8.2.2 Governing equations

### 8.2.2.1 In the electrodes

The local electric potential  $\psi(\mathbf{r}, t)$  in each electrode obeys Poisson's equation given by [106, 142]

$$\begin{aligned} \nabla \cdot (\sigma_P \nabla \psi) &= 0 \quad \text{in the pseudocapacitive electrode} \\ \text{and } \nabla \cdot (\sigma_C \nabla \psi) &= 0 \quad \text{in the carbon electrode} \end{aligned} \tag{8.2}$$

where  $\sigma_P$  and  $\sigma_C$  are the electrical conductivities of the pseudocapacitive and carbon electrode materials, respectively. The spatiotemporal evolution of the local concentration  $c_{1,P}(\mathbf{r}, t)$

of intercalated lithium ions in the pseudocapacitive electrode is governed by the mass diffusion equation written as [106, 143–145]

$$\frac{\partial c_{1,P}}{\partial t} = -\nabla \cdot \mathbf{N}_{1,P} \quad \text{with} \quad \mathbf{N}_{1,P} = -D_{1,P} \nabla c_{1,P}. \quad (8.3)$$

Here,  $\mathbf{N}_{1,P}$  is the molar flux vector given by Fick's law (in  $\text{mol m}^{-2}\text{s}^{-1}$ ) and  $D_{1,P}$  is the diffusion coefficient (in  $\text{m}^2\text{s}^{-1}$ ) of intercalated  $\text{Li}^+$  inside the pseudocapacitive material. Note that lithium intercalation did not take place in the carbon electrode assumed to be chemically inert.

### 8.2.2.2 In the electrolyte

The local electric potential  $\psi(\mathbf{r}, t)$  and the local ion concentrations  $c_{i,E}(\mathbf{r}, t)$  were modeled using the generalized modified Poisson-Nernst-Planck (GMPNP) model described in Section 2.4.3 [57, 106]. The electric potential  $\psi(\mathbf{r}, t)$  in the electrolyte is governed by Poisson's Equation (2.5). The local ion concentrations  $c_{i,E}(\mathbf{r}, t)$  in the diffuse layer are governed by the mass conservation Equation (2.6) with GMPNP ion flux  $\mathbf{N}_{i,E}(\mathbf{r}, t)$  given by Equation (2.11).

### 8.2.2.3 The faradaic current density

The transport processes in the pseudocapacitive electrode and in the electrolyte are coupled with the faradaic reaction occurring at their interface. The faradaic current density  $\mathbf{j}_F(\mathbf{r}_s, t)$  (in  $\text{A m}^{-2}$ ) due to the redox reaction and the intercalation of lithium ions (species 1) is typically described by the generalized Frumkin-Butler-Volmer model [26, 28, 106, 146, 147], i.e.,

$$\mathbf{j}_F(\mathbf{r}_s, t) = j_{F,0}(\mathbf{r}_s, t) \left\{ \exp \left[ \frac{(1 - \alpha) z_{1,E} F \eta(\mathbf{r}_s, t)}{R_u T} \right] - \exp \left[ \frac{-\alpha z_{1,E} F \eta(\mathbf{r}_s, t)}{R_u T} \right] \right\} \mathbf{n}_s \quad (8.4)$$

where  $\mathbf{r}_s$  is the position vector for a point on the electrode/electrolyte interface and  $\mathbf{n}_s$  is the unit normal vector to the electrode/electrolyte interface pointing into the electrolyte. Here,  $\alpha$ ,  $\eta(\mathbf{r}_s, t)$ , and  $j_{F,0}(\mathbf{r}_s, t)$  are the transfer coefficient, surface overpotential, and exchange current density, respectively. The surface overpotential  $\eta(\mathbf{r}_s, t) = \Delta\psi_H(\mathbf{r}_s, t) - \Delta\psi_{eq}(\mathbf{r}_s, t)$



(in V) represents the deviation of the electric potential drop across the Stern layer  $\Delta\psi_H$  from its value at equilibrium  $\Delta\psi_{eq}$  [28]. Here,  $\Delta\psi_H$  is defined as the difference between the potential at the pseudocapacitive electrode/electrolyte interface and that at the Stern/diffuse layer interface, i.e.,  $\Delta\psi_H(\mathbf{r}_s, t) = \psi(\mathbf{r}_s, t) - \psi(\mathbf{r}_s + H\mathbf{n}_s, t)$ . The exchange current density  $j_{F,0}$  is expressed as [143, 148]

$$j_{F,0}(\mathbf{r}_s, t) = z_{1,E} F k_0 [c_{1,E}(\mathbf{r}_s + H\mathbf{n}_s, t)]^{1-\alpha} [c_{1,P,max} - c_{1,P}(\mathbf{r}_s, t)]^\alpha [c_{1,P}(\mathbf{r}_s, t)]^\alpha \quad (8.5)$$

where  $c_{1,P,max}$  is the theoretical maximum concentration of intercalated  $\text{Li}^+$  in the pseudocapacitive electrode and  $k_0$  is the reaction rate constant in  $\text{m}^{1+3\alpha}\text{mol}^{-\alpha}\text{s}^{-1}$ . For the reaction considered in the present study [Equation (8.1)],  $z_{1,E} = 1$ . Note, however, that Equations (8.4) and (8.5) are also applicable to reactions of anions ( $z_{1,E} < 0$ ) or larger-valency cations ( $z_{1,E} > 1$ ). Finally, the transfer coefficient  $\alpha$  was taken as  $\alpha = 1/2$  corresponding to identical energy barriers for the forward and backward redox reactions [26, 28].

The above governing equations were expressed in their general form independent of the coordinate system or a specific cell geometry. The present study of a one-dimensional (1D) hybrid pseudocapacitor [Figure 8.2(b)] used 1D Cartesian coordinates with the origin located at the separator centerline. Then, the pseudocapacitive electrode/electrolyte interface was located at  $x = -L$  while the Stern/diffuse layer interface was at  $x = -L + H$ . The pseudocapacitive electrode was located at  $-L - L_P \leq x \leq -L$  and the carbon electrode at  $L \leq x \leq L + L_C$ . The present study will treat all vector variables (e.g.,  $\mathbf{j}_F$ ,  $\mathbf{N}_{i,P}$ ,  $\mathbf{N}_{i,E}$ ) as scalars, positive if they point in the positive  $x$ -direction, and negative if in the negative  $x$ -direction. In addition, because  $j_F$ ,  $j_{F,0}$ ,  $\eta$ , and  $\Delta\psi_H$  were defined only at a single point  $x = -L$ , they will be treated as functions of time only, i.e.,  $j_F(t)$ ,  $j_{F,0}(t)$ ,  $\eta(t)$ , and  $\Delta\psi_H(t)$ . Note that  $\text{Li}^+$  intercalation corresponds to faradaic current density in the negative  $x$ -direction, i.e.,  $j_F < 0 \text{ mA cm}^{-2}$ .

### 8.2.3 Initial and boundary conditions

The governing Equations (8.2), (2.5), (8.3), and (2.6) in 1D Cartesian coordinates for  $\psi(x, t)$ ,  $c_{1,P}(x, t)$ , and  $c_{i,E}(x, t)$  are first-order partial differential equations in time and second order

in space. Thus, each equation requires one initial condition and two boundary conditions in each region where it is solved.

### 8.2.3.1 Initial conditions

Initially, the potential was taken as uniform and equal to zero across the device such that

$$\psi(x, 0) = 0 \text{ V.} \quad (8.6)$$

The initial ion concentrations in the diffuse layer ( $-L + H \leq x \leq L - H$ ) were uniform with bulk concentrations  $c_{i,E,\infty}$  satisfying electroneutrality so that

$$c_{i,E}(x, 0) = c_{i,E,\infty} \quad \text{with} \quad \sum_{i=1}^2 z_{i,E} c_{i,E,\infty} = 0 \quad (8.7)$$

The initial concentration of  $\text{Li}^+$  intercalated in the pseudocapacitive electrode ( $-L - L_P \leq x \leq -L$ ) was uniform and equal to  $c_{1,P,0}$ , i.e.,

$$c_{1,P}(x, 0) = c_{1,P,0} \quad (8.8)$$

Note that an initial concentration  $c_{1,P,0}$  of identically zero resulted in zero faradaic current density  $j_F$  [Equation (8.4)] at all subsequent times. Thus, initially “empty” electrodes charged by intercalation were simulated using an arbitrary small, but non-zero, value of the initial  $\text{Li}^+$  concentration  $c_{1,P,0}$ . It was verified that the predictions for  $\psi(x, t)$ ,  $c_{1,P}(x, t)$ , and  $c_{i,E}(x, t)$  under oscillatory steady state were not sensitive to the choice of  $c_{1,P,0}$ .

### 8.2.3.2 Boundary conditions

Under galvanostatic cycling, the current density  $j_{im}(t) = \pm j_s$  was imposed at the interface between the current collector and the pseudocapacitive electrode located at  $x = -L - L_P$  according to Ohm’s law and expressed as [28]

$$-\sigma_P \frac{\partial \psi}{\partial x}(-L - L_P, t) = j_{im}(t). \quad (8.9)$$

In the present study, the amount of charge  $\Delta q_s = j_s t_c / 2$  stored during the charging step and retrieved during the discharging step was kept identical for all cycles and charging

corresponded to  $\text{Li}^+$  intercalation. The imposed current density  $j_{im}(t)$  alternated between charging and discharging as a square wave of fixed cycle period  $t_c$  expressed as

$$j_{im}(t) = \begin{cases} -j_s & \text{for charging } (n_c - 1)t_c \leq t < (n_c - 1/2)t_c \\ j_s & \text{for discharging } (n_c - 1/2)t_c \leq t < n_c t_c \end{cases} \quad (8.10)$$

where  $n_c = 1, 2, 3, \dots$  is the cycle number. Note that ECs are often experimentally cycled over a fixed potential window  $\Delta\psi_s$  rather than with fixed  $\Delta q_s$ . The fixed-charge method was used here to facilitate the physical interpretation and the comparison with previous EDLC simulations [2, 5].

Charge conservation required the electronic current density in the pseudocapacitive electrode at the electrode/electrolyte interface to equal the sum of the faradaic current density  $j_F(t)$ , given by Equation (8.4), and the capacitive current density  $j_C(t)$  at the Stern/diffuse layer interface such that

$$-\sigma_P \frac{\partial \psi}{\partial x}(-L, t) = j_F(t) + j_C(t). \quad (8.11)$$

The capacitive current density  $j_C(t)$  arises due to the formation and dissolution of the EDL near the pseudocapacitive electrode. It is defined as the displacement current density within the Stern layer at the pseudocapacitive electrode. It was uniform across the Stern layer due to the uniform potential gradient and given by

$$j_C(t) = -\epsilon_0 \epsilon_r \frac{\partial^2 \psi}{\partial x \partial t}(-L + H, t). \quad (8.12)$$

The electric potential gradient was uniform across the Stern layers near each electrode due to the lack of free charge [Equation (2.5)]. The potential  $\psi(x, t)$  in the Stern layers was not explicitly simulated. Instead, it was accounted for by the boundary conditions [54, 149]. At the Stern/diffuse layer interface near the pseudocapacitive electrode, it was expressed as [48, 125]

$$\frac{\partial \psi}{\partial x}(-L + H, t) = \frac{\psi(-L + H, t) - \psi(-L, t)}{H}. \quad (8.13)$$

Similarly, at the Stern/diffuse layer interface near the carbon electrode, the potential satisfied

$$\frac{\partial \psi}{\partial x}(L - H, t) = \frac{\psi(L, t) - \psi(L - H, t)}{H}. \quad (8.14)$$

At the carbon electrode/electrolyte interface, located at  $x = L$ , the electronic current density equaled the displacement current density at the Stern/diffuse layer interface such that

$$-\sigma_C \frac{\partial \psi}{\partial x}(L, t) = -\epsilon_0 \epsilon_r \frac{\partial^2 \psi}{\partial x \partial t}(L - H, t). \quad (8.15)$$

Finally, the interface between the carbon electrode and the current collector was electrically grounded such that

$$\psi(L + L_C, t) = 0 \text{ V}. \quad (8.16)$$

Note that the choice of reference potential is arbitrary. It did not affect the computed currents, ion concentrations, or cell potential  $\psi_s(t)$ .

Moreover, lithium ions could not intercalate into the current collector so that

$$N_{1,P}(-L - L_P, t) = 0 \text{ mol m}^{-2}\text{s}^{-1}. \quad (8.17)$$

The molar fluxes of  $\text{Li}^+$  in the electrolyte and intercalated  $\text{Li}^+$  entering and exiting the Stern layer near the pseudocapacitive electrode were proportional to the faradaic current density  $j_F(t)$  [Equation (8.4)], while the anion mass flux vanished so that

$$N_{1,P}(-L, t) = N_{1,E}(-L + H, t) = \frac{j_F(t)}{z_{1,E}F} \quad \text{and} \quad N_{2,E}(-L + H, t) = 0 \text{ mol m}^{-2}\text{s}^{-1}. \quad (8.18)$$

In addition, both ion mass fluxes vanished at the Stern/diffuse layer interface near the carbon electrode as no ion intercalation occurred, i.e.,

$$N_{i,E}(L - H, t) = 0 \text{ mol m}^{-2}\text{s}^{-1} \quad \text{for } i = 1 \text{ and } 2. \quad (8.19)$$

#### 8.2.4 Constitutive relationships

The present study uses arbitrary yet realistic material properties for the pseudocapacitive material. Its electrical conductivity  $\sigma_P$  was taken as  $\sigma_P = 7 \times 10^{-2} \text{ S m}^{-1}$ , within the range typical of metal oxides used in pseudocapacitors [150]. As previously mentioned, the transfer coefficient was taken as  $\alpha = 1/2$  corresponding to identical energy barriers for the reaction in both directions. For transition metal oxides, the reaction rate coefficient  $k_0$  for  $\text{Li}^+$  intercalation typically ranged from about  $10^{-11}$  to  $10^{-8} \text{ m}^{5/2}\text{mol}^{-1/2}\text{s}^{-1}$  [148, 151–

153] and the diffusion coefficient  $D_{1,P}$  from  $10^{-18}$  to  $10^{-10}$   $\text{m}^2\text{s}^{-1}$  [152, 154]. Here, they were taken as  $k_0 = 5 \times 10^{-9}$   $\text{m}^{5/2}\text{mol}^{-1/2}\text{s}^{-1}$  and  $D_{1,P} = 10^{-10}$   $\text{m}^2\text{s}^{-1}$  to provide favorable conditions for faradaic charge storage. The maximum concentration of intercalated  $\text{Li}^+$  in the pseudocapacitive electrode was approximated as  $c_{1,P,max} = 2\rho_P/M_P \approx 32.9$   $\text{mol L}^{-1}$  where  $M_P = 279.7$   $\text{g mol}^{-1}$  and  $\rho_P \approx 4.6$   $\text{g cm}^{-3}$  correspond to the molecular mass and density of fully-intercalated  $\text{Li}_2\text{Nb}_2\text{O}_5$ , respectively. The initial  $\text{Li}^+$  concentration in the electrode was  $c_{1,P,0} = 10^{-6}$   $\text{mol L}^{-1}$ . Finally, the electrical conductivity of the simulated carbon electrode was taken as  $\sigma_C = 100$   $\text{S m}^{-1}$  [14, 86, 87].

Experimental studies [123, 155] have shown that the equilibrium potential drop  $\Delta\psi_{eq}$  for pseudocapacitive electrodes may vary with the state of charge and thus change over time during operation. Ref. [123] expressed  $\Delta\psi_{eq}$  of  $\text{MnO}_2$  as a linear function of the oxidation state of the pseudocapacitive material according to

$$\Delta\psi_{eq} = A \left( Os_{max} - \frac{c_{1,P}}{c_{1,P,max}} \right) + B \quad (8.20)$$

where  $Os_{max} = 4$  was the theoretical maximum oxidation state for  $\text{MnO}_2$  and  $A$  and  $B$  were empirically fitted constants expressed in V. The present study expresses  $\Delta\psi_{eq}$  in slightly different form, i.e.,

$$\Delta\psi_{eq}(t) = \Delta\psi_{eq,0} - S_{eq} \left( \frac{c_{1,P}(-L, t) - c_{1,P,0}}{c_{1,P,max}} \right). \quad (8.21)$$

where  $\Delta\psi_{eq,0}$  is the initial value of  $\Delta\psi_{eq}$  corresponding to  $c_{1,P}(-L, t) = c_{1,P,0}$ . Equations (8.20) and (8.21) are equivalent with  $S_{eq} = A$  and  $\Delta\psi_{eq,0} = B + A(Os_{max} - c_{1,P,0}/c_{1,P,max})$ . The present study assumed that the cell started from an equilibrium state such that  $\Delta\psi_{eq,0} = 0$  V, consistent with Equation (8.6). Note that  $\Delta\psi_{eq,0} \neq 0$  V could be simulated with appropriate initial conditions, e.g., non-uniform electric potential and ion concentrations corresponding an equilibrium state such that  $\Delta\psi_H(0) = \Delta\psi_{eq,0}$ , but this is beyond the scope of the present investigation. Here, I primarily considered the ideal faradaic behavior  $S_{eq} = 0$  V when  $\Delta\psi_{eq}$  is constant. The effects of variable  $\Delta\psi_{eq}$  were investigated using  $S_{eq} = 1$  V and  $S_{eq} = 10.5$  V based on experimentally measured values for thin-film and thick porous  $\text{MnO}_2$  electrodes, respectively [123]. Equation (8.21) indicates that, for  $S_{eq} > 0$  V as

measured experimentally for  $\text{MnO}_2$ ,  $\Delta\psi_{eq}$  decreases with increasing  $c_{1,P}$ . This makes intuitive sense, since it results in further cation intercalation becoming increasingly “difficult” with increasing  $c_{1,P}$  (i.e., the potential drop  $\Delta\psi_H$  must be more negative to achieve the same  $\eta_F < 0$  V than for smaller  $c_{1,P}$ ) while deintercalation becomes “easier” (i.e.,  $\eta_F > 0$  V can be achieved with smaller  $\Delta\psi_H$ ).

The binary and asymmetric electrolyte simulated corresponded to 1 mol L<sup>-1</sup>  $\text{LiClO}_4$  in propylene carbonate (PC) solvent. The relative permittivity  $\epsilon_r = 66.1$  was taken as constant and equal to that of PC at zero electric field [58]. The solvated ion diameters of  $\text{Li}^+$  and  $\text{ClO}_4^-$  were taken as  $a_{1,E} = 0.67$  nm and  $a_{2,E} = 1.0$  nm, respectively [58, 156]. Their diffusion coefficients in PC were  $D_{1,E} = 2.6 \times 10^{-10}$  m<sup>2</sup>s<sup>-1</sup> and  $D_{2,E} = 3.3 \times 10^{-10}$  m<sup>2</sup>s<sup>-1</sup>, respectively [156, 157]. Their bulk concentrations equaled  $c_{1,E,\infty} = c_{2,E,\infty} = 1$  mol L<sup>-1</sup>.

The pseudocapacitive and carbon electrodes had the same thickness  $L_P = L_C = 5$  nm while the inter-electrode half-width was much larger and equal to  $L = 1$   $\mu\text{m}$ . The use of thin electrodes facilitated comparison to analytical calculations in the limiting case when the intercalated  $\text{Li}^+$  concentration  $c_{1,P}(x, t)$  remained uniform in the pseudocapacitive electrode. The temperature was taken as uniform, constant, and equal to  $T = 298$  K. The cell was cycled galvanostatically at various current densities  $j_s$  and cycle periods  $t_c$  such that the stored charge density  $\Delta q_s = j_s t_c / 2 = 0.3$  C m<sup>-2</sup> added to the cell during charging and removed during discharging was the same for all cases. This charge density was comparable to the charge density per unit electrode/electrolyte interfacial area for experimentally cycled EDLCs and hybrid pseudocapacitors reported in the literature [29, 78].

### 8.2.5 Method of solution

The 1D governing Equations (8.2), (2.5), (8.3), and (2.6) and the associated initial and boundary conditions were solved numerically using finite element methods. Numerical convergence was assessed based on the predicted potential  $\psi(x, t)$  and concentrations  $c_{1,E}(x, t)$ ,  $c_{2,E}(x, t)$ , and  $c_{1,P}(x, t)$  and using the procedure and convergence criteria described in Section 4.1.5.

Finally, several cycles were simulated and an oscillatory steady state in  $\psi(x, t)$ ,  $c_{1,E}(x, t)$ ,  $c_{2,E}(x, t)$ , and  $c_{1,P}(x, t)$  was considered to be reached when the maximum relative error between the value of each variable at time  $t$  and its value at time  $t - t_c$  was less than 1%. For small current densities  $j_s \lesssim 8 \text{ mA cm}^{-2}$ , these conditions were typically met by the third cycle. The number of cycles required to reach oscillatory steady state increased with increasing current density  $j_s$ . For example, at current density  $j_s = 256 \text{ mA cm}^{-2}$ , almost 80 cycles were required to reach oscillatory steady state.

### 8.2.6 Analytical expressions for limiting cases

The preceding model accounts simultaneously for two contributions to charge storage: (i) faradaic charge storage associated with the faradaic current density  $j_F(t)$  and (ii) EDL charge storage associated with the capacitive current density  $j_C(t)$ . The complex interactions between the faradaic reaction and the EDL formation can make physical interpretation of the model predictions difficult. The latter can be facilitated by simpler analytical expressions for certain variables such as  $c_{1,P}$  and  $\eta$  as functions of time derived in the limiting cases when one of the storage mechanisms dominates. This section analyzes these two limiting cases in more detail. Here, the intercalated  $\text{Li}^+$  concentration  $c_{1,P}$  was assumed to be uniform in the pseudocapacitive electrode due to its small thickness. Note that the expressions derived for  $c_{1,P}$  and  $\eta$  are valid for charging either by intercalation or by deintercalation.

#### 8.2.6.1 General expressions

First, it is useful to express the  $\text{Li}^+$  concentration  $c_{1,P}$  and the overpotential  $\eta$  as functions of the current densities  $j_F$  and  $j_C$ . Based on mass conservation, the uniform intercalated  $\text{Li}^+$  concentration  $c_{1,P}(x, t)$  at time  $t$  is the sum of the initial concentration  $c_{1,P,0}$  and the net  $\text{Li}^+$  intercalated due to the faradaic reaction per unit volume of the electrode, i.e.,

$$c_{1,P}(x, t) = c_{1,P,0} + \frac{A_P}{z_1 F} \int_0^t [-j_F(t)] dt. \quad (8.22)$$

Here,  $A_P$  is the pseudocapacitive electrode/electrolyte interfacial area per unit volume of pseudocapacitive material (in  $\text{m}^{-1}$ ). It is given by  $A_P = 1/L_P$  for a 1D cell with planar electrodes. The second term is positive and  $c_{1,P}$  increases during  $\text{Li}^+$  intercalation corresponding to negative  $j_F(t)$ , as previously mentioned.

Moreover, for  $\alpha = 1/2$ , the expression of  $j_F(t)$  given by Equations (8.4) and (8.5) can be solved for  $\eta(t)$  to yield

$$\eta(t) = 2 \frac{R_u T}{z_{1,E} F} \sinh^{-1} \left( \frac{j_F(t)}{2 z_{1,E} F k_0 \sqrt{c_{1,E}(-L+H,t)} \sqrt{c_{1,P,max} - c_{1,P}(-L,t)} \sqrt{c_{1,P}(-L,t)}} \right). \quad (8.23)$$

Alternatively,  $\eta(t)$  can be expressed in terms of the EDL surface charge density  $q_{s,C}(t)$  stored in the EDL at the pseudocapacitive electrode and of the Stern layer capacitance  $C_s^{St} = \epsilon_0 \epsilon_r / H$  as [48]

$$\eta(t) = \Delta\psi_H(t) - \Delta\psi_{eq}(t) = \frac{q_{s,C}(t)}{C_s^{St}} - \Delta\psi_{eq}(t) = \frac{H q_{s,C}(t)}{\epsilon_0 \epsilon_r} - \Delta\psi_{eq}(t). \quad (8.24)$$

The EDL surface charge density  $q_{s,C}(t)$  at the pseudocapacitive electrode is equal to  $q_{s,C}(t) = \int_0^t j_C(t') dt'$ . Thus, the time rate of change of  $\eta$  varies linearly with the capacitive current density  $j_C(t) = dq_{s,C}/dt$  according to

$$\frac{d\eta}{dt}(t) = \frac{j_C(t)H}{\epsilon_0 \epsilon_r} - \frac{d\Delta\psi_{eq}(t)}{dt}. \quad (8.25)$$

### 8.2.6.2 Asymptotic faradaic regime

In the faradaic regime, the faradaic current density  $j_F(t)$  carries most of the imposed current density  $j_s$  so that  $j_F(t) \approx \pm j_s$  and  $j_C(t) \approx 0 \text{ mA cm}^{-2}$ . Then, based on Equation (8.22), the corresponding  $\text{Li}^+$  concentration  $c_{1,P,F}(x,t)$  varies linearly as a function of  $t$  with slope  $j_s A_P / z_{1,E} F$  and can be expressed as

$$c_{1,P,F}(t) = c_{1,P,0} + (-1)^p \begin{cases} \frac{j_s t_c A_P}{z_{1,E} F} \left( \frac{t}{t_c} - n_c + 1 \right) & \text{for charging} \\ \frac{j_s t_c A_P}{z_{1,E} F} \left( n_c - \frac{t}{t_c} \right) & \text{for discharging} \end{cases} \quad (8.26)$$

where  $p = 0$  for charging by  $\text{Li}^+$  intercalation (analogous to  $\text{Nb}_2\text{O}_5$  negative electrodes) and  $p = 1$  for charging by  $\text{Li}^+$  deintercalation (analogous to  $\text{Mn}_2\text{O}_5$  positive electrodes). In



the faradaic regime, EDL formation near the pseudocapacitive electrode is expected to be negligible, and the ion concentrations at the Stern/diffuse layer interface to remain close to their bulk concentrations such that  $c_{1,E}(-L + H, t) \approx c_{1,E,\infty}$  and  $c_{2,E}(-L + H, t) \approx c_{2,E,\infty}$ . Then, Equation (8.23) for the surface overpotential  $\eta_F(t)$  simplifies as

$$\eta_F(t) = \frac{2R_u T}{z_{1,E} F} \sinh^{-1} \left[ \frac{j_{im}(t)}{2z_{1,E} F k_0 \sqrt{c_{1,E,\infty}} \sqrt{c_{1,P,max} - c_{1,P,F}(t)} \sqrt{c_{1,P,F}(t)}} \right]. \quad (8.27)$$

Here, the overpotential magnitude  $|\eta_F|$  required to drive the current density  $j_F(t) = \pm j_s$  and predicted by Equation (8.27) decreases with decreasing  $j_s$ , increasing reaction rate constant  $k_0$ , increasing  $c_{1,E,\infty}$ , and/or  $c_{1,P,F}$  approaching  $c_{1,P,max}/2$ .

### 8.2.6.3 Asymptotic capacitive regime

I define the capacitive regime as the limiting case in which the capacitive current density  $j_C(t)$  carries the entire imposed current density  $j_{im}(t)$  such that  $j_C(t) \approx \pm j_s$  while the faradaic current density is negligible, i.e.,  $j_F(t) \approx 0 \text{ mA cm}^{-2}$ . Then, the  $\text{Li}^+$  concentration inside the pseudocapacitive electrode and thus  $\Delta\psi_{eq}$  [Equation (8.21)] are approximately constant, i.e.,  $c_{1,P}(x, t) \approx c_{1,P,C}$  and  $\Delta\psi_{eq} \approx \Delta\psi_{eq,C}$ . Note that the steady-state concentration  $c_{1,P,C}$  could differ significantly from the initial value  $c_{1,P,0}$  despite the small magnitude of  $j_F(t)$  when the number of cycles required to reach oscillatory steady state is large. Then, according to Equation (8.25), the overpotential  $\eta_C(t)$  varies linearly with time such that

$$\frac{d\eta_C}{dt}(t) = \frac{j_{im}(t)H}{\epsilon_0 \epsilon_r} = \pm \frac{j_s H}{\epsilon_0 \epsilon_r}. \quad (8.28)$$

The value of  $\eta_C$  at the beginning of the cycle depends on the EDL charge density  $q_{s,C}(n_c t_c - t_c)$ . For cycling with fixed  $\Delta q_s$ , the total stored charge density from the external circuit  $q_s(t) = q_{s,C}(t) + q_{s,F}(t)$  is zero at the beginning of the cycle, so the EDL charge density is given by  $q_{s,C}(n_c t_c - t_c) = -q_{s,F}(n_c t_c - t_c) = z_{1,E} F (c_{1,P,C} - c_{1,P,0}) / A_p$  and

$$\eta_C(n_c t_c - t_c) = \frac{H}{\epsilon_0 \epsilon_r} \frac{z_{1,E} F (c_{1,P,C} - c_{1,P,0})}{A_p} - \Delta\psi_{eq,C}. \quad (8.29)$$

Note that for EDLCs with no faradaic reactions [2, 5],  $c_{1,P,C} = c_{1,P,0}$  and  $\eta(t)$  returned to 0 V at the end of each cycle.

## 8.3 Results and discussion

This section presents simulation results for the previously described hybrid pseudocapacitor charged by  $\text{Li}^+$  intercalation, analogous to  $\text{Nb}_2\text{O}_5$  as a negative electrode. Various current densities  $j_s$  and cycle periods  $t_c$  were explored for the same amount of stored charge  $\Delta q_s = j_s t_c / 2 = 0.3 \text{ C m}^{-2}$ . Sections 8.3.1 to 8.3.4 present detailed results for constant equilibrium potential drop  $\Delta\psi_{eq}$ . Section 8.3.5 briefly illustrates the effect of state-of-charge-dependent  $\Delta\psi_{eq}$ . Finally, Section 8.3.6 briefly presents results for a hybrid cell charged by  $\text{Li}^+$  deintercalation with constant equilibrium potential drop  $\Delta\psi_{eq}$ .

### 8.3.1 Current densities

Figures 8.3(a) and 8.3(b) respectively show the numerically predicted faradaic current density  $j_F(t)$  [Equation (8.4)] and capacitive current density  $j_C(t)$  [Equation (8.12)] as functions of dimensionless time  $t/t_c$  for various pairs of  $[j_s, t_c]$  under galvanostatic cycling at oscillatory steady state. For small values of  $j_s$  ( $< 4 \text{ mA cm}^{-2}$ ), the faradaic current density  $j_F(t)$  was negative during charging, positive during discharging, and constant in magnitude during most of the cycle. The capacitive current density  $j_C(t)$  was small compared to  $j_F(t)$ . On the other hand, for large values of  $j_s$  ( $> 32 \text{ mA cm}^{-2}$ ), the capacitive current density  $j_C(t)$  was significantly larger than  $j_F(t)$  at all times. In fact, the maximum value of  $|j_C|$  increased continuously with increasing  $j_s$ . By contrast, the faradaic current density  $j_F(t)$  approached an asymptotic limit at large  $j_s$ .

Figures 8.3(c) and 8.3(d) respectively show the fractions of the imposed current density  $j_F(t)/j_s$  carried by the faradaic current and  $j_C(t)/j_s$  carried by the capacitive current as functions of dimensionless time  $t/t_c$  for various values of  $j_s$  and  $t_c$  under galvanostatic cycling. For small values of  $j_s$ , the current density was almost exclusively faradaic, i.e.,  $j_F(t) \gg j_C(t)$  and  $j_F(t)/j_s \approx \pm 1$ . Then,  $j_F(t)$  diverged from the imposed current density  $j_{im}(t) = \pm j_s$  only around the charging/discharging transitions at  $t/t_c = n_c - 1$  and  $t/t_c = n_c - 0.5$ . Simultaneously, the capacitive current fraction  $j_C(t)/j_s$  featured peaks following these transitions so that the sum  $j_F(t) + j_C(t)$  always equaled  $j_{im}(t) = \pm j_s$ . The faradaic contribution  $j_F(t)/j_s$

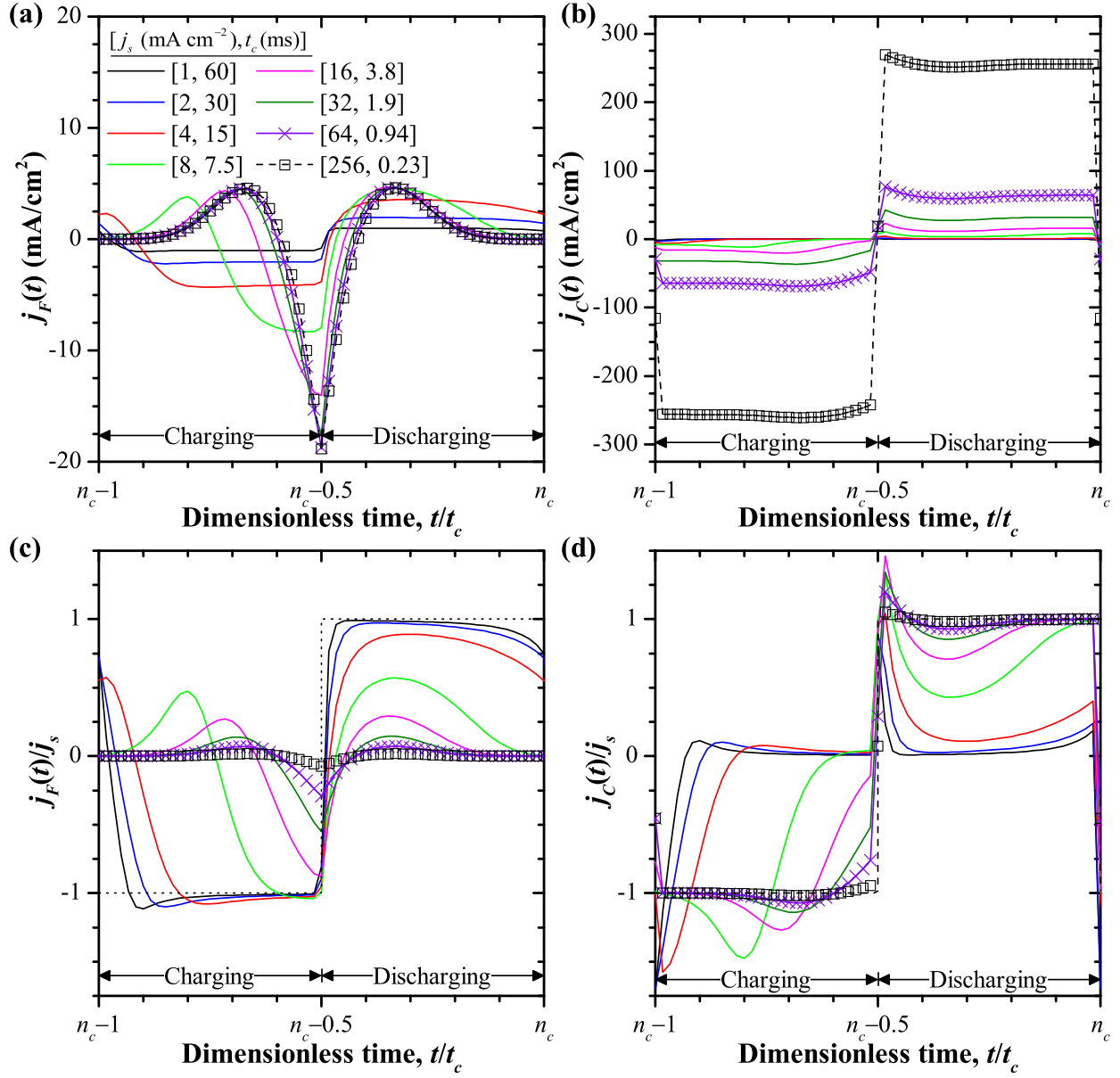


Figure 8.3: Predicted (a) faradaic current density  $j_F(t)$  and (b) capacitive current density  $j_C(t)$  as well as the faradaic and capacitive fractions (c)  $j_F(t)/j_s$  and (d)  $j_C(t)/j_s$  of the total current density as functions of dimensionless time  $t/t_c$  for different values of  $j_s$  and  $t_c$  under galvanostatic cycling and oscillatory steady state. Here,  $j_s$  and  $t_c$  were chosen such that  $\Delta q_s = j_s t_c / 2 = 0.3 \text{ C m}^{-2}$ .

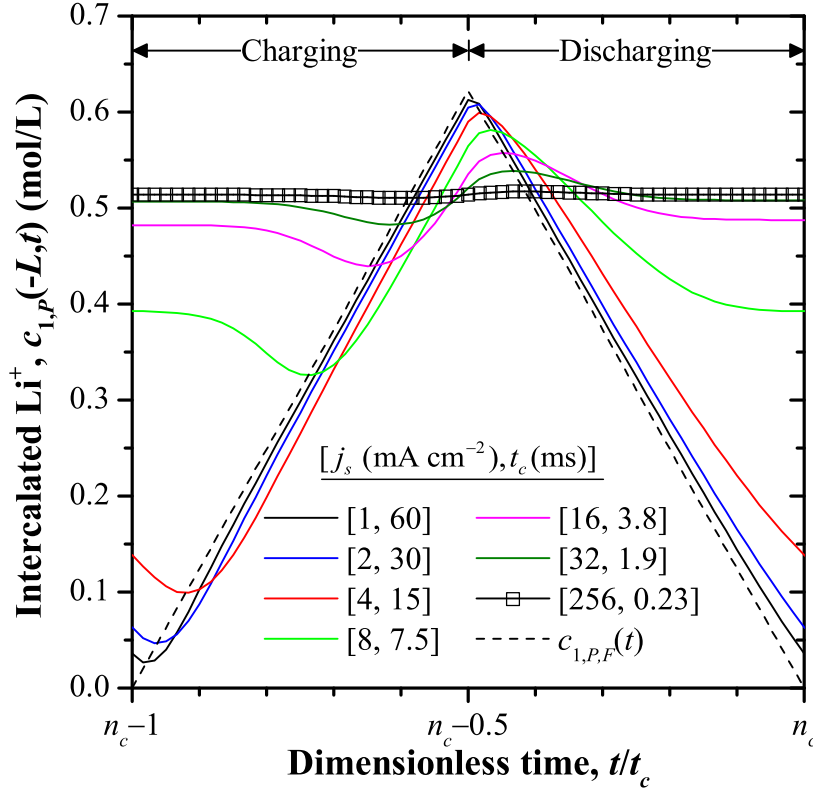


Figure 8.4: Predicted concentration  $c_{1,P}(-L, t)$  of intercalated  $\text{Li}^+$  in the pseudocapacitive electrode as a function of dimensionless time  $t/t_c$  over one cycle at oscillatory steady state for different values of  $j_s$  and  $t_c$  such that  $\Delta q_s = j_s t_c / 2 = 0.3 \text{ C m}^{-2}$ . The concentration was uniform throughout the pseudocapacitive electrode.

decreased with increasing  $j_s$ . Indeed, for  $j_s = 256 \text{ mA cm}^{-2}$ , the current density was almost entirely capacitive, i.e.,  $j_C(t) \gg j_F(t)$  at all times and  $j_C(t)/j_s \approx \pm 1$ .

Overall, two asymptotic regimes were evident: a faradaic regime characterized by  $j_F(t) \approx j_{im}(t)$  for small values of  $j_s$  and slow cycling and a capacitive regime featuring  $j_C(t) \approx j_{im}(t)$  for large values of  $j_s$  and fast cycling.

### 8.3.2 Intercalated $\text{Li}^+$ concentration in the pseudocapacitive electrode

Figure 8.4 shows the predicted concentration of intercalated  $\text{Li}^+$   $c_{1,P}(-L, t)$  at the pseudocapacitive electrode/electrolyte interface as a function of dimensionless time  $t/t_c$  for different values of  $j_s$  and  $t_c$  under galvanostatic cycling. In all cases,  $c_{1,P}$  was uniform throughout

the electrode due to the small electrode thickness  $L_P = 5$  nm and to the relatively large diffusion coefficient  $D_{1,P}$ . In fact, the penetration depth, defined as  $d_p = \sqrt{D_{1,P}t_c}$ , ranged from 150 nm to 2400 nm as the cycle period ranged from 0.23 ms to 60 ms. Thus,  $d_p$  was much larger than the electrode thickness  $L_P$  of 5 nm. In other words,  $\text{Li}^+$  diffusion in the electrode was fast and never limiting.

*In the faradaic regime*,  $c_{1,P}$  increased almost linearly during the charging step and decreased linearly during the discharging step. Indeed, for  $j_s = 1 \text{ mA cm}^{-2}$ , the numerically predicted  $\text{Li}^+$  concentration  $c_{1,P}(-L, t)$  agreed very well with that predicted by Equation (8.26), derived from mass conservation considerations and assuming  $j_F(t) = \pm j_s$ . The largest discrepancies occurred near the transition from discharging to charging, when  $c_{1,P}$  was small and  $j_F(t)$  differed from  $\pm j_s$  (Figure 8.3). *In the capacitive regime*,  $c_{1,P}$  remained approximately constant and equal to  $c_{1,P,C} \approx 0.514 \text{ mol L}^{-1}$ .

### 8.3.3 Electric potentials

Figure 8.5 shows (a) the cell potential  $\psi_s(t) = \Delta\psi_C(t) - \Delta\psi_P(t) = \psi(L + L_C, t) - \psi(-L - L_P, t)$ , (b) the surface overpotential  $\eta(t)$ , and the potential drop between the electrode/current collector interface and the electrolyte centerline (c)  $\Delta\psi_P(t) = \psi(-L - L_P, t) - \psi(0, t)$  for the pseudocapacitive electrode half-cell and (d)  $\Delta\psi_C(t) = \psi(L + L_C, t) - \psi(0, t)$  for the carbon electrode half-cell as functions of dimensionless time  $t/t_c$  for different current densities  $j_s$  and cycle periods  $t_c$  for galvanostatic cycling at oscillatory steady state. Here,  $\Delta\psi_P(t)$  and  $\Delta\psi_C(t)$  are equivalent to the electrode potentials measured relative to a reference electrode in three-electrode measurements (plus or minus a constant), since reference electrodes are designed to have constant potential relative to the electrolyte solution [26, 28].

Figure 8.5(a) indicates that  $\psi_s(t)$  increased throughout the charging step and decreased during the discharging step for all cases considered. The potential window  $\Delta\psi_s = \psi_{max} - \psi_{min}$  increased with increasing  $j_s$ , corresponding to decreasing integral capacitance  $C_{s,int}$  [Equation (2.2)] as the faradaic fraction of the charge storage decreased. *In the faradaic regime*, corresponding to small current density  $j_s$ , the cell potential  $\psi_s$  returned to  $\psi_{max} \approx 0 \text{ V}$

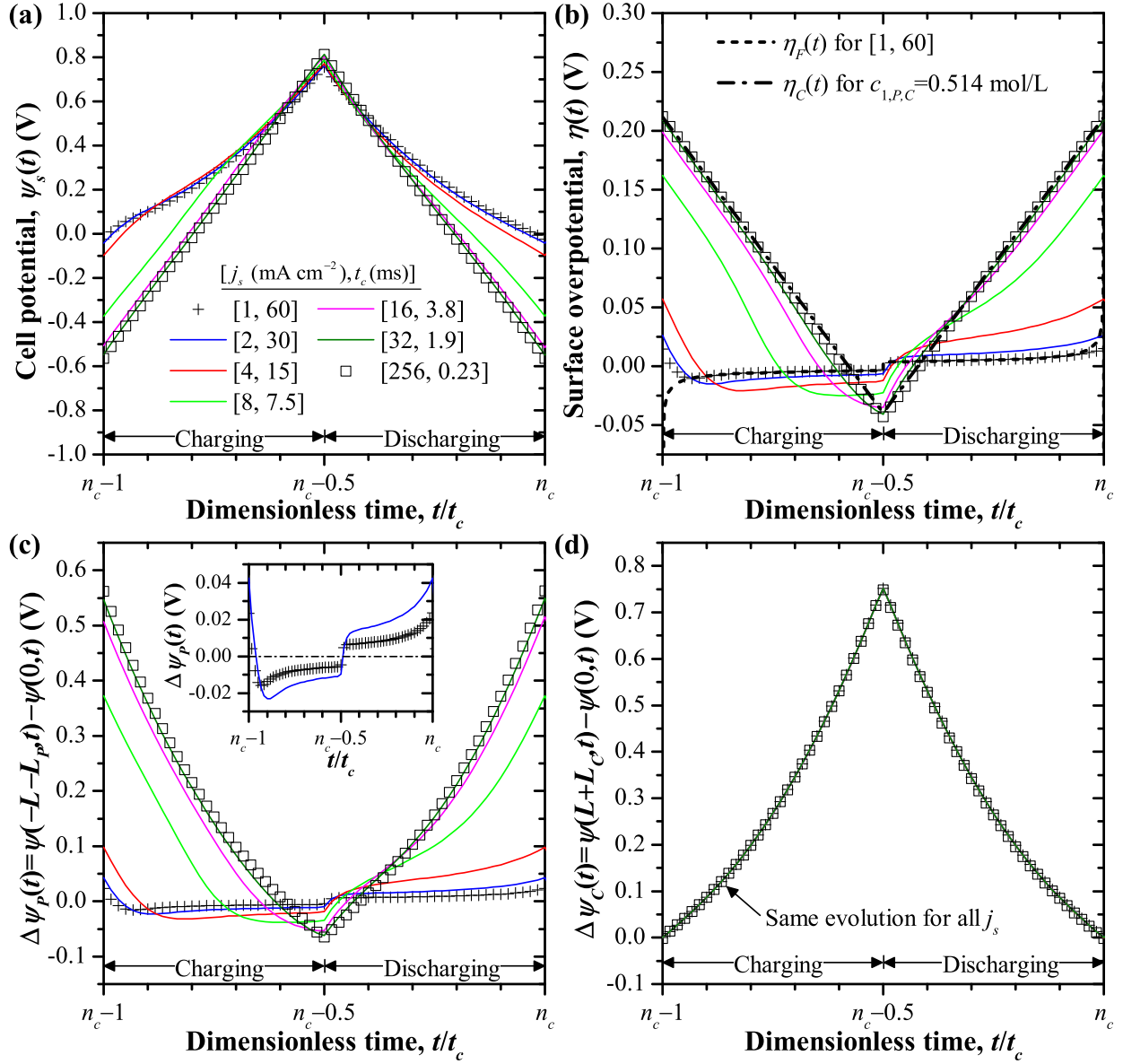


Figure 8.5: Predicted (a) cell potential  $\psi_s(t) = \Delta\psi_C(t) - \Delta\psi_P(t)$  and (b) pseudocapacitive electrode surface overpotential  $\eta(t)$  as well as the potentials of the (c) pseudocapacitive  $\Delta\psi_P(t) = \psi(-L-L_P, t) - \psi(0, t)$  and (d) carbon  $\Delta\psi_C(t) = \psi(L+L_C, t) - \psi(0, t)$  electrodes relative to the bulk electrolyte as functions of dimensionless time  $t/t_c$  over one cycle during galvanostatic cycling for various values of  $j_s$  and  $t_c$  such that  $\Delta q_s = j_s t_c / 2 = 0.3 \text{ C m}^{-2}$ .

at the beginning and end of the cycle when fully discharged. The temporal evolution of  $\psi_s$  was asymmetric around the transition from charging to discharging at  $t/t_c = n_c - 0.5$ . At the beginning of the charging step, the time rate of change  $|\mathrm{d}\psi_s/\mathrm{d}t|$  was relatively large for a short period. After this brief period,  $|\mathrm{d}\psi_s/\mathrm{d}t|$  sharply decreased, resulting in a distinct “kink” in the  $\psi_s(t)$  curve. In fact, it qualitatively resembled that measured experimentally [Figure 8.1(a)] [107,109,116,118]. This kink can be attributed to the brief peak of capacitive current  $j_C$  at the beginning of the charging step [Figure 8.3(d)] and associated with relatively small differential capacitance  $C_{s,diff}$  and large  $|\mathrm{d}\psi_s/\mathrm{d}t|$  [Equation (2.2)]. Then,  $C_{s,diff}$  abruptly increased and  $|\mathrm{d}\psi_s/\mathrm{d}t|$  decreased as the faradaic current  $j_F$  became dominant [Figure 8.3(c)]. *In the capacitive regime*, under large current density  $j_s$ , the temporal evolution of  $\psi_s$  was linear and symmetric around  $t/t_c = n_c - 0.5$ . The cell changed polarity during each cycle, and  $\psi_s$  was equal to  $\psi_{min} \approx -0.55$  V at the beginning and end of the cycle. This non-zero cell potential for the fully discharged cell occurred because a significant amount of  $\mathrm{Li}^+$  originally from the electrolyte remained intercalated as  $\mathrm{Li}^+$  in the electrode, as evidenced by  $c_{1,P,C}$  being significantly larger than the initial concentration  $c_{1,P,0}$ , i.e.,  $c_{1,P,C} - c_{1,P,0} \approx c_{1,P,C} = 0.514 \text{ mol L}^{-1}$  (Figure 8.4). Then, the electrolyte retained a net negative charge, because more  $\mathrm{ClO}_4^-$  than  $\mathrm{Li}^+$  ions remained in the electrolyte, while the pseudocapacitive electrode had a net positive charge of equal magnitude.

Figure 8.5(b) shows that the sign of the surface overpotential  $\eta(t)$  was always the same as that of the faradaic current density  $j_F(t)$ , as suggested by Equations (8.4) and (8.23). The magnitude of  $\eta$  increased with increasing  $j_s$ . *In the faradaic regime*, the magnitude of  $\eta(t)$  was small and varied relatively little with time. For  $j_s = 1 \text{ mA cm}^{-2}$ , the numerical predictions of  $\eta(t)$  agreed very well with  $\eta_F(t)$  predicted analytically by Equation (8.27) over most of the cycle. The numerical and analytical predictions differed from one another immediately after each charging/discharging transition and at the very end of the cycle. Then,  $\eta_F(t)$  increased rapidly and  $j_C(t)$  was significant, as suggested by Equation (8.25). Equation (8.27) indicates that the overpotential  $\eta_F(t)$  required to drive faradaic current density  $j_F(t) = j_{im}(t)$  changed instantaneously when  $j_{im}(t)$  changed sign at the transitions between charging and discharging steps. However, the actual time rate of change of  $\eta(t)$

was finite and related to  $j_C(t) = j_{im}(t) - j_F(t)$  by Equation (8.25). Thus, the capacitive current density  $j_C(t)$  dominated immediately after charging/discharging transitions until the overpotential approached  $\eta_F(t)$ , as observed in Figure 8.3. Similarly,  $\eta_F(t)$  increased rapidly and  $j_C$  was significant at the end of the cycle as  $c_{1,P,F}$  approached zero. *In the capacitive regime*,  $\eta(t)$  varied linearly with  $t/t_c$  with slope  $\pm j_s t_c H / \epsilon_0 \epsilon_r$ . Indeed, for  $j_s = 256 \text{ mA cm}^{-2}$ ,  $\eta(t)$  showed excellent agreement with  $\eta_C(t)$  predicted analytically by Equations (8.28) and (8.29) with  $c_{1,P,C} - c_{1,P,0} \approx c_{1,P,C} = 0.514 \text{ mol L}^{-1}$  (Figure 8.4). Attempts were made to derive an analytical expression for  $\eta(t)$  for intermediate values of  $j_s$ , but were unsuccessful.

Figure 8.5(c) indicates that, for the pseudocapacitive electrode, the evolution of  $\Delta\psi_P(t)$  qualitatively resembled that of the surface overpotential  $\eta(t)$  [Figure 8.5(b)]. *In the faradaic regime*, it was small, asymmetric around the transition from charging to discharging, and varied relatively little in magnitude over most of the cycle (see inset). As previously mentioned, such a constant potential drop during charging or discharging is characteristic of batteries [19]. Like  $\eta(t)$  and the experimentally measured  $\Delta\psi_P(t)$  [Figure 8.1(a)] [107], the potential drop  $\Delta\psi_P(t)$  featured relatively steep slopes  $|\text{d}\Delta\psi_P/\text{d}t|$  immediately following each charging/discharging transition and near the end of the cycle. However, the experimental  $\Delta\psi_P(t)$  featured significant slope outside  $|\text{d}\Delta\psi_P/\text{d}t|$  throughout the cycle, while the numerical  $\Delta\psi_P(t)$  was almost constant when  $j_F$  dominated. This difference may result from SOC-dependence of  $\Delta\psi_{eq}$  which was neglected in the simulations shown in Figure 8.5(c). For the simulated cell with identical surface area for both planar electrodes,  $\Delta\psi_P(t)$  was much smaller than  $\Delta\psi_C(t)$  since the faradaic charge storage yielded a larger capacitance than EDL charge storage. This explains why the large changes in  $\text{d}\Delta\psi_P/\text{d}t$  resulted in relatively small kinks in the cell potential  $\psi_s(t)$  [Figure 8.5(a)] compared to those observed for experimental cells with oversized porous carbon electrodes [Figure 8.1(a)]. By contrast, *in the capacitive regime*, the temporal evolution of  $\Delta\psi_P(t)$  was linear and symmetric around the transition from charging to discharging. These distinct asymptotic behaviors suggest that measuring the potential of the pseudocapacitive electrode relative to a reference electrode provides a practical way to assess whether it is operating in the faradaic or the capacitive regime.

Figure 8.5(d) establishes that, for the carbon electrode, the evolution of  $\Delta\psi_C(t)$  was



symmetric around the transition from charging to discharging. Its variation was nearly linear, but the slope  $|d\psi_s/dt|$  did vary noticeably over the cycle, indicating that the EDL differential capacitance  $C_{s,diff}$  was not constant, as assumed by many existing models [127–132]. Here,  $\Delta\psi_C(t)$  was also self-similar and identical for all values of  $j_s$  when plotted as a function of  $t/t_c$ . This implies that there was no ion diffusion limitation in the electrolyte, even at large values of  $j_s$  when  $j_F$  was negligible. Thus, the changes in the cell potential  $\psi_s(t)$  with increasing  $j_s$  were associated solely with changes on the pseudocapacitive side of the cell. Here, the carbon electrode had zero net charge and  $\Delta\psi_C = 0$  V at the end of each cycle with fixed  $\Delta q_s$ , as it exchanged charge only with the external circuit.

### 8.3.4 Ion concentrations in the electrolyte

Figure 8.6 shows the predicted concentrations of (a)  $\text{Li}^+$  cations  $c_{1,E}(-L+H, t)$  and (b)  $\text{ClO}_4^-$  anions  $c_{2,E}(-L+H, t)$  at the Stern/diffuse layer interface near the pseudocapacitive electrode as functions of dimensionless time  $t/t_c$  for different values of  $j_s$  and  $t_c$  under oscillatory steady state. Similarly, Figures 8.6(c) and 8.6(d) respectively show the predicted cation  $c_{1,E}(L-H, t)$  and anion  $c_{2,E}(L-H, t)$  concentrations at the Stern/diffuse layer interface near the carbon electrode. Here, ion concentrations larger than the bulk concentrations  $c_{1,E,\infty} = c_{2,E,\infty}$  correspond to the presence of an EDL.

Figures 8.6(a) and 8.6(b) indicate that EDLs formed near the pseudocapacitive electrode for all  $j_s$  considered. However, the concentrations of both  $\text{Li}^+$  and  $\text{ClO}_4^-$  remained closer to their bulk concentrations  $c_{1,E,\infty} = c_{2,E,\infty} = 1 \text{ mol L}^{-1}$  as  $j_s$  decreased. In fact, *in the faradaic regime*, the deviations from the bulk concentrations did not result in a large error in the value of  $\eta_F(t)$  predicted by Equation (8.27) and derived by assuming  $c_{1,E}(-L+H, t) \approx c_{2,E}(-L+H, t) \approx c_{1,E,\infty} = c_{2,E,\infty}$ . In this regime, an EDL of  $\text{Li}^+$  formed near the pseudocapacitive electrode during the charging step and an EDL of  $\text{ClO}_4^-$  during the discharging step. As  $j_s$  increased, the formation of the  $\text{Li}^+$  EDL near the pseudocapacitive electrode occurred later in the charging step. *In the capacitive regime*, an EDL consisting of  $\text{ClO}_4^-$  formed at the beginning and end of the cycle while a  $\text{Li}^+$  EDL formed briefly

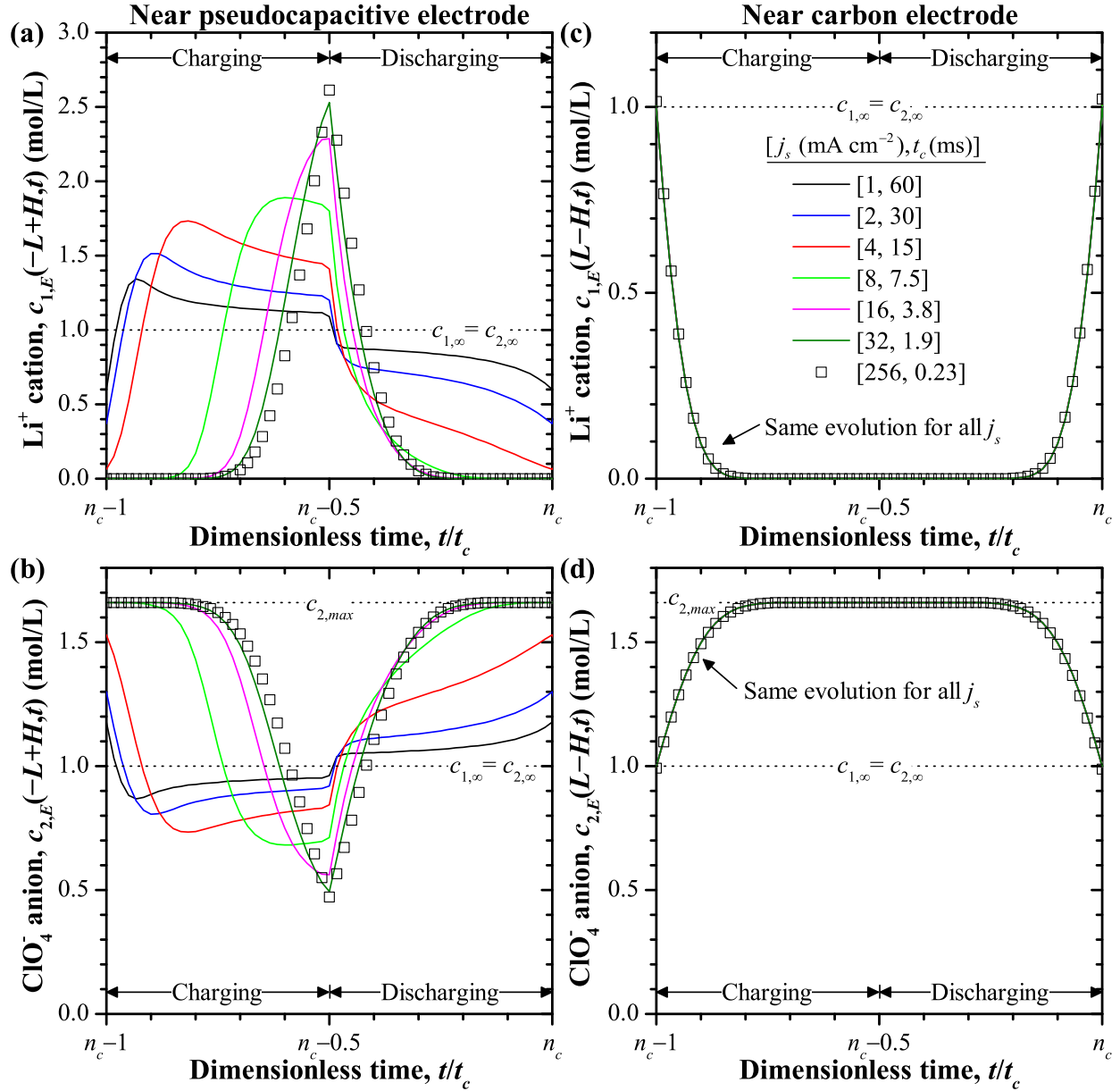


Figure 8.6: Predicted concentrations of (a)  $\text{Li}^+$  cation  $c_{1,E}(-L+H,t)$  and (b)  $\text{ClO}_4^-$  anion  $c_{2,E}(-L+H,t)$  at the Stern/diffuse layer interface near the pseudocapacitive electrode as well as concentrations of (c)  $\text{Li}^+$   $c_{1,E}(L-H,t)$  and (d)  $\text{ClO}_4^-$   $c_{2,E}(L-H,t)$  at the Stern/diffuse layer interface near the carbon electrode as functions of dimensionless time  $t/t_c$  over one cycle at oscillatory steady state for different values of  $j_s$  and  $t_c$  such that  $\Delta q_s = j_s t_c / 2 = 0.3 \text{ C m}^{-2}$ .

around the transition from charging to discharging (around  $t/t_c \approx n_c - 0.5$ ). In addition, the  $\text{Li}^+$  concentration  $c_{1,E}(-L + H, t)$  approached zero at the beginning and end of the cycle when  $\Delta\psi_H$  was positive and large. This resulted in a very small faradaic current density  $j_F$  [Figure 8.3(a)] as the exchange current density  $j_{F,0}$  vanished due to  $\text{Li}^+$  starvation [Equation (8.5)]. In both regimes, the sign of the electric field  $E(-L + H, t) = \Delta\psi_H(t)/H$  at the Stern/diffuse layer interface near the pseudocapacitive electrode determined which ion species formed the EDL. For  $\Delta\psi_{eq} = 0$  V,  $E(-L + H, t)$  always had the same sign as the surface overpotential  $\eta(t)$  [Figure 8.5(b)]. Positive  $\eta(t)$  and  $E(-L + H, t)$  corresponded to an EDL of  $\text{ClO}_4^-$  and negative  $\eta(t)$  and  $E(-L + H, t)$  to an EDL of  $\text{Li}^+$ . When they were equal to zero, the EDL vanished and both ion species were at their bulk concentrations, i.e.,  $c_{1,E}(-L + H, t) = c_{2,E}(-L + H, t) = c_{1,E,\infty} = c_{2,E,\infty}$ .

Figures 8.6(c) and 8.6(d) establish that the temporal evolutions of the ion concentrations near the carbon electrode were self-similar and were identical when plotted as functions of  $t/t_c$  for all current densities  $j_s$  and cycle periods  $t_c$  considered. This further confirms that ion transport in the electrolyte was not diffusion limited in the range of  $j_s$  considered. In addition, the results obtained near the carbon electrode resembled those observed in previous simulations of EDLCs [5]. Figure 8.6(d) indicates that, during the charging step, the concentration  $c_{2,E}(L - H, t)$  of the anion  $\text{ClO}_4^-$  increased until it reached its maximum value  $c_{2,E,max}$ , corresponding to the formation of an EDL of  $\text{ClO}_4^-$ .

### 8.3.5 Effect of variable equilibrium potential drop $\Delta\psi_{eq}$

Figure 8.7 shows the numerically predicted (a) faradaic  $j_F(t)/j_s$  and (b) capacitive  $j_C(t)/j_s$  fractions of the total current density, (c) potential  $\Delta\psi_P(t)$  of the pseudocapacitive electrode relative to bulk electrolyte, and (d) cell potential  $\psi_s(t)$  as functions of dimensionless time  $t/t_c$  for  $S_{eq}$  equal to 0 V, 1 V, and 10.5 V. The selected cases with  $[j_s \text{ (mA cm}^{-3}\text{)}, t_c \text{ (ms)}] = [2, 30]$  and  $[256, 0.23]$  respectively corresponded to the faradaic and capacitive regimes previously identified for ideal faradaic behavior with  $S_{eq} = 0$  V (Figure 8.3). Figures 8.7(a) and 8.7(b) show that the evolutions of  $j_F/j_s$  and  $j_C/j_s$  for a given  $[j_s, t_c]$  were qualitatively similar for

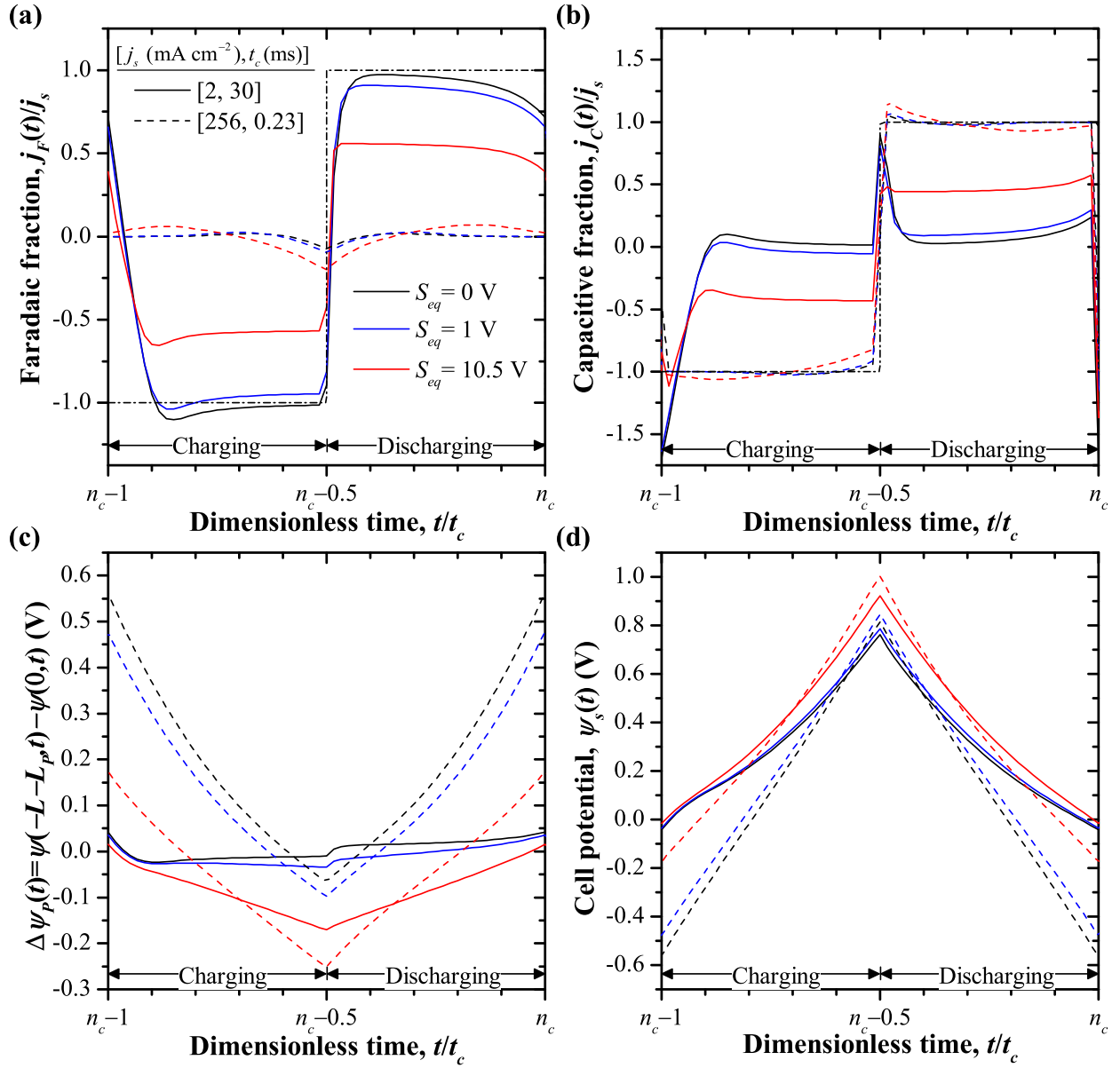


Figure 8.7: Predicted (a) faradaic  $j_F(t)/j_s$  and (b) capacitive  $j_C(t)/j_s$  fractions of the total current density, (c) potential  $\Delta\psi_P(t)$  of the pseudocapacitive electrode relative to bulk electrolyte, and (d) cell potential  $\psi_s(t)$  as functions of dimensionless time  $t/t_c$  for  $S_{eq} = 0, 1$ , and  $10.5$  V under galvanostatic cycling. The two selected cases  $[j_s, t_c]$  corresponded to the faradaic and capacitive regimes identified for  $S_{eq} = 0$  V and satisfying  $\Delta q_s = j_s t_c / 2 = 0.3 \text{ C m}^{-2}$ .

all values of  $S_{eq}$  considered. For  $j_s = 256 \text{ mA cm}^{-3}$ , the capacitive current density  $j_C(t)$  dominated (capacitive regime) and was not significantly affected by changes in  $S_{eq}$ . The changes in  $j_F(t)/j_s$  and the corresponding small changes in  $j_C(t)/j_s$  can be attributed to the fact that the  $\text{Li}^+$  concentration  $c_{1,E}(-L + H, t)$  at the Stern/diffuse layer interface near the pseudocapacitive electrode increased with increasing  $S_{eq}$  (not shown). As a result, the  $\text{Li}^+$  starvation observed at the beginning and end of the cycle in Figure 8.6(a) and causing very small  $j_F(t)$  vanished for  $S_{eq} = 10.5 \text{ V}$ . For  $j_s = 2 \text{ mA cm}^{-3}$ , the faradaic fraction of the total current  $|j_F(t)/j_s|$  decreased with increasing  $S_{eq}$ . This can be attributed to the fact that non-zero rate of change  $d\Delta\psi_{eq}/dt$  resulted in non-zero capacitive current density  $j_C$ . Rearranging Equation (8.25) and combining it with  $j_{im}(t) = j_F(t) + j_C(t)$  yields

$$j_C(t) = j_{im}(t) - j_F(t) = \frac{\epsilon_0 \epsilon_r}{H} \left[ \frac{d\eta(t)}{dt} + \frac{d\Delta\psi_{eq}(t)}{dt} \right]. \quad (8.30)$$

After substitution for  $\Delta\psi_{eq}$  based on Equations (8.21) and (8.22),  $j_F$  can be expressed as

$$j_F(t) = \frac{j_{im}(t) - \frac{\epsilon_0 \epsilon_r}{H} \frac{d\eta(t)}{dt}}{1 + \frac{\epsilon_0 \epsilon_r S_{eq} A_P}{H c_{1,P,max} z_{1,E} F}}. \quad (8.31)$$

As a result,  $S_{eq} > 0 \text{ V}$  prevented the hybrid pseudocapacitor from reaching the faradaic limit  $j_F(t) \approx j_{im}(t)$  even when  $d\eta(t)/dt$  was negligible. For the cases considered in the present study and  $d\eta/dt \approx 0$ , Equation (8.31) predicted  $j_F = 0.93j_{im}$  for  $S_{eq} = 1 \text{ V}$  and  $j_F = 0.56j_{im}$  for  $S_{eq} = 10.5 \text{ V}$ . This agrees well with the numerical predictions shown in Figure 8.7(a). Figure 8.7(c) shows that, for  $j_s = 2 \text{ mA cm}^{-2}$ , the potential drop  $\Delta\psi_P(t)$  across the pseudocapacitive electrode half-cell decreased with increasing  $S_{eq}$ . For  $S_{eq} = 10.5 \text{ V}$ ,  $\Delta\psi_P(t)$  had a significant slope  $d\Delta\psi_P(t)/dt$  throughout the cycle and qualitatively resembled that measured experimentally [Figure 8.1(a)]. Figure 8.7(d) shows that this resulted in the potential window  $\Delta\psi_s$  increasing and thus the integral capacitance  $C_{s,int}$  decreasing with increasing  $S_{eq}$  for  $j_s = 2 \text{ mA cm}^{-2}$ .

It is interesting to note that experimental measurements for  $\text{MnO}_2$  electrodes showed smaller values of  $S_{eq}$  for thin-film electrodes than for thick porous electrodes [123]. The present results suggest that this would cause smaller faradaic current and smaller capacitances for thick porous electrodes compared with thin films. Indeed, smaller capacitance

for thicker electrodes has been observed experimentally [158]. It is also noteworthy that the predicted  $j_F$  and  $j_C$  corresponding to ideal faradaic behavior with  $S_{eq} = 0$  V were quite close to those for  $S_{eq} = 1$  V, approximately the value measured for thin  $\text{MnO}_2$  films [123]. This suggests that constant  $\Delta\psi_{eq}$  is a reasonable first approximation for simulating thin electrodes.

### 8.3.6 Charging by $\text{Li}^+$ deintercalation

As previously mentioned, for some hybrid pseudocapacitors, such as those using  $\text{MnO}_2$  positive electrodes, charging corresponds to deintercalation of the cation. This can be implemented by replacing Equation (8.10) with

$$j_{im}(t) = \begin{cases} j_s & \text{for charging } (n_c - 1)t_c \leq t < (n_c - 1/2)t_c \\ -j_s & \text{for discharging } (n_c - 1/2)t_c \leq t < n_c t_c. \end{cases} \quad (8.32)$$

In addition, a significant initial concentration of intercalated  $\text{Li}^+$   $c_{1,P,0} = 1 \text{ mol L}^{-1}$  was used in order to accommodate the initial deintercalation of  $\text{Li}^+$ , as done during material synthesis of  $\text{MnO}_2$  electrodes [112, 115]. As in Sections 8.3.1 to 8.3.4,  $S_{eq}$  was taken as  $S_{eq} = 0$  V corresponding to ideal faradaic behavior.

Figure 8.8 shows (a) the faradaic  $j_F(t)/j_s$  and (b) capacitive  $j_C(t)/j_s$  fractions of the imposed current as well as (c) the surface overpotential  $\eta(t)$  and (d) the cell potential  $\psi_s(t) = \Delta\psi_P(t) - \Delta\psi_C(t)$  for the hybrid pseudocapacitor charged by deintercalation. Figures 8.8(a) and 8.8(b) indicated that the previously observed faradaic and capacitive regimes also occurred for charging by deintercalation. In addition, Figure 8.8(c) shows that the numerically predicted overpotential  $\eta$  agreed well with the analytical predictions  $\eta_F$  and  $\eta_C$  [Equations (8.27) to (8.29)]. Here,  $|\eta_F|$  reached a maximum at the end of the charging step when  $c_{1,P,F}$  was minimum. Moreover,  $|\eta_C|$  was large and positive around the transition from charging to discharging. This resulted in  $\text{Li}^+$  starvation in the electrolyte, i.e.,  $c_{1,E}(-L + H, t) \approx 0 \text{ mol L}^{-1}$  (not shown), and  $j_F \approx 0 \text{ mA cm}^{-2}$  at this time rather than around the transition from discharging to charging as previously observed [Figure 8.3(a)]. Figure 8.8(d) shows that the cell potential evolution  $\psi_s(t)$  had similar qualitative behavior

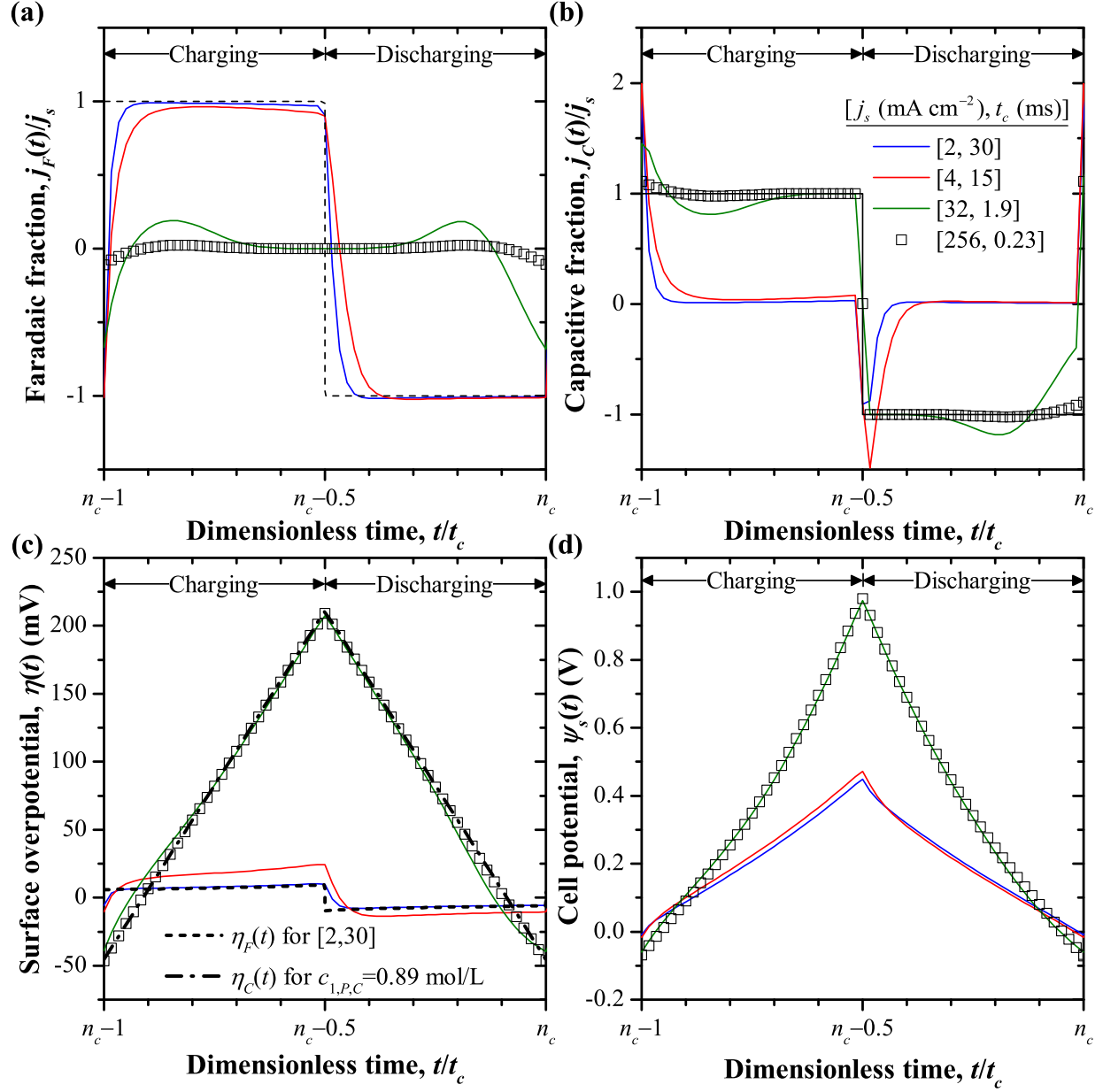


Figure 8.8: Predicted (a) the faradaic  $j_F(t)/j_s$  and (b) capacitive  $j_C(t)/j_s$  fractions of the imposed current as well as (c) the surface overpotential  $\eta(t)$  and (d) the cell potential  $\psi_s(t) = \Delta\psi_P(t) - \Delta\psi_C(t)$  for the hybrid pseudocapacitor charged by deintercalation for various  $[j_s, t_c]$  satisfying  $\Delta q_s = j_s t_c / 2 = 0.3 \text{ C m}^{-2}$ .

to that observed for charging by intercalation [Figure 8.5(a)]. *In the faradaic regime*, it qualitatively resembled experimental measurements [Figure 8.1(b)]. The potential window  $\Delta\psi_s$  was smaller than that for the same values of  $j_s$  and  $t_c$  when charging by intercalation. Thus, charging by deintercalation, with the present planar electrodes, resulted in a larger integral capacitance  $C_{s,int}$ . At the pseudocapacitive electrode,  $|\eta_F|$  remained relatively small because  $c_{1,P,F}$  remained relatively large ( $> 0.38 \text{ mol L}^{-1}$ ). At the carbon electrode, the EDL was formed by the smaller  $\text{Li}^+$  ions rather than  $\text{ClO}_4^-$ , leading to larger maximum concentration  $c_{1,E,max}$  and thus to larger EDL capacitance [5]. Here also, a faradaic “kink” in  $\psi_s(t)$  was evident at the beginning of both the charging and discharging steps. However, it was more prominent at the beginning of the discharging step. This can be attributed to the fact that  $|\eta_F|$  was maximum at the transition from charging to discharging, requiring a relatively large change in  $\eta$  before the faradaic current could become dominant again.

## 8.4 Conclusion

The present study investigated the electrochemical transport phenomena occurring inside hybrid pseudocapacitors under galvanostatic cycling using a rigorous physical model accounting for coupled faradaic reaction and EDL formation. Detailed numerical simulations were performed for a hybrid pseudocapacitor with planar electrodes under various current densities and cycle periods. First, two asymptotic regimes were identified: (i) a faradaic regime dominated by redox reactions at small  $j_s$  and slow charging and (ii) a capacitive regime dominated by EDL formation under large  $j_s$  and fast charging. In these regimes, simple analytical expressions were derived for the  $\text{Li}^+$  concentration in the pseudocapacitive electrode and for the surface overpotential as functions of time during a galvanostatic cycle. The surface overpotential was important in determining whether EDL or faradaic charge storage dominated. The larger its value at the charging/discharging transitions, the smaller the faradaic fraction of the charge storage. In addition, large and positive overpotential resulted in small faradaic current due to  $\text{Li}^+$  starvation in the electrolyte. Second, the predicted cell potentials resembled those reported experimentally. In particular, characteristic “kinks”



occurred immediately after charging/discharging transitions and were attributed to brief periods of capacitive operation as the surface overpotential and ion concentrations adjusted to the new direction of the current, before the faradaic charge storage became dominant again. Finally, variation of the equilibrium potential drop  $\Delta\psi_{eq}$  with the state of charge negatively affected the faradaic charge storage and prevented the device from operating in the faradaic regime, even at small current, thus reducing its capacitance. Overall, this study indicates that accounting for coupling between EDL formation and faradaic reactions is essential for reproducing experimental features such as the faradaic kinks in the cell potential and for determining whether the cell operates in the faradaic or the capacitive regimes. The numerical model and the derived analytical expressions provide useful tools for optimizing hybrid pseudocapacitor performance.

## CHAPTER 9

### **First-principles thermal modeling of hybrid pseudocapacitors under galvanostatic cycling**

This chapter presents a theoretical framework developed from first principles for predicting the spatiotemporal thermal behavior of hybrid pseudocapacitors under galvanostatic cycling. It accounts for irreversible and reversible heat generation rates in the electrolyte and in the electrodes due to Joule heating, electric double layer (EDL) formation, and redox reactions. Detailed numerical simulations were performed to investigate the different local heat generation rates and the temperature as functions of time and cycling current. Numerical predictions showed good qualitative agreement with the limited experimental data available in the literature. Such numerical simulations can be used to physically interpret experimental measurements. For example, the present results suggest that a distinctive endothermic peak observed in the experimental heat generation rate resulted from cation starvation in the electrolyte reducing the faradaic current density. In addition, heating due to EDL formation significantly affected the local temperature and must be accounted for. The thermal model and the present results will help to define safe modes of operation and to develop thermal management strategies for pseudocapacitors.

#### **9.1 Analysis**

##### **9.1.1 Schematic and assumptions**

Figure 8.2(b) illustrates the one-dimensional (1D) hybrid pseudocapacitor cell considered in the present study. It was identical to that considered in Chapter 8.

To make the problem mathematically tractable, Assumptions (1)–(8) from Chapter 8 were used in the present chapter. In addition, I assumed that (9) the Dufour energy flux, i.e., the energy flux due to gradients of electrochemical potential and/or pressure, was negligible [28,32,90]. Finally, (10) the temperature was assumed to be uniform within the narrow Stern layers at all times, and (11) the cell was thermally insulated. For simplicity and in the interest of physical interpretation, the governing equations for the thermal model are presented in 1D Cartesian coordinates. The general 3D derivation of the faradaic heat generation rates can be found in Appendix C.

### 9.1.2 Electrochemical transport model

The governing equations for (i) the local electric potential  $\psi(x, t)$  in both electrodes and in the electrolyte, (ii) the local concentrations  $c_{i,E}(x, t)$  of ion species  $i$  in the diffuse layer of the electrolyte, and (iii) the local intercalated  $\text{Li}^+$  concentration  $c_{1,P}(x, t)$  in the pseudocapacitive electrode as well as the expressions of the faradaic  $j_F(t)$  and capacitive  $j_C(t)$  current densities were the same as those presented in Section 8.2. Here also, the subscripts  $P$ ,  $E$ , and  $C$  denote concentrations and properties within the pseudocapacitive electrode, the electrolyte, and the carbon electrode, respectively.

### 9.1.3 Thermal model

The governing equation for the temperature and the local heat generation rates in each region of the hybrid pseudocapacitor can be derived from energy conservation principles applied to a fixed control volume [2, 5]. The temperature is governed by the heat diffusion Equation (2.12).

#### 9.1.3.1 Heat generation rates in the electrodes and electrolyte diffuse layer

In the electrodes and in the diffuse layer, there is negligible bulk motion and Dufour energy flux [Assumptions (2) and (8)]. The general mass conservation equation accounting for

homogeneous chemical reactions can be expressed as [28]

$$\frac{\partial c_i}{\partial t} = -\frac{\partial N_i}{\partial x} + \dot{r}_i \quad (9.1)$$

where  $\dot{r}_i$  is the local production rate of species  $i$  (in  $\text{mol m}^{-3}\text{s}^{-1}$ ) due to chemical reactions. Then, following the derivation procedure used in Chapters 4 for EDLCs, the local volumetric heat generation rate  $\dot{q}(\mathbf{r}, t)$  (in  $\text{W m}^{-3}$ ) can be expressed as

$$\dot{q} = -\sum_{i=0}^{n+1} N_i \frac{\partial \bar{H}_i}{\partial x} - \sum_{i=0}^{n+1} \bar{H}_i \dot{r}_i \quad (9.2)$$

where  $\bar{H}_i$  is the partial molar enthalpy of ion species  $i$  ( $1 \leq i \leq n$ ) or of the electrons, corresponding to  $i = n + 1$ . The first term on the right-hand side of Equation (9.2) is the same as that derived for EDLCs in Chapters 4 and 7. It is the sum of the heat generation rates (i)  $\dot{q}_E$  [Equation (7.1)] arising from electric charge carriers (ions or electrons) decreasing their electrical potential energy and (ii) the “heat of mixing”  $\dot{q}_S$  [Equation (7.5)] arising from fluxes of ions and/or electrons along gradients of chemical potential, partial molar entropy, and temperature [2, 67]. Finally, the second term on the right-hand side of Equation (9.2) corresponds to heat generated by homogeneous chemical reactions.

**In the 1D electrodes** The current density  $j$  results from the flux of electrons and is related to the electric field  $E$  by Ohm’s law expressed as  $j = \sigma_P E$  in the pseudocapacitive electrode and  $j = \sigma_C E$  in the carbon electrode [28]. Here, the transport of intercalated  $\text{Li}^+$  ions is accompanied by equal numbers of electrons according to Equation (8.1) and thus does not affect the net electric current. Thus, the electrical heat generation rate  $\dot{q}_E$  reduces to irreversible Joule heating expressed as

$$\dot{q}_E = \dot{q}_{J,irr} = \begin{cases} \frac{j^2}{\sigma_P} & \text{in the pseudocapacitive electrode} \\ \frac{j^2}{\sigma_C} & \text{in the carbon electrode.} \end{cases} \quad (9.3)$$

The heat of mixing due to the 1D electron flux  $N_{n+1,P} = -j/F$  and to the 1D flux of intercalated  $\text{Li}^+$   $N_{1,P} = -D_{1,P} \partial c_{1,P} / \partial x$  could potentially produce a reversible heat generation rate in the electrode expressed as

$$\dot{q}_S = -R_u \left\{ \frac{j}{F} \frac{\partial}{\partial x} \left[ T^2 \frac{\partial \ln(\gamma_{n+1,P})}{\partial T} \right] + D_{1,P} \frac{\partial c_{1,P}}{\partial x} \frac{\partial}{\partial x} \left[ T^2 \frac{\partial \ln(\gamma_{1,P})}{\partial T} \right] \right\}. \quad (9.4)$$

The present study neglects  $\dot{q}_S$  in the electrodes. Indeed, the first term associated with the electrons is expected to be negligible as (i) the EDL region in an electrode is negligibly thin [27] and (ii) reversible heating in the electrode has not been reported for other applications such as dielectric capacitors where this expression would also apply. The second term on the right-hand side of Equation (9.4) was neglected as the required expression for the activity coefficient  $\gamma_{1,P}$  of intercalated  $\text{Li}^+$  as a function of temperature and of  $\text{Li}^+$  concentration inside the pseudocapacitive material is, to the best of my knowledge, not available in the literature.

Finally, in the pseudocapacitive electrode, the heat generation rate  $\dot{q}_{F,P}(x, t) = \sum_{i=0}^{n+1} (\bar{H}_{i,P} \dot{r}_{i,P})(x, t)$  arises as intercalated  $\text{Li}^+$  ions move from one lattice site to the next. Here, the local rate of  $\text{Li}_m\text{M}_p\text{O}_q$  production can be related to the concentration  $c_{1,P}$  predicted by the electrochemical transport model as  $(1/m)\partial c_{1,P}/\partial t$ . In addition, the production rates  $\dot{r}_{i,P}$  are related by stoichiometry. As a result, the heat generation rate  $\dot{q}_{F,P}$  can be expressed as

$$\dot{q}_{F,P}(x, t) = \dot{q}_{F,P,rev}(x, t) = -\frac{\Delta H_r}{m} \frac{\partial c_{1,P}}{\partial t} \quad (9.5)$$

where  $\Delta H_r = \bar{H}_{\text{Li}_m\text{M}_p\text{O}_q} - \bar{H}_{\text{M}_p\text{O}_q} - m\bar{H}_{\text{Li}^+} - m\bar{H}_{\text{e}^-}$  is the enthalpy of reaction corresponding to Equation (8.1), i.e., the enthalpy change resulting from the production of one mole of  $\text{Li}_m\text{M}_p\text{O}_q$  [159, 160]. Since  $\partial c_{1,P}/\partial t$  changes sign based on the direction of the reaction while  $\Delta H_r$  does not,  $\dot{q}_{F,P}$  is a reversible heat generation rate. Note that, for constant  $\Delta H_r$ , the total contribution of  $\dot{q}_{F,P}(x, t)$  in the electrode  $\int_{-L_P-L}^{-L} \dot{q}_{F,P}(x, t) dx = -(\Delta H_r/m) \frac{\partial}{\partial t} \int_{-L_P-L}^{-L} c_{1,P}(x, t) dx$  is proportional to the faradaic current density  $j_F(t)$ .

**In the diffuse layer** The physical processes causing heat generation in the diffuse layer of hybrid pseudocapacitors are identical to those taking place in EDLCs and derived in Chapter 7. Thus, the overall heat generation rate  $\dot{q}$  in the diffuse layer was equal to  $\dot{q} = \dot{q}_{J,irr} + \dot{q}_{E,d} + \dot{q}_{E,s} + \dot{q}_{S,c} + \dot{q}_{S,T}$ . The irreversible Joule heating  $\dot{q}_{J,irr}$  was given by Equation (7.3). The reversible heat generation rates  $\dot{q}_{E,d}$ ,  $\dot{q}_{E,s}$ ,  $\dot{q}_{S,c}$ ,  $\dot{q}_{S,T}$  were associated with EDL formation. They were given by Equation (7.4) for  $\dot{q}_{E,d}$  and  $\dot{q}_{E,s}$  and by Equation (7.7) for  $\dot{q}_{S,c}$  and  $\dot{q}_{S,T}$ .

### 9.1.3.2 Stern layers

The temperature across the Stern layer was assumed to be uniform due to its small thickness. Then, in the absence of ion or solvent accumulation, the energy conservation equation for each Stern layer can be expressed as

$$\frac{\partial(\rho_E u)}{\partial t} = \rho_{EC_{p,E}} \frac{\partial T}{\partial t} = \frac{q''_{in} - q''_{out}}{H}. \quad (9.6)$$

Here,  $u$  is the specific internal energy of the electrolyte in the Stern layer while  $q''_{in}$  and  $q''_{out}$  are the energy fluxes into and out of the Stern layer, respectively. Near the carbon electrode, the energy fluxes  $q''_{in}$  and  $q''_{out}$  are solely due to heat conduction. Then, the energy conservation equation can be written as

$$\rho_{EC_{p,E}} \frac{\partial T}{\partial t} = \frac{1}{H} \left[ k_C \frac{\partial T}{\partial x}(L, t) - k_E \frac{\partial T}{\partial x}(L - H, T) \right]. \quad (9.7)$$

Near the pseudocapacitive electrode, the energy fluxes result not only from heat conduction but also from chemical reactants entering and exiting the Stern layer. Assuming negligible Dufour effect, the local energy fluxes  $q''_{in}(t) = q''(-L, t)$  at the electrode/electrolyte interface and  $q''_{out}(t) = q''(-L + H, t)$  at the Stern/diffuse layer interface can be expressed as [28]

$$q''_{in}(t) = -k_P \frac{\partial T}{\partial x}(-L, t) + \sum_{i=1}^{n+1} (\bar{H}_{i,P} N_{i,P})(-L, t) \quad (9.8)$$

$$\text{and } q''_{out}(t) = -k_E \frac{\partial T}{\partial x}(-L + H, t) + \sum_{i=1}^n (\bar{H}_{i,E} N_{i,E})(-L + H, t). \quad (9.9)$$

Then, in the Stern layer near the pseudocapacitive electrode, Equation (9.6) becomes

$$\rho_{EC_{p,E}} \frac{\partial T}{\partial t} = \frac{1}{H} \left[ k_E \frac{\partial T}{\partial x}(-L + H, t) - k_P \frac{\partial T}{\partial x}(-L, t) \right] + \dot{q}_{F,E}(t) \quad (9.10)$$

where  $\dot{q}_{F,E}$  is the heat generation rate due to the faradaic reaction given by

$$\dot{q}_{F,E}(t) = -\frac{1}{H} \left[ \sum_{i=1}^n (\bar{H}_{i,E} N_{i,E})(-L + H, t) - \sum_{i=1}^{n+1} (\bar{H}_{i,P} N_{i,P})(-L, t) \right]. \quad (9.11)$$

The only non-zero terms in Equation (9.11) correspond to species involved in the redox reaction [Equation (8.1)] because no other species enter or exit the Stern layer. The fluxes  $N_{i,E}$  and  $N_{i,P}$  of all reacting species are related to the electron flux  $N_{n+1,P}$  and the faradaic

current density  $j_F$  by stoichiometry [28]. Let us consider the general redox reaction occurring at the pseudocapacitive electrode/electrolyte interface  $\sum_{i=0}^{n+1} (s_{i,P}M_{i,P} + s_{i,E}M_{i,E}) \rightleftharpoons 0$ , where  $s_i$  is the stoichiometric coefficient for reactant  $M_i$  and subscripts  $P$  and  $E$  respectively refer to the pseudocapacitive electrode and the electrolyte. For this reaction, the fluxes of reactants  $N_{i,E}$  in the electrolyte and  $N_{i,P}$  in the pseudocapacitive electrode are related by  $j_F(t)/F = -N_{n+1,P}(-L, t) = -(s_{n+1,P}/s_{i,P})N_{i,P}(-L, t) = (s_{n+1,P}/s_{i,E})N_{i,E}(-L + H, t)$ . Then,  $\dot{q}_{F,E}$  can be expressed as

$$\dot{q}_{F,E} = -\frac{j_F(t)}{HF s_{n+1,P}} \sum_{i=1}^{n+1} [s_{i,E}\bar{H}_{i,E}(-L + H, t) + s_{i,P}\bar{H}_{i,P}(-L, t)]. \quad (9.12)$$

Expressing the partial molar enthalpy as  $\bar{H}_i = \tilde{\mu}_i + T\bar{S}_i$  [91] yields

$$\begin{aligned} \dot{q}_{F,E} = -\frac{j_F(t)}{H} \left\{ \frac{1}{s_{n+1,P}F} \sum_{i=1}^{n+1} [s_{i,E}\tilde{\mu}_{i,E}(-L + H, t) + s_{i,P}\tilde{\mu}_{i,P}(-L, t)] \right. \\ \left. + \frac{1}{s_{n+1,P}F} T \sum_{i=1}^{n+1} [s_{i,E}\bar{S}_{i,E}(-L + H, t) + s_{i,P}\bar{S}_{i,P}(-L, t)] \right\}. \end{aligned} \quad (9.13)$$

The two terms within the brackets correspond to expressions for the surface overpotential  $\eta$  and the Peltier coefficient  $\Pi$ , respectively defined as [28]

$$\eta = -\sum_{i=0}^{n+1} \frac{(s_{i,P}\tilde{\mu}_{i,P} + s_{i,E}\tilde{\mu}_{i,E})}{s_{n+1,P}F} \quad \text{and} \quad \Pi = -\frac{T}{F} \sum_{i=0}^{n+1} \frac{(s_{i,P}\bar{S}_{i,P} + s_{i,E}\bar{S}_{i,E})}{s_{n+1,P}}. \quad (9.14)$$

Then,  $\dot{q}_{F,E}(x, t)$  can be divided into one irreversible  $\dot{q}_{F,E,irr}$  and one reversible  $\dot{q}_{F,E,rev}$  contribution such that  $\dot{q}_{F,E} = \dot{q}_{F,E,irr} + \dot{q}_{F,E,rev}$  with the remarkably simple expressions

$$\dot{q}_{F,E,irr}(t) = \frac{j_F(t)}{H} \eta(t) \quad \text{and} \quad \dot{q}_{F,E,rev}(t) = \frac{j_F(t)}{H} \Pi(t). \quad (9.15)$$

These heat generation rates were confined to the Stern layer adjacent to the pseudocapacitive electrode, i.e.,  $-L \leq x \leq -L + H$ . Note that the form of the heat generation rates defined by Equation (9.15) was also derived in Ref. [28] for an electrochemical reaction at steady state but ignoring EDL formation.

Here,  $\dot{q}_{F,E,rev}$  generated at the electrode/electrolyte interface [Equation (9.15)] and the total heat generation rate due to  $\dot{q}_{F,P,rev}$  inside the pseudocapacitive electrode [Equation

Table 9.1: Summary of the irreversible and reversible heat generation rates  $\dot{q}_{irr}$  and  $\dot{q}_{rev}$  simulated in each region for the 1D hybrid pseudocapacitor illustrated in Figure 8.2 such that  $\dot{q} = \dot{q}_{irr} + \dot{q}_{rev}$ .

Region	Coordinates	Irreversible heat generation rate (W m <sup>-3</sup> )	Reversible heat generation rate (W m <sup>-3</sup> )
<b>Pseudocapacitive electrode</b>	$-L_p - L \leq x < -L$	$\dot{q}_{irr} = \frac{j^2}{\sigma_p}$	N/A
<b>Pseudocapacitive electrode Stern layer</b>	$-L \leq x < -L + H$	$\dot{q}_{irr} = \frac{j_F \eta}{H}$	$\dot{q}_{rev} = \frac{j_F \Pi}{H}$
<b>Electrolyte diffuse layer</b>	$-L + H \leq x < L - H$	$\dot{q}_{irr} = \frac{j^2}{\sigma_E}$	$\dot{q}_{rev} = \dot{q}_{E,d} + \dot{q}_{E,s} + \dot{q}_{S,c} + \dot{q}_{S,T}$
<b>Carbon electrode Stern layer</b>	$L - H \leq x < L$	N/A	N/A
<b>Carbon electrode</b>	$L \leq x < L + L_C$	$\dot{q}_{irr} = \frac{j^2}{\sigma_C}$	N/A

(9.5)] are both proportional to  $j_F$ . Experimentally, it would be difficult to distinguish between them to measure separate values for  $\Pi$  and  $\Delta H_r$ . Indeed, to the best of my knowledge, the data required to evaluate  $\Delta H_r$  for the homogeneous reaction inside the electrode is not available in the literature. As a result, the present study simulates  $\dot{q}_{F,E,rev}$  inside the Stern layer only and neglects  $\dot{q}_{F,P,rev}$ .

To summarize, Table 9.1 gives the expressions for the irreversible and reversible heat generation rates simulated in each region of the 1D hybrid pseudocapacitor for the present study.

#### 9.1.4 Initial and boundary conditions

The governing Equations (8.2) and (2.5) for  $\psi(x, t)$ , Equation (8.3) for  $c_{1,P}(x, t)$ , Equation (2.6) for  $c_{1,E}(x, t)$  and  $c_{2,E}(x, t)$ , and Equation (2.12) for  $T(x, t)$  are first-order partial differential equations (PDEs) in time and second-order PDEs in space. Each equation requires



one initial condition and two boundary conditions in each region where it is solved. Here, the  $\text{Li}^+$  concentration  $c_{1,P}(x, t)$  was computed only in the pseudocapacitive electrode, and the ion concentrations  $c_{1,E}(x, t)$  and  $c_{2,E}(x, t)$  only in the diffuse layer. Meanwhile, the potential  $\psi(x, t)$  and the temperature  $T(x, t)$  were computed in the pseudocapacitive and carbon electrodes as well as the diffuse layer of the electrolyte. The potential  $\psi$  and temperature  $T$  inside the Stern layers were not explicitly simulated. Instead, the Stern layers and the faradaic heat generation rate  $\dot{q}_{F,E}$  therein were accounted for by using the boundary conditions at the electrode/electrolyte and at the Stern/diffuse layer interfaces.

The initial and boundary conditions for the potential  $\psi(x, t)$  and the concentrations  $c_{1,P}(x, t)$ ,  $c_{1,E}(x, t)$ , and  $c_{2,E}(x, t)$  during galvanostatic cycling under current density  $\pm j_s$  were the same as those given in Section 8.2.3, except for the expression of the imposed current density  $j_{im}(t)$ . In contrast to Chapter 8, the present chapter considers galvanostatic cycling over a fixed potential window  $\psi_{min} \leq \psi_s \leq \psi_{max}$ , analogous to that performed experimentally. Then, for charging corresponding to  $\text{Li}^+$  deintercalation,  $j_{im}(t)$  was expressed as

$$j_{im}(t) = \begin{cases} j_s & \text{if } \psi_{min} < \psi_s < \psi_{max} \text{ and } d\psi_s/dt \geq 0 \text{ or } \psi_s = \psi_{min} \\ -j_s & \text{if } \psi_{min} < \psi_s < \psi_{max} \text{ and } d\psi_s/dt < 0 \text{ or } \psi_s = \psi_{max}. \end{cases} \quad (9.16)$$

In this method, the duration of the charging and discharging steps was allowed to vary, as implemented experimentally.

Moreover, the initial temperature was uniform and equal to  $T_0$  throughout the device so that

$$T(x, 0) = T_0. \quad (9.17)$$

The pseudocapacitive electrode was thermally insulated at the electrode/current collector interface such that

$$-k_P \frac{\partial T}{\partial x}(-L - L_P, t) = 0 \text{ W m}^{-2}. \quad (9.18)$$

The temperature at the electrode/electrolyte interface was equal to that at the Stern/diffuse layer interface [Assumption (10)], i.e.,

$$T(-L, t) = T(-L + H, t). \quad (9.19)$$

The heat flux at the Stern/diffuse layer interface was obtained from the energy conservation Equation (9.10) so that

$$-k_E \frac{\partial T}{\partial x}(-L + H, t) = -k_P \frac{\partial T}{\partial x}(-L, t) + H \left[ \dot{q}_{F,E}(t) - \rho_E c_{p,E} \frac{\partial T}{\partial t}(-L, t) \right]. \quad (9.20)$$

Moreover, the temperature was constant across the Stern layer near the carbon electrode so that

$$T(L - H, t) = T(L, t). \quad (9.21)$$

In the carbon electrode, the heat flux at the electrode/electrolyte interface satisfied Equation (9.7) such that

$$-k_C \frac{\partial T}{\partial x}(L, t) = -k_E \frac{\partial T}{\partial x}(L - H, t) - H \rho_E c_{p,E} \frac{\partial T}{\partial t}(L, t). \quad (9.22)$$

Finally, the carbon electrode was thermally insulated at the electrode/current collector interface so that

$$-k_C \frac{\partial T}{\partial x}(L + L_C, t) = 0 \text{ W m}^{-2}. \quad (9.23)$$

### 9.1.5 Constitutive relationships

Table 9.2 summarizes the properties of the electrodes and electrolyte used to solve the electrochemical transport model for  $\psi(x, t)$ ,  $c_{1,E}(x, t)$ ,  $c_{2,E}(x, t)$ , and  $c_{1,P}(x, t)$  for a hybrid pseudocapacitor with binary and asymmetric electrolyte. They were the same as those used in Chapter 8. Arbitrary but realistic material properties were chosen for the pseudocapacitive material. Its density  $\rho_P$  and specific heat  $c_{p,P}$  were based on those of  $\text{Nb}_2\text{O}_5$  and taken as  $\rho_P = 4550 \text{ kg m}^{-3}$  [162] and  $c_{p,P} = 496 \text{ J kg}^{-1}\text{K}^{-1}$  [163], respectively. Its thermal conductivity was taken as  $k_P = 10 \text{ W m}^{-1}\text{K}^{-1}$ , typical of various metal oxides [164]. The electrolyte simulated was  $1 \text{ mol L}^{-1}$   $\text{LiClO}_4$  in propylene carbonate (PC) solvent, with the  $\text{Li}^+$  and  $\text{ClO}_4^-$  ion species denoted by  $i = 1$  and 2, respectively. Its density  $\rho_E = 1205 \text{ kg m}^{-3}$ , specific heat  $c_{p,E} = 2141 \text{ J kg}^{-1}\text{K}^{-1}$ , and thermal conductivity  $k_E = 0.164 \text{ W m}^{-1}\text{K}^{-1}$  were taken as those of PC [58]. The density, specific heat, and thermal conductivity of the carbon electrode were taken as  $\rho_C = 2248 \text{ kg m}^{-3}$ ,  $c_{p,C} = 710 \text{ J kg}^{-1}\text{K}^{-1}$ , and  $k_C = 1.7 \text{ W m}^{-1}\text{K}^{-1}$ , respectively [165]. In the absence of reported values for  $\text{Li}^+$  intercalation in pseudocapacitive

Table 9.2: Electrochemical transport properties used for simulating the hybrid pseudocapacitor with binary and asymmetric electrolyte [161].

Electrodes			Electrolyte		
$\sigma_P$	$7 \times 10^{-2}$	S/m	$\epsilon_r$	66.1	
$L_P$	5	nm	$a_{1,E}$	0.67	nm
$D_{1,P}$	$10^{-10}$	m <sup>2</sup> /s	$a_{2,E}$	1.0	nm
$c_{1,P,max}$	32.9	mol/L	$D_{1,E}$	$2.6 \times 10^{-10}$	m <sup>2</sup> /s
$\alpha$	1/2		$D_{2,E}$	$3.3 \times 10^{-10}$	m <sup>2</sup> /s
$k_0$	$5 \times 10^{-9}$	m <sup>5/2</sup> /mol <sup>1/2</sup> s	$c_{1,E,\infty}$	1	mol/L
$\Delta\psi_{eq}$	0	V	$c_{2,E,\infty}$	1	mol/L
$\sigma_C$	100	S/m	$L$	1	$\mu\text{m}$
$L_C$	5	nm			

materials, the Peltier coefficient  $\Pi$  was taken as constant and approximated as  $\Pi = -0.363$  V based on measurements for the reaction  $\text{Li} \rightarrow \text{Li}^+ + \text{e}^-$  [166].

Finally, the initial  $\text{Li}^+$  concentration  $c_{1,P,0}$  in the pseudocapacitive electrode was equal to  $c_{1,P,0} = 1$  mol L<sup>-1</sup>. The initial temperature was  $T_0 = 298$  K. The cell was cycled galvanostatically at various current densities  $j_s$  over a fixed potential window with minimum and maximum cell potentials equal to  $\psi_{min} = 0$  V and  $\psi_{max} = 0.45$  V, respectively.

### 9.1.6 Method of solution

The one-dimensional governing equations given by Equations (8.2) and (2.5), (8.3), (2.6), and (2.12) and the associated initial and boundary conditions were solved numerically using finite element methods. Numerical convergence was assessed based on the predicted potential  $\psi(x, t)$ , concentrations  $c_{1,E}(x, t)$ ,  $c_{2,E}(x, t)$ , and  $c_{1,P}(x, t)$ , and temperature  $T(x, t)$  using the procedure and convergence criteria described in Section 4.1.5. Oscillatory steady state in  $\psi(x, t)$ ,  $c_{1,E}(x, t)$ ,  $c_{2,E}(x, t)$ , and  $c_{1,P}(x, t)$  was determined as described in Section 8.2.5.

### 9.1.7 Data processing

It is difficult to directly compare the various local volumetric heat generation rates within the hybrid pseudocapacitor because they act within different sections of the device (Table 9.1). For example, the faradaic heat generation rates  $\dot{q}_{F,E,irr}$  and  $\dot{q}_{F,E,rev}$  were non-zero only inside the narrow Stern layer near the pseudocapacitive electrode while Joule heating  $\dot{q}_{J,irr}$  was non-zero throughout both electrodes and the diffuse layer. To assess the contribution of each heat generation rate to the total heat generation, they should be integrated over the entire volume of the cell. Thus, the total Joule heat generation rate  $\dot{Q}_{J,irr}''(t)$  per unit electrode surface area (in  $\text{W m}^{-2}$ ) was defined as

$$\dot{Q}_{J,irr}''(t) = \int_{-L-L_P}^{L+L_C} \dot{q}_{J,irr}(x, t) dx = \int_{-L-L_P}^{-L} \frac{j^2}{\sigma_P} dx + \int_{-L+H}^{L-H} \frac{j^2}{\sigma_E} dx + \int_L^{L+L_C} \frac{j^2}{\sigma_C} dx. \quad (9.24)$$

It can also be defined based on averaging over each half-cell as

$$\dot{Q}_{J,irr}''(t) = \int_{-L-L_P}^0 \dot{q}_{J,irr}(x, t) dx + \int_0^{L+L_C} \dot{q}_{J,irr}(x, t) dx = \dot{Q}_{J,irr,P}''(t) + \dot{Q}_{J,irr,C}''(t). \quad (9.25)$$

Similarly, the total irreversible  $\dot{Q}_{F,irr,P}''(t)$  and reversible  $\dot{Q}_{F,rev,P}''(t)$  faradaic heat generation rates at the pseudocapacitive electrode were defined as

$$\begin{aligned} \dot{Q}_{F,irr,P}''(t) &= \int_{-L}^{-L+H} \dot{q}_{F,E,irr}(t) dx = \dot{q}_{F,E,irr}(t) H \\ \text{and } \dot{Q}_{F,rev,P}''(t) &= \int_{-L}^{-L+H} \dot{q}_{F,E,rev}(t) dx = \dot{q}_{F,E,rev}(t) H. \end{aligned} \quad (9.26)$$

To facilitate comparison with experimental measurements from Ref. [78], the reversible heat generation rates due to EDL formation were computed separately for the pseudocapacitive electrode half-cell  $\dot{Q}_{EDL,rev,P}''$  and for the carbon electrode half-cell  $\dot{Q}_{EDL,rev,C}''$  and defined as

$$\begin{aligned} \dot{Q}_{EDL,rev,P}''(t) &= \int_{-L+H}^0 (\dot{q}_{E,d} + \dot{q}_{E,s} + \dot{q}_{S,c} + \dot{q}_{S,T}) dx \\ \text{and } \dot{Q}_{EDL,rev,C}''(t) &= \int_0^{L-H} (\dot{q}_{E,d} + \dot{q}_{E,s} + \dot{q}_{S,c} + \dot{q}_{S,T}) dx. \end{aligned} \quad (9.27)$$

Then, the overall heat generation rate  $\dot{Q}_P''(t)$  from all sources in the pseudocapacitive electrode half-cell was given by

$$\dot{Q}_P''(t) = \int_{-L-L_P}^0 \dot{q}(x, t) dx = \dot{Q}_{J,irr,P}''(t) + \dot{Q}_{EDL,rev,P}''(t) + \dot{Q}_{F,irr,P}''(t) + \dot{Q}_{F,rev,P}''(t) \quad (9.28)$$

while  $\dot{Q}_C''(t)$  in the carbon electrode half-cell was expressed as

$$\dot{Q}_C''(t) = \int_0^{L+L_C} \dot{q}(x, t) dx = \dot{Q}_{J,irr,C}''(t) + \dot{Q}_{EDL,rev,C}''(t). \quad (9.29)$$

Finally, in order to effectively compare time-dependent heat generation rates, the time-average  $\overline{\dot{Q}}_j''$  of heat generation rate  $\dot{Q}_j''(t)$  at oscillatory steady state was defined as

$$\overline{\dot{Q}}_j'' = \frac{1}{t_c} \int_{(n_c-1)t_c}^{n_c t_c} \dot{Q}_j''(t) dt \quad (9.30)$$

where cycle  $n_c$  is at oscillatory steady state while subscript  $j$  refers to the different heat generation rate contributions.

## 9.2 Results and discussion

This section presents simulation results for charging the hybrid pseudocapacitor by  $\text{Li}^+$  deintercalation and cycling over a fixed potential window  $0 \text{ V} \leq \psi_s \leq 0.45 \text{ V}$  under several current densities  $j_s$ . Predictions for the heat generation rates and temperature are qualitatively compared with experimental measurements reported in the literature [78, 79]. To better interpret the results, it is informative to consider the electrochemical transport in the device.

### 9.2.1 Electrochemical transport

Figure 9.1 shows the cell potential  $\psi_s(t) = \psi(-L - L_P, t) - \psi(L + L_C, t)$  as a function of time  $t - n_c t_c$  under oscillatory steady state for (a) small values of  $j_s$  and (b) large values of  $j_s$ . Here, the cycle period corresponded to the time required for  $\psi_s$  to vary from  $\psi_{min}$  to  $\psi_{max}$  and back to  $\psi_{min}$ . Figure 9.1(a) shows that the evolution of  $\psi_s(t)$  for small current densities  $j_s$  features a characteristic “kink” after the charging/discharging transitions.

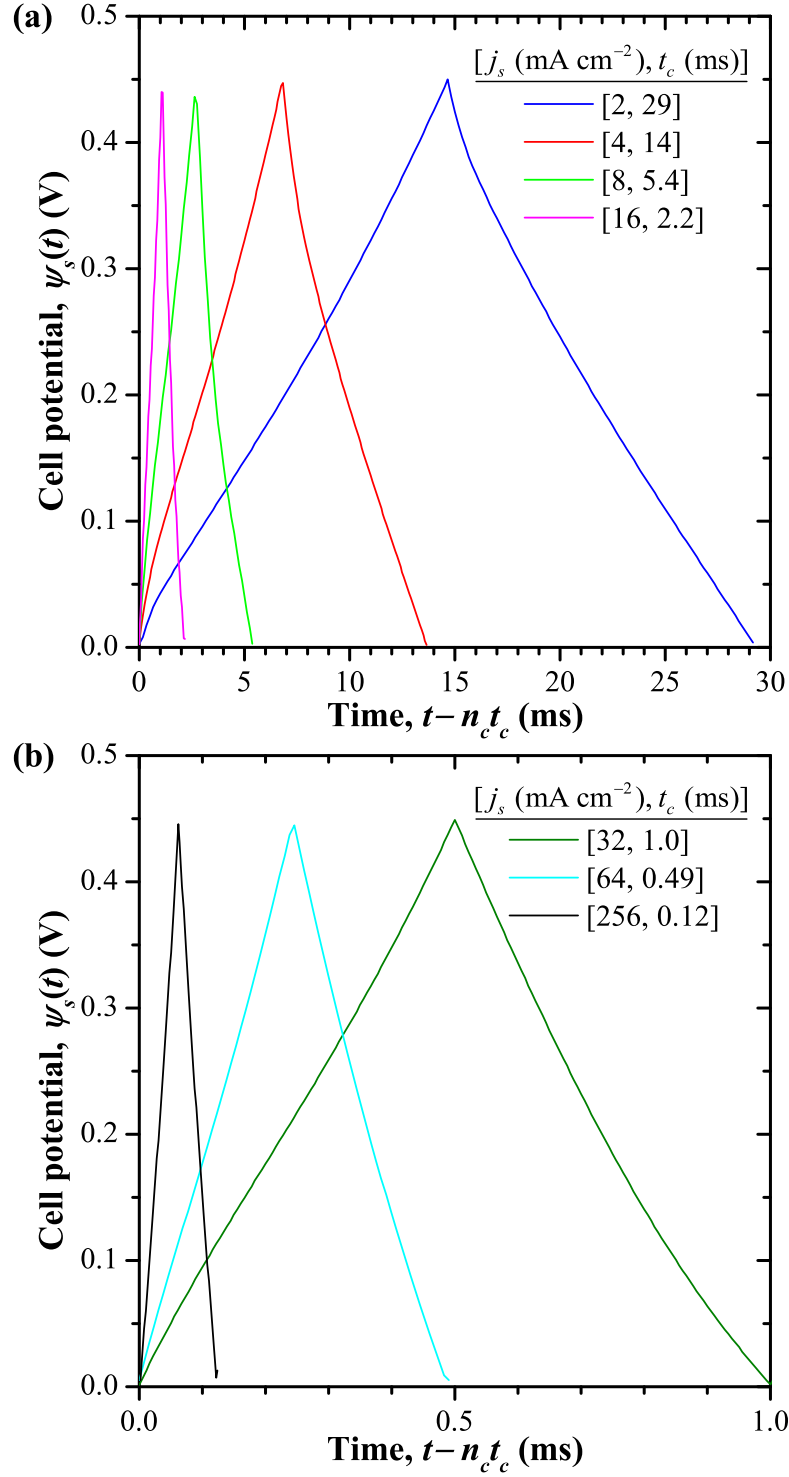


Figure 9.1: Predicted cell potential  $\psi_s(t)$  as a function of time  $t - n_c t_c$  for different current densities  $j_s$  at oscillatory steady state between  $\psi_{min} = 0$  V and  $\psi_{max} = 0.45$  V.

Similar kinks have also been observed experimentally for hybrid pseudocapacitors under galvanostatic cycling [107, 116–118]. They were reproduced numerically in Chapter 8 and were associated with a transition between capacitive-dominated and faradaic-dominated current. The relatively large slope  $|\mathrm{d}\psi_s/\mathrm{d}t|$  immediately following the switch in the current direction can be attributed to a brief period of dominant capacitive current. Then,  $|\mathrm{d}\psi_s/\mathrm{d}t|$  abruptly decreased as the faradaic current became dominant, resulting in the kink. At large values of  $j_s$ , this faradaic kink vanished and the evolution of  $\psi_s(t)$  became approximately symmetric around the peak  $\psi_s = \psi_{max}$ . Note that the faradaic kink is distinct from the instantaneous “IR” drops arising from the electrical resistance of the cell. Indeed, the IR drops for the simulated cell were negligibly small, since the overall cell thickness was small, resulting in small electrical resistance  $RA = 9.7 \text{ m}\Omega\cdot\text{cm}^2$ . However, the present model can also reproduce the IR drops (see Appendix B).

Figure 9.2 shows the (a) faradaic  $j_F(t)/j_s$  and (b) capacitive  $j_C(t)/j_s$  fractions of the imposed current density as functions of dimensionless time  $t/t_c$  at oscillatory steady state. The cycle period  $t_c$  was retrieved from Figure 9.1. For small current densities  $j_s$ , the cell operated in the faradaic regime, i.e., the faradaic current dominated so that  $j_F(t) \approx \pm j_s$  [Figure 9.2(a)] while the capacitive current was small except for brief peaks following the charging/discharging transitions [Figure 9.2(b)]. For large current densities  $j_s$ , the cell operated in the capacitive regime, i.e.,  $j_C(t) \approx \pm j_s$  [Figure 9.2(b)] while the faradaic current was small [Figure 9.2(a)]. These regimes are the same as those previously defined and analyzed in Chapter 8 for a hybrid pseudocapacitor charged by  $\text{Li}^+$  intercalation under constant charge instead of constant potential window.

Figure 9.3 shows the intercalated  $\text{Li}^+$  concentration  $c_{1,P}(-L, t)$  in the pseudocapacitive electrode as a function of dimensionless time  $t/t_c$ . In all cases,  $c_{1,P}$  was uniform throughout the pseudocapacitive electrode due to its small thickness  $L_P = 5 \text{ nm}$ . Figure 9.3 indicates that, in the faradaic regime,  $c_{1,P}$  decreased almost linearly throughout the charging step as  $\text{Li}^+$  deintercalated and increased throughout the discharging step as  $\text{Li}^+$  intercalated. In fact, for  $j_s = 2 \text{ mA cm}^{-2}$ , the evolution of  $c_{1,P}$  showed excellent agreement with the faradaic limit  $c_{1,P,F}$  predicted by Equation (8.26). In the capacitive regime,  $c_{1,P}$  was approximately

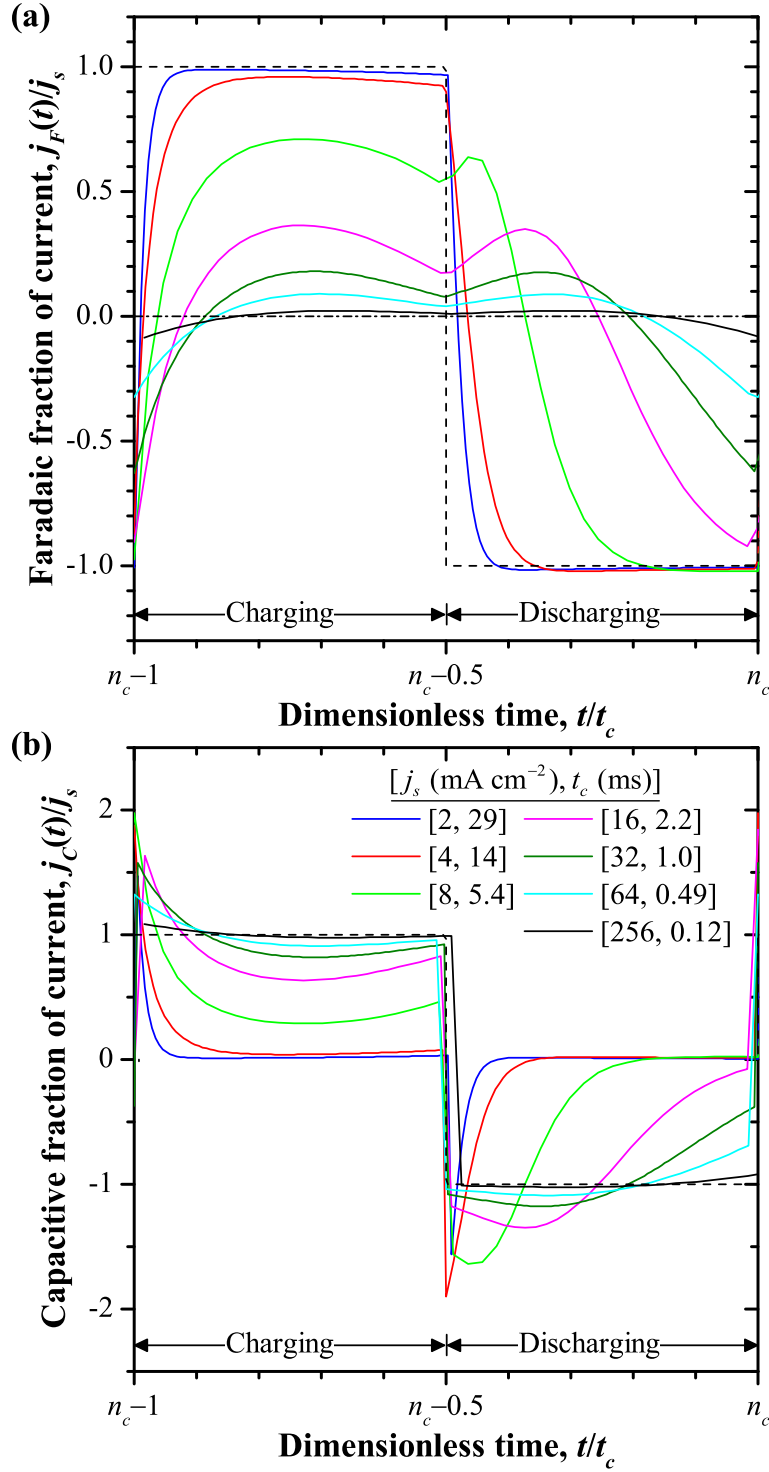


Figure 9.2: Predicted (a) faradaic  $j_F(t)/j_s$  and (b) capacitive  $j_C(t)/j_s$  fractions of the imposed current density as functions of dimensionless time  $t/t_c$ . All cases are plotted over one cycle under oscillatory steady state for different values of  $j_s$  and the same potential window  $0 \text{ V} \leq \psi_s \leq 0.45 \text{ V}$ .



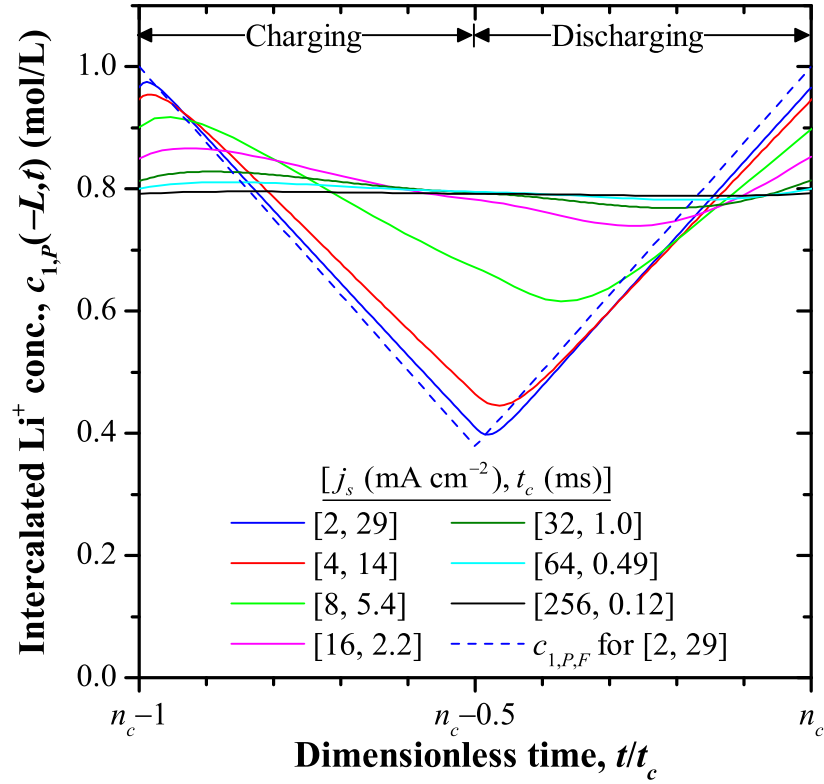


Figure 9.3: Predicted intercalated  $\text{Li}^+$  concentration  $c_{1,P}(-L, t)$  in the pseudocapacitive electrode as a function of dimensionless time  $t/t_c$  for various current densities  $j_s$  at oscillatory steady state as well as the analytical prediction  $c_{1,P,F}$  [Equation (8.26)] for  $j_s = 2$  mA cm $^{-2}$  and  $t_c = 29$  ms in the faradaic regime.

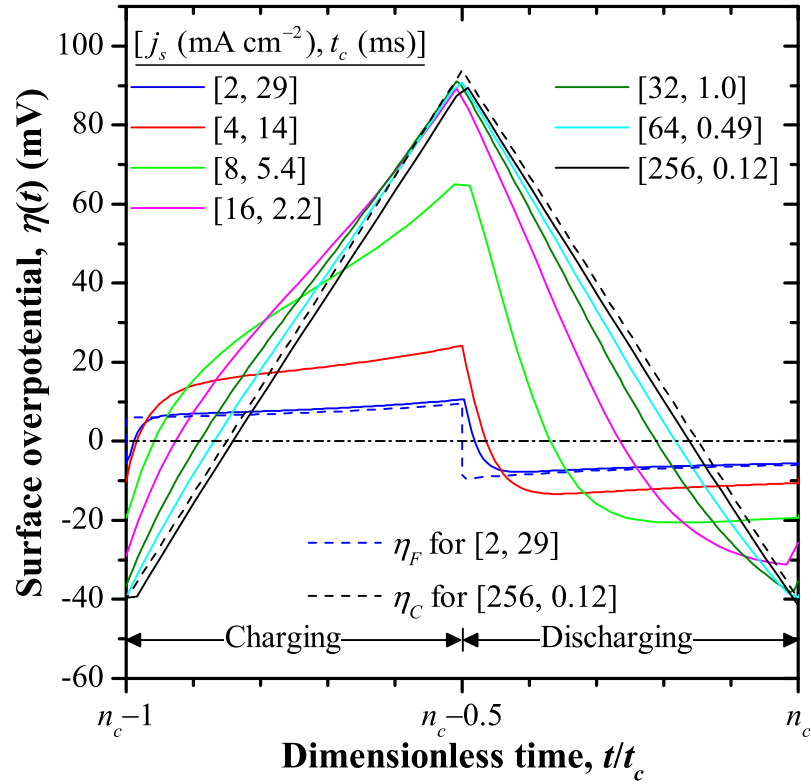


Figure 9.4: Predicted surface overpotential  $\eta(t)$  as a function of dimensionless time  $t/t_c$  for different  $j_s$  as well as the analytical predictions of  $\eta_F$  [Equation (8.27)] for  $j_s = 2 \text{ mA cm}^{-2}$  in the faradaic regime and  $\eta_C$  [Equation (8.28)] for  $j_s = 256 \text{ mA cm}^{-2}$  in the capacitive regime.

constant due to the small faradaic current  $j_F$  and equal to  $c_{1,P,C} = 0.8 \text{ mol L}^{-1}$ . Note that no  $\text{Li}^+$  starvation occurred inside the electrode for any of the cases considered with  $\Delta\psi_s = 0.45 \text{ V}$ .

Figure 9.4 shows the surface overpotential  $\eta(t)$  as a function of dimensionless time  $t/t_c$ . As previously observed in Chapter 8, the magnitude  $|\eta(t)|$  was almost constant in the faradaic regime, except for brief transition periods immediately following the charging/discharging transitions. The evolution of  $\eta(t)$  in the limits of small and large current density  $j_s$  agreed well with analytical predictions  $\eta_F(t)$  in the faradaic regime [Equation (8.27)] and  $\eta_C(t)$  in the capacitive regime [Equation (8.28)].

Figure 9.5 shows the predicted (a)  $\text{Li}^+$  concentration  $c_{1,E}(-L + H, t)$  and (b)  $\text{ClO}_4^-$

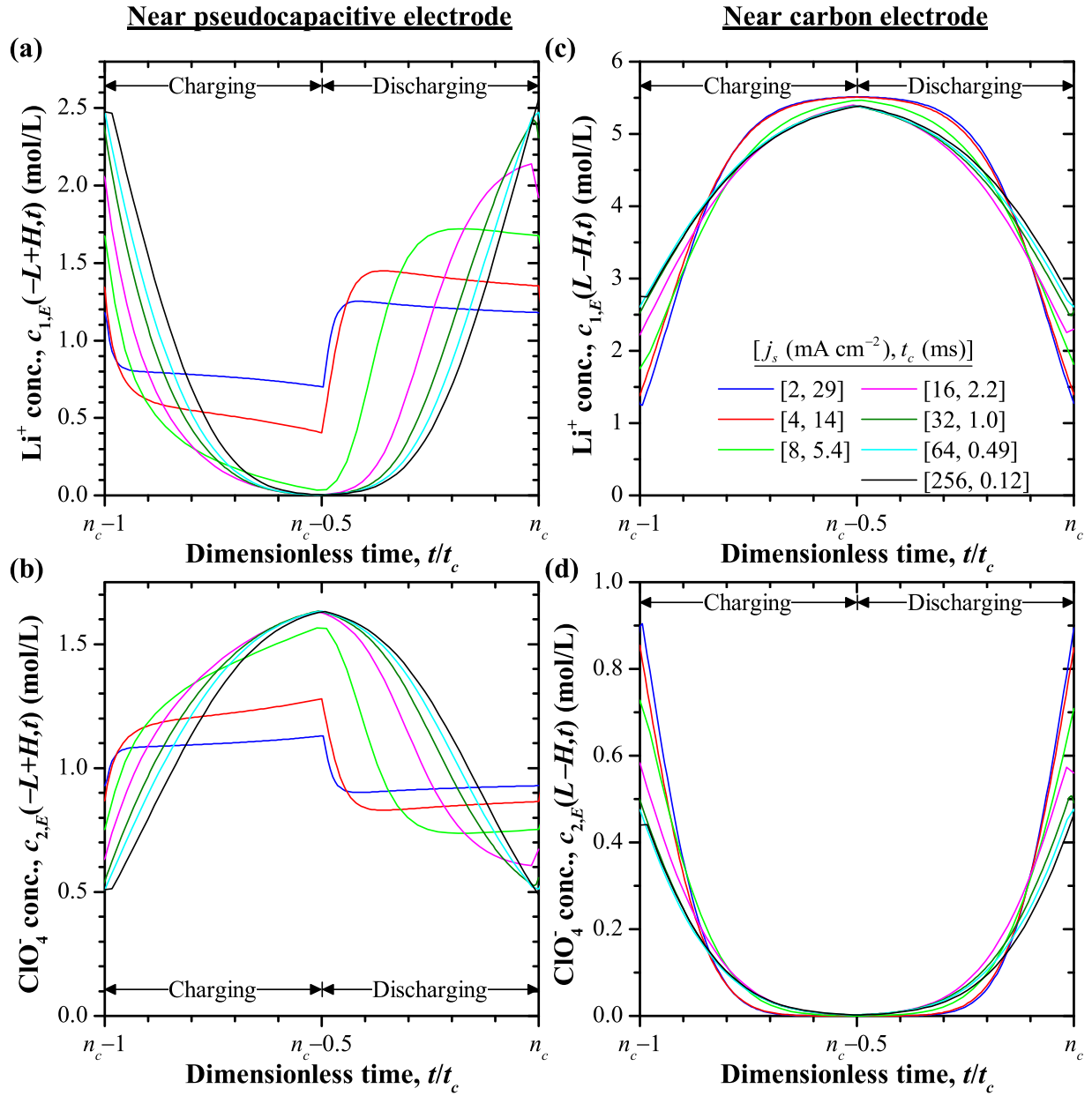


Figure 9.5: Predicted concentrations (a)  $c_{1,E}(-L+H,t)$  of  $\text{Li}^+$  and (b)  $c_{2,E}(-L+H,t)$  of  $\text{ClO}_4^-$  in the electrolyte near the pseudocapacitive electrode as well as (c)  $c_{1,E}(L-H,t)$  of  $\text{Li}^+$  and (d)  $c_{2,E}(L-H,t)$  of  $\text{ClO}_4^-$  near the carbon electrode.

concentration  $c_{2,E}(-L + H, t)$  at the Stern/diffuse layer interface near the pseudocapacitive electrode. In the faradaic regime, Figure 9.5 indicates that a  $\text{ClO}_4^-$  EDL existed at the pseudocapacitive electrode during the charging step and was replaced by a  $\text{Li}^+$  EDL during the discharging step. For large values of  $j_s$ , a  $\text{Li}^+$  EDL formed at the beginning and end of the cycle while a  $\text{ClO}_4^-$  EDL formed in the middle of the cycle. The concentrations  $c_{1,E}(-L + H, t)$  and  $c_{2,E}(-L + H, t)$  were strongly correlated with the Stern layer electric field  $E(-L + H, t) = \Delta\psi_H(t)/H = \eta(t)/H$ , with  $\eta(t)$  reported in Figure 9.4. In the middle of the cycle, when the surface overpotential  $\eta(t)$  and thus  $E(-L + H, t)$  were positive and large (Figure 9.4), the  $\text{Li}^+$  ions were repelled and their concentration  $c_{1,E}(-L + H, t)$  was small, approaching zero for  $j_s \geq 8 \text{ mA cm}^{-2}$ . This  $\text{Li}^+$  starvation decreased the faradaic current density  $j_F(t)$ , explaining the dip in  $j_F$  around the charging/discharging transition at  $t/t_c = n_c - 0.5$  [Figure 9.2(a)]. The positive peak in  $j_F$  during the discharging step resulted from  $c_{1,E}(-L + H, t)$  increasing as the  $\text{ClO}_4^-$  EDL dissipated while  $\eta(t)$  was still positive.

Figure 9.5 also shows the concentrations (c)  $c_{1,E}(L - H, t)$  of  $\text{Li}^+$  and (d)  $c_{2,E}(L - H, t)$  of  $\text{ClO}_4^-$  near the carbon electrode. A  $\text{Li}^+$  EDL existed near the carbon electrode for the entire cycle without ever completely dissipating. This can be attributed to the fact that  $\text{Li}^+$  originally from the pseudocapacitive electrode remained in the electrolyte, i.e.,  $c_{1,P}$  was smaller than its initial value  $c_{1,P,0}$  [Figure 9.3]. As a result, the electrolyte retained a net positive charge even when the cell potential  $\psi_s$  was zero, while the electrodes retained a corresponding negative charge.

## 9.2.2 Heat generation rates

In all cases, the Joule heat generation rate  $\dot{q}_{J,irr}$  in the diffuse layer of the electrolyte was found to be constant and uniform for galvanostatic cycling, except very close to the Stern/diffuse layer interfaces where it decreased sharply to zero, as observed in previous simulations of EDLCs [2, 5]. It was also constant and uniform within each electrode. The total Joule heat generation rate  $\dot{Q}_{J,irr}''$  ranged from  $3.9 \times 10^{-5}$  to  $0.64 \text{ mW cm}^{-2}$  as  $j_s$  ranged from 2 to  $256 \text{ mA cm}^{-2}$ .

### 9.2.2.1 Heat generation rates in the pseudocapacitive electrode half-cell

Figure 9.6 shows the total (a) irreversible faradaic  $\dot{Q}_{F,irr,P}''(t)$  and (b) reversible faradaic  $\dot{Q}_{F,rev,P}''(t)$  heat generation rates as well as the reversible EDL heat generation rate  $\dot{Q}_{EDL,rev,P}''(t)$  of the pseudocapacitive electrode half-cell for (c) small and (d) large values of  $j_s$  as functions of dimensionless time  $t/t_c$ . First, Figure 9.6(a) shows that the *irreversible* faradaic heat generation rate  $\dot{Q}_{F,irr,P}''$  was always positive. In the faradaic regime ( $j_s \leq 4 \text{ mA cm}^{-2}$ ),  $\dot{Q}_{F,irr,P}''$  was proportional to the surface overpotential  $|\eta_F(t)|$  given by Equation (8.27) such that  $\dot{Q}_{F,irr,P}'' \approx j_s |\eta_F(t)|$  (see inset). The heat generation rate  $\dot{Q}_{F,irr,P}''$  reached a maximum half-way through the cycle corresponding to the smallest  $\text{Li}^+$  concentrations  $c_{1,P}(-L, t)$  in the pseudocapacitive electrode and to the largest values of  $|\eta_F(t)|$  (Figure 9.3). As  $j_s$  increased, the maximum  $\dot{Q}_{F,irr,P}''$  increased. In addition, several distinct peaks in  $\dot{Q}_{F,irr,P}''$  were evident for large current densities  $j_s$  in the capacitive regime. These peaks corresponded to those observed in the faradaic current density magnitude  $|j_F(t)|$  [Figure 9.2(a)].

Figure 9.6(b) shows that the reversible faradaic heat generation rate  $\dot{Q}_{F,rev,P}''(t)$  was significantly larger in magnitude than its irreversible counterpart  $\dot{Q}_{F,irr,P}''(t)$  [Figure 9.6(a)] for all  $j_s$  considered. It was also larger than the reversible EDL heat generation rate  $\dot{Q}_{EDL,rev,P}''(t)$  [Figure 9.6(c)] for small  $j_s$ . This can be attributed to the fact that the surface overpotential  $\eta(t)$  (Figure 9.4) was smaller in magnitude ( $|\eta(t)| \lesssim 0.1 \text{ V}$ ) than the Peltier coefficient  $|\Pi| = 0.363 \text{ V}$  for all  $j_s$  considered and that the EDL contribution was small in the faradaic regime. Indeed,  $\dot{Q}_{F,rev,P}''(t)$  dominated  $\dot{Q}_P''(t)$  [Equation (9.28)] for  $j_s \leq 8 \text{ mA cm}^{-2}$ . In all cases,  $\dot{Q}_{F,rev,P}''(t)$  was directly proportional to  $j_F(t)$  due to the constant value of  $\Pi$  [Equations (9.15) and (9.26)]. Because  $\Pi$  was negative, the sign of  $\dot{Q}_{F,rev,P}''$  was opposite to that of  $j_F$ . In other words, it was endothermic (i.e., negative) during charging by  $\text{Li}^+$  deintercalation and exothermic (i.e., positive) during discharging by  $\text{Li}^+$  intercalation. Thus, the mid-cycle dip in  $|\dot{Q}_{F,rev,P}''|$  and subsequent endothermic peak during discharging for  $j_s \geq 8 \text{ mA cm}^{-2}$  can be attributed to  $\text{Li}^+$  starvation limiting the faradaic current density  $j_F$ . Moreover, the time-averaged reversible faradaic heat generation  $\overline{\dot{Q}_{F,rev,P}''}$  over a cycle was zero at oscilla-

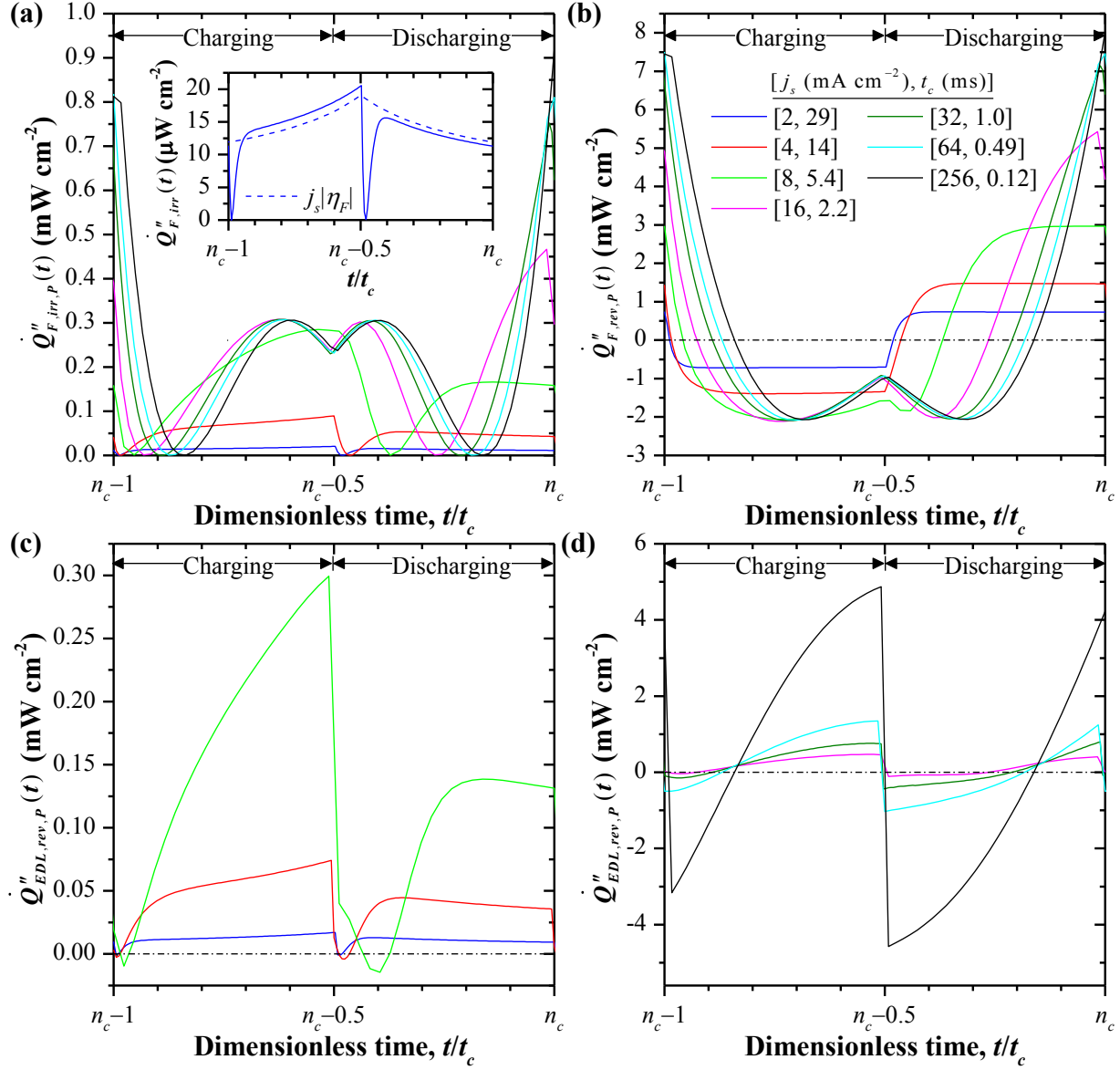


Figure 9.6: Predicted overall (a) irreversible faradaic  $\dot{Q}_{F,irr,P}''(t)$ , (b) reversible faradaic  $\dot{Q}_{F,rev,P}''(t)$ , and reversible EDL  $\dot{Q}_{EDL,rev,P}''(t)$  heat generation rates for (c) small and (d) large current densities  $j_s$  as functions of dimensionless time  $t/t_c$ . All cases are plotted over one cycle under oscillatory steady state for different values of  $j_s$  and the same potential window  $0 \text{ V} \leq \psi_s \leq 0.45 \text{ V}$ .

tory steady state, since  $\dot{Q}_{F,rev,P}''(t)$  was proportional to  $j_F(t)$  and no net  $\text{Li}^+$  intercalation occurred, i.e.,  $\int_{(n_c-1)t_c}^{t_c} j_F(t)dt = 0$ .

Figures 9.6(c) and (d) show that the magnitude of the EDL heating  $\dot{Q}_{EDL,rev,P}''(t)$  increased with increasing  $j_s$ . However, the temporal evolution of  $\dot{Q}_{EDL,rev,P}''$  near the pseudocapacitive electrode was distinctly different from that of  $\dot{Q}_{EDL,rev,C}''$  near the carbon electrode or in previous simulations of EDLCs (Chapters 4 and 7). For small current densities  $j_s$  [Figure 9.6(c)],  $\dot{Q}_{EDL,rev,P}''(t)$  was exothermic during both the charging and the discharging steps. It also featured both exothermic and endothermic periods during each step for larger values of  $j_s$  [Figure 9.6(d)]. Over a full cycle, the time average  $\overline{\dot{Q}_{EDL,rev,P}}''$  was positive for all  $j_s$  considered and will be discussed in more detail in Section 9.2.2.3. By contrast, the EDL reversible heating in EDLCs or in the carbon electrode half-cell was exothermic throughout the entire charging step, endothermic throughout the entire discharging step, and its time average  $\overline{\dot{Q}_{EDL,rev,C}}''$  over a full cycle was zero. Indeed, near the carbon electrode at oscillatory steady state, the temporal evolution of the ion concentrations was symmetric around the charging/discharging transition [Figures 9.5(c) and 9.5(d)], while the direction of the current density changed sign. As a result, the reversible heat generation rates  $\dot{q}_{E,d}$ ,  $\dot{q}_{E,s}$ ,  $\dot{q}_{S,c}$  [Equations (7.4) and (7.7)] in the carbon electrode half-cell were symmetric in magnitude but opposite in sign during charging and discharging. However, faradaic reactions at the pseudocapacitive electrode resulted in an asymmetric evolution of the ion concentrations [Figures 9.5(a) and 9.5(b)]. As a result,  $\dot{Q}_{EDL,rev,P}''(t)$  did not average to zero over the full cycle period. In other words, although the EDL heat generation rates are *reversible*, they behave reversibly only for symmetric EDL formation between charging and discharging such as that in EDLCs.

### 9.2.2.2 Overall half-cell heat generation rates

Figure 9.7 shows the numerically predicted overall heat generation rate (a)  $\dot{Q}_P''(t)$  [Equation (9.28)] of the pseudocapacitive electrode half-cell and (b)  $\dot{Q}_C''(t)$  [Equation (9.29)] of the carbon electrode half-cell as functions of dimensionless time  $t/t_c$  over one cycle under

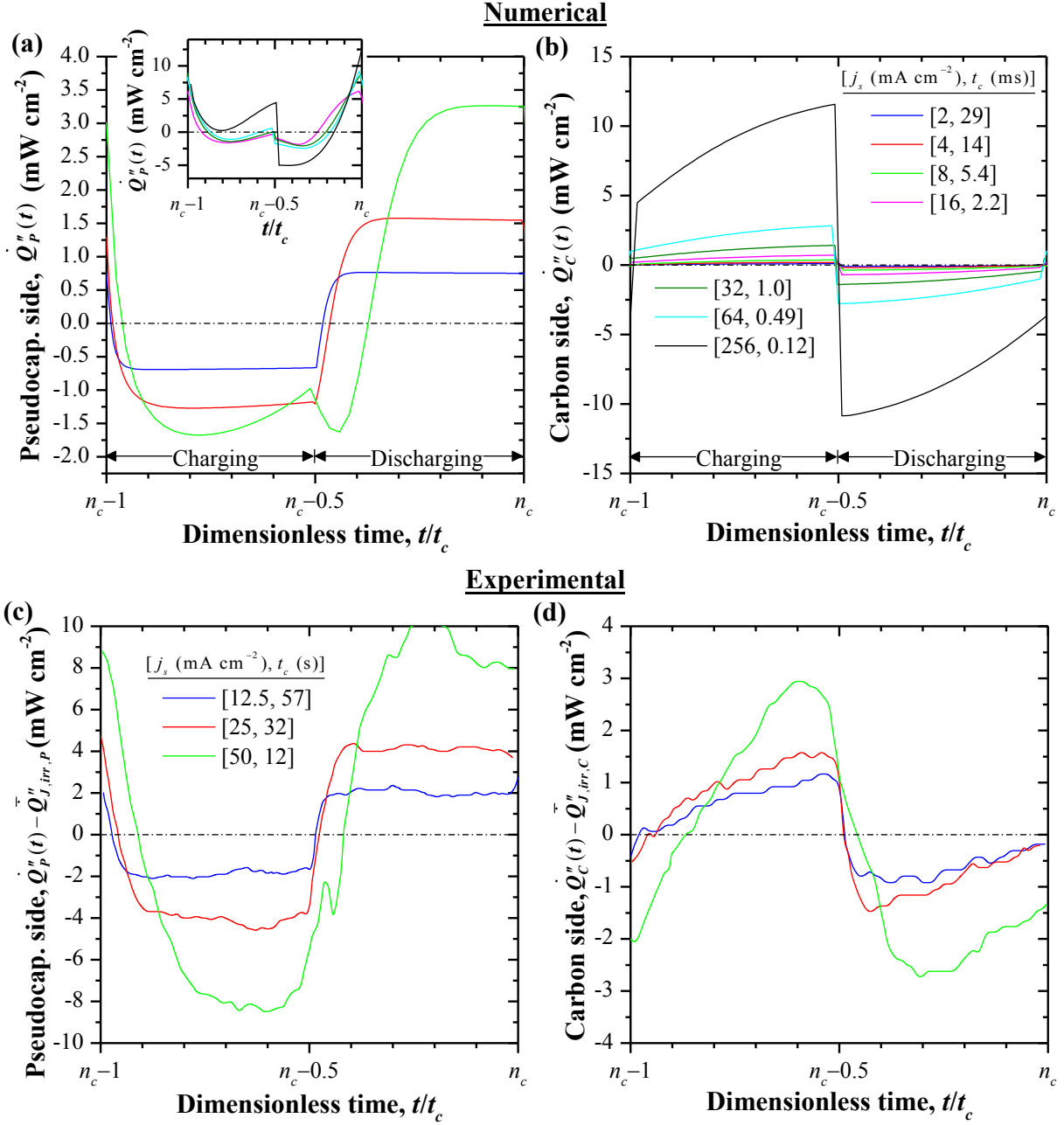


Figure 9.7: Numerically predicted total heat generation rates (a)  $\dot{Q}_P''(t)$  of the pseudocapacitive electrode half-cell and (b)  $\dot{Q}_C''(t)$  of the carbon electrode half-cell for  $0 \text{ V} \leq \psi_s \leq 0.45 \text{ V}$  as well as experimentally measured total heat generation rates minus Joule heating (c)  $\dot{Q}_P''(t) - \dot{Q}_{J,irr,P}''$  of the pseudocapacitive electrode half-cell and (d)  $\dot{Q}_C''(t) - \dot{Q}_{J,irr,C}''$  of the carbon electrode half-cell for a hybrid pseudocapacitor cycled over the potential window  $0 \text{ V} \leq \psi_s \leq 1.0 \text{ V}$  [78] as functions of dimensionless time  $t/t_c$  for different values of  $j_s$ .



oscillatory steady state for different values of  $j_s$  and for  $0 \text{ V} \leq \psi_s \leq 0.45 \text{ V}$ . Figure 9.7(a) establishes that  $\dot{Q}_P''(t)$  was endothermic during charging and exothermic during discharging for small current densities  $j_s$ , as the contribution  $\dot{Q}_{F,rev,P}''(t)$  dominated (Figure 9.6). For larger values of  $j_s$ ,  $\dot{Q}_P''(t)$  featured both endothermic and exothermic periods during the charging and discharging steps. In particular, for  $j_s \geq 8 \text{ mA cm}^{-2}$ ,  $\dot{Q}_P''(t)$  featured the endothermic peak during discharging previously noted in  $\dot{Q}_{F,rev,P}''$  and associated with  $\text{Li}^+$  starvation in the electrolyte. Figure 9.7(b) indicates that  $\dot{Q}_C''(t)$  was exothermic during charging and endothermic during discharging for all values of  $j_s$  considered. This was consistent with the fact that the EDL always consisted of  $\text{Li}^+$  [Figure 9.5(b)] and agreed with my previous simulations of EDLCs (Chapters 4 and 7).

Figure 9.7 also reproduces experimentally measured total heat generation rates minus constant Joule heating (c)  $\dot{Q}_P''(t) - \bar{Q}_{J,irr,P}''$  for the porous  $\text{MnO}_2$  pseudocapacitive electrode half-cell and (d)  $\dot{Q}_C''(t) - \bar{Q}_{J,irr,C}''$  for the carbon electrode half-cell as functions of dimensionless time  $t/t_c$  for galvanostatic cycling over fixed potential window  $0 \text{ V} \leq \psi_s \leq 1.0 \text{ V}$  (Figure 12 of Ref. [78]). Here, the authors subtracted the constant Joule heat generation rate estimated from the IR drops at charging/discharging transitions [78, 79]. The remainder was presented as the “reversible heat” associated with each electrode half-cell [78]. However, these values comprise all time-dependent contributions to the heat generation rate including irreversible faradaic heat generation rate. For this reason, the experimental data are compared to the numerically predicted overall heat generation rates  $\dot{Q}_P''(t)$  and  $\dot{Q}_C''(t)$  rather than to the reversible contributions only. It is interesting to note that the experimental measurements for  $j_s = 12.5, 25$ , and  $50 \text{ mA cm}^{-2}$  qualitatively resembled the numerically predicted evolutions of  $\dot{Q}_P''(t)$  and  $\dot{Q}_C''(t)$  for  $j_s = 2, 4$ , and  $8 \text{ mA cm}^{-2}$  in both shape and in relative magnitudes for the different currents. For  $j_s = 50 \text{ mA cm}^{-2}$ , experimentally  $\dot{Q}_P''(t) - \bar{Q}_{J,irr,P}''$  [Figure 9.7(c)] featured an endothermic peak at the beginning of the discharging step very similar to that observed numerically in Figure 9.7(a) for  $j_s = 8 \text{ mA cm}^{-2}$  and caused by  $\text{Li}^+$  starvation at the Stern/diffuse layer interface, as previously discussed.

### 9.2.2.3 Time-averaged heat generation rates

Figure 9.8(a) shows the numerically predicted time-averaged heat generation rates over a full cycle at oscillatory steady state due to (i) Joule heating  $\bar{Q}_{J,irr}''$ , (ii) irreversible faradaic heating  $\bar{Q}_{F,irr,P}''$ , and (iii) EDL reversible heating near the pseudocapacitive electrode  $\bar{Q}_{EDL,rev,P}''$  as well as (iv) the overall time-averaged heat generation rate for the entire cell  $\bar{Q}''$  as functions of current density  $j_s$  for  $\psi_{max} = 0.45$  V and for  $\psi_{max} = 1.0$  V. First, as previously mentioned,  $\bar{Q}_{F,rev,P}''$  and  $\bar{Q}_{EDL,rev,C}''$  were zero and were not plotted. Thus, the overall  $\bar{Q}''$  can be expressed as  $\bar{Q}'' = \bar{Q}_{J,irr}'' + \bar{Q}_{F,irr,P}'' + \bar{Q}_{EDL,rev,P}''$ . In addition, Figure 9.8(a) indicates that the Joule heat generation rate  $\bar{Q}_{J,irr}''$  was proportional to  $j_s^2$  for all  $j_s$ , as indicated by Equation (9.25). It also establishes that, *in the faradaic regime*, the irreversible faradaic heat generation rate  $\bar{Q}_{F,irr,P}''$  was proportional to  $j_s^2$  for small values of  $j_s$ . This was consistent with the fact that, in this regime,  $|j_F| \approx j_s$  and the magnitude of the surface overpotential  $\eta_F$  was approximately proportional to  $j_s$ , as indicated by the first-order Taylor series approximation of Equation (8.27). Here,  $\bar{Q}_{F,irr,P}''$  was also several orders of magnitude larger than the Joule heat generation rate  $\bar{Q}_{J,irr}''$  for small values of  $j_s$  due to the small electrical resistance of the simulated cell. At larger current densities  $j_s$ , *in the capacitive regime*,  $\bar{Q}_{F,irr,P}''$  reached a plateau and became independent of  $j_s$  because both  $j_F$  and  $\eta$  were found to be independent of  $j_s$ . As a result,  $\bar{Q}_{J,irr}''$  eventually exceeded  $\bar{Q}_{F,irr,P}''$  for large enough values of  $j_s$ . Moreover, the average EDL heat generation rate  $\bar{Q}_{EDL,rev,P}''$  near the pseudocapacitive electrode was smaller but followed the same trend as  $\bar{Q}_{F,irr,P}''$  for all  $j_s$ . It provided a significant contribution to the net heat generated over a cycle, despite being a “reversible” heat generation rate. Finally, the overall average heat generation rate  $\bar{Q}''$  was (i) proportional to  $j_s^2$  and dominated by the irreversible faradaic  $\bar{Q}_{F,irr,P}''$  and the reversible EDL  $\bar{Q}_{EDL,rev,P}''$  heat generation rates *in the faradaic regime*, (ii) proportional to  $j_s^2$  and dominated by the Joule heat generation rate  $\bar{Q}_{J,irr}''$  *in the capacitive regime*, and (iii) featured a transition zone between these two regimes when it was independent of  $j_s$ . For the broader potential window  $\Delta\psi_s = 1.0$  V and a given current  $j_s$ , the Joule heating  $\bar{Q}_{J,irr}''$  remained identical to that for  $\Delta\psi_s = 0.45$  V. However, the irreversible faradaic  $\bar{Q}_{F,irr,P}''$  and reversible EDL  $\bar{Q}_{EDL,rev,P}''$  heat generation rates increased with increasing potential window. Indeed, for  $\Delta\psi_s = 1.0$  V, the intercalated

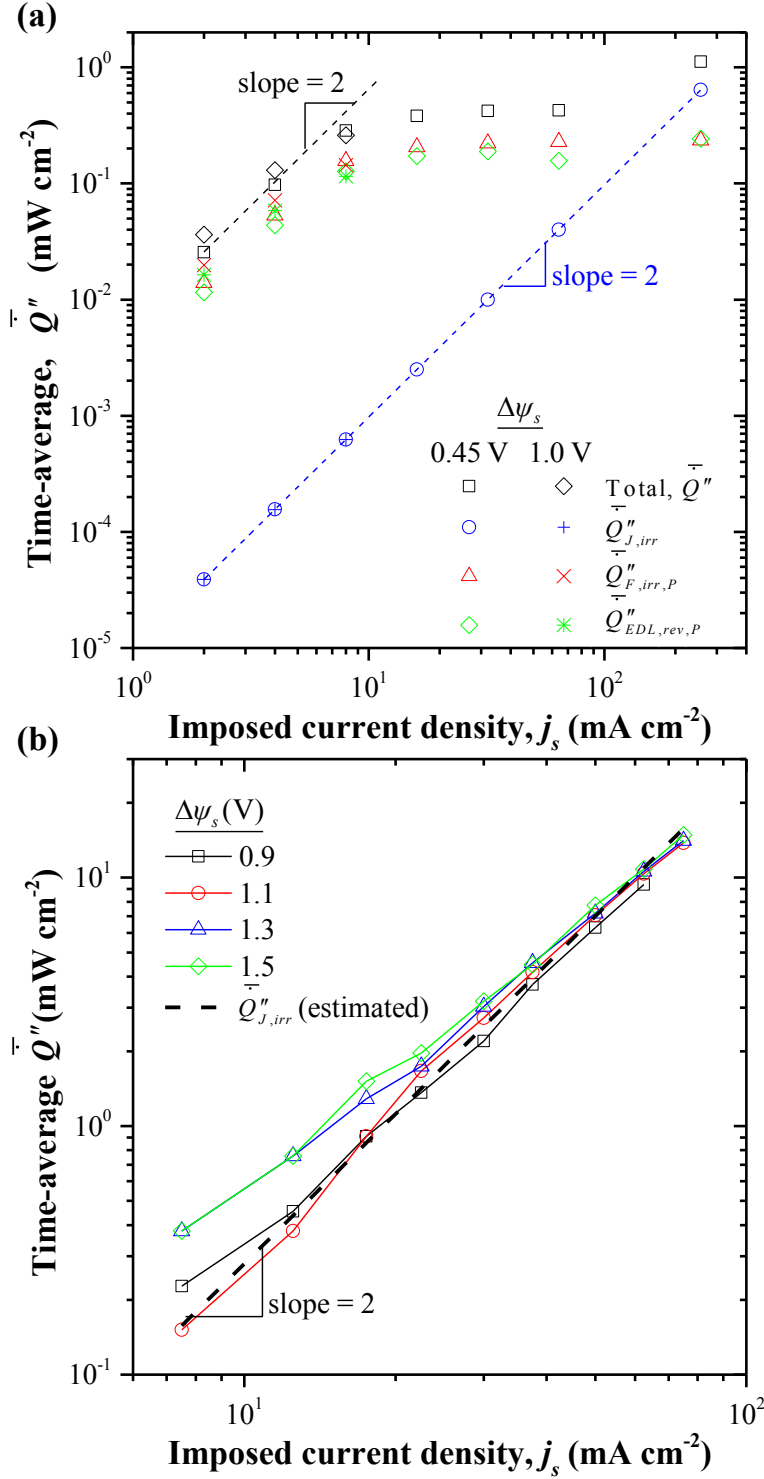


Figure 9.8: Time-averaged (a) numerically predicted Joule  $\bar{Q}''_{J,irr}$ , irreversible faradaic  $\bar{Q}''_{F,irr,P}$ , reversible EDL  $\bar{Q}''_{EDL,rev,P}$ , and overall  $\bar{Q}'' = \bar{Q}''_{J,irr} + \bar{Q}''_{F,irr,P} + \bar{Q}''_{EDL,rev,P}$  heat generation rates as well as (b) experimental overall  $\bar{Q}''$  [79] and estimated Joule  $\bar{Q}''_{J,irr}$  heating as functions of current density  $j_s$ .

$\text{Li}^+$  concentration  $c_{1,P}$  reached smaller values than for  $\Delta\psi_s = 0.45$  V, resulting in  $\text{Li}^+$  starvation in the electrode for  $j_s = 2$  mA cm<sup>-2</sup> as well as longer periods of  $\text{Li}^+$  starvation in the electrolyte. This resulted in larger values of  $\eta(t)$  and larger EDLs near the pseudocapacitive electrode, thus increasing  $\bar{Q}_{F,irr,P}''$  and  $\bar{Q}_{EDL,rev,P}''$ . As a result, the total heat generation rate  $\bar{Q}''$  increased with increasing  $\Delta\psi_s$  for small values of  $j_s$ .

Figure 9.8(b) reproduces experimentally measured time-averaged overall heat generation rates  $\bar{Q}''$  reported by Dandeville [79] as a function of  $j_s$  for several potential windows with  $\psi_{min} = 0$  V and  $\psi_{max}$  ranging from 0.9 and 1.5 V (Figure III.15 in Ref. [79]). The dashed line corresponds to the estimated time-averaged Joule heating  $\bar{Q}_{J,irr}''$  for the entire device. Here, I estimated the electrical resistance as  $2.8 \Omega \text{ cm}^2$  based on the IR drop in  $\psi_s(t)$  reported for  $\Delta\psi_s = 1.0$  V and  $j_s = 25$  mA cm<sup>-2</sup> [78]. For large values of  $j_s$ ,  $\bar{Q}''$  for all potential windows  $0.9 \text{ V} \leq \Delta\psi_s \leq 1.5 \text{ V}$  fell approximately along the same line corresponding to the estimated Joule heat generation rate. For small values of  $j_s$ ,  $\bar{Q}''$  exceeded the estimated  $\bar{Q}_{J,irr}''$ , particularly for the broader potential windows  $\Delta\psi_s = 1.3$  V and 1.5 V. This behavior is qualitatively similar to that predicted numerically [Figure 9.8(a)] and attributed to  $\bar{Q}_{F,irr,P}''$  and  $\bar{Q}_{EDL,rev,P}''$  increasing with increasing  $\Delta\psi_s$  due to  $\text{Li}^+$  starvation in the pseudocapacitive electrode and the electrolyte. The transition between the faradaic and capacitive regime behaviors was not as distinct for the experimental cell, particularly for small  $\Delta\psi_s$ . This can be attributed to the relatively large electrical resistance and thus large value of  $\bar{Q}_{J,irr}''$  in the experimental cell.

### 9.2.3 Temperature

Figure 9.9 shows the predicted temperature  $T(0, t)$  at the cell centerline as a function of time  $t$  for  $0 \text{ V} \leq \psi_s \leq 0.45 \text{ V}$  and (a) small and (b) large current densities  $j_s$ . For all current densities  $j_s$ , temperature oscillations around an overall temperature rise  $T_{irr}(t)$  from cycle to cycle due to irreversible heating were evident. The slope of this irreversible temperature rise was proportional to the overall time-averaged heat generation rate  $\bar{Q}''$  over a cycle and

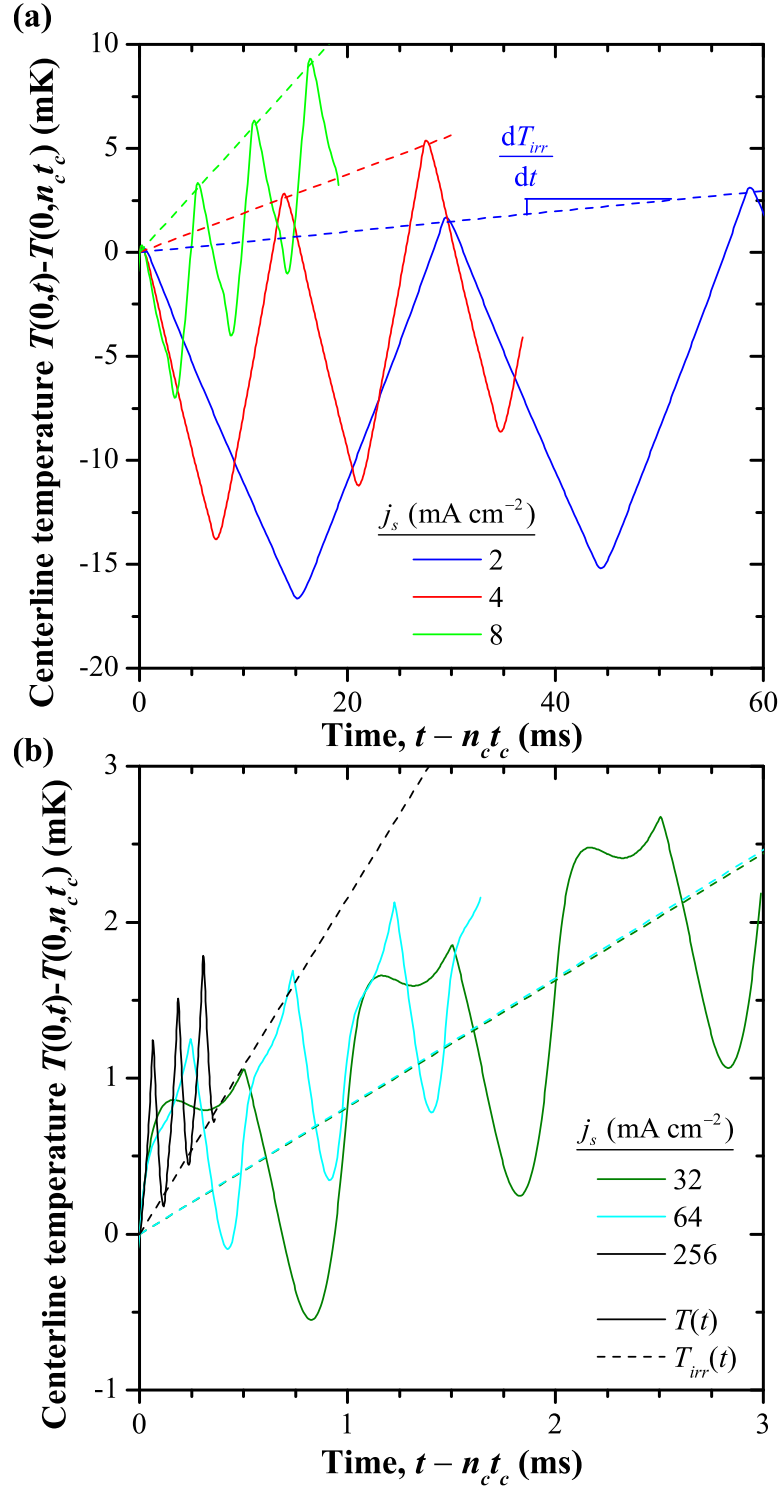


Figure 9.9: Predicted centerline temperature  $T(0, t) - T(0, t_c)$  as a function of time  $t$  over the potential window  $0 \text{ V} \leq \psi_s \leq 0.45 \text{ V}$  for (a) small and (b) large current densities  $j_s$ .

given by

$$\frac{dT_{irr}}{dt} = \frac{\overline{\dot{Q}}''}{C_{th}} = \frac{\overline{\dot{Q}}''_{J,irr} + \overline{\dot{Q}}''_{F,irr,P} + \overline{\dot{Q}}''_{EDL,rev,P}}{C_{th}} \quad (9.31)$$

where  $C_{th} = \rho_P c_{p,P} L_P + 2\rho_E c_{p,E} L + \rho_C c_{p,C} L_C$  was the total heat capacity per unit surface area, equal to  $5.18 \text{ J m}^{-2}\text{K}^{-1}$ .

Figure 9.9(a) shows that the overall slope increased significantly with increasing  $j_s$  as these cases were in the faradaic regime when  $\overline{\dot{Q}}''$  was approximately proportional to  $j_s^2$  [Figure 9.8(a)]. The temperature oscillations had a triangular shape and the temperature initially decreased. This can be attributed to the dominance of  $\dot{Q}''_{F,rev,P}$ , which was endothermic for  $\text{Li}^+$  deintercalation, i.e., during the charging step, and approximately constant in magnitude [Figure 9.6(b)]. Similar triangular oscillations were measured experimentally for a hybrid pseudocapacitor charged by deintercalation and reported in Ref. [78].

By contrast, Figure 9.9(b) shows that the slope  $dT_{irr}/dt$  was approximately the same for  $j_s = 32$  and  $64 \text{ mA cm}^{-2}$ . In fact, these cases were in the transition region observed in Figure 9.8(a) when  $\overline{\dot{Q}}''$  was nearly independent of  $j_s$ . In addition, the temperature oscillations featured local maxima and minima within each cycle. This can be attributed to the fact that the total reversible heat generation rates due to the faradaic reaction  $\dot{Q}''_{F,rev,P}$  and due to EDL formation  $\dot{Q}''_{EDL,rev,P}$  and  $\dot{Q}''_{EDL,rev,C}$  were of similar magnitude and all had a significant effect on the temperature evolution. Finally, in the capacitive regime for  $j_s = 256 \text{ mA cm}^{-2}$ , the temperature oscillations were triangular and the temperature initially increased, similar to the EDLC temperatures reported in Ref. [78]. This can be attributed to the fact that  $\dot{Q}''_C$  [Figure 9.7(b)] dominated the heat generation rate.

### 9.3 Conclusion

The present study developed a novel first-principles continuum thermal model for hybrid pseudocapacitors accounting for local irreversible and reversible heat generation rates arising from Joule heating, faradaic reactions, and EDL formation. First, the temporal evolution of the different heat generation rates and of the temperature predicted numerically for a hybrid

pseudocapacitor with planar electrodes charged by deintercalation of  $\text{Li}^+$  under galvanostatic cycling showed excellent qualitative agreement with those measured experimentally [78]. This suggests that the model successfully captured the key physical phenomena governing the thermal behavior in pseudocapacitors. Interestingly, the predicted reversible heat generation rates due to EDL formation produced significant net heating over a cycle near the pseudocapacitive electrode and thus contributed to the overall cycle-to-cycle temperature rise of the device. In addition,  $\text{Li}^+$  starvation in the electrolyte near the pseudocapacitive electrode resulted in a distinctive endothermic peak in the heat generation rate that was also observed in the experimental data. These observations indicate that both EDL formation and faradaic reactions and the resulting heat generation rates must be considered simultaneously in thermal models of pseudocapacitors. Moreover, two asymptotic regimes of operation were observed, depending on the imposed cycling current density. In the faradaic regime, corresponding to small imposed current density and slow charging, irreversible faradaic and reversible EDL heating dominated the time-average heat generation rate. In the capacitive regime, corresponding to large imposed current density and fast charging, Joule heating dominated. The time-averaged heat generation rate  $\overline{\dot{Q}}''$  and the slope of the overall temperature rise were proportional to the square of the imposed current density  $j_s^2$  in both the faradaic and capacitive regimes with different proportionality coefficients. In addition,  $\overline{\dot{Q}}''$  was nearly independent of  $j_s$  in the transition region between the faradaic and capacitive regimes.

# CHAPTER 10

## Future work

This chapter presents recommendations for future modeling and experimental efforts to further the understanding and optimization of both EDLCs and pseudocapacitors.

### 10.1 Thermal modeling for porous electrode geometries

The simulations presented in the present study have focused on one-dimensional geometries, i.e., EDLCs and pseudocapacitors with planar electrodes, in order to elucidate the fundamental physical phenomena involved in idealized ECs. The use of planar electrodes vastly simplified both the numerical computations and the physical interpretation of the results by paring the EC cells down to their fundamentals. Indeed, this approach was very successful, resulting in remarkably good qualitative agreement between the numerical simulations using planar electrodes and experimental data involving porous electrodes.

However, simulations using planar electrodes cannot (i) provide quantitative predictions for practical EC devices with porous electrodes or (ii) provide insight into the effects of electrode geometry including pore size, tortuosity, and curvature of the electrode surface, in order to provide design rules. Indeed, the use of porous rather than planar electrodes is expected to impact the thermal behavior in several ways. First, the local current density will no longer be uniform throughout the cell. For example, the Joule heating in the current collectors and in the bulk electrolyte would be controlled by the current per unit current collector surface area. By contrast, the EDL and faradaic heat generation rates would be driven by the current per unit electrode/electrolyte interfacial area. For porous electrodes, these areas can differ by several orders of magnitude, resulting in very different magnitudes



of the current density as well as increasing the volume where the interfacial heat generation rates are significant. This may alter the relative importance of these heat generation rates to the total cell heat generation rate. Second, tortuosity and geometric confinement of the pores could result in diffusion limitations and/or ion depletion. A significant reduction in the local ion concentrations would affect the magnitudes of both Joule and EDL heat generation rates through the local electrolyte conductivity. In pseudocapacitors, ion starvation would significantly affect the faradaic heat generation rates by altering the surface overpotential and the relative faradaic and capacitive fractions of the current. Quantitative thermal models accounting for porous electrodes could be accomplished using several approaches.

### **10.1.1 First-principles simulations of porous electrodes**

First, local heat generation rates and temperature for two-dimensional or three-dimensional (3D) electrode geometries could be directly simulated using the general 3D formulations of the first-principles thermal models derived in the present study. Indeed, simulations of the electrochemical transport phenomena of ordered 3D EDLC electrodes are currently underway in our laboratory using the GMPNP model. The heat generation rates derived in Chapter 7 could be incorporated into this model. However, the simulations are computationally intensive and time-consuming, and accounting for the heat generation rates and temperature would add additional complexity. As a result, it would be prohibitively costly to simulate practical EC devices using materials such as activated carbon with multiscale and disordered pore distribution. This approach could be useful for simulating electrode geometries that are highly ordered, so that symmetry conditions reduce the necessary computational domain. Such simulations could provide insight into the key differences in the thermal behavior between planar and porous electrodes.

### **10.1.2 Empirical fitting of scaling laws for planar electrodes**

As previously mentioned in Chapters 6 and 7, scaling laws developed using simulations of planar electrodes could be extended to account for porous electrodes using semi-empirical

geometric parameters accounting for electrode morphology. This approach was successfully applied by Wang *et al.* [102] to model the equilibrium areal capacitance of nanoporous carbon electrodes as the product of the theoretical planar-electrode capacitance and a semi-empirical function depending on the average electrode pore radius and on the effective ion diameter. Similarly, the scaling laws obtained in Chapter 6 or developed from the expanded models in Chapters 7 and 9 could be adapted to predict the heat generation rates and temperature oscillations in actual EC devices with porous electrodes. I anticipate that the qualitative observations obtained for planar electrodes, e.g., the effects of ion valency and size and the faradaic and capacitive regimes in hybrid pseudocapacitors, will also apply to porous electrodes regardless of their morphology. However, this approach would require a broad range of experimental data for the heat generation rates and/or the detailed temperature evolution for ECs with different porous electrode structures and electrolytes. The experimental temperature data currently available in the literature for ECs would be insufficient for this purpose [7, 8, 25, 29, 76–78].

## 10.2 Experimental measurements of heat generation rates and temperature

Experimental measurements are vital for developing and validating thermal models. For example, the detailed temperature measurements reported and analyzed by Schiffer *et al.* [29] for a commercial EDLC cycled under a wide range of operating conditions was invaluable for qualitatively validating the EDLC thermal model developed in Chapter 4. Similarly, the time-dependent heat generation rates measured by Dandeville *et al.* [78, 79] were important for validating the hybrid pseudocapacitor model in Chapter 9. Unfortunately, there is relatively little experimental data for heat generation rates and temperature evolution of ECs available in the literature, especially for pseudocapacitors. In addition, most of the existing thermal studies investigated commercial EC devices whose electrolyte composition and electrode morphologies are not readily available [7, 8, 25, 29, 76].

For validating thermal models and improving physical interpretation of experimental

measurements, it would be helpful to measure detailed temperature and/or heat generation rate evolutions (i) for the same EC under a wide range of operating conditions, i.e., various cycling currents and potential windows, as performed in Ref. [29] and (ii) for ECs with different electrolytes and electrode morphologies under the same operating conditions. To be most useful for comparing to model predictions and for physical interpretation, the temperature evolutions should have sufficient resolution to show the shape of the temperature oscillations.

### 10.3 Expanding available property data for EC materials

Currently, a major limitation for first-principles modeling of ECs is the difficulty of finding transport properties of the electrode materials and the electrolytes. More extensive experimental characterization of EC materials could help to alleviate this problem. For electrolytes, it is difficult to find values for the solvated ion diameter  $a_i$  and diffusion coefficient  $D_i$  of ions in various solvents and as functions of concentration and temperature as well as the relative permittivity  $\epsilon_r$  as a function of electric field. Similarly, for modeling pseudocapacitors, values of properties such as the electrical conductivity  $\sigma_P$  and the diffusion coefficient  $D_{1,P}$  for intercalated species in the pseudocapacitive electrode as well as the reaction rate  $k_0$  and equilibrium potential drop  $\Delta\psi_{eq}$  are lacking. Ideally, these would be obtained as functions of the concentration  $c_{1,P}$  and the temperature. Here, accounting for temperature dependence of the transport properties would be necessary to simulate full coupling between the electrochemical transport and the temperature, such that the temperature rise affects the EC resistance and capacitance as observed experimentally.

Unfortunately, some of the key properties used in the GMPNP and MPNP ion transport models are difficult to measure. For example, it is challenging to obtain the diffusion coefficient  $D_i$  of an individual ion species independent of its counterion due to the electrical forces between the ions tending to keep the local concentrations of both ion species the same. Similarly, obtaining the electric-field-dependent relative permittivity  $\epsilon_r$  of the solvent is challenging, since the predicted values of the electric field in the EDL are extremely large,

on the order of 1 V/nm. Measuring  $\epsilon_r$  under such large electric field would require applying very large voltages on either side of the solvent sample and/or a test apparatus with very small yet well-controlled separation between the electrodes. As a result, finding alternative methods for obtaining such properties would also be helpful. For example, molecular dynamics (MD) models accounting for inter-atomic forces may provide useful data and insights into these properties. Indeed, I have been collaborating with researchers performing MD simulations of a planar EDLC in order to identify appropriate definitions of the effective ion diameters and the electric-field-dependent relative permittivity based on the MD results such that the continuum and MD models give consistent capacitance predictions. Such methods could help to fill the gaps in available experimental data.

Chapter 8 suggests that the equilibrium potential drop  $\Delta\psi_{eq}$  is of particular interest to explore further. Experimental measurements for  $\text{MnO}_2$  electrodes indicated that the variation of  $\Delta\psi_{eq}$  with the state of charge was weaker for thin-film electrodes than for thick porous electrodes, i.e., the thin-film electrodes featured smaller values of  $S_{eq}$  [123]. Simulation results suggest that this would result in thick porous electrodes having a smaller faradaic fraction  $j_F/j_s$  of the current than thin-film electrodes and could explain why smaller capacitances are measured for thick porous electrodes compared to thin films [158]. However, it remains unclear why the relationship between  $\Delta\psi_{eq}$  and the state of charge would depend on the electrode geometry. This phenomenon should be investigated further, given the significant limitation on the faradaic current predicted when  $\Delta\psi_{eq}$  varied strongly with SOC. First, it would be valuable to collect more experimental data for  $\Delta\psi_{eq}$  as a function of intercalated cation concentration  $c_{1,P}$  for different pseudocapacitive materials with different electrode geometries and thicknesses. A wide range of data would make it possible to identify trends and could be used in future simulations. Second, identifying the physical phenomena responsible for the measured differences in  $S_{eq}$  would be valuable to guide the design of individual electrodes and devices. For example, do the experimentally observed differences in  $S_{eq}$  between thin-film and thick porous electrodes reflect differences in the local reaction properties of the material or do the apparent changes in  $S_{eq}$  result from other transport limitations in porous electrodes? Numerical simulations of two-dimensional or three-dimensional pseudocapaci-

tive electrode geometries could help to differentiate between the effects of porous-electrode transport limitations and actual changes in the local  $S_{eq}$ .

## APPENDIX A

### Supplementary material for Chapter 6

#### A.1 Illustration of scaling analysis: Dimensionless heat generation rates

Figure A.1(a) shows the local irreversible volumetric heat generation rate  $\dot{q}_{irr}(x, 7t_c/5)$  as a function of location  $x$  at time  $7t_c/5$  during charging near Electrode A for Cases 1 to 3 summarized in Table 6.2. It was uniform and equal to  $j_s^2/\sigma_\infty$  throughout most of the electrolyte domain, where  $\sigma_\infty$  is the electrolyte conductivity at the bulk concentration  $c_\infty$ . However,  $\dot{q}_{irr}$  decreased sharply to zero near the electrode surface because ion insertion into the electrode was negligible and the ionic current density  $j$  vanished. The transition from the plateau value of  $j_s^2/\sigma_\infty$  to zero occurred over a region only a few nanometers thick. Both the value of  $j_s^2/\sigma_\infty$  and the thickness of the transition region differed for Cases 1 to 3. However, Figure A.1(b) shows the dimensionless irreversible volumetric heat generation rate  $\dot{q}_{irr}^*(x^*, 7t_c^*/5)$  as a function of dimensionless location  $x^*$  for Cases 1 to 3. It indicates that the data in dimensionless form collapsed onto a single curve with  $\dot{q}_{irr}^* = j_s^{*2}/2$  far from the electrode.

Similarly, Figure A.2(a) shows the local reversible volumetric heat generation rate  $\dot{q}_{rev}(x, 7t_c/5) = \dot{q}_{E,d}(x, 7t_c/5) + \dot{q}_{E,s}(x, 7t_c/5) + \dot{q}_{S,c}(x, 7t_c/5)$  as a function of location  $x$  near Electrode A at time  $7t_c/5$  for Cases 1 to 3. The time  $t = 7t_c/5$  occurred during a charging step, so the reversible heat generation rates were positive (Chapter 4). This is reflected by the large positive peak of  $\dot{q}_{rev}$  observed in all three cases. Its height and width varied significantly among Cases 1 to 3. However, Figure A.2(b) shows that the corresponding dimensionless reversible volumetric heat generation rates  $\dot{q}_{rev}^*(x^*, 7t_c^*/5)$  as a function of dimensionless loca-

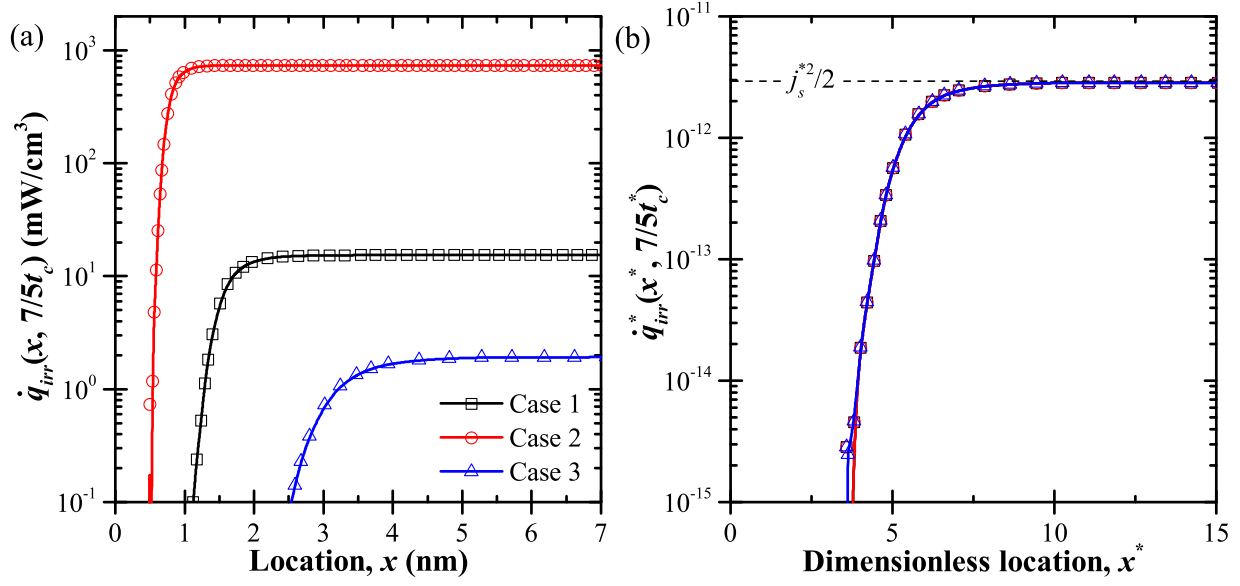


Figure A.1: Computed (a) irreversible volumetric heat generation rate  $\dot{q}_{irr}(x, 7t_c/5)$  as a function of location  $x$  and (b) corresponding dimensionless irreversible volumetric heat generation rate  $\dot{q}_{irr}^*(x^*, 7t_c^*/5)$  as a function of dimensionless location  $x^*$  for Cases 1 to 3 (Table 6.2).

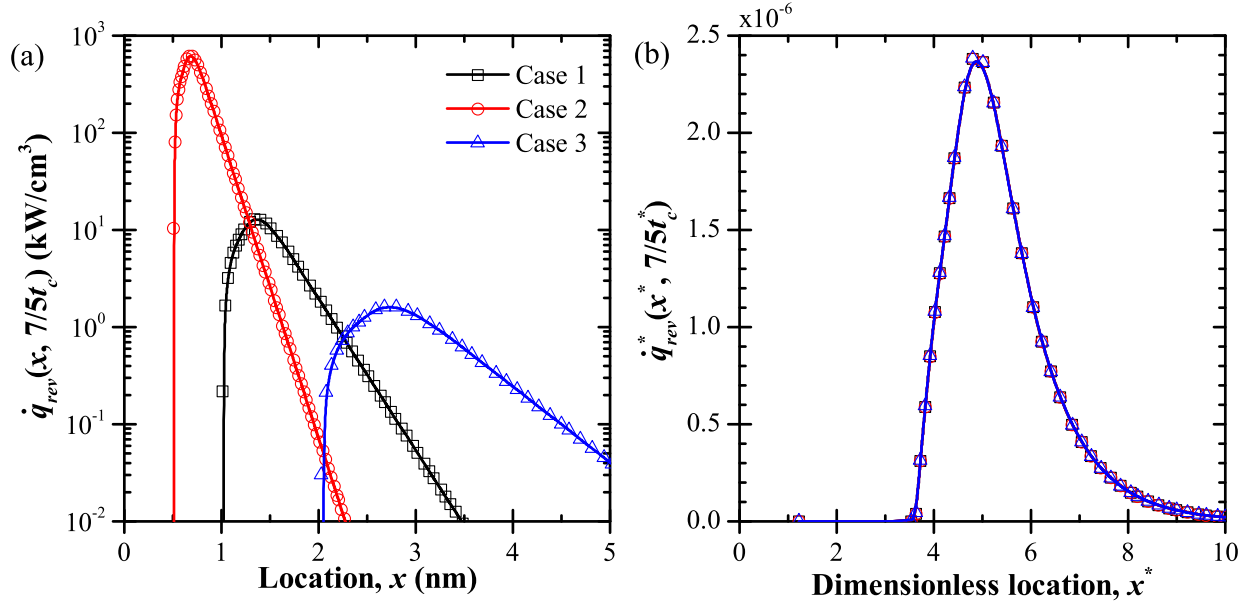


Figure A.2: Computed (a) reversible volumetric heat generation rate  $\dot{q}_{rev}(x, 7t_c/5)$  as a function of location  $x$  and (b) corresponding dimensionless reversible volumetric heat generation rate  $\dot{q}_{rev}^*(x^*, 7t_c^*/5)$  as a function of dimensionless location  $x^*$  for Cases 1 to 3 (Table 6.2).

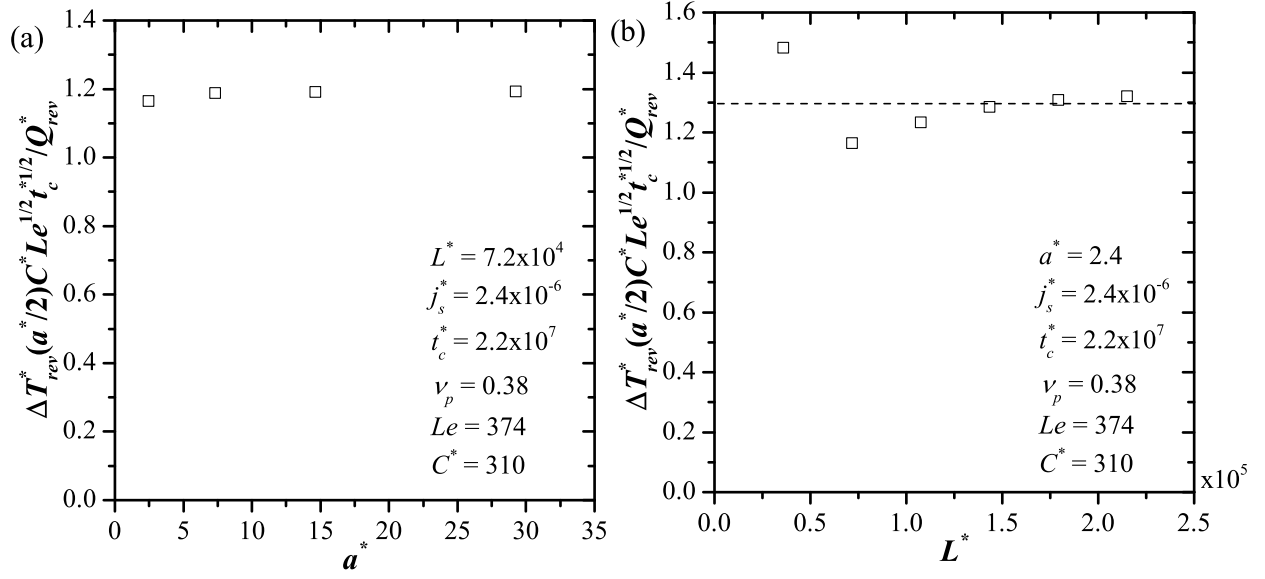


Figure A.3: Computed values of  $\Delta T_{rev}^* C^* Le^{1/2} t_c^{*1/2} / Q_{rev}^*$  as a function of (a)  $a^*$  and (b)  $L^*$ .

tion  $x^*$  collapsed onto the same curve. This demonstrates that the scaling captured the large spatial variations associated with the irreversible and reversible volumetric heat generation rates.

## A.2 Correlations for thermal effects

### A.2.1 Temperature oscillation amplitude

Figure A.3 plots  $\Delta T_{rev}^* (a^*/2) C^* Le^{1/2} t_c^{*1/2} / Q_{rev}^*$  as a function of (a)  $a^*$  ranging from 2.4 to 29 with  $L^* = 7.2 \times 10^4$  and (b)  $L^*$  ranging from  $3.6 \times 10^4$  to  $2.1 \times 10^5$  with  $a^* = 2.4$ , while the other dimensionless similarity parameters were taken as  $j_s^* = 2.4 \times 10^{-6}$ ,  $t_c^* = 2.2 \times 10^7$ ,  $\nu_p = 0.38$ ,  $Le = 374$ , and  $C^* = 310$ . Figure A.3(a) indicates that  $\Delta T_{rev}^* (a^*/2) C^* Le^{1/2} t_c^{*1/2} / Q_{rev}^*$  was independent of  $a^*$ . Figure A.3(b) features small variations of  $\Delta T_{rev}^* (a^*/2) C^* Le^{1/2} t_c^{*1/2} / Q_{rev}^*$  with  $L^*$ , but the average value  $\Delta T_{rev}^* (a^*/2) C^* Le^{1/2} t_c^{*1/2} / Q_{rev}^* = 1.3$  was used for the correlation.



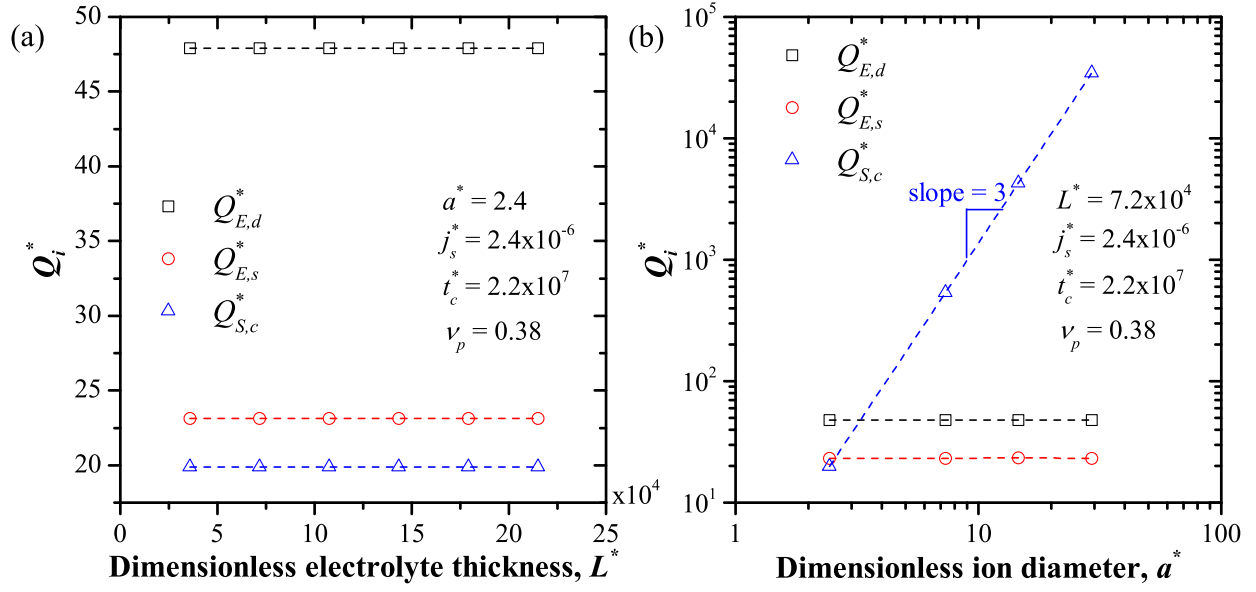


Figure A.4: Predicted dimensionless heat generation integrals  $Q_{E,d}^*$ ,  $Q_{E,s}^*$ , and  $Q_{S,c}^*$  as functions of (a) dimensionless inter-electrode spacing  $L^*$  and (b) dimensionless ion diameter  $a^*$ .

### A.2.2 Heat generation

Figure A.4 plots  $Q_{E,d}^*$ ,  $Q_{E,s}^*$ , and  $Q_{S,c}^*$  as functions of (a) the dimensionless interelectrode spacing  $L^*$  ranging from  $3.6 \times 10^4$  to  $2.1 \times 10^5$  with  $a^* = 2.4$  and (b) the dimensionless ion diameter  $a^*$  ranging from 2.4 to 29 with  $L^* = 7.2 \times 10^4$ , while the other relevant dimensionless similarity parameters were taken as  $j_s^* = 2.4 \times 10^{-6}$ ,  $t_c^* = 2.2 \times 10^7$ , and  $\nu_p = 0.38$ . It indicates that the dimensionless interelectrode spacing  $L^*$  had no effect on  $Q_{E,d}^*$ ,  $Q_{E,s}^*$ , and  $Q_{S,c}^*$ . Indeed, for sufficiently large  $L^*$ , the EDLs did not overlap, i.e.,  $L^* \gg 1$ , and the EDL concentration profiles, responsible for reversible heating, were independent of  $L^*$ , as previously observed by Wang *et al.* [42, 43, 47]. In addition, the heat of mixing contribution  $Q_{S,c}^*$  was proportional to  $a^{*3}$  while  $Q_{E,d}^*$  and  $Q_{E,s}^*$  were independent of  $a^*$ .

Figure A.5 plots (a)  $Q_{E,d}^*$ , (b)  $Q_{E,s}^*$ , and (c)  $Q_{S,c}^*/a^{*3}$  as functions of the dimensionless product  $j_s^* t_c^*$  for two values of  $\nu_p$  and several values of  $j_s^*$  and  $t_c^*$  with  $a^* = 2.4$  and  $L^* = 7.2 \times 10^4$ . It is evident that predictions for the same values of  $\nu_p$  and  $j_s^* t_c^*$  overlapped despite the different values of  $j_s^*$  and  $t_c^*$ . This indicates that  $Q_{E,d}^*$ ,  $Q_{E,s}^*$ , and  $Q_{S,c}^*$  depended only on the product  $j_s^* t_c^*$  rather than on the individual parameters  $j_s^*$  and  $t_c^*$ .

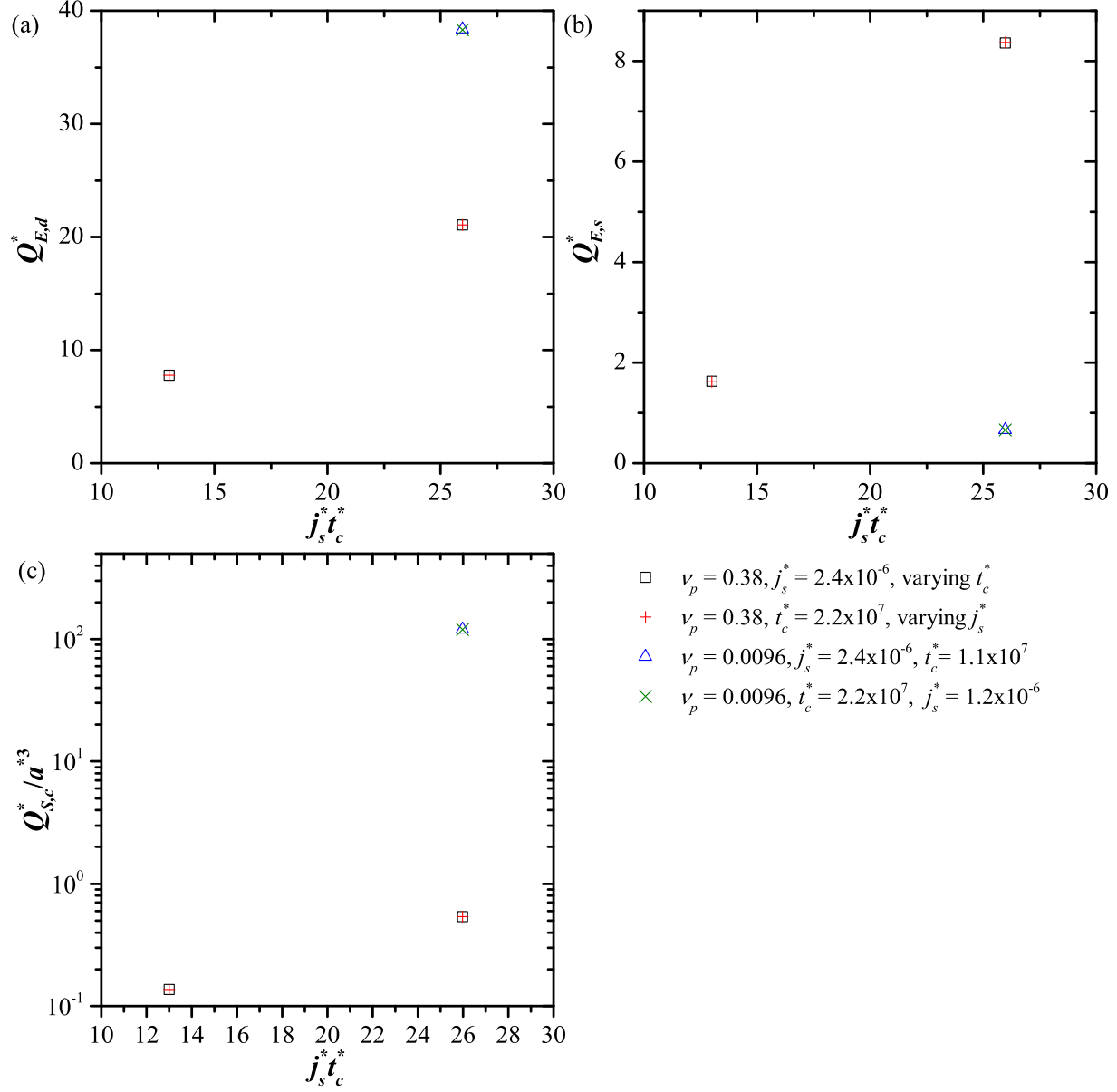


Figure A.5: Computed dimensionless heat generation (a)  $Q_{E,d}^*$ , (b)  $Q_{E,s}^*$ , and (c)  $Q_{S,c}^*$  as functions of  $j_s^* t_c^*$  for  $a^* = 2.4$ ,  $L^* = 7.2 \times 10^4$ , and various  $j_s^*$ ,  $t_c^*$ , and  $\nu_p$ .

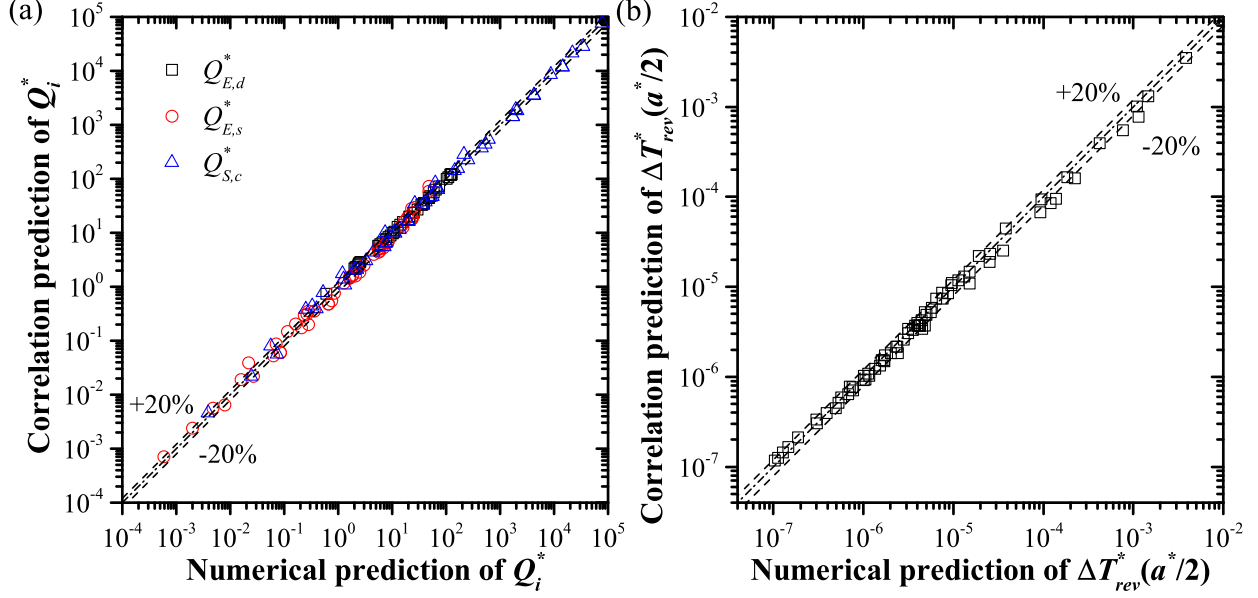


Figure A.6: Values of (a)  $Q_{E,d}^*$ ,  $Q_{E,s}^*$ , and  $Q_{S,c}^*$  and (b)  $\Delta T_{rev}^*(a^*/2)$  predicted by correlations as function of those computed numerically.

Figure A.6(a) plots the values of  $Q_{E,d}^*$ ,  $Q_{E,s}^*$ , and  $Q_{S,c}^*$  predicted by Equations (6.19) to (6.21) versus those predicted numerically for all simulations used to develop the correlations. The data covers the ranges  $1.2 \leq a^* \leq 29$ ,  $3.6 \times 10^4 \leq L^* \leq 2.1 \times 10^5$ ,  $3.0 \times 10^{-7} \leq j_s^* \leq 8.7 \times 10^{-6}$ ,  $5.5 \times 10^6 \leq t_c^* \leq 8.7 \times 10^7$ ,  $0.0012 \leq \nu_p \leq 0.88$ ,  $187 \leq Le \leq 748$ , and  $78 \leq C^* \leq 735$ . Similarly, Figure A.6(b) shows the temperature oscillation amplitude  $\Delta T_{rev}^*$  predicted by Equation (6.17) with  $Q_{E,d}^*$ ,  $Q_{E,s}^*$ , and  $Q_{S,c}^*$  predicted by Equations (6.19)–(6.21) versus that predicted by numerical simulations. The average relative error for  $\Delta T_{rev}^*$  was 12%.

## APPENDIX B

### Supplementary material for Chapter 7

#### B.1 IR drops in cell potential

Figure B.1 shows the cell potential  $\psi_s(t) = \psi(0, t) - \psi(2L, t)$  as a function of time  $t$  for a symmetric electrolyte with  $-z_1 = z_2 = 1$ ,  $a_1 = a_2 = 0.56$  nm, and  $D_1 = D_2 = 1 \times 10^{-11}$  m<sup>2</sup>s<sup>-1</sup>. Aside from the smaller diffusion coefficients, the electrolyte properties were the same as those of Case 1. Here, significant “IR drops” due to the ohmic resistance of the electrolyte were evident at the beginning and end of each charging and discharging step. The magnitude of the potential drop due to the electrolyte resistance was equal to  $j_s(2L)/\sigma_\infty = 0.075$  V. It was positive during the charging step and negative during the discharging step. Thus, the IR drop at the transition from charging to discharging at time  $t_c/2 = 3.8$  ms was equal to twice this value, i.e., 0.15 V.

#### B.2 Irreversible heat generation rate

Figure B.2 shows the irreversible heat generation rate  $\dot{q}_{irr}(x, 11t_c/8)$  as a function of location  $x$  for (a) Cases 1-4 with varying  $z_i$  and (b) Cases 1, 7, and 8 with varying  $D_i$  near the end of a charging step. Note that the heat generation rate was plotted at a slightly earlier time than the concentrations shown in Figure 7.2 in order to show the profiles characteristic of the charging step rather than those during the switch in current direction from charging to discharging occurring at  $t = 3t_c/2$ .

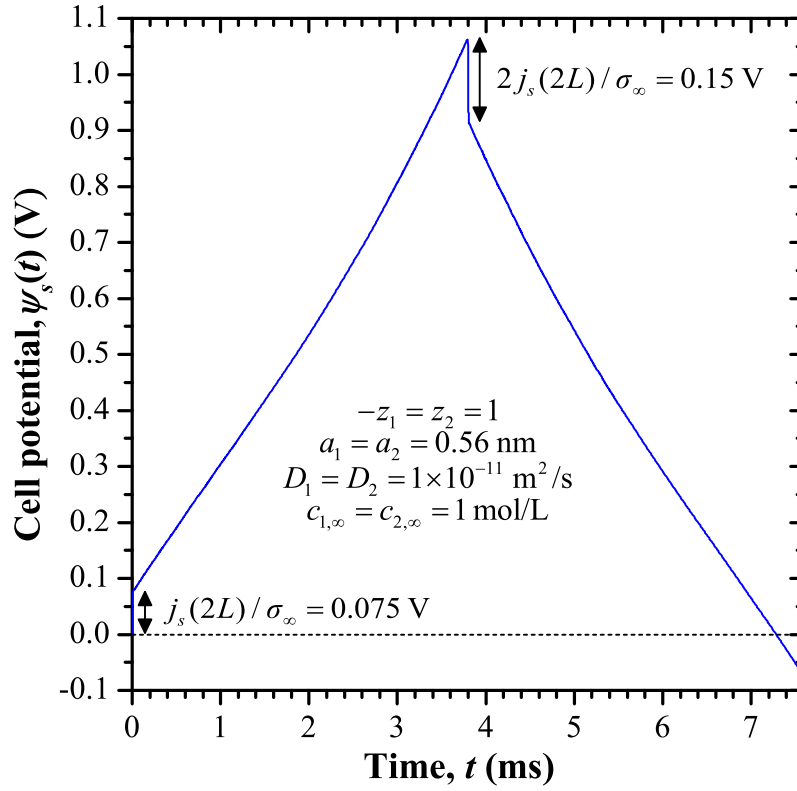


Figure B.1: Cell potential  $\psi_s(t) = \psi(0, t) - \psi(2L, t)$  as a function of time  $t$  for a symmetric electrolyte with  $-z_1 = z_2 = 1$ ,  $a_1 = a_2 = 0.56$  nm, and  $D_1 = D_2 = 1 \times 10^{-11} \text{ m}^2\text{s}^{-1}$ . Significant IR drops were evident due to the relatively low conductivity  $\sigma_\infty$  resulting from the small diffusion coefficients.

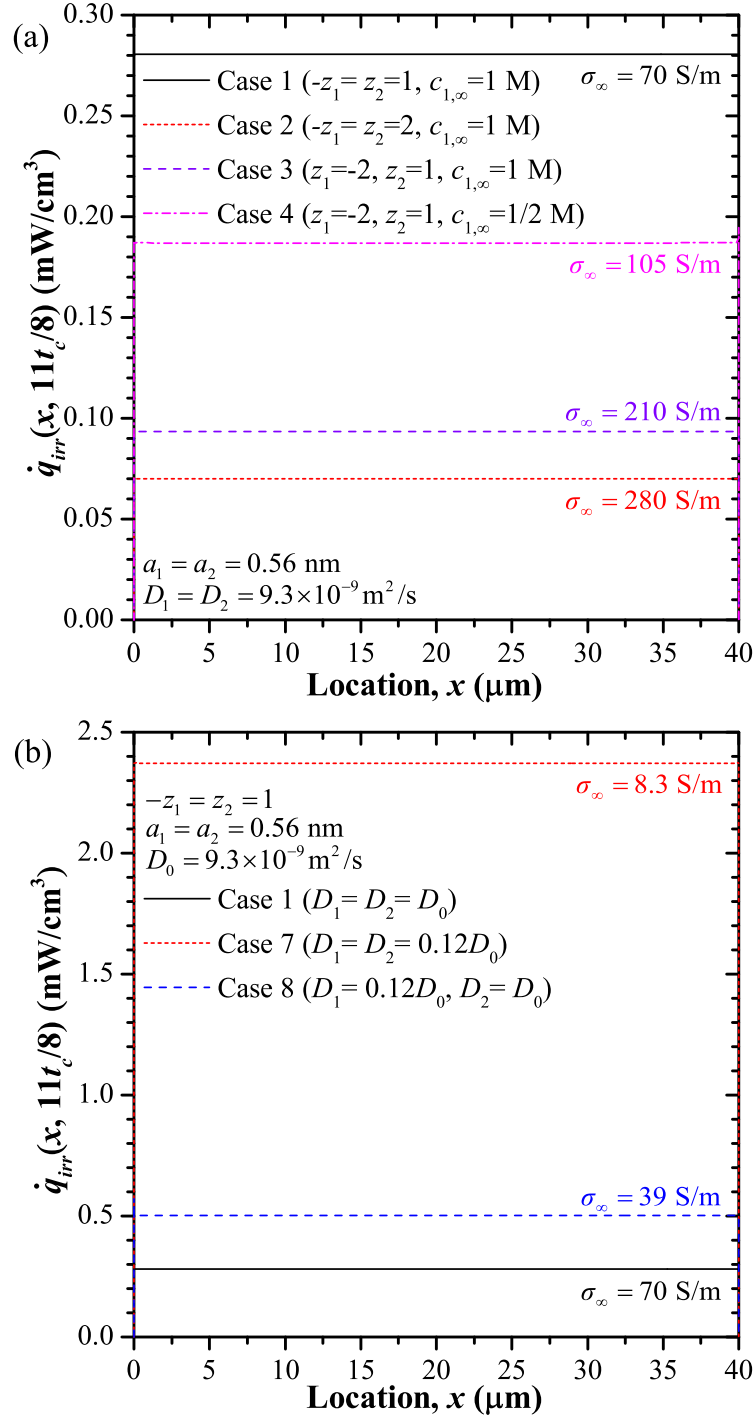


Figure B.2: Irreversible heat generation rate  $\dot{q}_{irr}(x, 11t_c/8)$  as a function of location  $x$  for (a) Cases 1-4 featuring different  $z_i$  and (b) Cases 1, 7, and 8 featuring different  $D_i$ . All cases correspond to time  $t = 11t_c/8$  near the end of a charging step.

## APPENDIX C

### Three-dimensional formulation of faradaic heat generation rates

The temperature across the Stern layer was assumed to be uniform due to its small thickness. Then, in the absence of ion or solvent accumulation, the energy conservation equation for each Stern layer can be expressed as

$$\frac{\partial(\rho_E u)}{\partial t} = \rho_E c_{p,E} \frac{\partial T}{\partial t} = \frac{[\mathbf{q}''(\mathbf{r}_s, t) - (A_H/A_s)\mathbf{q}''(\mathbf{r}_s + H\mathbf{n}_s, t)] \cdot \mathbf{n}_s}{V_H/A_s}. \quad (\text{C.1})$$

where  $\mathbf{r}_s$  is the position vector for a point on the electrode/electrolyte interface and  $\mathbf{n}_s$  is the unit normal vector to the electrode/electrolyte interface pointing into the electrolyte. Here,  $u$  is the specific internal energy of the electrolyte in the Stern layer while  $\mathbf{q}''(\mathbf{r}_s, t)$  and  $\mathbf{q}''(\mathbf{r}_s + H\mathbf{n}_s, t)$  are the energy fluxes into and out of the Stern layer, respectively. In addition,  $A_s$  and  $A_H$  are the areas of the electrode/electrolyte and Stern/diffuse layer interfaces, respectively, while  $V_H$  is the Stern layer volume. The ratio  $A_H/A_s$  can be expressed for simple electrode geometries as

$$\frac{A_H}{A_s} = \begin{cases} 1 & \text{for planar electrodes} \\ \frac{R_s + H}{R_s} & \text{for cylindrical electrodes} \\ \frac{(R_s + H)^2}{R_s^2} & \text{for spherical electrodes} \end{cases} \quad (\text{C.2})$$

and  $V_H/A_s$  as

$$\frac{V_H}{A_s} = \begin{cases} H & \text{for planar electrodes} \\ H \left( 1 + \frac{H}{2R_s} \right) & \text{for cylindrical electrodes} \\ H \left( 1 + \frac{H}{R_s} + \frac{H^2}{3R_s^2} \right) & \text{for spherical electrodes} \end{cases} \quad (\text{C.3})$$

where  $R_s$  is the radius of curvature of the electrode/electrolyte interface. Near the carbon electrode, the energy fluxes  $\mathbf{q}_{in}''$  and  $\mathbf{q}_{out}''$  are solely due to heat conduction. Then, the energy conservation equation can be written as

$$\rho_{ECp,E} \frac{\partial T}{\partial t} = \frac{[k_E \nabla T(\mathbf{r}_s + H\mathbf{n}_s, t)(A_H/A_s) - k_C \nabla T(\mathbf{r}_s, t)] \cdot \mathbf{n}_s}{V_H/A_s}. \quad (\text{C.4})$$

Near the pseudocapacitive electrode, the energy fluxes result not only from heat conduction but also from chemical reactants entering and exiting the Stern layer. Assuming negligible Dufour effect, the energy fluxes  $\mathbf{q}_{in}'' = \mathbf{q}''(\mathbf{r}_s, t)$  and  $\mathbf{q}_{out}'' = \mathbf{q}''(\mathbf{r}_s + H\mathbf{n}_s, t)$  can be expressed as [28]

$$\mathbf{q}_{in}'' = -k_P \nabla T(\mathbf{r}_s, t) + \sum_{i=0}^{n+1} (\bar{H}_{i,P} \mathbf{N}_{i,P}) (\mathbf{r}_s, t) \quad (\text{C.5})$$

$$\text{and } \mathbf{q}_{out}'' = -k_E \nabla T(\mathbf{r}_s + H\mathbf{n}_s, t) + \sum_{i=0}^n (\bar{H}_{i,E} \mathbf{N}_{i,E}) (\mathbf{r}_s + H\mathbf{n}_s, t) \quad (\text{C.6})$$

where  $\bar{H}_i$  is the partial molar enthalpy of ion species  $i$  ( $1 \leq i \leq n$ ) in the electrolyte, of the electrons  $i = n + 1, P$  or of the intercalated  $\text{Li}^+$   $i = 1, P$  in the pseudocapacitive electrode. Then, in the Stern layer near the pseudocapacitive electrode, Equation (C.4) becomes

$$\rho_{ECp,E} \frac{\partial T}{\partial t} = \frac{[k_E \nabla T(\mathbf{r}_s + H\mathbf{n}_s, t)(A_H/A_s) - k_P \nabla T(\mathbf{r}_s, t)] \cdot \mathbf{n}_s}{V_H/A_s} + \dot{q}_{F,E}(\mathbf{r}_s, t) \quad (\text{C.7})$$

Here,  $\dot{q}_{F,E}$  is the heat generation rate in the Stern layer due to the faradaic reaction and given by

$$\dot{q}_{F,E}(\mathbf{r}_s, t) = -\frac{A_s}{V_H} \left[ \sum_{i=1}^n (\bar{H}_{i,E} \mathbf{N}_{i,E})(\mathbf{r}_s + H\mathbf{n}_s, t) \frac{A_H}{A_s} - \sum_{i=1}^{n+1} (\bar{H}_{i,P} \mathbf{N}_{i,P})(\mathbf{r}_s, t) \right] \cdot \mathbf{n}_s. \quad (\text{C.8})$$

The only non-zero terms in Equation (C.8) correspond to species involved in the redox reaction because no other species enter or exit the Stern layer. The electron flux  $\mathbf{N}_{n+1,P}$  and the faradaic current density  $\mathbf{j}_F$  are related by  $\mathbf{j}_F(\mathbf{r}_s, t) = -F\mathbf{N}_{n+1,P}(\mathbf{r}_s, t)$  [28]. Similarly, the fluxes  $\mathbf{N}_{i,E}$  and  $\mathbf{N}_{1,P}$  of all other reacting species are related to  $\mathbf{N}_{n+1,P}$  and  $\mathbf{j}_F$  by stoichiometry. Let us consider the general redox reaction occurring at the pseudocapacitive electrode/electrolyte interface  $\sum_{i=0}^{n+1} (s_{i,P} M_{i,P} + s_{i,E} M_{i,E}) \rightleftharpoons 0$ , where  $s_i$  is the stoichiometric coefficient for reactant  $M_i$  and subscripts  $P$  and  $E$  respectively refer to the pseudocapacitive electrode and the electrolyte. For this reaction, the reactant fluxes are related by  $\mathbf{j}_F(\mathbf{r}_s, t)/F =$



$-\mathbf{N}_{n+1,P}(\mathbf{r}_s, t) = -(s_{n+1,P}/s_{i,P})\mathbf{N}_{i,P}(\mathbf{r}_s, t) = (s_{n+1,P}/s_{i,E})(A_H/A_s)\mathbf{N}_{i,E}(\mathbf{r}_s + H\mathbf{n}_s, t)$ . Then,  $\dot{q}_{F,E}$  can be expressed as

$$\dot{q}_{F,E}(\mathbf{r}_s, t) = \frac{\mathbf{j}_F(\mathbf{r}_s, t) \cdot \mathbf{n}_s}{(V_H/A_s)F s_{n+1,P}} \left\{ - \sum_{i=1}^{n+1} [s_{i,E}\bar{H}_{i,E}(\mathbf{r}_s + H\mathbf{n}_s, t) + s_{i,P}\bar{H}_{i,P}(\mathbf{r}_s, t)] \right\}. \quad (\text{C.9})$$

Expressing the partial molar enthalpy as  $\bar{H}_i = \tilde{\mu}_i + T\bar{S}_i$  [91] yields

$$\dot{q}_{F,E}(\mathbf{r}_s, t) = \frac{\mathbf{j}_F(\mathbf{r}_s, t) \cdot \mathbf{n}_s}{(V_H/A_s)} \left\{ - \frac{1}{s_{n+1,P}F} \sum_{i=1}^{n+1} [s_{i,E}\tilde{\mu}_{i,E}(\mathbf{r}_s + H\mathbf{n}_s, t) + s_{i,P}\tilde{\mu}_{i,P}(\mathbf{r}_s, t)] \right. \quad (\text{C.10})$$

$$\left. - \frac{1}{s_{n+1,P}F} \sum_{i=1}^{n+1} [s_{i,E}\bar{S}_{i,E}(\mathbf{r}_s + H\mathbf{n}_s, t) + s_{i,P}\bar{S}_{i,P}(\mathbf{r}_s, t)] \right\}. \quad (\text{C.11})$$

The two terms within the brackets correspond to the surface overpotential  $\eta$  and the Peltier coefficient  $\Pi$  given by Equation (9.14) [28]. Then,  $\dot{q}_{F,E}(t)$  can be divided into one irreversible and one reversible contribution such that  $\dot{q}_{F,E} = \dot{q}_{F,E,irr} + \dot{q}_{F,E,rev}$  where

$$\dot{q}_{F,E,irr}(\mathbf{r}_s, t) = \frac{\mathbf{j}_F(\mathbf{r}_s, t)\eta(\mathbf{r}_s, t) \cdot \mathbf{n}_s}{V_H/A_s} \quad \text{and} \quad \dot{q}_{F,E,rev}(t) = \frac{\mathbf{j}_F(\mathbf{r}_s, t)\Pi(\mathbf{r}_s, t) \cdot \mathbf{n}_s}{V_H/A_s}. \quad (\text{C.12})$$

## REFERENCES

- [1] A. d'Entremont, H. Wang, and L. Pilon, "Scaling analysis of thermal behavior of electrical double layers," in *ASME 2012 Heat Transfer Summer Conference*, pp. 395–403, American Society of Mechanical Engineers, 2012.
- [2] A. L. d'Entremont and L. Pilon, "First-principles thermal modeling of electric double layer capacitors under constant-current cycling," *Journal of Power Sources*, vol. 246, pp. 887 – 898, 2014.
- [3] A. L. d'Entremont and L. Pilon, "First-order thermal model of commercial EDLCs," *Applied Thermal Engineering*, vol. 67, pp. 439–446, 2014.
- [4] A. L. d'Entremont and L. Pilon, "Scaling laws for heat generation and temperature oscillations in EDLCs under galvanostatic cycling," *International Journal of Heat and Mass Transfer*, vol. 75, pp. 637–649, 2014.
- [5] A. L. d'Entremont and L. Pilon, "Thermal effects of asymmetric electrolytes in electric double layer capacitors," *Journal of Power Sources*, vol. 273, pp. 196–209, 2015.
- [6] US Department of Energy, "Basic Research Needs for Electrical Energy Storage: Report of the Basic Energy Sciences Workshop for Electrical Energy Storage," tech. rep., Office of Basic Energy Sciences, DOE, 2007.
- [7] J. R. Miller, "Electrochemical capacitor thermal management issues at high-rate cycling," *Electrochimica Acta*, vol. 52, no. 4, pp. 1703–1708, 2006.
- [8] H. Gualous, H. Louahlia-Gualous, R. Gallay, and A. Miraoui, "Supercapacitor thermal modeling and characterization in transient state for industrial applications," *IEEE Transactions on Industry Applications*, vol. 45, no. 3, pp. 1035–1044, 2009.
- [9] F. Rafik, H. Gualous, R. Gallay, A. Crausaz, and A. Berthon, "Frequency, thermal and voltage supercapacitor characterization and modeling," *Journal of Power Sources*, vol. 165, no. 2, pp. 928 – 934, 2007.
- [10] B. Conway, *Electrochemical Supercapacitors: Scientific Fundamentals and Technological Applications*. New York, NY: Kluwer Academic/Plenum Publishers, 1999.
- [11] M. Brain, "How lithium-ion batteries work." HowStuffWorks.com, 14 November 2006. Accessed February 25, 2013.
- [12] A. Burke, "Ultracapacitors: why, how, and where is the technology," *Journal of Power Sources*, vol. 91, pp. 37–50, 2000.
- [13] M. S. Halper and J. C. Ellenbogen, "Supercapacitors: A brief overview," Tech. Rep. No. MP 05W0000272, The MITRE Corporation, McLean, VA, 2006.
- [14] A. G. Pandolfo and A. F. Hollenkamp, "Carbon properties and their role in supercapacitors," *Journal of Power Sources*, vol. 157, pp. 11–27, 2006.

- [15] C. A. Vincent and B. Scrosati, eds., *Modern Batteries: An Introduction to Electrochemical Power Sources*. Burlington, MA: Butterworth-Heinemann, 2nd ed., 2003.
- [16] E. Frackowiak, “Electrode materials with pseudocapacitive properties,” in *Supercapacitors: Materials, Systems, and Applications* (F. Béguin and E. Frackowiak, eds.), ch. 6, pp. 207–237, Weinheim, Germany: Wiley-VCH Verlag, 2013.
- [17] P. Simon, Y. Gogotsi, and B. Dunn, “Where do batteries end and supercapacitors begin?,” *Science*, vol. 343, pp. 1210–1211, 2014.
- [18] B. E. Conway, V. Birss, and J. Wojtowicz, “The role and utilization of pseudocapacitance for energy storage by supercapacitors,” *Journal of Power Sources*, vol. 66, pp. 1–14, 1997.
- [19] T. Pandolfo, V. Ruiz, S. Sivakkumar, and J. Nerkar, “General properties of electrochemical capacitors,” in *Supercapacitors: Materials, Systems, and Applications* (F. Béguin and E. Frackowiak, eds.), ch. 2, pp. 69–109, Weinheim, Germany: Wiley-VCH Verlag, 2013.
- [20] H. Chen, T. N. Cong, W. Yang, C. Tan, Y. Li, and Y. Ding, “Progress in electrical energy storage systems: A critical review,” *Progress in Natural Sciences*, vol. 19, pp. 291–312, 2009.
- [21] P. Guillemet, Y. Scudeller, and T. Brousse, “Multi-level reduced-order thermal modeling of electrochemical capacitors,” *Journal of Power Sources*, vol. 157, no. 1, pp. 630–640, 2006.
- [22] P. Simon and Y. Gogotsi, “Materials for electrochemical capacitors,” *Nature Materials*, vol. 7, pp. 845–854, 2008.
- [23] J. W. Kim, V. Augustyn, and B. Dunn, “The effect of crystallinity on the rapid pseudocapacitive response of  $\text{Nb}_2\text{O}_5$ ,” *Advanced Energy Materials*, vol. 2, pp. 141–148, 2012.
- [24] P. Liu, M. Verbrugge, and S. Soukiazian, “Influence of temperature and electrolyte on the performance of activated-carbon supercapacitors,” *Journal of Power Sources*, vol. 156, pp. 712–718, 2006.
- [25] M. Al Sakka, H. Gualous, J. Van Mierlo, and H. Culcu, “Thermal modeling and heat management of supercapacitor modules for vehicle applications,” *Journal of Power Sources*, vol. 194, no. 2, pp. 581–587, 2009.
- [26] A. Bard and L. Faulkner, *Electrochemical Methods: Fundamentals and Applications*. New York, NY: John Wiley & Sons, 2001.
- [27] V. Bagotsky, *Fundamentals of Electrochemistry*. Hoboken, NJ: John Wiley & Sons, 2006.
- [28] J. S. Newman and K. E. Thomas-Alyea, *Electrochemical Systems*. Hoboken, NJ: John Wiley & Sons, 3rd ed., 2004.

- [29] J. Schiffer, D. Linzen, and D. U. Sauer, “Heat generation in double layer capacitors,” *Journal of Power Sources*, vol. 160, no. 1, pp. 765–772, 2006.
- [30] O. Bohlen, J. Kowal, and D. U. Sauer, “Ageing behaviour of electrochemical double layer capacitors: Part II. Lifetime simulation model for dynamic applications,” *Journal of Power Sources*, vol. 173, no. 1, pp. 626–632, 2007.
- [31] H. Wang and L. Pilon, “Reply to comments on “Intrinsic limitations of impedance measurements in determining electric double layer capacitances” by H. Wang, L. Pilon [Electrochimica Acta 63 (2012) 55],” *Electrochimica Acta*, vol. 76, pp. 529–531, 2012.
- [32] R. F. Probstein, *Physicochemical Hydrodynamics: An Introduction*. Hoboken, NJ: John Wiley & Sons, 2nd ed., 2003.
- [33] H. von Helmholtz, “Ueber einige Gesetze der Vertheilung elektrischer Ströme in körperlichen Leitern mit Anwendung auf die thierisch-elektrischen Versuche,” *Annalen der Physik (Leipzig)*, vol. 89, pp. 211–233, 1853.
- [34] G. Gouy, “Sur la constitution de la charge électrique à la surface d’un électrolyte,” *Journal de Physique Théorique et Appliquée*, vol. 9, p. 457, 1910.
- [35] D. L. Chapman, “A contribution to the theory of electrocapillarity,” *Philosophical Magazine Series 6*, vol. 25, no. 148, pp. 475–481, 1913.
- [36] G. Gouy, “Sur la fonction electrocapillaire,” *Annales de Physique (Paris)*, vol. 7, no. 9, pp. 129–184, 1917.
- [37] O. Stern, “Zur Theorie der elektrolytischen Doppelschicht,” *Zeitschrift für Elektrochemie und Angewandte Physikalische Chemie*, vol. 30, pp. 508–516, 1924.
- [38] M. S. Kilic, M. Z. Bazant, and A. Ajdari, “Steric effects in the dynamics of electrolytes at large applied voltages. II. Modified Poisson-Nernst-Planck equations,” *Physical Review E*, vol. 75, no. 2, p. 021503, 2007.
- [39] D. C. Grahame, “The electrical double layer and the theory of electrocapillarity,” *Chemical Reviews*, vol. 41, no. 3, pp. 441–501, 1947.
- [40] M. S. Kilic, M. Z. Bazant, and A. Ajdari, “Steric effects in the dynamics of electrolytes at large applied voltages. I. Double-layer charging,” *Physical Review E*, vol. 75, p. 021502, 2007.
- [41] B. J. Kirby, *Micro- and Nanoscale Fluid Mechanics: Transport in Microfluidic Devices*. New York, NY: Cambridge University Press, 2010.
- [42] H. Wang and L. Pilon, “Intrinsic limitations of impedance measurements in determining electric double layer capacitances,” *Electrochimica Acta*, vol. 63, pp. 55–63, 2012.
- [43] H. Wang and L. Pilon, “Physical interpretation of cyclic voltammetry for measuring electric double layer capacitances,” *Electrochimica Acta*, vol. 64, pp. 130–139, 2012.

- [44] J. H. Masliyah and S. Bhattacharjee, *Electrokinetic and Colloid Transport Phenomena*. Hoboken, NJ: John Wiley & Sons, 2006.
- [45] R. J. Hunter, *Foundations of Colloid Science*. New York, NY: Oxford University Press, 2nd ed., 2001.
- [46] J. Lyklema, *Fundamentals of Interface and Colloid Science, Vol. II: Solid-Liquid Interfaces*. San Diego, CA: Academic Press, 2001.
- [47] H. Wang and L. Pilon, “Accurate simulations of electric double layer capacitance of ultramicroelectrodes,” *Journal of Physical Chemistry C*, vol. 115, pp. 16711–16719, 2011.
- [48] H. Wang and L. Pilon, “Mesoscale modeling of electric double layer capacitors with three-dimensional ordered structures,” *Journal of Power Sources*, vol. 221, pp. 252–260, 2013.
- [49] J. Baker-Jarvis and B. Riddle, “Ion dynamics near charged electrodes with excluded volume effect,” *IEEE Transactions on Dielectrics and Electrical Insulation*, vol. 6, no. 2, pp. 226–235, 1999.
- [50] J. Cervera, V. García-Morales, and J. Pellicer, “Ion size effects on the electrokinetic flow in nanoporous membranes caused by concentration gradients,” *Journal of Physical Chemistry B*, vol. 107, pp. 8300–8309, 2003.
- [51] K. T. Chu and M. Z. Bazant, “Surface conservation laws at microscopically diffuse interfaces,” *Journal of Colloid and Interface Science*, vol. 315, pp. 319–329, 2007.
- [52] M. Z. Bazant, M. S. Kilic, B. D. Storey, and A. Ajdari, “Towards an understanding of induced-charge electrokinetics at large applied volages in concentrated solutions,” *Advances in Colloid and Interfacial Science*, vol. 152, no. 1-2, pp. 48–88, 2009.
- [53] M. J. Aranda-Rascón, C. Grosse, J. J. López-García, and J. Horno, “Influence of the finite ion size on the predictions of the standard electrokinetic model: Frequency response,” *Journal of Colloid and Interface Science*, vol. 336, no. 2, pp. 857–864, 2009.
- [54] L. H. Olesen, M. Z. Bazant, and H. Bruus, “Strongly nonlinear dynamics of electrolytes in large AC voltages,” *Physical Review E*, vol. 82, p. 011501, 2010.
- [55] J. Cervera, P. Ramírez, J. A. Manzanares, and S. Mafé, “Incorporating ionic size in the transport equations for charged nanopores,” *Microfluidics and Nanofluidics*, vol. 9, pp. 41–53, 2010.
- [56] H. Zhao, “Diffuse-charge dynamics of ionic liquids in electrochemical systems,” *Physical Review E*, vol. 84, p. 051504, 2011.
- [57] H. Wang, A. Thiele, and L. Pilon, “Simulations of cyclic voltammetry for electric double layers in asymmetric electrolytes: A generalized modified Poisson-Nernst-Planck model,” *The Journal of Physical Chemistry C*, vol. 117, pp. 18286–18297, 2013.

- [58] W. M. Haynes, T. J. Bruno, and D. R. Lide, eds., *CRC Handbook of Chemistry and Physics*. Boca Raton, FL: CRC Press, 94th ed., 2013.
- [59] J. N. Israelachvili, *Intermolecular and Surface Forces*. London, UK: Academic Press, 2nd ed., 1991.
- [60] A. L. Horvath, *Handbook of Aqueous Electrolyte Solutions: Physical Properties, Estimation and Correlation Methods*. Chichester, UK: Ellis Horwood Ltd, 1985.
- [61] R. Lin, P.-L. Taberna, S. Fantini, V. Presser, C. R. Pérez, F. Malbosc, N. L. Rupesinghe, K. B. K. Teo, Y. Gogotsi, and P. Simon, “Capacitive energy storage from -50 to 100°C using an ionic liquid electrolyte,” *The Journal of Physical Chemistry Letters*, vol. 2, pp. 2396–2401, 2011.
- [62] S. Li, G. Feng, P. F. Fulvio, P. C. Hillesheim, C. Liao, and D. Shang, “Molecular dynamics simulation study of the capacitive performance of a binary mixture of ionic liquids near an onion-like carbon electrode,” *The Journal of Physical Chemistry Letters*, vol. 3, pp. 2465–2469, 2012.
- [63] R. Palm, H. Kurig, K. Tönurist, A. Jänes, and E. Lust, “Is the mixture of 1-ethyl-3-methylimidazolium tetrafluoroborate and 1-butyl-3-methylimidazolium tetrafluoroborate applicable as electrolyte in electrical double layer capacitors?,” *Electrochemistry Communications*, vol. 22, pp. 203 – 206, 2012.
- [64] Z. Adamczyk and P. Warszyński, “Role of electrostatic interactions in particle adsorption,” *Advances in Colloid and Interface Science*, vol. 63, pp. 41–149, 1996.
- [65] F. P. Incropera, D. P. DeWitt, T. L. Bergman, and A. S. Lavine, *Fundamentals of Heat and Mass Transfer*. Hoboken, NJ: John Wiley & Sons, 6th ed., 2007.
- [66] G. Tang, D. Yan, H. Gong, C. Chai, and Y. Lam, “Joule heating and its effects on electrokinetic transport of solutes in rectangular microchannels,” *Sensors and Actuators A*, vol. 139, pp. 221–232, 2007.
- [67] W. B. Gu and C. Y. Wang, “Thermal-electrochemical modeling of battery systems,” *Journal of the Electrochemical Society*, vol. 147, no. 8, pp. 2910–2922, 2000.
- [68] J. P. Joule, “On the heat evolved by metallic conductors of electricity, and in the cells of a battery during electrolysis,” *Philosophical Magazine*, vol. 19, pp. 260–277, 1841.
- [69] G. Rizzoni, *Principles and Applications of Electrical Engineering*. New York, NY: McGraw-Hill, 5th ed., 2007.
- [70] W. T. Scott, *The Physics of Electricity and Magnetism*. New York, NY: John Wiley & Sons, 2nd ed., 1966.
- [71] G. Y. Tang, C. Yang, J. C. Chai, and H. Q. Gong, “Joule heating effect on electroosmotic flow and mass species transport in a microcapillary,” *International Journal of Heat and Mass Transfer*, vol. 47, no. 2, pp. 215–227, 2004.

- [72] N. G. Green, A. Ramos, A. González, A. Castellanos, and H. Morgan, “Electrothermally induced fluid flow on microelectrodes,” *Journal of Electrostatics*, vol. 53, pp. 71–87, 2001.
- [73] P. M. Biesheuvel, D. Brogioli, and H. V. M. Hamelers, “Negative Joule heating in ion-exchange membranes.” arXiv:1402.1448v1, 2014.
- [74] O. Bohlen, J. Kowal, and D. U. Sauer, “Ageing behaviour of electrochemical double layer capacitors: Part I. Experimental study and ageing model,” *Journal of Power Sources*, vol. 172, no. 1, pp. 468–475, 2007.
- [75] R. Kötz, P. W. Ruch, and D. Cericola, “Aging and failure mode of electrochemical double layer capacitors during accelerated constant load tests,” *Journal of Power Sources*, vol. 195, no. 3, pp. 923 – 928, 2010.
- [76] H. Gualous, H. Louahlia, and R. Gallay, “Supercapacitor characterization and thermal modelling with reversible and irreversible heat effect,” *IEEE Transactions on Power Electronics*, vol. 26, no. 11, pp. 3402–3409, 2011.
- [77] C. Pascot, Y. Dandeville, Y. Scudeller, P. Guillemet, and T. Brousse, “Calorimetric measurement of the heat generated by a double-layer capacitor cell under cycling,” *Thermochimica Acta*, vol. 510, pp. 53–60, 2010.
- [78] Y. Dandeville, P. Guillemet, Y. Scudeller, O. Crosnier, L. Athouel, and T. Brousse, “Measuring time-dependent heat profiles of aqueous electrochemical capacitors under cycling,” *Thermochimica Acta*, vol. 526, pp. 1–8, 2011.
- [79] Y. Dandeville, *Analyse Thermique et Électrochimique de Supercondensateurs Carbone-MnO<sub>2</sub> en Milieu Aqueux*. PhD thesis, Université de Nantes, 2012.
- [80] D. H. Lee, U. S. Kim, C. B. Shin, B. H. Lee, B. W. Kim, and Y.-H. Kim, “Modelling of the thermal behaviour of an ultracapacitor for a 42-V automotive electrical system,” *Journal of Power Sources*, vol. 175, no. 1, pp. 664 – 668, 2008.
- [81] K. Wang, L. Zhang, B. Ji, and J. Yuan, “The thermal analysis on the stackable supercapacitor,” *Energy*, vol. 59, pp. 440 – 444, 2013.
- [82] C.-J. Chiang, J.-L. Yang, and W.-C. Cheng, “Temperature and state-of-charge estimation in ultracapacitors based on extended Kalman filter,” *Journal of Power Sources*, vol. 234, pp. 234–243, 2013.
- [83] J. Lee, J. Yi, D. Kim, C. B. Shin, K.-S. Min, J. Choi, and H.-Y. Lee, “Modeling of the electrical and thermal behaviors of an ultracapacitor,” *Energies*, vol. 7, pp. 8264–8278, 2014.
- [84] V. Srinivasan and J. W. Weidner, “Mathematical modeling of electrochemical capacitors,” *Journal of The Electrochemical Society*, vol. 146, pp. 1650–1658, 1999.
- [85] C. Zoski, ed., *Handbook of Electrochemistry*. Oxford, UK: Elsevier, 1st ed., 2007.

- [86] K. H. Radeke, K. O. Backhaus, and A. Swiatkowski, “Electrical conductivity of activated carbons,” *Carbon*, vol. 29, pp. 122–123, 1991.
- [87] A. Subrenat, J. N. Baléo, P. Le Cloirec, and P. E. Blanc, “Electrical behaviour of activated carbon cloth heated by the Joule effect: Desorption application,” *Carbon*, vol. 39, pp. 707–716, 2001.
- [88] COMSOL, Inc., *COMSOL Multiphysics Reference Guide*, COMSOL 4.2 ed., 2011.
- [89] Nippon Kodoshi Corporation. <http://www.kodoshi.co.jp/english/0301-product.htm>, 2004. Accessed April 2012.
- [90] R. B. Bird, W. E. Stewart, and E. N. Lightfoot, *Transport Phenomena*. New York, NY: John Wiley & Sons, 1962.
- [91] T. Engel and P. Reid, *Thermodynamics, Statistical Thermodynamics, and Kinetics*. Upper Saddle River, NJ: Prentice Hall, 2nd ed., 2010.
- [92] J. Chmiola, G. Yushin, Y. Gogotsi, C. Portet, P. Simon, and P. L. Taberna, “Anomalous increase in carbon capacitance at pore sizes less than 1 nanometer,” *Science*, vol. 313, no. 5794, pp. 1760–1763, 2006.
- [93] E. Y. Tyunina, V. N. Afanasiev, and M. D. Chekunova, “Electroconductivity of tetraethylammonium tetrafluoroborate in propylene carbonate at various temperatures,” *Journal of Chemical and Engineering Data*, vol. 56, no. 7, pp. 3222–3226, 2011.
- [94] *CRC Handbook of Chemistry and Physics*. Boca Raton, FL: CRC Press, 92nd ed., 2011.
- [95] COMSOL, Inc., *COMSOL Multiphysics Reference Manual*, COMSOL 4.4 ed., 2013.
- [96] P. Bogacki and L. F. Shampine, “A 3(2)pair of Runge-Kutta formulas,” *Applied Mathematics Letters*, vol. 2, pp. 321–325, 1989.
- [97] “Datasheet: K2 series ultracapacitors,” Product data sheet 1015370.3, Maxwell Technologies, Inc., San Diego, CA.
- [98] “Datasheet: BC series ultracapacitors,” Product data sheet 1017105.3, Maxwell Technologies, Inc., San Diego, CA.
- [99] “Nesscap ultracapacitor products,” product specification sheet: large, prismatic ultracapacitors, Nesscap Co., Ltd., South Korea, 2008.
- [100] M. Tuluszka, F. Jaroszyk, and M. Portalski, “Absolute measurement of the thermal conductivity of propylene carbonate by the AC transient hot-wire technique,” *International Journal of Thermophysics*, vol. 12, no. 5, pp. 791–800, 1991.
- [101] A. Salazar, “On thermal diffusivity,” *European Journal of Physics*, vol. 24, pp. 351–358, 2003.



- [102] H. Wang, J. Fang, and L. Pilon, “Scaling laws for carbon-based electric double layer capacitors,” *Electrochimica Acta*, vol. 109, pp. 316–321, 2013.
- [103] F. Booth, “Dielectric constant of polar liquids at high field strengths,” *Journal of Chemical Physics*, vol. 23, no. 3, pp. 453–457, 1955.
- [104] P. Debye and E. Hückel, “Zur Theorie der Elektrolyte. I. Gefrierpunktserniedrigung und verwandte Erscheinungen,” *Physikalische Zeitschrift*, vol. 24, pp. 185–206, 1923.
- [105] S. Whitaker, *The Method of Volume Averaging*. Dordrecht, the Netherlands: Kluwer Academic Press, 2010.
- [106] H.-L. Girard, H. Wang, A. d’Entremont, and L. Pilon, “Physical interpretation of cyclic voltammetry for hybrid pseudocapacitors,” *Journal of Physical Chemistry C*, vol. 119, no. 21, pp. 11349–11361, 2015.
- [107] J. Come, V. Augustyn, J. W. Kim, P. Rozier, P.-L. Taberna, P. Gogotsi, J. W. Kong, B. Dunn, and P. Simon, “Electrochemical kinetics of nanostructured Nb<sub>2</sub>O<sub>5</sub> electrodes,” *Journal of the Electrochemical Society*, vol. 161, pp. A718–A725, 2014.
- [108] K. Brezesinski, J. Wang, J. Haetge, C. Reitz, S. O. Steinmueller, S. H. Tolbert, B. M. Smarsly, B. Dunn, and T. Brezesinski, “Pseudocapacitive contributions to charge storage in highly ordered mesoporous group V transition metal oxides with iso-oriented layered nanocrystalline domains,” *Journal of the American Chemical Society*, vol. 132, pp. 6982–6990, 2010.
- [109] X. Wang, G. Li, Z. Chen, V. Augustyn, X. Ma, G. Wang, B. Dunn, and Y. Lu, “High-performance supercapacitors based on nanocomposites of Nb<sub>2</sub>O<sub>5</sub> nanocrystals and carbon nanotubes,” *Advanced Energy Materials*, vol. 1, pp. 1089–1093, 2011.
- [110] V. Augustyn, J. Come, M. A. Lowe, J. W. Kim, P.-L. Taberna, S. H. Tolbert, H. D. Abruña, P. Simon, and B. Dunn, “High-rate electrochemical energy storage through Li<sup>+</sup> intercalation pseudocapacitance,” *Nature Materials*, vol. 12, pp. 518–522, 2013.
- [111] D. Bélanger, T. Brousse, and J. W. Long, “Manganese oxides: Battery materials make the leap to electrochemical capacitors,” *The Electrochemical Society Interface*, vol. 17, pp. 49–52, 2008.
- [112] M. Toupin, T. Brousse, and D. Bélanger, “Charge storage mechanism of MnO<sub>2</sub> electrode used in aqueous electrochemical capacitor,” *Chemistry of Materials*, vol. 16, pp. 3184–3190, 2004.
- [113] T. Cottineau, M. Toupin, T. Delahaye, T. Brousse, and D. Bélanger, “Nanostructured transition metal oxides for aqueous hybrid electrochemical supercapacitors,” *Applied Physics A*, vol. 82, no. 4, pp. 599–606, 2006.
- [114] T. Brousse, P.-L. Taberna, O. Crosnier, R. Dugas, P. Guillemet, Y. Scudeller, Y. Zhou, F. Favier, D. Bélanger, and P. Simon, “Long-term cycling behavior of asymmetric activated carbon/MnO<sub>2</sub> aqueous electrochemical supercapacitor,” *Journal of Power Sources*, vol. 173, no. 1, pp. 633–641, 2007.

- [115] Y.-G. Wang and Y.-Y. Xia, “Hybrid aqueous energy storage cells using activated carbon and lithium-intercalated compounds I. the C/LiMn<sub>2</sub>O<sub>4</sub> system,” *Journal of The Electrochemical Society*, vol. 153, pp. A450–A454, 2006.
- [116] L. Kong, C. Zhang, S. Zhang, J. Wang, R. Cai, C. Lv, W. Qiao, L. Ling, and D. Long, “High-power and high-energy asymmetric supercapacitors based on Li<sup>+</sup>-intercalation into a T-Nb<sub>2</sub>O<sub>5</sub>/graphene pseudocapacitive electrode,” *Journal of Materials Chemistry A*, vol. 2, no. 42, pp. 17962–17970, 2014.
- [117] M. S. Hong, S. H. Lee, and S. W. Kim, “Use of KCl aqueous electrolyte for 2 V manganese oxide/activated carbon hybrid capacitor,” *Electrochemical and Solid-State Letters*, vol. 5, no. 10, pp. A227–A230, 2002.
- [118] E. Lim, H. Kim, C. Jo, J. Chun, K. Ku, S. Kim, H. I. Lee, I.-S. Nam, S. Yoon, K. Kang, and J. Lee, “Advanced hybrid supercapacitor based on a mesoporous niobium pentoxide/carbon as high-performance anode,” *ACS Nano*, vol. 8, no. 9, pp. 8968–8978, 2014.
- [119] E. Lim, C. Jo, H. Kim, M.-H. Kim, Y. Mun, J. Chun, Y. Ye, J. Hwang, K.-S. Ha, K. C. Roh, K. Kang, S. Yoon, and J. Lee, “Facile synthesis of Nb<sub>2</sub>O<sub>5</sub>@carbon core-shell nanocrystals with controlled crystalline structure for high-power anodes in hybrid supercapacitors,” *ACS Nano*, vol. 9, no. 7, pp. 7497–7505, 2015.
- [120] B. E. Conway, “Transition from supercapacitor to battery behavior in electrochemical energy storage,” *Journal of the Electrochemical Society*, vol. 138, no. 6, pp. 1539–1548, 1991.
- [121] Y. Zhang and H. Yang, “Modeling and characterization of supercapacitors for wireless sensor network applications,” *Journal of Power Sources*, vol. 196, no. 8, pp. 4128–4135, 2011.
- [122] R. H. Nilson, M. T. Brumbach, and B. C. Bunker, “Modeling the electrochemical impedance spectra of electroactive pseudocapacitor materials,” *Journal of The Electrochemical Society*, vol. 158, no. 6, pp. A678–A688, 2011.
- [123] P. Guillemet, T. Brousse, O. Crosnier, Y. Dandeville, L. Athouel, and Y. Scudeller, “Modeling pseudo capacitance of manganese dioxide,” *Electrochimica Acta*, vol. 67, pp. 41–49, 2012.
- [124] J. F. Robinson and Y. P. Kayinamura, “Charge transport in conducting polymers: insights from impedance spectroscopy,” *Chemical Society Reviews*, vol. 38, pp. 3339–3347, 2009.
- [125] M. Z. Bazant, K. Thornton, and A. Ajdari, “Diffuse-charge dynamics in electrochemical systems,” *Physical review E*, vol. 70, no. 2, p. 021506, 2004.
- [126] K. T. Chu and M. Z. Bazant, “Nonlinear electrochemical relaxation around conductors,” *Physical Review E*, vol. 74, no. 1, p. 011501, 2006.

- [127] C. Lin, J. A. Ritter, B. N. Popov, and R. E. White, “A mathematical model of an electrochemical capacitor with double-layer and faradaic processes,” *Journal of the Electrochemical Society*, vol. 146, no. 9, pp. 3168–3175, 1999.
- [128] H. Kim and B. N. Popov, “A mathematical model of oxide/carbon composite electrode for supercapacitors,” *Journal of the Electrochemical Society*, vol. 150, no. 9, pp. A1153–A1160, 2003.
- [129] K. Somasundaram, E. Birgersson, and A. S. Mujumdar, “Analysis of a model for an electrochemical capacitor,” *Journal of The Electrochemical Society*, vol. 158, no. 11, pp. A1220–A1230, 2011.
- [130] H. Farsi and F. Gobal, “A mathematical model of nanoparticulate mixed oxide pseudocapacitors; Part II: the effects of intrinsic factors,” *Journal of Solid State Electrochemistry*, vol. 15, no. 1, pp. 115–123, 2011.
- [131] S. Devan, V. R. Subramanian, and R. E. White, “Transient analysis of a porous electrode,” *Journal of The Electrochemical Society*, vol. 152, no. 5, pp. A947–A955, 2005.
- [132] J. A. Staser and J. W. Weidner, “Mathematical modeling of hybrid asymmetric electrochemical capacitors,” *Journal of The Electrochemical Society*, vol. 161, no. 8, pp. E3267–E3275, 2014.
- [133] H. Farsi and F. Gobal, “A mathematical model of nanoparticulate mixed oxide pseudocapacitors; Part I: model description and particle size effects,” *Journal of Solid State Electrochemistry*, vol. 13, pp. 433–443, 2009.
- [134] Y. Liu, F. Zhou, and V. Ozolins, “*Ab initio* study of the charge-storage mechanisms in RuO<sub>2</sub>-based electrochemical ultracapacitors,” *The Journal of Physical Chemistry C*, vol. 116, no. 1, pp. 1450–1457, 2011.
- [135] V. Ozolins, F. Zhou, and M. Asta, “Ruthenia-based electrochemical supercapacitors: Insights from first-principles calculations,” *Accounts of Chemical Research*, vol. 46, no. 5, pp. 1084–1093, 2013.
- [136] J. Kang, S.-H. Wei, K. Zhu, and Y.-H. Kim, “First-principles theory of electrochemical capacitance of nanostructured materials: Dipole-assisted subsurface intercalation of lithium in pseudocapacitive TiO<sub>2</sub> anatase nanosheets,” *The Journal of Physical Chemistry C*, vol. 115, no. 11, pp. 4909–4915, 2011.
- [137] D. A. Tompsett, S. C. Parker, P. G. Bruce, and M. S. Islam, “Nanostructuring of  $\beta$ -MnO<sub>2</sub>: The important role of surface to bulk ion migration,” *Chemistry of Materials*, vol. 25, no. 4, pp. 536–541, 2013.
- [138] H. Ding, K. G. Ray, V. Ozolins, and M. Asta, “Structural and vibrational properties of  $\alpha$ -MoO<sub>3</sub> from van der Waals corrected density functional theory calculations,” *Physical Review B*, vol. 85, no. 1, p. 012104, 2012.

- [139] G. Feng and P. T. Cummings, "Supercapacitor capacitance exhibits oscillatory behavior as a function of nanopore size," *The Journal of Physical Chemistry Letters*, vol. 2, no. 22, pp. 2859–2864, 2011.
- [140] Y. Shim and H. J. Kim, "Nanoporous carbon supercapacitors in an ionic liquid: A computer simulation study," *ACS nano*, vol. 4, no. 4, pp. 2345–2355, 2010.
- [141] H. Wang, J. Varghese, and L. Pilon, "Simulation of electric double layer capacitors with mesoporous electrodes: Effects of morphology and electrolyte permittivity," *Electrochimica Acta*, vol. 56, pp. 6189–6197, 2011.
- [142] C.-Y. Wang, "Fundamental models for fuel cell engineering," *Chemical Reviews*, vol. 104, no. 10, pp. 4727–4766, 2004.
- [143] C.-W. Wang and A. M. Sastry, "Mesoscale modeling of a Li-ion polymer cell," *Journal of the Electrochemical Society*, vol. 154, no. 11, pp. 1035–1047, 2007.
- [144] X. Xiao, W. Wu, and X. Huang, "A multi-scale approach for the stress analysis of polymeric separators in a lithium-ion battery," *Journal of Power Sources*, vol. 195, no. 11, pp. 7649–7660, 2010.
- [145] R. Chandrasekaran, A. Magasinski, G. Yushin, and T. F. Fuller, "Analysis of lithium insertion/deinsertion in a silicon electrode particle at room temperature," *Journal of the Electrochemical Society*, vol. 157, no. 10, pp. 1139–1151, 2010.
- [146] P. M. Biesheuvel, M. van Soestbergen, and M. Z. Bazant, "Imposed currents in galvanic cells," *Electrochimica Acta*, vol. 54, no. 21, pp. 4857–4871, 2009.
- [147] A. Frumkin, "Hydrogen overvoltage and the structure of the double layer," *Zeitschrift für Elektrochemie*, vol. 164A, pp. 121–133, 1933.
- [148] S. R. Subramanian, V. Boovaragavan, V. Ramadesigan, and M. Arabandi, "Mathematical model reformulation for lithium-ion battery simulations: Galvanostatic boundary conditions," *Journal of the Electrochemical Society*, vol. 156, no. 4, pp. 260–271, 2009.
- [149] A. Bonnefont, F. Argoul, and M. Z. Bazant, "Analysis of diffuse-layer effects on time-dependent interfacial kinetics," *Journal of Electroanalytical Chemistry*, vol. 500, no. 1–2, pp. 52–61, 2001.
- [150] J. Desilvestro and O. Haas, "Metal oxide cathode materials for electrochemical energy storage: A review," *Journal of the Electrochemical Society*, vol. 137, pp. 5C–22C, 1990.
- [151] D. Zhang, B. N. Popov, and R. E. White, "Modeling lithium intercalation of a single spinel particle under potentiodynamic control," *Journal of the Electrochemical Society*, vol. 147, no. 3, pp. 831–838, 2000.
- [152] A. M. Colclasure and R. J. Kee, "Thermodynamically consistent modeling of elementary electrochemistry in lithium-ion batteries," *Electrochimica Acta*, vol. 55, pp. 8960–8973, 2010.

- [153] G. M. Goldin, A. M. Colclasure, A. H. Wiedemann, and R. J. Kee, “Three-dimensional particle-resolved models of li-ion batteries to assist the evaluation of empirical parameters in one-dimensional models,” *Electrochimica Acta*, vol. 64, pp. 118–129, 2012.
- [154] M. D. Chung, J. H. Seo, X. C. Zhang, and A. M. Sastry, “Implementing realistic geometry and measured diffusion coefficients into single particle electrode modeling based on experiments with single  $\text{LiMn}_2\text{O}_4$  spinel particles,” *Journal of the Electrochemical Society*, vol. 158, pp. 371–378, 2011.
- [155] T. R. Jow and J. P. Zheng, “Electrochemical capacitors using hydrous ruthenium oxide and hydrogen inserted ruthenium oxide,” *Journal of the Electrochemical Society*, vol. 145, pp. 49–52, 1998.
- [156] K. Nishikawa, Y. Fukunaka, T. Sakka, Y. H. Ogata, and J. R. Selman, “Measurement of  $\text{LiClO}_4$  diffusion coefficient in propylene carbonate by Moiré pattern,” *Journal of the Electrochemical Society*, vol. 153, pp. A830–A834, 2006.
- [157] J. Xu and G. C. Farrington, “A novel electrochemical method for measuring salt diffusion coefficients and ion transference numbers,” *Journal of the Electrochemical Society*, vol. 143, no. 2, pp. L44–L47, 1996.
- [158] V. Augustyn, P. Simon, and B. Dunn, “Pseudocapacitive oxide materials for high-rate electrochemical energy storage,” *Energy and Environmental Science*, vol. 7, pp. 1597–1614, 2014.
- [159] E. R. Cohen, T. Cvitas, J. G. Frey, B. Holmström, K. Kuchitsu, R. Marquardt, I. Mills, F. Pavese, M. Quack, J. Stohner, H. . Strauss, M. Takami, and A. J. Thor, eds., *Quantities, Units and Symbols in Physical Chemistry*. IUPAC Green Book, Cambridge, UK: IUPAC and RSC Publishing, 3rd ed., 2008.
- [160] M. A. Liberman, *Introduction to Physics and Chemistry of Combustion*. Springer-Verlag Berlin Heidelberg, 2008.
- [161] A. L. d’Entremont and L. Pilon, “Electrochemical transport phenomena in hybrid pseudocapacitors under galvanostatic cycling,” *Journal of The Electrochemical Society*, vol. (under review), 2015.
- [162] J. E. Schlewitz, “Niobium and niobium compounds,” in *Kirk-Othmer Encyclopedia of Chemical Technology*, pp. 1–27, John Wiley & Sons, Inc., 2009.
- [163] E. S. Domalski and E. D. Hearing, ““Condensed phase heat capacity data”,,” in *NIST Chemistry WebBook, NIST Standard Reference Database Number 69* (P. J. Linstrom and W. G. Mallard, eds.), Gaithersburg, MD: National Institute of Standards and Technology, 2011.
- [164] R. W. Powell, C. Y. Ho, and P. E. Liley, *Thermal conductivity of selected materials*. National Standard Reference Data Series. (NSRDS-NBS 8), Washington, D.C.: U.S. Dept. of Commerce, National Bureau of Standards, 1966.

- [165] Design Institute for Physical Properties, “DIPPR Project 801 - Full version.” American Institute of Chemical Engineers (AIChE), 2012.
- [166] Q. Huang, M. Yan, and Z. Jiang, “Thermal study on single electrodes in lithium-ion battery,” *Journal of Power Sources*, vol. 156, pp. 541–546, 2006.